

The self-healing mechanism of macro cracks in asphalt mortar and its influencing factors



**University of
Nottingham**
UK | CHINA | MALAYSIA

by Daniel Grossegger
Nottingham Transportation Engineering Centre
Department of Engineering
University of Nottingham

This dissertation is submitted for the degree of Doctor of Philosophy
May 2019

List of publications

The following publications were issued based on the results obtained during the PhD and are used in the thesis:

Grossegger D., Garcia A. (2019, Mai) Asphalt self-healing, explained. *Paper presented at the 7th International Conference on Self-healing Materials (ICSHM2019)*, Yokohama, Japan.

Grossegger D., Garcia A. (resubmitted) The effect of water and pressure on the self-healing of macro cracks in asphalt mortar beams. *Construction and Building Materials*

Grossegger D., Garcia A. (2019) Influence of the thermal expansion of bitumen on asphalt self-healing. *Applied Thermal Engineering*, 156, 23-33.

Grossegger D., Gomez-Meijide B., Senise S., Garcia A., Airey G. (2018, June) Factors affecting the reachable healing level of induced self-healing of mastic beams. *Paper presented at the 2018 International Society for Asphalt Pavement conference (ISAP2018)*, Fortaleza, Brazil.

Grossegger D., Gomez-Meijide B., Vansteenkiste S., Garcia A. (2018) Influence of rheological and physical bitumen properties on heat-induced self-healing of asphalt mastic beams. *Construction and Building Materials*, 182, 298-308.

Abstract

Road structures deteriorate with advancing time. This is a result of the exposure to aperiodic mechanical stress due to traffic and changes in the chemical composition and physical behaviour due to exposure to atmospheric radicals, radiation and temperature changes. A specific part of the deterioration, namely the occurrence of cracks and involved loss or reduction of mechanical properties, can be partly healed or recovered by the intrinsic ability of asphalt to self-heal. The asphalt component bitumen is responsible for the self-healing occurring at different scale lengths of bituminous materials. This is based on the thermal and viscoelastic properties of bitumen.

The self-healing of macro cracks in asphalt mortar is mainly governed by the viscous flow of bitumen rich mortar or mastic from the vicinity of the crack into it. The flow is driven by gravity, capillary force and thermal expansion if a positive temperature change occurs. The asphalt composition, grain structure, filler content, bitumen content, bitumen type, modifications, additives and the temperature change determine the self-healing rate and efficiency, defined as the self-healing ratio. A crucial aspect is the formation of a load bearing connection between the fracture surfaces of a fractured aggregate. This is achieved if bitumen/mastic drains into the crack of the aggregate and adheres the fracture surfaces together. However, this results in a lower breaking resistance.

Based on physical principles, a model was developed which regards the self-healing as a flow process between two parallel plates, conceptionally representing a crack. This model was used to accurately fit the self-healing ratios obtained by three-point breaking of asphalt mortar beams. Furthermore, to determine the relation of properties of bitumen on the self-healing of a macro crack, a Pearson correlation analysis was conducted. The bitumen types investigated and used to produce the asphalt mortar beams are commonly used for asphalt production and were similar. The correlation analysis revealed that the self-healing is linearly correlated to the softening point and the surface tension. Other properties were not significantly different, resulting in the similar healing ratios obtained.

Pressure, which forces the crack surfaces together and mastic to drain into the crack, was identified to be a main contributor for the self-healing. Pressure can originate from confined thermal expansion, porewater, hydrostatic or mechanical sources. That pressure arising from thermal expansion affected the self-healing was shown as the self-healing rate and the self-healing level increased with increasing temperature difference. The effect of confinement on the thermal expansion was illustrated through two capillary experiments and the crucial influence of the capillary diameter and the flow process. Water filling the crack prevented self-healing. However, during the evaporation of water, the water free crack healed better compared to non-water treated asphalt mortar beams, due to the remaining porewater in the beam. By applying a horizontal/circumferential pressure during the self-healing, higher self-healing ratios were achieved and the self-healing rate was increased, supporting the positive influence of compressive pressure on the crack surface for self-healing. In contrast, uniform pressure did not affect the self-healing.

Contents

List of publications	2
Abstract.....	3
Contents.....	4
1 Introduction.....	7
1.1 Background.....	7
1.2 Research aims.....	9
1.3 Research objectives.....	9
1.4 Limitations of the research.....	9
1.5 Organisation of the thesis.....	9
2 Literature review	11
2.1 Introduction.....	11
2.2 Materials.....	11
2.2.1 Bitumen.....	11
2.2.1.1 Petroleum origin and bitumen production.....	12
2.2.1.2 Chemical properties.....	14
2.2.1.3 Generic fractional composition of bitumen.....	15
2.2.1.4 Structural features.....	17
2.2.1.5 Physical properties.....	18
2.2.1.6 Rheological properties.....	18
2.2.1.7 Bitumen ageing.....	19
2.2.2 Modifications and additives.....	20
2.2.2.1 Modifications.....	20
2.2.2.2 Additives.....	21
2.2.3 Aggregates.....	21
2.2.3.1 Mineral aggregates.....	21
2.2.3.2 Filler.....	22
2.2.4 Asphalt.....	22
2.2.4.1 Asphalt production.....	23
2.2.4.2 Asphalt properties.....	23
2.3 Road structure.....	24
2.4 Road failure.....	25
2.4.1 Cracks/fractures.....	25
2.4.2 Moisture susceptibility.....	26
2.5 Self-healing mechanism.....	26
2.5.1 Self-healing materials.....	27
2.5.2 Intrinsic self-healing mechanics.....	28
2.5.3 Extrinsic self-healing mechanics.....	29
2.5.4 Self-healing models.....	30
2.5.5 Self-healing in bituminous materials.....	32
2.5.5.1 Self-healing at the nanoscale (bitumen microstructure).....	33
2.5.5.2 Self-healing at the microscale (mastic and bitumen).....	34
2.5.5.3 Self-healing at the mesoscale (mortar).....	36
2.5.5.4 Self-healing at the macroscale (asphalt).....	36
2.5.5.5 Induced self-healing in asphalt.....	37
2.5.5.6 Extrinsic self-healing in asphalt.....	38

2.6	Summary	39
3	Materials and methods.....	41
3.1	Materials	41
3.1.1	Bitumen.....	41
3.1.2	Aggregates	41
3.1.3	Asphalt mortar, mastic and bitumen beams	42
3.2	Methods	43
3.2.1	Needle penetration	43
3.2.2	Softening point.....	43
3.2.3	Bitumen ageing	43
3.2.3.1	Rolling Thin Film Oven Test (RTFOT)	43
3.2.3.2	Pressure Ageing Vessel (PAV).....	44
3.2.4	Viscosity	44
3.2.5	Viscoelasticity.....	44
3.2.6	Density and thermal expansion coefficient	45
3.2.7	Bulk density and void characteristics of bituminous material	45
3.2.8	Capillary rise.....	46
3.2.9	Surface tension	47
3.2.9.1	Capillary height method	47
3.2.9.2	Sessile droplet method	47
3.2.9.3	Wilhelmy plate method.....	47
3.2.10	Fractional distribution	48
3.2.11	Attenuated total reflection Fourier transformed infrared spectroscopy	48
3.2.12	Bitumen and mortar flow in a Hele-Shaw cell	48
3.2.13	Determining gap flow and drainage composition	49
3.2.14	Self-drainage of viscous liquids on a vertical surface	50
3.2.15	Specific surface area	50
3.2.16	Water evaporation	51
3.2.17	Mechanical testing (three-point breaking).....	51
3.2.18	Self-healing conditions	52
3.2.19	Adhesion testing and healing	54
3.2.20	Computer tomography scans (CT scans)	55
3.2.21	Optical images	55
4	Self-healing of cracks	56
4.1	Conceptual model of asphalt self-healing	56
4.2	Physical model of asphalt self-healing	57
4.2.1	Modelling the energy input into the self-healing system	61
5	Material properties of bitumen, aggregates and their mixture.....	64
5.1	Physical, rheological and chemical properties of bitumen	64
5.1.1	Conventional tests	64
5.1.2	Viscosity	64
5.1.3	Viscoelasticity.....	66
5.1.4	Density and thermal expansion	68
5.1.5	Bitumen flow in vertical glass capillaries	69
5.1.5.1	Unconfined capillary flow	69
5.1.5.2	Confined capillary flow.....	71
5.1.6	Surface tension	73
5.1.7	Dynamic contact angle inside a capillary	75
5.1.8	Fractions of bitumen	77

5.1.9	Infrared analysis and methyl to methylene ratio	79
5.2	<i>Correlation of bitumen properties</i>	82
5.3	<i>Aggregate properties</i>	84
5.4	<i>Mastic properties</i>	84
5.4.1	Viscosity	84
5.4.2	Density and thermal expansion	85
5.5	<i>Asphalt mortar beam properties</i>	86
5.6	<i>Summary</i>	88
6	Self-healing of macro cracks due to induced heating	90
6.1	<i>Thermal behaviour of asphalt mortar beams</i>	90
6.1.1	Convection heating for different oven temperatures	90
6.1.2	Induction heating with different current intensities	91
6.1.3	Self-healing at different oven temperatures with and without circumferential pressure	92
6.1.4	Self-healing due to induction heating with different current intensities	97
6.2	<i>Summary</i>	98
7	Influence of the bitumen type on the self-healing of macro cracks	100
7.1	<i>Thermal behaviour of asphalt mortar beams with different bitumen types</i>	100
7.1.1	Convection heating	100
7.1.2	Induction heating	101
7.1.3	Convection cooling	103
7.1.4	Calculation of the pseudo healing energy parameter	104
7.2	<i>Induced self-healing of macro cracks for different bitumen types</i>	105
7.3	<i>Correlation of chemical, rheological and physical parameters to self-healing parameters</i>	109
7.4	<i>Summary</i>	112
8	Self-healing of macro cracks in different mortar mixtures	113
8.1	<i>Thermal behaviour of asphalt mortar beams with varying bitumen or filler content</i>	113
8.2	<i>Self-healing of asphalt mortar beams with varying bitumen or filler content</i>	114
8.3	<i>Flow of mastic and mortar</i>	115
8.4	<i>Summary</i>	120
9	Influence of water on the self-healing mechanism	121
9.1	<i>The effect of water on selected bitumen properties</i>	121
9.1.1	The effect on bitumen's viscosity	121
9.1.2	The effect on bitumen's surface tension	122
9.2	<i>The effect of water on the gravitational flow</i>	125
9.3	<i>Water evaporation from asphalt mortar beams</i>	127
9.4	<i>Self-healing of asphalt mortar beams</i>	128
9.5	<i>Summary</i>	133
10	Summary and conclusion	134
10.1	<i>Summary</i>	134
10.2	<i>Conclusion</i>	139
10.3	<i>Recommended further investigations on self-healing</i>	140
	Bibliography	141

1 Introduction

1.1 Background

A functioning infrastructure network is the backbone of any civilisation, as economy and civil life rely on working transportation systems. The durability of these systems is strained by the growing challenges of increasing traffic volume and axle loads, resource consumption, decreasing investments in maintenance, climate change and environmental issues. Modern road networks have to last longer until mended or replaced, but yet, are subjected to increasing strain and stress from traffic and weather, which shortens the lifetime of roads.

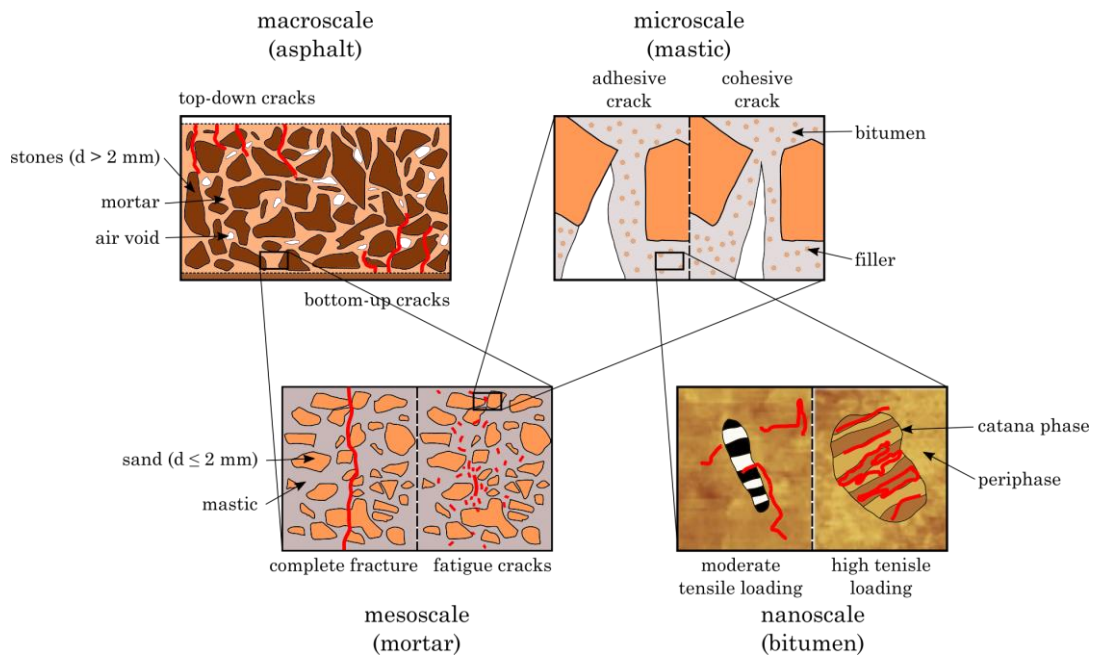


Figure 1.1: Cracks from macro- to nanoscale.

The most common material to support modern transportation is asphalt [1]. Asphalt is a composite material, consisting of aggregates (mineral particles with dimensions smaller than 55 mm), a viscoelastic liquid, known as bitumen, and air voids [2]. The degradation of asphalt roads is a consequence of its usage by vehicles, ageing and inter layer separation due to moisture and loss of bonding. Due to internal and atmospheric chemical reactions, aged asphalt roads are more brittle and have a reduced relaxation capacity. Hence, defects like cracks (a main defect in roads), ravelling, potholes and other forms can develop, as the probability of crack appearance and propagation increases, deteriorating the road's condition [3-8]. Different types of cracks can be observed in bituminous materials ranging from macroscale to nanoscale, as illustrated in Figure 1.1. At the macroscale, cracks in asphalt roads can be top-down, due to tensile and shear stress in the top layer and additional contribution from environmental conditions and ageing, or bottom-up, due to tensile stress at the bottom asphalt layer [3]. At low temperatures loading can cause a complete fracture (complete break, causing it to be separated into two or more pieces). Repeated loading causes localised structural damage, mostly in the form of micro cracks (below 0.1 mm) [9, 10]. These micro cracks are initiated at the microscale level and propagate to the mesoscale as they grow and coalesce [7, 11]. The interface of a crack can

either be between mastic/bitumen and aggregates (adhesive crack), within mortar/bitumen (cohesive crack) or most commonly, a combination of these crack types [3]. However, certain cracks sometimes vanish. This contributes to a prolonged lifetime of the road at the macroscale.

The ability to inherently recover part of lost functionalities or from damage is known as self-healing [12]. Bitumen and bituminous materials (for example asphalt) exhibit this self-healing phenomenon. Since the 1960s, the recovery of fatigue characteristics due to rest periods has been investigated [10, 13, 14]. In the last 20 years the research on self-healing in bituminous materials increased [15-25] and methods to enhance the self-healing, such as rejuvenator filled capsules [26], microwave heating [27], infrared radiation heating [28] and induction heat generation [29], have been developed.

A general definition of the self-healing mechanism is derived from polymer chemistry. It states that the self-healing starts if two pieces of the same material are brought into contact at a temperature above the glass transition temperature [30]. This concept applies to bituminous material as well, as the material has to be in contact to form a load bearing connection after a crack was initiated [31]. The temperature has to be high enough to allow fracture surface deformation, flow of bitumen and molecular movement across the interface of rejoined crack surfaces. However, no uniform agreed definition of the self-healing mechanism exists for bituminous materials yet. Most models and concepts include the approach of fracture surfaces, which is time-dependent and condition-dependent (temperature, pressure and moisture). Self-healing is often quantified by mechanical tests. Therefore, the start of the self-healing was defined to be the start of a measurable increase in the mechanical property monitored. This was in most cases the moment that crack surfaces were in contact, neglecting the approach of the crack surfaces. In other cases, for example the hypothesis of capillary flow [17], the approach of crack surfaces is neglected as it is stated that the crack is filled due to bitumen flowing from the surrounding mixture into the crack. Furthermore, asphalt, mortar and mastic can be perceived as a continuous material at their respective superordinate scale. However, the inhomogeneity at the respective scale results in a more complex or different self-healing mechanism of bituminous material at different scales.

So far, the self-healing mechanism has been investigated for factors affecting the healing process based on laboratory experiments, linking the mechanism to hypotheses and universal models. The self-healing of asphalt or bitumen was evaluated either regarding the healing of complete fractures (usually a macro crack separating a sample into two) [19, 32] or the healing of fatigue induced damage [33-35]. Self-healing of complete fractures or fatigue cracks depends on several factors, such as bitumen type, filler type, temperature, degree of ageing, rest period between loading and loading history [13, 36-39]. Other factors with regard to triggerable healing methods have also been investigated. Some factors like moisture or the pollution of fracture surface with micro particles have yet to be investigated, and these factors may have an effect on the self-healing of asphalt. More specifically, aspects such as the inter-correlation of healing at different scale lengths, in regards to the understanding of the self-healing mechanism are yet missing.

1.2 Research aims

The main aim of this research is to contribute to a better understanding of the self-healing mechanism of fractures in asphalt. Therefore bitumen's physical, rheological and chemical characteristics, linking to the self-healing of asphalt, are important parameters to understand the healing mechanism and how it is affected by environmental conditions. Furthermore, to clarify which part of an asphalt contributes to the healing and how a crack disappears, material available to move in the asphalt structure to fill cracks needs to be identified.

1.3 Research objectives

To achieve the above aims, this research had three objectives:

1. The physical, rheological and chemical characteristics of five different bitumen will be determined over a wide temperature range (about 20 °C to 160 °C, depending on characteristic and method used). These characteristics will be inter-correlated to evaluate compliance with known correlations and further correlated to defined self-healing parameters obtained from fracture-healing tests.
2. The recovery of the three-point breaking strength of asphalt mortar beams will be determined after self-healing is initiated by different heating methods. The heating methods are convection heating and induction heating. The main focus is on convection heating with a range of different temperatures (40 °C to 120 °C). Furthermore, the influence of pressure on asphalt self-healing will be analysed. In addition, the effect of water exposure pre and during self-healing will be investigated.
3. The effects of variations of bitumen content and filler content on the self-healing of asphalt mortar mixtures will be determined. In addition, the flow of material through a gap during the healing duration will be investigated. The drained material will be analysed with regards to its composition and compared to the composition of the mixture.

1.4 Limitations of the research

The main research was conducted on mortar mixtures and five different bitumen types. This limits some observed results to the mixture design and the type of bitumen used. In order to confirm the conformity at other scale lengths, similar experiments should be conducted in asphalt mixtures.

1.5 Organisation of the thesis

The thesis is divided into nine chapters.

A general introduction into the topic of self-healing phenomenon and mechanism in bituminous material is provided in Chapter 1. Further, the research problem is defined and the concept of the research and structure of the thesis is provided.

Chapter 2 summarises the detailed literature on the topic of bituminous materials and the self-healing phenomenon. This chapter includes general material properties of asphalt compositions, asphalt and asphalt road production, two common forms of road failures, a

definition of the self-healing mechanism, self-healing models and findings on damage recovery on the scale of bitumen, mastic, mortar and asphalt. New research approaches on novel induced recovery systems are also reviewed.

The research approach is given in Chapter 3, outlining detailed information about materials and methods used. The mechanical based self-healing ratio is defined by experimental methods and the condition of mixture compositions and self-healing conditions are stated.

Chapter 4 provides a theoretical consideration of the self-healing in an asphalt road and provides a simple augmented self-healing model of cracks based on the capillary flow hypothesis. The final equation of the self-healing ratio function was derived from the Navier-Stokes equation for the flow between two parallel, permeable plates, which should have a gap distance allowing the capillary force to be effective.

In Chapter 5, the material properties obtained are compared to each other, to trends known in the literature and their known influence on the self-healing. Beside bitumen and aggregate properties, properties of mastic mixtures and the different produced asphalt mortar beams are provided.

The self-healing of macro cracks in asphalt mortar beams due to different temperatures through convection heating and different current intensities through induction heating are described in Chapter 6.

Chapter 7 compares the self-healing of different bitumen types for convection and induction heating. Furthermore, the material properties of Chapter 5 are correlated to the self-healing to gain insight on the healing in relation to the derived physical model.

The influence of bitumen content and filler content is outlined in Chapter 8. Moreover, the drainage of mixture material into a horizontal gap during the heating phase of convection heating was studied to identify flowable parts of the mixture contributing to the self-healing.

The effect of water on the self-healing of a macro crack in asphalt mortar beams is presented in Chapter 9. Conditions before the self-healing and conditions during the self-healing affected the self-healing, beside the known influence of healing duration and temperature. On one hand, water had a preventing effect and on the other hand, water enhanced the self-healing. In addition, the influence of uniform pressure was investigated.

Chapter 10 summarises the findings and presents the conclusions of this research and further recommendations.

2 Literature review

2.1 Introduction

Approximately 90% of the European road network consists of asphalt roads [1]. Asphaltic material is further used in, for example, railway constructions, embankment constructions and roofing. The lifetime of these constructions is limited as asphalt is exposed to different weather conditions (temperatures and humidities), atmospheric radicals, other chemical reactions, radiation, abrasion and mechanical loading (permanent and/or regularly/irregularly oscillating). These exposures cause material loss (abrasion), changes within the material due to chemical reactions or emplacement of water and the appearance and propagation of cracks. In situ observations of road constructions have often shown a longer lifetime compared to lifetime expectancies predicted by laboratory tests [10, 13, 14]. The difference in lifetime (predicted to actual) can be partly explained by the recovery of functionalities due to the closing of cracks, known as healing. In asphaltic (bituminous) materials the component bitumen is mainly responsible for the self-healing of cracks [21, 31]. At the beginning of the 21st century, engineers are exploiting ways to enhance and trigger the self-healing phenomenon in a targeted manner.

The literature review comprises materials, road structure, road failure and the self-healing phenomenon and mechanism. Materials comprise bitumen, mineral aggregates, additives and modifications and the mixture – asphalt. In road structure, the general layer structure of roads is described. Road failure summarises the appearance and propagation of cracks to form macro cracks in the road structure and the influence of moisture. Inherent healing phenomenon introduces the concept of self-healing materials and focuses on the self-healing mechanism in bituminous materials.

2.2 Materials

First, the single components of the composite material asphalt are introduced with the description of the chemical complex, viscoelastic liquid bitumen, followed by modifications and additives for bitumen and the component aggregates. Afterwards asphalt and asphalt production are described.

2.2.1 Bitumen

Bitumen is a demand orientated residue product from petroleum distillation and is further post-processed by e.g. air blowing, deasphalting or blending to achieve the properties desired in the final product, as shown in Figure 2.1. As a product of petroleum refining, it consists mainly of hydrocarbons and can be described as a composite, due to the high variety of different molecules. Other elements present in bitumen are sulphur, nitrogen, oxygen and traces of other elements, mostly metals like iron, nickel and vanadium [1-3, 40, 41]. Beside industrially produced bitumen, naturally occurring bitumen (native bitumen) is obtained from asphalt lakes. The largest asphalt lake is Pitch Lake in the southwest of Trinidad and it is also the largest natural deposition of asphalt. Native bitumen differs from petroleum bitumen as it is unrefined and often contains low-molecular hydrocarbons, mineral particles and occasionally water [1].



Figure 2.1: Bitumen flowing out of a tin, due to gravity. The high viscosity of bitumen is responsible for spilling of bitumen at ambient temperature taking a long time [42].

The use of high viscous, adhesive petroleum (likely native bitumen) dates back to the Middle Palaeolithic, when it was used as adhesive to craft tools. In the Antiquity, native bitumen was utilised due to its adhesivity and waterproofing and found applications in medicine. After vanishing in deployment for nearly two and a half centuries, the usage of bitumen was rediscovered in the 19th century. Native bitumen began to be replaced by the residue from the vacuum distillation of petroleum in the 1910s. And at the beginning of the 21st century bitumen is mainly obtained by petroleum refinery and 85% is applied as a binder in road and other pavement constructions [41]. Other relevant applications include roofing (about 10%) and secondary uses (about 5%) [1].

The properties of bitumen mainly depend on the properties of the original petroleum and the treatment processes afterwards [41]. Hence, certain properties vary in a broad spectrum while others are similar for all bitumen.

2.2.1.1 Petroleum origin and bitumen production

An inorganic and an organic hypothesis exist about the origin of petroleum. The inorganic hypothesis is based on the polymerisation and condensation reaction of ethylene (C_2H_2) at high temperature and pressure. Ethylene is formed in the reaction of water (H_2O) with calcium carbide (CaC_2), as calcium carbonate ($CaCO_3$) reacts with alkali metals (Li, Na, K, Rb, Cs or Fr). This hypothesis was soon replaced by the organic hypothesis due to logical evidence. In contrast to the mineral's carbon based inorganic hypothesis, the carbon source for the organic hypothesis is biomass that inhabited the seas and oceans (special microorganisms like phytoplankton). The highest concentration of organic material forms at the bottom of the sea. This material can be trapped by mineral accumulation on top of it (sedimentation or submarine landslide). The encapsulation prevents contact with oxygen and hence decomposition, which would lead to more soluble products. Additional layers of material and plate tectonics trap the organic material and it might pass through zones of rifts or subductions, where the temperature increases by 100 °C to 400 °C (in a depth of 2 km to 3 km). This temperature range provides the necessary energy to dissociate various organic compounds and results in the formation of petroleum [2, 40].

In order to unearth petroleum, it is either extracted from oil wells under natural pressure (primary recovery), by pumping (secondary recovery) or by enhancing oil mobility (enhanced/tertiary recovery). These methods concurrently extract petroleum and water layers. Thereby petroleum, most frequently the continuous phase, and water, the

discontinues phase, forms an emulsion. The degree of dispersion varies with the extraction method and transportation through pipes. Natural or added (tertiary recovery) emulsifier further influences the formation and properties of the mixture. The following subsequent drying process is based on the amount of water. If the emulsion is non-stabilised, it can be separated by settling methods with or without moderate heating. A stabilised emulsion is more difficult to separate. The methods applied include heating, chemical processing, electrical processing or a combination of those methods. A desalting step is often implemented in the drying process, by removing water contacting dissolved minerals (chemical or electrical separation) [40].

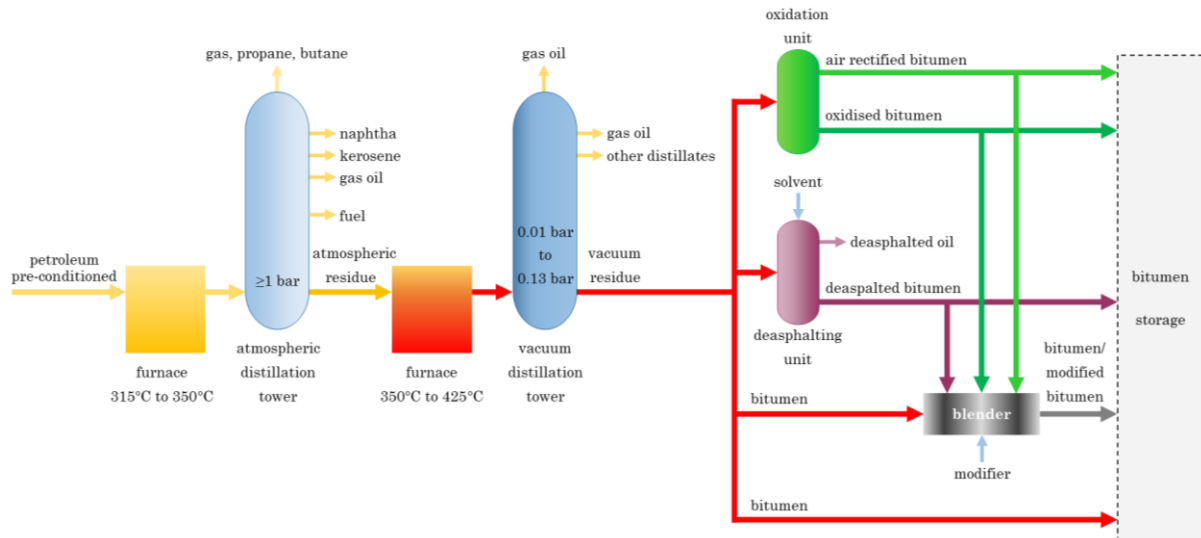


Figure 2.2: Bitumen production scheme (based on [1, 41]).

The pre-conditioned oil is the starting material for the petroleum refinery, which is shown in Figure 2.2. The first process in the refinery is rectification, which is used as the boiling points of the petroleum components are close to one another. Two different towers are used for the rectification process according to the predominant pressure: atmospheric towers and vacuum towers. The pre-conditioned petroleum is pumped from storage tanks through heat exchangers and ovens to preheat the fluid to 315 °C to 350 °C and enters at the lower part of the atmospheric tower. Atmospheric towers operate at a pressure ranging from ambient pressure to over pressure and are heated at the bottom of the tower to ensure lighter components rise as vapour. Condensing fluids are extracted at different levels and either are fed back in as reflux, further purified in side cut strippers or removed as product. The residue of the atmospheric tower is further separated in the vacuum tower, which functions on the same principles, though the operating pressure ranges from 1,333 Pa to 13,332 Pa. Thermal cracking is avoided by maintaining temperatures below 425 °C. The residue of the vacuum tower is either used as feedstock for thermal cracking or coking units or is used for the bitumen production [1, 3, 40, 41].

Only certain petroleum types are selected for the production of bitumen, which is approximately 10vol.% to 15vol.% of the petroleum unearthed. This is to ensure that the final product has the right properties and does not change (age) too fast during environmental exposure [43]. Bitumen has a share of 3% to 4% of the refinery products [1].

During post-process, the chemical compositions of bitumen are altered, as the vacuum residue does not always have the desired properties. The processes of thermal cracking, catalytic cracking and visbreaking breaks intramolecular bonds and thus reduces viscosity. This process is often followed by further vacuum distillation to remove lighter compounds. The viscosity can be increased through oxidation. Two grades of oxidised bitumen exist: air rectified (semi-blown) and oxidised (blown) bitumen. Further, in the process of deasphalting the asphaltene fraction is removed with solvents (mostly alkanes). Sulphur is removed by desulfurisation. The final product is often blended with different bitumen to achieve the desired properties. If the blending process includes the addition of polymers, polymer modified bitumen (PMB) is produced. Oxidation during transport and storage is avoided by pressurising the heated tanks with nitrogen [1-3, 40, 41].

2.2.1.2 Chemical properties

As a product of the petroleum refinery process, bitumen consists mainly of hydrogen and carbon, forming hydrocarbons and hydrocarbon derivatives. The average molecular weight of bitumen ranges from $600 \text{ g}\cdot\text{mol}^{-1}$ to $1500 \text{ g}\cdot\text{mol}^{-1}$. The ratio between hydrogen and carbon (H/C) is approximately 1.5. Hence, bitumen ranges between aromatic structures and double bond rich alkenes with the lowest ratio of 1 for benzene and saturated alkenes with a ratio approaching 2 with increasing chain length. Other elements can be present in varying concentrations and are nitrogen, oxygen, sulphur and traces of mostly metals [1, 2, 40, 41]. The concentration depends mainly on the petroleum source and the production process. During production, the presence of some elements may increase due to abrasion of pumps or pipes (mostly increase of metals), oxidation (an increase of oxygen and potential decrease of sulphur) or desulfurisation (decrease of sulphur) [1, 8, 40, 41]. Table 2.1 shows elements and their concentration range found in bitumen.

Table 2.1: Elemental composition of bitumen [1, 40, 41, 44].

element	content [wt.%]
carbon (C)	80.2 – 86.8
hydrogen (H)	9.8 – 11.3
sulphur (S)	0.9 – 6.9
oxygen (O)	0.4 – 1.1
nitrogen (N)	0.2 – 1.2
vanadium (V)	$7\cdot 10^{-4}$ – $1590\cdot 10^{-4}$
nickel (Ni)	$10\cdot 10^{-4}$ – $130\cdot 10^{-4}$
sodium (Na)	$6\cdot 10^{-4}$ – $159\cdot 10^{-4}$
iron (Fe)	$5\cdot 10^{-4}$ – $147\cdot 10^{-4}$
calcium (Ca)	$1\cdot 10^{-4}$ – $335\cdot 10^{-4}$
magnesium (Mg)	$1\cdot 10^{-4}$ – $134\cdot 10^{-4}$
manganese (Mn)	$0.1\cdot 10^{-4}$ – $3.7\cdot 10^{-4}$

Due to the tremendous variation in arrangements of elements and molecular structures, a proposed 10^5 to 10^6 different molecules constitute bitumen and bitumen is generally further separated into groups of chemical related compounds [41]. These groups are the

so called empirical fractions and a common classification is shown in Figure 2.3. A comparison of fractions obtained through different methods is hardly possible, since identical nomenclatures are used but separated by different chemical aspects. In addition, separation methods are sensitive to the applied chemicals and concentrations [43, 45, 46]. The most common first separation is the separation by solubility with a linear alkene of low carbon number (five to seven) as solvent. The soluble part is referred to as maltene fraction, whereas the insoluble part is called asphaltene fraction. The asphaltene fraction is further defined as soluble in methylbenzene and the insoluble part consists of carbenes and carboids. The maltene fraction can be fractionated into three generic fractions by adsorption liquid column chromatography: saturates, aromatics and resins (other nomenclatures for the same fractions exist). A complementary analysis is the ion exchange chromatography, which reveals that bitumen consists of approximately 60wt.% of neutral molecules, which are almost free of polar groups. Therefore, the dominant interaction between molecules is the London dispersion force. Due to the higher content of hetero atoms in resin and asphaltene fractions, polar interactions (Kessom force and Debye force) occur and due to the planar fused carbon ring structure of asphaltene molecules, π - π interactions occur [41].

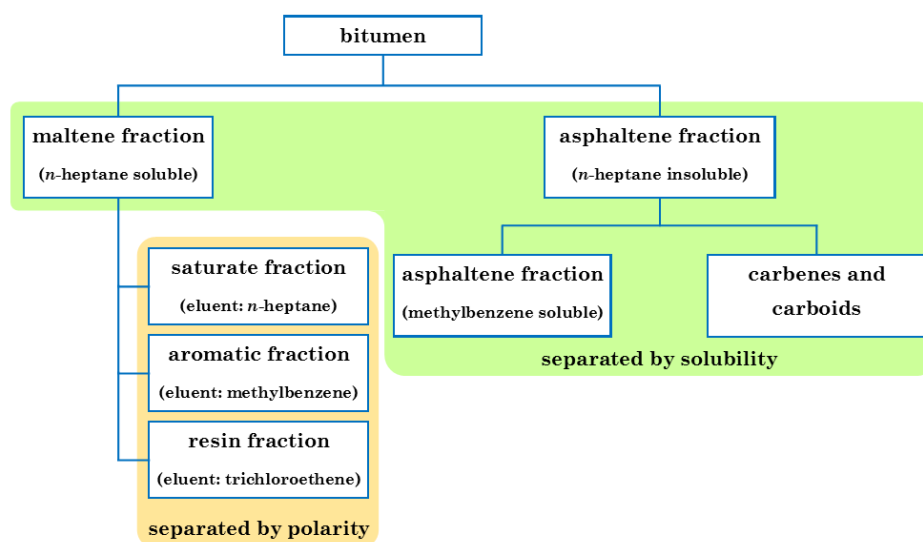


Figure 2.3: Scheme of bitumen separation into fractions (based on [41]).

2.2.1.3 Generic fractional composition of bitumen

Fractionating bitumen is mainly based on solubility and polarity (Figure 2.3). Each fraction is more homogeneous compared to the bitumen itself and allows to study their impact on the bitumen properties and time dependent changes. Although, the fractions are arbitrarily divisions of the continuous distribution of molecules composing bitumen.

2.2.1.3.1 Asphaltene fraction

The asphaltene fraction is one of the most investigated fractions of bitumen and petroleum. Defined as generally insoluble in linear alkene (*n*-heptane as most commonly used) and soluble in aromatic solvents (methylbenzene commonly used). The asphaltene fraction obtained depends on the carbon number of the solvent. The lower the carbon number, the higher is the asphaltene content [3, 41, 47]. Further, the extraction method

(filter paper, temperature and duration) also affect the amount of asphaltene fraction obtained [48].

The asphaltene fraction is between 5wt.% and 31wt.% of bitumen and occurs at ambient temperature as a black powder with an average density of $1.15 \text{ g}\cdot\text{cm}^{-3}$. The molecular structure consists on average of 4 to 10 fused aromatic rings and aliphatic side chains, which can link multiple groups of condensed ring systems. Due to the planar aromatic ring systems, asphaltene molecules tend to stack through π - π bonding. The amount of stacked planar sections is limited by the aliphatic side chains – steric hindrance [41, 46, 47]. This formation observed in solvent ($>0.1 \text{ mg}\cdot\text{cm}^{-3}$) [49, 50] is assumed to be one reason for the structural formations observed on bitumen boundary surfaces [41, 51]. Three classes of compounds can be identified in asphaltenes: polyaromatics with saturated substituents, metal organic compounds (like porphyrins) [41] and *n*-alkanes with more than 40 carbon atoms [52]. The polarity of asphaltene molecules ranges from non-polar (*n*-alkenes) to highly polar (high content of hetero elements) [41, 52].

2.2.1.3.2 Saturate fraction

The saturate fraction occurs at ambient temperature as a colourless or lightly yellow coloured liquid. With a hydrogen to carbon ratio of nearly 2 and an average molecular weight of approximately $600 \text{ g}\cdot\text{mol}^{-1}$, the saturate fraction mainly consists of straight and branched aliphatic hydrocarbons with few heteroatoms or aromatic rings. Its density is about $0.9 \text{ g}\cdot\text{cm}^{-3}$ and it amounts to 5wt.% to 20wt.% of bitumen [1, 41].

2.2.1.3.3 Aromatic fraction

The aromatic fraction is also known as naphthene aromatic fraction and appears as a dark red coloured liquid with a higher viscosity than the saturate fraction. The main molecular structure is of lightly condensed aromatic and naphthenic rings with aliphatic side chains. Due to their molecular structure, the aromatic fraction has a high dissolving potential for polar and high molecular weight fractions. The average molecular weight is around $800 \text{ g}\cdot\text{mol}^{-1}$ and its density is about $1.0 \text{ g}\cdot\text{cm}^{-3}$. The aromatic fraction content in bitumen is between 30wt.% and 60wt.% [1, 3].

2.2.1.3.4 Resin fraction

At ambient temperature the resin or polar aromatic fraction is a black solid or semi-solid and liquefy at higher temperatures. The average molecular weight is about $1100 \text{ g}\cdot\text{mol}^{-1}$ with a wide distribution. The molecular structure consists of 2 to 4 fused aromatic rings and probably aliphatic side chains [41]. The resin fraction can be more polar than asphaltenes [43, 46] and has a density of approximately $1.07 \text{ g}\cdot\text{cm}^{-3}$. Bitumen includes between 15wt.% and 55wt.% resin fraction [1, 41].

2.2.1.3.5 Wax fraction

Two different types of wax are present in bitumen: paraffin wax and microcrystalline wax [41].

Waxes are in general *n*-alkanes with carbon number of 15 to 57, isoalkanes, cycloalkanes and aromatics, depending on the bitumen origin. The wax fraction can be part of other fractions with dominant occurrence in saturate and asphaltene fraction. Bitumen with predominant *n*-alkane wax melts and crystallises over a narrow temperature range [41,

52, 53]. Different structural geometries in images in the size of 1 μm to 10 μm are found to respond to different wax types [53].

2.2.1.4 Structural features

Surface imaging techniques, such as atomic force microscopy, scanning electron microscopy or confocal laser scanning microscopy, reveal the appearing of microstructural features over time at temperatures below 60 $^{\circ}\text{C}$ [41], shown in Figure 2.4. A handful of hypotheses were proposed to explain these appearing features and were linked to segregation of fractions in bitumen [54-56]. The fractional composition has an influence on the microstructure, which was shown by doping bitumen with innate and foreign fractions [51, 57, 58]. However, no clear trend of structural change due to doping was dominant and occasionally contradictory. Source of petroleum and manufacturing seemed to have a major influence on the microstructural features, as well as sample thickness, heat treatment and duration [41, 59].

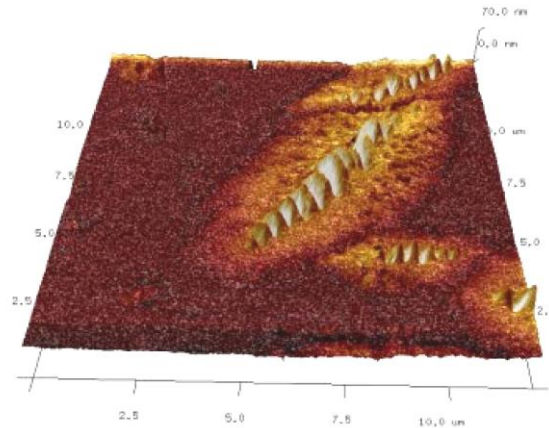


Figure 2.4: Topological mapping by atomic force microscopy, showing the surface structure with the protruding catana phase (“bee structure”) in the centre of the peri phase, surrounded by the continuous para phase [60].

The first description of structural features was done by Nellensteyn [61], describing the colloidal structure of bitumen. Primarily the asphaltene fraction was considered to be dispersed in a continuous phase. This was in conformity with the sol-gel model adopted for bitumen. At a critical concentration of dispersed phase, a change from a sol structure to a gel structure occurs. After further development and including saturate, aromatic and resin fractions, a colloid model consisting of micelles was proposed. An ongoing discussion is if the core of the micelles consists of aggregated asphaltene molecules or crystallised waxes. The core is surrounded by an aromatic or resin shell, which acts as stabiliser [3, 41, 55, 62].

The microstructural features are in the range of 1 to 10 μm [57, 63-65] and strongly depend on the bitumen type, imaging technique and time. Time is a crucial factor, as features are detectable only after a certain duration, which is ascribed to a diffusion-based organization process [56, 66, 67]. Beside a diffusion controlled structural arrangement of molecules within bitumen, another hypothesis is that the microstructural surface features might be due to rearrangements on the surface and the topographic features are due to minimisation of surface energy and different contraction properties in the surface [68]. This theory is supported by the lack of structural features observed with transition

electron microscopy [60] and with atomic force microscopy on [69]. However, circular structures were observed on recent fractured bitumen surfaces and similar features are indicated to be present in the bulk observed by scanning acoustic microscopy [70].

2.2.1.5 Physical properties

Some of the physical properties of bitumen are linked to its chemical/fractional composition. Other properties seem to be less affected or unaffected by chemical changes and thus vary only in a small range [3].

The visual appearance of bitumen is black to dark brown. The refractive index correlates to fractions, density, sulphur and methylene content. As a macromolecular hydrocarbon substance, bitumen is an electrical insulator [2].

The density of bitumen fluctuates over the range of $1.01 \text{ g}\cdot\text{cm}^{-3}$ to $1.04 \text{ g}\cdot\text{cm}^{-3}$ at ambient temperature [2, 41] and therefore is in general heavier than water with $0.998 \text{ g}\cdot\text{cm}^{-3}$ [71]. The absorption of water is less than 0.1wt.% and therefore negligible. An increase in asphaltene, resin or aromatic fraction increases density, whereas the saturate fraction causes a decrease in density. The weight loss due to heating is between 0.5wt.% and 1.0wt.% and is often considered as insignificant [2, 72]. More significant is the chemical change during heating and the involved rheological changes (increased viscosity) [3, 73].

The thermal properties of bitumen vary only slightly. For example, the volumetric thermal expansion coefficient is between $55\cdot 10^{-5} \text{ K}^{-1}$ and $63\cdot 10^{-5} \text{ K}^{-1}$ and often a value of $60\cdot 10^{-5} \text{ K}^{-1}$ is used [3, 74]. The thermal expansion coefficient increases as the amount of asphaltene fraction decreases. Furthermore, the thermal expansion coefficient changes at the glass transition temperature. Below the glass transition temperature, the thermal expansion coefficient is reduced compared to the coefficient above the glass transition temperature [75]. The glass transition temperature, marking the transition from an amorphous solid state to a liquid state, varies widely from $-40 \text{ }^{\circ}\text{C}$ to $+5 \text{ }^{\circ}\text{C}$, essentially depending on the bitumen source [41]. The thermal conductivity of bitumen is approximately $0.13 \text{ W}\cdot\text{m}^{-1}\cdot\text{K}^{-1}$ and therefore lower than the conductivity of the mineral aggregates [2].

Bitumen spreads freely and covers most dry surfaces, which implies a small contact angle (below 90° for wetting) between bitumen and the surface material [2, 76, 77]. The adhesiveness of bitumen is strongly governed by rheological properties and not by molecular adhesion. Only at lower temperatures, once a solid like behaviour occurs, is the track of bitumen determined by molecular adhesion. A high amount of paraffin wax lowers adhesiveness [2].

Similar surface energies were identified for bitumen and the petroleum source it originated from. The surface energy ranges from $0.0125 \text{ J}\cdot\text{m}^{-2}$ to $0.0467 \text{ J}\cdot\text{m}^{-2}$ at ambient temperatures [2, 78-80] and decreases linearly with increasing temperature in the region of $40 \text{ }^{\circ}\text{C}$ to $90 \text{ }^{\circ}\text{C}$ [80, 81]. The surface energy changes with fractional content, though the trend is only of a weak nature and not explicit for individual bitumen [79, 82].

2.2.1.6 Rheological properties

Bitumen is a temperature dependent viscoelastic liquid. The viscoelastic response to a mechanical force depends on temperature, applied force and loading time. At higher temperatures it behaves like a fluid and it is less viscous (above approximately $40 \text{ }^{\circ}\text{C}$).

Viscosity nearly exponentially increases with decreasing temperature, as well as the elastic proportion in its behaviour increases [41, 83-86]. At low temperature, marked by the glass transition temperature, an elastic/brittle behaviour prevails, which is indicated by a phase angle approaching zero. The phase angle determines the lag (phase shift) between action and response (for example stress and strain). The phase angle depends on temperature, approaching $\pi/2$ at higher temperatures (ideal viscous) and zero at lower temperatures. Furthermore, the phase angle depends on the frequency during periodic loading. Temperature and frequency can be interchanged to obtain a similar viscoelastic material response [2, 41]. Medium or higher temperatures are equivalent to lower frequencies and lower temperatures correlate with higher frequencies [72].

At lower temperatures bitumen exhibits a highly non-Newtonian behaviour. This is assumed to be the result of the structuring effects of the asphaltene molecules. The dependence on shear rate decreases with increasing temperature [2, 84, 87]. Additionally, time dependent shear thinning (thixotropy) [85, 88] originates in the microstructural development [41]. At higher temperatures the rheological behaviour becomes nearly Newtonian [87].

The chemical/fractional composition has a major influence on the rheological behaviour of bitumen. An increase in resin or asphaltene fraction increases viscosity and elastic behaviour. Whereas, an increase in saturate or aromatic fraction decreases viscosity and increases viscous behaviour [41]. Steric hardening increases the viscosity and creep strain with time. This effect can be reversed by thermal energy or mechanical work and is assumed to be in association with structural formation in bitumen [66, 89, 90].

2.2.1.7 Bitumen ageing

The ageing process involves irreversible chemical changes. Hence, rheological and physical properties change during the ageing progression. Two common characteristics of ageing are the increase in viscosity and the decrease of endurable stress at lower temperatures [8, 72, 91].

The chemical changes during ageing involve oxidation reaction, fragmentation and polymerisation [8]. Due to these changes, the microstructure changes accordingly [92]. During the reaction with oxidative species, the molecules increase in size (mostly by the uptake of oxygen) and increase in polarity. This causes a reduction in the amount of the aromatic fraction and an increase of the resin and asphaltene fractions. The saturate fraction remains constant, due to the inert nature of saturated aliphatic compounds and the higher reactivity of the other fractions [8]. Alongside oxidation, fragmentation occurs and more volatile products are lost due to evaporation. The volatile organic compounds mainly have ketones, alkenes, aldehydes and aromatics as functional groups [93]. Polymerisation can be induced by atmospheric radicals or due to radicals present within the bitumen [94]. This leads to an increase in higher molecular weight molecules [8]. Ageing is a complex process involving environmental interaction and dependencies of temperature and reactivity.

2.2.2 Modifications and additives

Different substances are added in minor concentrations to bitumen to improve bulk or bitumen-aggregate interface properties. A dispersion of bitumen and a polymer is known as polymer modified bitumen. The polymer network influences the viscoelastic properties and morphology of bitumen. Additives may affect the bitumen properties, though they primarily improve the workability of asphalt, by lowering manufacturing temperatures or enhancing wettability.

2.2.2.1 Modifications

Bitumen is modified with polymers to improve its viscoelastic properties (higher stiffness at high temperatures, higher cracking resistance at lower temperatures, better moisture resistance or longer fatigue life). Commonly 3wt.% to 7wt.% of polymer is mechanically dispersed into bitumen or generated due to chemical reactions to produce polymer modified bitumen (PMB). The main polymer group applied is elastomer (75%), followed by plastomer (15%) and of minor relevance rubber and reactive polymers (10%). The polymer influences the rheological properties of bitumen even if added in relatively small quantities. A physical network, which affects the morphologies as phase separation occurs, is developed. For the blending, temperature and time are important, due to economic reasons and to avoid induced ageing and degradative phenomena. Poly(styrene-butadiene-styrene) block copolymer (SBS) is the most common used thermoplastic elastomer for bitumen modification. Other elastomers used are Poly(styrene-isoprene-styrene) (SIS) and poly(styrene-ethylene-butylene-styrene). Popular plastomers are polyethylene (PE), polypropylene (PP), Poly(ethylene-vinyl acetate) (EVA) and poly(ethylene-butyl acrylate) (EBA). Reactive polymers form a network of chemical bridges instead of physical bridges, connecting macromolecules with each other [3, 41, 95].

The bitumen properties with regard to performance during service are positively affected by the structure of the polymeric network. The compatibility between bitumen and polymer is strongly dependent on the chemical composition of bitumen [41]. In general, high aromaticity and low asphaltene content favour the compatibility. However, the storage stability is affected by many factors, which are complex due to interconnections [96]. Solubility measurements reveal that polystyrene is not swollen by bitumen or bitumen components, though it would have a chemical affinity to the saturate and aromatic fraction. Modified binders with linear SBS display higher storage stability than the modified binders with branched SBS [97]. Masson, Collins, Robertson, Woods, Margeson [98] concluded that molecular weight and the molecular shape determine the rate of segregation, while branching has a minor effect on stability, which depends mainly on the copolymer composition and molecular weight. Furthermore, SBS and SIS are intrinsically chemically instable due to a high number of unsaturated double bonds, which causes a low resistance to heat, atmospheric radicals and ultraviolet light [95]. Plastomers mainly increase rigidity and improve resistance to deformation under loading. A phase separation occurs once heated above the melting point of the polymer. Below the melting point, the network is stable even in the presence of high asphaltene concentrations [99-101]. Another aspect is the tendency to crystallise, resulting in phase separation and increased temperature for flowing [102]. EVA's have an improved storage stability compared to polyolefins, due to their functional groups (especially ester groups) [103].

2.2.2.2 Additives

Additives can be categorised into two types: waxes and chemical additives.

Waxes are added to reduce the viscosity, increase workability and aggregate covering at mixing temperature. At low temperature waxes crystallise, forming microscopic particles which reinforce bitumen (increase stiffness and deformation resistance) at application conditions. This affects the bulk properties of bitumen. Between 2wt.% to 3wt.% of wax is usually added to bitumen or directly to the mixture to achieve the desired properties. Due to the addition of waxes, the mixing temperature is reduced by 20 °C to 30 °C [3, 104].

Chemical additives act at the interface between mineral aggregate and bitumen and are added only in small doses (0.3wt.% to 0.6wt.%). Polar molecules are introduced to improve the adhesion, as the concentration of polar molecules is higher at the interface, improving the bond between bitumen and aggregates. The improved bond is further used to reduce the phenomenon of stripping, caused by moisture. Chemical additives are added during the asphalt production process and can reduce the mixing temperature by about 20 °C [3, 41, 104].

2.2.3 Aggregates

Aggregates are the main component by weight (about 94wt.% to 96wt.%) and volume of asphalt. A rough classification is done by grain size into three groups. Coarse aggregates are greater than 4760 µm. Fine aggregates range from 4760 µm to 75 µm, see Figure 2.5. Below 75 µm is classified as filler. Another differentiation is into natural (gravel and sand), processed (crushed) and synthetic (slag) aggregates [2]. In the following section, only mineral aggregates are considered, as recycling material, waste or reinforcement due to admixing of fibres were not considered in this research.



Figure 2.5: Mineral aggregates in the size range for asphalt mortar, which comprises of fine aggregates and filler.

2.2.3.1 Mineral aggregates

The majority of aggregates are solid and inert materials, obtained from stones either natural or processed. The important properties of aggregates are grain-size distribution (gradation), hardness, mineral composition, grain shape, water absorptivity, density, freeze thaw resistance and resistance against radiation (especially for aggregates of basalt) [2].

To produce asphalt, the aggregates are separated into particle size groups and either mineral content or origin. The desired grain-size distribution is adjusted during production by adding a specific amount by weight of each group [2, 3].

Aggregates are primarily responsible for the strength of the asphalt, with a substantial contribution from the shape (round or crushed) of the fine aggregates. Crushed aggregates perform better than rounded aggregates [105]. However, an increasing amount of crushed aggregates causes an increase in voids [106]. The shape and surface area of the aggregates have a direct effect on the asphalt layer thickness and its flow characteristic, as these determine the amount of bitumen required for an optimum performance [69].

In regard to the interaction between bitumen and aggregates, the mineralogical properties are an important factor. Bitumen, which is considered to be slightly acidic, shows a better adherence to alkaline surfaces (mafic stones) than acidic surfaces (siliceous stones). The adherence to limestone or similar minerals is quite good and these show fewer problems with stripping through water. Furthermore, the absorptivity of certain bitumen compounds, known as exudation, has to be considered, as it influences the properties of the remaining non-absorbed bitumen. It is unclear if the bitumen compounds are absorbed into the micro pores of the aggregates or adhere strongly to the surface [3].

2.2.3.2 Filler

Particles passing through a sieve with a mesh size of 75 μm are classified as filler. The function of filler is to reduce the amount of bitumen to fill the voids in the mixture of coarse and fine aggregates, which increases asphalt stability, and to stiffen the asphalt [2, 107]. This reduces the susceptibility to changes in consistency caused by heat. In addition, the mixture of bitumen and filler has an increased viscosity compared to pure bitumen. The viscosity increase could be achieved by using pure bitumen with higher viscosity, but this results in shorter serviceability. An increase in the amount of filler causes an increase in viscosity and tensile strength and decreases ductility. Viscosity nearly changes linearly with filler amount up to approximately 10wt.%, followed by a rapid increase from 40wt.% to 50wt.%. Moreover, the particle size and shape have a significant influence. Finer graded filler decreases the viscosity more strongly and is more suspended in bitumen. The mineral composition of the filler can show physio-chemical activity at the interface. Adsorption of bitumen to the filler surface is significant, due to the large surface area of filler [2, 83, 108]. Adsorbed bitumen films can be stiffer than the bulk bitumen and confocal laser scanning microscopy has shown that some filler tends to be coated with fluorescence capable molecules [55].

2.2.4 Asphalt

Asphalt is the mixture of mineral aggregates and bitumen and contains varying amounts of air voids depending on the mixture design (Figure 2.6).

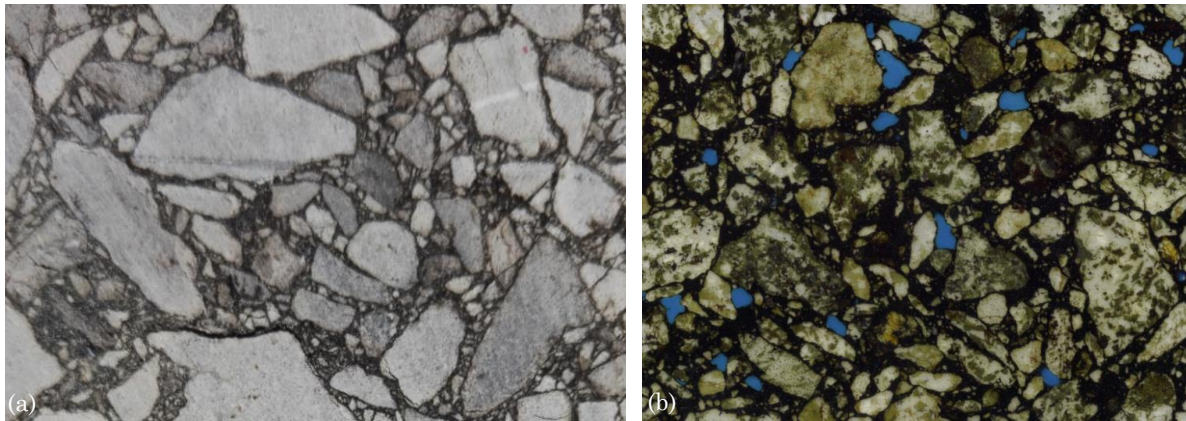


Figure 2.6: Cross section of (a) an asphalt core and (b) a section of asphalt microslide. The blue areas in (b) are air voids, which are filled with epoxy.

2.2.4.1 Asphalt production

The mineral aggregates and fillers, once dried, are stored in hot bins partitioned by particle size and mineral composition. Drying consumes a lot of energy, though it ensures that bitumen covers the aggregate surface completely and prevents unwanted foaming due to hot bitumen water interaction. Bitumen is stored in different heated tanks according to its rheological values and modifications. Any other additives are stored under appropriate conditions. The correct proportion of aggregates is dosed into the mixture by releasing a determined quantity into a weigh hopper. Bitumen and additives are mixed beforehand and are added through a bitumen dosing apparatus. The filler is either added during or after bitumen is added to the mixture by a filler weigh hopper. After the mixing process in a mixing drum, which can be heated, the asphalt mixture is stored inside a heated silo. Transporters are loaded from the silo. The placement is done with a paver and compacted through rollers. The placement temperature range depends on the mixing process and asphalt mixture design. The high temperatures during the mixing process, storage, transportation and placement leads to a pre-ageing of bitumen. This initial ageing is termed as short-term ageing [3, 8, 109].

The asphalt can be produced in a stationary mixing plant (mix in plant) or at the construction side with a moveable mixer (mix in place). A further classification is the mixing temperature. For hot mix asphalt the temperature is above 130 °C for unmodified bitumen and can be above 200 °C for modified bitumen. Hot mix asphalt is commonly used for surface course in the United Kingdom. Warm mix asphalt is produced in the temperature range of 100 °C to 130 °C. The reduction in temperature is achieved by adding additives (e.g. zeolites, waxes or emulsions). For asphalt produced in the temperature range of 60 °C to 100 °C the term half-warm mix asphalt is used. If the temperature is below 40 °C, the term cold mix asphalt is used, which is obtained by mixing aggregates with a bitumen-water-emulsion [3, 110].

2.2.4.2 Asphalt properties

Bitumen functions as an adhesive for the aggregates in asphalt. The bitumen content varies in general between 4wt.% and 8.5wt.%. The main function of the coarse and fine aggregates is as load bearing support, providing grip and abrasion resistance on the asphalt surface. The exception is mastic asphalt with a high bitumen and filler content, which results in negligible air void content (near zero) and the asphalt can be treated like

a liquid (no compaction necessary). The void content ranges from 0vol.% to a maximum of 25vol.% for porous asphalt. The air void content and the void distribution have a significant influence on the physical and mechanical performance of asphalt [111]. The size and distribution of air voids depends on the aggregate properties, bitumen content and compaction process. The ratio between coarse and fine aggregates mainly determines the air void content and distribution. Other mesostructural factors like bitumen content, aggregate type or gradation affect the asphalt performance as well [2, 3, 69].

A classification of asphalt can be done by the resulting density. Dense-graded asphalt has a high density, which is achieved by a nearly ideal grain-size distribution curve, leading to a minimum of air void content. This type of mixture is commonly used for roads. If the grain size distribution has a gap grading, it is termed as gap-graded. The advantage is an increased durability and improvement of plastic deformation resistance. By extending the gap in the grain-size distribution an open-graded asphalt or porous asphalt is achieved. Porous asphalt drains water from the surface faster due to the high, enclosed air void content and reduces wheel noise [3].

Asphalt has three main functions. It distributes vehicle loading to the underlying layers and ensures that the transmitted stress does not exceed the bearing capacity of the underlying material. The asphalt layer protects the underlying material from weather conditions, which is mainly water in the form of precipitation or melted snow. The surface has to be suitable for vehicle contact. As the load bearing layer the stiffness modulus mainly serves as an indicator how well the asphalt structure performs. However, a determination is difficult, as the stiffness modulus depends on temperature, loading rate, asphalt composition and bitumen ageing condition [3, 112].

2.3 Road structure

Three different road types can be distinguished depending on the load distribution to the subgrade. Rigid roads and semi-rigid roads are cement based and have a high Young's modulus to distribute the load. Whereas, flexible roads consist of several distinct layers of asphalt (Figure 2.7). Stress is transmitted downwards through the layers and diminishes as it is spread over an increasing area. Hence, structural integrity is not compromised [3-5].

The top layer of an asphalt road is the surface course or wearing course. Its main purposes are to provide grip for automobile tyres, distribute traffic load downwards, protect the underlying layers and drain off water. Therefore, it generally contains higher quality material. Under the surface course is the binder course, followed by the base course. In both layers the traffic load is further distributed. In addition, the binder course provides stability to reduce rutting. If the natural subgrade is not suitable for direct placement, an unbound or hydraulically bound layer (subbase) underlies the base course and the natural subgrade can be stabilised to fulfil necessary requirements, like structural support and sub-surface drainage. The natural subgrade is compacted and should not be overstressed. The layers differ in grain size, thickness, void content and binder content. The layer thickness and the grain size are gradually reduced with succeeding layers upwards [3, 5].

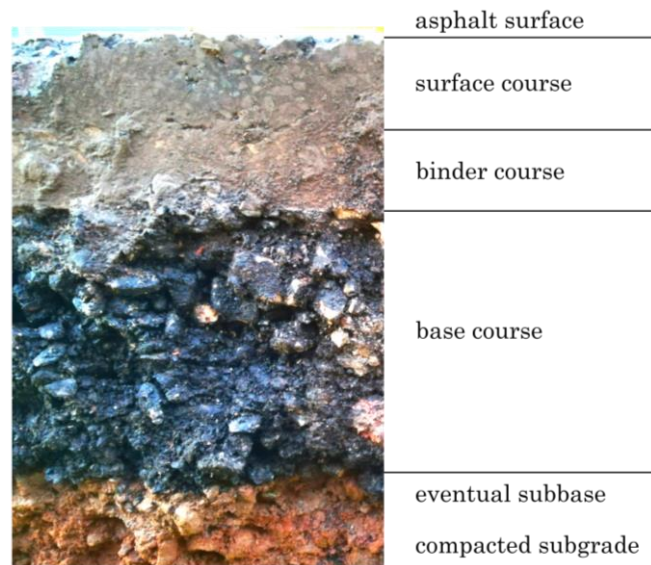


Figure 2.7: Asphalt road layers.

The design considers anticipated traffic, subgrade and layer succession, which is influenced by the highway classification. Those requirements influence the composition of aggregates, which determines volumetrics and compatibility [3-5].

2.4 Road failure

Failure in the road structure occurs due to chemical and microstructural changes (ageing and steric hardening), inter and intra layer separation (stripping, adhesive and cohesive cracks), loss of material (abrasion, ravelling and potholes) and permanent deformation (rutting, shoving, depression and upheaval) [113]. Only cracks are further discussed, as this thesis is focused on the self-healing of cracks.

2.4.1 Cracks/fractures

Cracks appear within the road structure as a result of low-temperature and/or multiple loadings. Changes in the properties of the material support the development of cracks [6, 114]. These changes are mostly time dependent and can be classified into environmentally triggered and intrinsic changes. The environmentally triggered changes are due to oxidation, radical reactions, chain breaking or loss of volatile compounds. These are irreversible changes in the bitumen chemistry and mostly related to the ageing process of bitumen [8, 42, 114]. In contrast, intrinsic changes can be reversible. Reversible intrinsic changes are steric or physical hardening [41]. Irreversible intrinsic changes are polymeric reactions due to the presence of natural radicals in bitumen [94]. All these changes lead to a higher viscosity, reduce relaxation and elastic behaviour. Thus, they result in a more brittle or ductile response towards loading and low-temperature induced stresses. Hence, the risk of crack appearance is increased [3, 41]. In addition, cracks are generated in asphalt roads due to common compaction procedures. These initial cracks have a typical length of 25 mm to 100 mm and are spaced 25 mm to 76 mm apart [115].

Two main types of crack can be defined: fracture cracks and fatigue cracks. A fracture crack is generated by surpassing the maximum stress in the material, whereas fatigue cracks are the response to long term repeated loading. The load causes stress lower than

the maximum stress of the material but above a certain threshold [11, 22, 116, 117]. At the microscale the type of the crack can be either cohesive or adhesive. Adhesive cracks develop if the bitumen film is thin, whereas cohesive cracks occur if the bitumen film is thick [118].

2.4.2 Moisture susceptibility

Moisture damage is due to the presence of water in a liquid or vapour state in the material. This progressively deteriorates the functionality of the road by losing the adhesive bond between bitumen/mastic and the aggregate surface and/or the cohesive strength within bitumen/mastic. Moisture damage depends on the material and road characteristics for the moisture transport into the material and the response of the road structure (internal structure) [111].

Moisture is transported by infiltration of surface water, capillary rise of subsurface water and permeation/diffusion of water [119]. The permeability of asphalt has an exponential correlation to the air void content. The capillary rise depends mainly on the geometrical characteristics and the contact angle between water and the solid (bitumen or aggregate) [111]. Water diffusion depends on the concentration gradient, thus the relative humidity, diffusion coefficient and storage capacity in the material [120, 121]. The presence of water weakens the boundary layer between bitumen and aggregates by accumulating at the interface. This results in a loss of cohesive strength. The adhesive strength can be changed due to the incorporation of water molecules in the molecular structure, changing the dipole interaction between bitumen molecules or due to chemical reactions changing the electrostatic interaction in bitumen [111, 122]. In both cases the surface energy and potential is changed, allowing an easier formation and propagation of cracks [111].

2.5 Self-healing mechanism

Certain materials exhibit the ability to repair damaged parts and restore lost or diminished functionalities by using inherent resources. This ability, also known as self-healing, is either triggered by the incident that causes the loss or diminishment, or through an external stimulus [123]. Another definition of self-healing, which was proposed for polymers, is if two fractured surfaces are brought into contact at a temperature above the glass transition temperature, the fracture interface disappears and the mechanical strength increases with time until the original properties of the material (polymer) are restored [30, 124, 125]. However, damage, degradation and failure are natural consequences of applications and self-healing mechanisms can only prolong utilisation time. Similar to biological healing processes [126], from which the concept is derived, the self-healing can not be carried out indefinitely and at a certain point in time the self-healing rate is insufficient to restore an adequate amount of functionality and the system fails [123, 127].

To measure and compare the self-healing, the self-healing efficiency ($\eta_{self-healing}$) is defined by the rate of recovery of a certain property/properties or functionality/functionalities by comparing initial and self-healed materials, see Figure 2.8. It is important to understand that self-healing of a certain property or functionality does not imply that other properties or functionalities are restored [126].

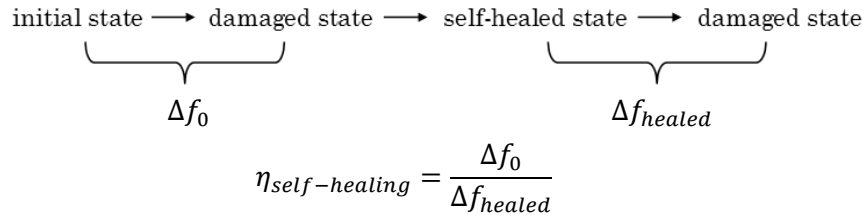


Figure 2.8: Evaluation of the self-healing efficiency through the comparison of property or functionality changes between the initial state (Δf_0) of the material and the self-healed state (Δf_{healed}) of the material.

2.5.1 Self-healing materials

There is a wide range of materials that exhibit an inherent healing mechanism, either natural or synthetic. Among these are polymers, metals, ceramics, composites [123] and some other materials which can not be classified into the previous categories, like cementitious materials, bitumen and biological tissues. Only a few materials possess the ability of intrinsically self-healing. In particular, most synthetic materials require an external healing agent for the self-healing process [123, 128].

The following features are favoured for materials, which possess either intrinsic or extrinsic self-healing abilities: the self-healing mechanism should be autonomous (does not require constant regulation), repeated (zones recovered are often weak points and it is likely that damage occurs close to those zones again), efficient (recovering a high percentage of the lost functionalities), timely (recovery occurs in a reasonable time frame), molecular (re-establishing of chemical bonds or physical crosslinks), structural (closing of different crack geometries and widths) and in service [129].

It is important to understand the self-healing mechanism, as this mechanism might be influenced by many parameters. Important factors which should be considered are the material characteristics and behaviour (during the damage and recovery process), loading conditions, damage form and environmental conditions. The self-healing process depends primarily on the material behaviour, as the material determines the intrinsic self-healing process or how incorporated material induces an external self-healing process. Furthermore, loading conditions and damage form affect the healing. A remaining tensile stress can prohibit self-healing by pulling the fracture surfaces apart, preventing the surface approach stage. For extrinsic self-healing materials, the damage form is important, as certain systems can only respond to or repair a specific damage form [123, 128-130]. The material properties, including host material and healing agent for extrinsic self-healing materials, can as well be affected by environmental conditions. An example of an environmental factor is temperature, which influences viscosity, diffusion, surface tension and chemical reactions [131]. Some environmental conditions might prohibit or diminish the self-healing process, like liquids covering the fracture surfaces and hence, preventing self-wetting or wetting of a healing agent. Figure 2.9 provides an outline of the self-healing mechanism in materials. While for intrinsic self-healing the material has the self-healing potential, extrinsic self-healing materials incorporate healing agents for the self-healing process.

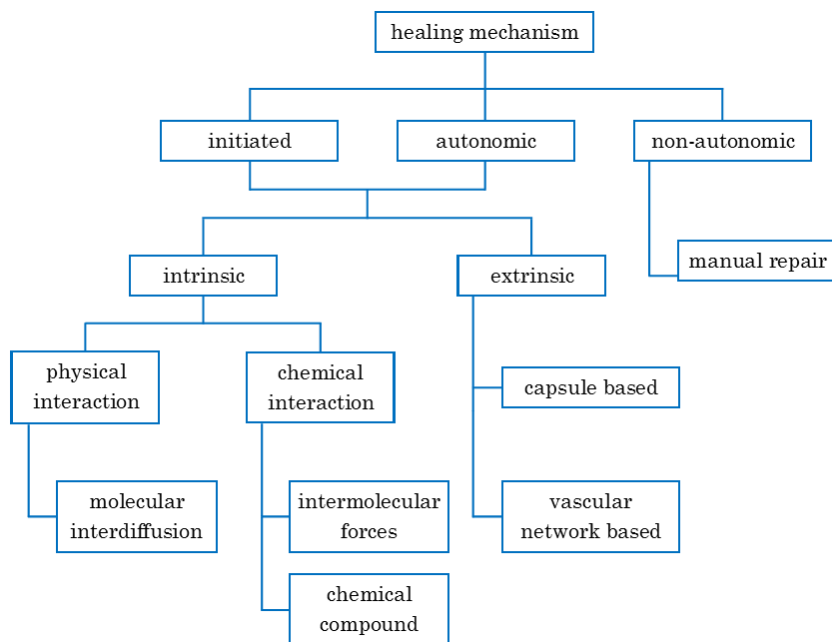


Figure 2.9: Concept of the self-healing mechanism in materials.

Many polymers have demonstrated inherent healing abilities [12, 131]. Thermoplastics are similar to bitumen as their strength results from intermolecular forces, which are weakened with increasing temperature and this results in lower stiffness and thermal instability. Damage is healed by heating the material above its melting point, which recasts the object. In cross-linked polymers (thermoset polymers) the bond between polymer chains can be physical (Keesom force, molecular entanglement) or chemical (chemical bond). This gives thermal stability and higher stiffness but prevents chain mobility, reducing the healing of damage like thermoplastics [12, 132, 133]. A solution is the design of breakable molecular connections (reversibility of bonding), which can interlink after being separated allowing multiple self-healing events. These connections are reversible cross links similar to ribonucleic acid (RNA) and contain supramolecular polymers, ionomers and specific reversible binding reactions [37]. An alternative is the use of healing agents, which can be incorporated in nearly all materials based on the coactions of the base material, healing agent and healing agent containing system [37, 131].

2.5.2 Intrinsic self-healing mechanics

An intrinsic self-healing ability is a latent healing ability, which is triggered by damage or by an external stimulus like heat, light or pressure. Since the self-healing mainly relies on molecular chain mobility (diffusion and viscosity), entanglement, van der Waals bonding, melting of dispersed phases or triggered reversible chemical bonding, multiple healing events or continuous healing is possible. An advantage of intrinsic self-healing is that there are no healing agents needed, which avoids integration and compatibility problems. However, the materials must meet the desired physical and chemical properties for its application [123, 129].

2.5.3 Extrinsic self-healing mechanics

Extrinsic self-healing materials rely on healing agents, which are incorporated within the material. The healing agent can be solid, liquid or biological. Solid healing agents can be directly distributed during the manufacturing process and often require a temperature increase to start the self-healing mechanism. Liquid healing agents, on the other hand, need to be stored and released on demand and sometimes a catalyst for hardening/polymerisation of the liquid agent is necessary. The two most common methods of storing a liquid healing agent are capsules and vascular networks, see Figure 2.10. In both cases, the healing agent is enclosed within either a capsule or a hollow channel network and is released in the region of damage if the containing shell is damaged too. The healing agent flows then into the damaged zone by capillary force and gravity. Depending on the agent, it either polymerises, chemically reacts and forms a precipitate or diffuses into the surrounding material and enhances chain mobility to amplify flow processes of intrinsic self-healing. For capsule based materials only a single local healing event is possible, as the healing agent is depleted afterwards. This problem can be resolved by multi-layer capsules, allowing multiple local healing events. The vascular network, which can be interconnected one- two- or three-dimensionally, can be refilled by an external source or through connected undamaged capillaries or hollow channels. This allows multiple healing events until the healing agent source is depleted or the network system is plugged during the healing process. A disadvantage of introducing foreign material is to find the optimal balance between incorporated material and the overall performance of the system. Higher amount of healing agent can alter the physical properties of the host material. Additionally, larger capsules or thicker channels might act as weak spots once the healing agent is released. If the crack width is too big, the liquid healing agent could be drained without sufficient closing of the crack [123, 127-129, 134, 135]. Biological healing agents have been applied in concrete mixtures. Hibernating bacteria or bacterial spores and a calcium nutrient source are added to the concrete mixture, directly or encapsulated in hydrogel. Bacteria are activated by crack formation. Due to their metabolism, calcium carbonate is segregated and precipitates to calcite. This occurs until the crack is filled and the bacteria return to their hibernated state [136, 137].

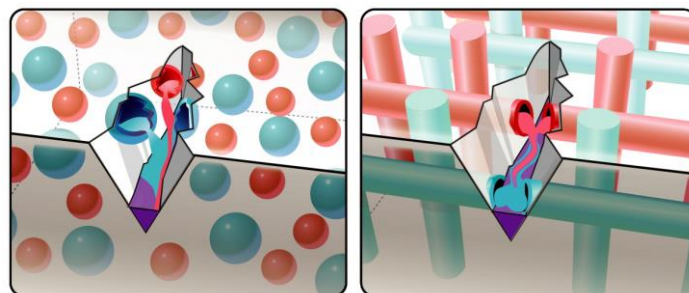


Figure 2.10: Extrinsic self-healing approaches: (a) capsules and (b) vascular network. The healing agent is stored in either capsules or hollow channels/fibres until ruptured by damage. The healing agent can be a single component or consist of multiple components stored in different parts or entities (a two component system is shown in red and turquoise) [123].

2.5.4 Self-healing models

For polymers a conceptual model has been derived that focuses on the chemical and physical aspects during the self-healing process. To recover functionalities and to close a crack the following five stages occur [12]:

Surface rearrangement: Depending on the fracture mechanism and the original surface topography or roughness, the fracture surface changes with time [38, 58]. This occurs as the free surface energy is minimised and surface molecules diffuse into the bulk and vice versa. Further, foreign substances can permeate the fracture and cause chemical reactions, partly or completely covering of the fracture surface or diffusing into the bulk. This is intended for extrinsic recovery as the healing agent permeates the crack [12, 128]. The two fracture surfaces might not fit perfectly together, which affects the rate of crack closing. The change rate of the surface depends on material, temperature and pressure [138, 139].

Surface approach: The most crucial stage for intrinsic self-healing is by bringing the two fracture surfaces in contact or close vicinity. The creation of an interface can be irregular across the fracture surface and is time dependent [12]. Surface irregularities and mismatches due to the surface rearrangement are reduced by elastic-plastic or viscoelastic deformations [130]. At this stage, an instantaneous strength gain can occur due to cohesion. Extrinsic self-healing benefits from a minor crack volume, as less healing agent is needed to fill the crack. And an interface is created between the fracture surface and the healing agent [131].

Surface wetting: The healing starts from contact areas, where the two fracture surfaces are in contact, including the crack tip. The wetting process is time and topography dependent. The areas in contact are nucleation points of wetting pools. They appear randomly distributed over the interface until coalescence and complete wetting is obtained [12]. Surface wetting is governed by the flow of the healing agent into the crack for extrinsic self-healing [140]. An instantaneous strength gain can occur due to cohesion.

Diffusion: Molecular diffusion across the interface physically connects the two surfaces and the interface starts to disappear [141]. Rapid interdiffusion occurs within a small distance from the interface. The distance can be approximated at 3 nm, depending on the gyration radius of the molecules [140]. The diffusion is driven by Brownian motion (self-diffusion) and can even occur below the glass transition temperature. Therefore, the top surface layer has to become more mobile compared to the bulk [142]. For extrinsic self-healing diffusion occurs if the healing agent can permeate the host material (chemical diffusion) and for example reduce viscosity or the healing agent starts to polymerise. If the healing agent changes the properties of the host material, the same sequence of stages proceeds for the modified material [128].

Randomisation: The randomisation stage is often seen separated from the diffusion stage. It is less important for intrinsic self-healing as no chemical gradient is present, although impurities might be present from chemical reactions or surface contamination. Extrinsic self-healing, based on a change of host properties, has a concentration gradient of the healing agent from the interface outwards. Randomisation refers to a reduction of the gradient, due to chemical diffusion, to achieve homogenous properties of the material.

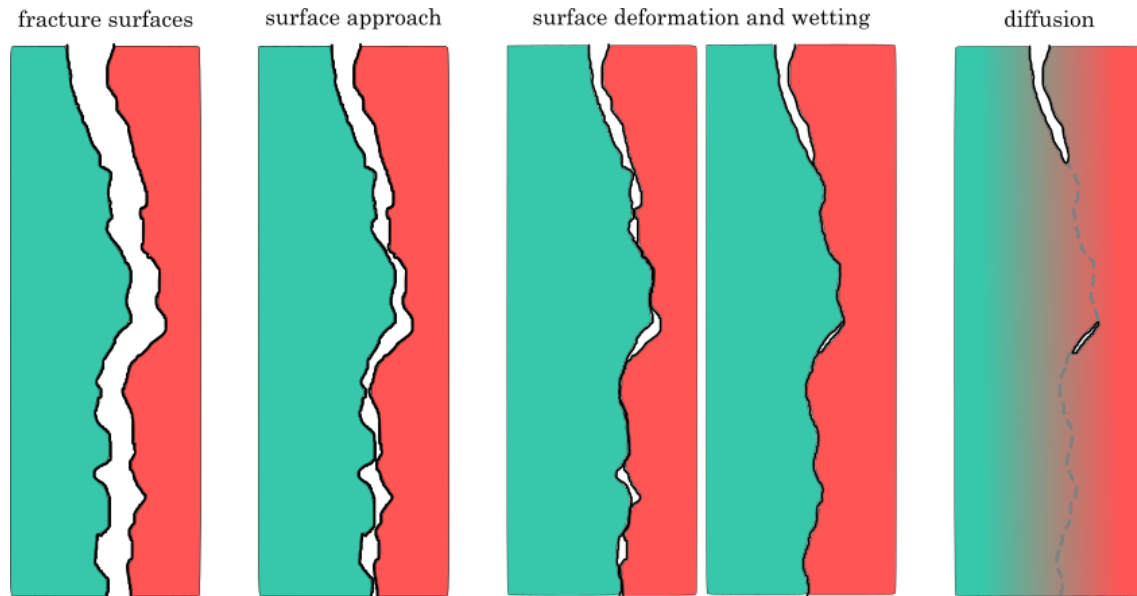


Figure 2.11: Stages of self-healing; from initial fractured surfaces to partly self-healed crack.

Figure 2.11 illustrates these stages. The initial contact is due to deformation of the material as the surfaces approach, followed by surface wetting and the last stage includes diffusion and randomisation. During the self-healing process, those stages can proceed at different speeds and hence, co-occur. Similar conceptual models have been adapted for the self-healing in bitumen respectively asphalt and other materials like alloys [143] or ceramics [144].

Different models have been developed to describe the self-healing of bituminous materials at various scales. These conceptual models depend on the investigated characteristic, testing methods, mainly mechanical testing, testing conditions and the definition of the self-healing efficiency. Hence, a comparison between models and self-healing efficiencies is difficult.

A model developed to describe the self-healing in asphalt is the multi-step model. This model describes the damage and self-healing process of fatigue induced damage in three steps [24]. Macro cracks are closed due to consolidation stress and the flow of bitumen or mastic. This is followed by the closing of micro cracks due to surface wetting. The mechanical properties are restored through diffusion-limited structuring of the microstructural features observable in bitumen [64]. A two stage model for self-healing for bitumen includes the instantaneous strength gain due to interfacial adhesion/cohesion, followed by a time dependent strength gain due to molecular diffusion across the interface. This physical model is mainly based on a molecular diffusion mechanism [145].

Another physical model (phase field healing model) is based on thermodynamic concepts. The dissipative thermodynamic concept uses a chemo-mechanical approach, including the appearance of microstructural features due to the separation of fractions [62, 146]. In the viscoelastic continuum damage model, the self-healing is incorporated as cross-section ratio of remaining micro cracks and micro voids to disappeared micro cracks and micro voids after self-healing [147, 148].

Since experimental results have shown a relationship between temperature and self-healing and in addition, the viscosity of bitumen indicates a strong correlation to self-

healing parameters, the closing of cracks has been related to the drainage of bitumen into cracks. Driven by surface tension and hydrostatic pressure, cracks and air voids disappear, mainly starting in lower regions of asphalt [17, 32, 149].

2.5.5 Self-healing in bituminous materials

Two main methods are used to study the self-healing of bituminous materials, which range from bitumen to asphalt: fracture-based testing method and fatigue-based testing method [13, 33, 150]. The fatigue-based testing method introduces damage due to periodic loading, fatigue damage. The self-healing occurs mainly either at the end of each loading cycle, which is called intermittent fatigue test [151-153], or after a defined number of cycles as a rest period, interrupted fatigue test [19, 154, 155]. A defined parameter, for example the complex modulus, is monitored during the fatigue test and occasionally continued at a low damaging level during the rest period, and compared to a reference sample or the initial value at the start of the test. A combination of both methods has been used to reflect a more realistic damage induction and self-healing in the material [21]. The fracture-based test investigates the self-healing of two fracture surfaces. The fracture surfaces are created by breaking a sample in two halves or preparing two test samples. The halves or samples are put in contact and healed under defined conditions over a set time duration. A common approach is to compare the initial breaking force with the breaking force after healing for fractured samples. In the case of two test sample, reference samples are commonly used to evaluate the self-healing [17, 32, 36, 141, 156, 157].

Other methods to evaluate the self-healing of bituminous materials are by field tests or computational simulation. Field tests are limited, as the comparison to laboratory tests is difficult and conditions are not controllable. Two methods used were the falling weight deflectometer and the measurement of surface waves to measure the stiffness of the asphalt [23]. Computational simulation can support the analysis of the time varying, multi-scale self-healing of bituminous materials [15, 158-162]. However, these models are often limited to certain self-healing processes and in their dimensional scale.

The viscoelasticity of asphalt has two main implications for the self-healing of the material. The first implication is that permanent deformation can not be reversed by self-healing [149]. Hence, properties lost or diminished due to permanent deformation would influence the degree of recoverable properties due to self-healing. This limits the self-healing of bituminous materials mainly to the closure of cracks, the increase of transferable strength across the closed crack and the recovery of properties due to the colloid nature of bitumen. The second implication is the occurrence of non-linearity, thixotropy and steric hardening, which are often separated from the self-healing observed in the material. Nevertheless, these properties can have a positive contribution to the self-healing [163].

Non-linearity occurring at the initial start of fatigue tests is often negligible due to the inconsiderable small deviation from a linear behaviour for the first fatigue cycle under a low strain amplitude [164]. Thixotropy is the time dependent decrease of viscosity (shear thinning) under an applied shear force [165]. This could contribute to the self-healing, regarded as a flow process. However, the increase of viscosity with time after the shear force vanished could negatively affect the self-healing [161, 163, 166]. Steric hardening is

a heat reversible structural formation leading to an increase of the viscosity and other mechanical properties of bitumen at temperatures below 80 °C [66, 89]. This time and temperature dependent structural change can have a significant influence on the self-healing, especially in the case of prolonged rest times during fatigue cycles [167]. These three phenomena result from the development of ordered structural features within bitumen, which could be considered as a form of healing. Yet, it is necessary to quantify the contribution of non-linearity, thixotropy, steric hardening and self-healing, not including structural rearrangements, on the overall recovering of certain material properties (self-healing).

2.5.5.1 Self-healing at the nanoscale (bitumen microstructure)

Mechanical loading at the nanoscale has shown that micro cracks (as the structural features are in the micrometre range) occur randomly orientated with the origin at the interface of the continuum phase (periphase) and the microstructural features (catana phase). The micro cracks mainly propagate in the catana phase, which is stiffer than the surrounding continuum phase. The catana phase becomes fragmented into a lamellar structure at high tensile loading. The lamellar structure is orientated in the direction of loading and the topographic valley-hill structure of the catana phase [168, 169], as shown in Figure 2.12(a) and (c). An increase in temperature to approximately 45 °C, which was below the temperature at which structural features disappear (about 60 °C to 90 °C), softened the periphase, which penetrated the fractured catana phase. Due to the penetration, the fractured structural features were pushed apart. During cooling, the gaps in the structural features were closed due to contraction and molecular rearrangement. Strength was recovered due to the filling of the micro crack and diffusion processes. The grade of bitumen influenced the healing of these micro cracks, as softer bitumen had remaining cracks and appeared more fractured compared to harder bitumen, which nearly recovered its original rearrangement as shown in Figure 2.12. The microstructural features significantly affect the self-healing of bitumen [18, 169].

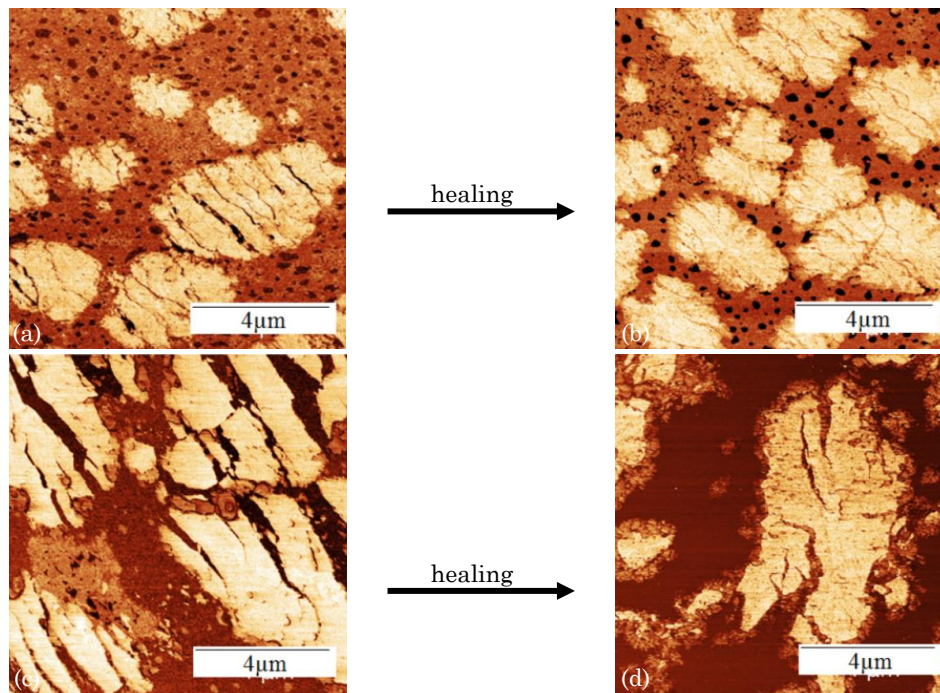


Figure 2.12: Atomic force microscopy phase images of the bitumen microstructure for (a) and (b) 70/100 and (c) and (d) 160/220 at 25 °C. (a) and (c) show the microstructural damage after applying a tensile load. (b) and (d) show the healed structure after moderate heating at 45 °C [170].

Self-healed fractures observed by scanning electron microscopy and environmental scanning electron microscopy have shown irregular bitumen strands bridging across voids, see Figure 2.13(a) and therefore are assumed to enable interfacial transmission of stress. These strands arise through the flow of bitumen from both surface sides. The excavation of fibre-like structural features by the electron beam showed them to be orientated in the flow direction and parabolic rounded fracture edges were an indication of viscous flow under the influence of gravity, as indicated in Figure 2.13(b) [64].

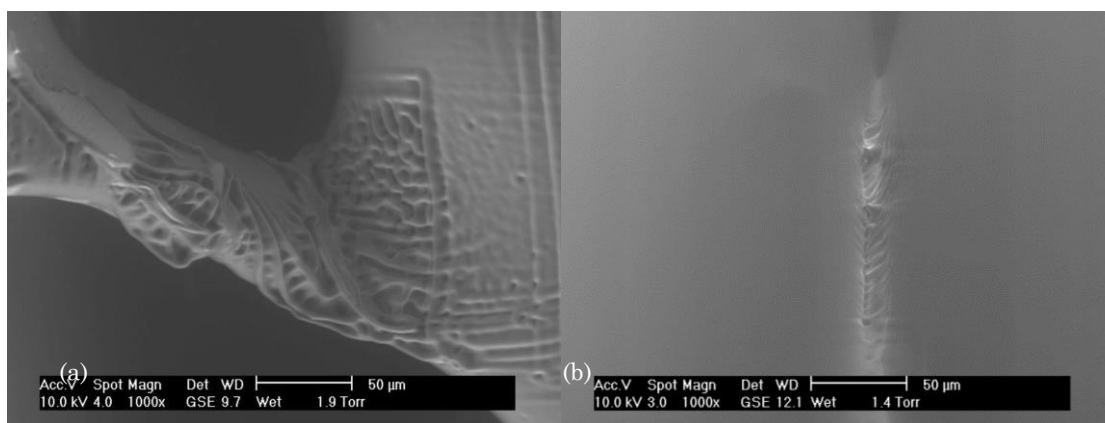


Figure 2.13: (a) Scanning electron microscopy image of an interfacial bridging across a void with underlying structure exposed by 5 minutes of irradiation. (b) Environmental scanning electron microscopy image with high magnification of a crack interface after healing at 40 °C for 30 minutes showing individual fibres interpenetrating the healing plane [64].

2.5.5.2 Self-healing at the microscale (mastic and bitumen)

Gaps induced into bitumen drops vanish over time. This process is faster at the beginning of the flow and slowly decreases. An important influence is due to the gap distance, as wider gaps need longer to vanish compared to shorter gap distances, as shown in

Figure 2.14. Temperature and the ageing state influences the viscosity of bitumen. Hence, gaps vanish faster as temperature is increased and gaps vanish slower in the case of aged bitumen. At temperatures below 10 °C the flow of bitumen stops, as gaps do not vanish [171].

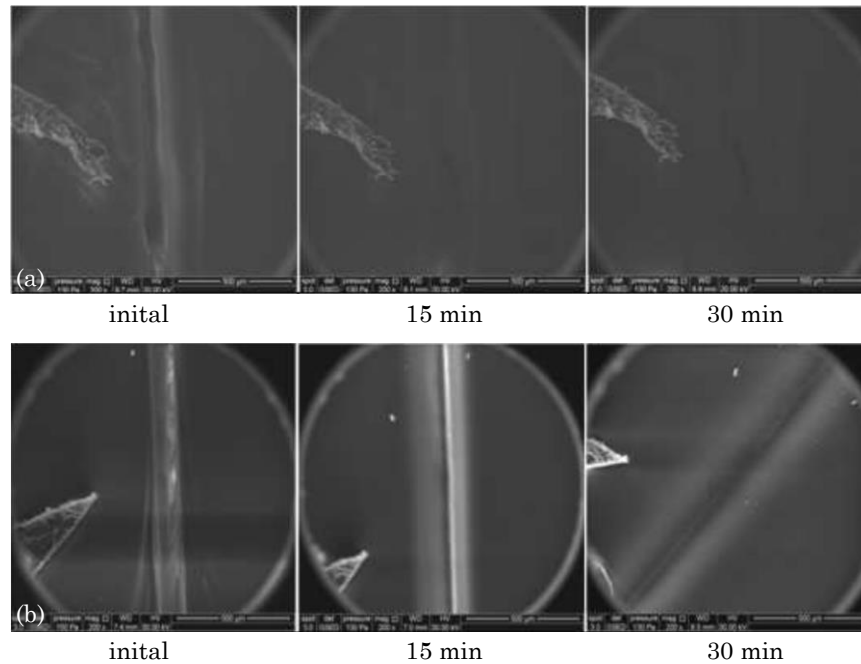


Figure 2.14: Vanishing of gaps in a bitumen droplet with (a) a narrow and (b) wide gap width at 30 °C [171].

The healing of damage in bitumen is related to its viscoelastic properties and is correlated to the viscosity. Long-chain aliphatic molecules and aliphatic side chains decrease the viscosity and increase the self-healing potential of bitumen, as the molecular mobility is increased. The methyl methylene hydrogen to carbon ratio (MMHC) and the methylene to methyl group ratio has been introduced to correlate the chemical properties of bitumen to the self-healing. An increase in the MMHC ratio and a decrease in the methylene to methyl group ratio reduces the self-healing ability of bitumen [39, 145]. These two parameters are limited to pure bitumen, as for modified bitumen viscosity shows a better correlation to the self-healing [172]. The modification of bitumen has controversial results for the self-healing, depending on the testing method. Fracture tests show a negative influence on the self-healing as polymers are added. Fatigue tests show a slight positive effect on the self-healing, which is attributed to the polymeric network, which supports the recovery during the resting time [161]. The damage history has an influence on the self-healing and on the damage progression after the healing, indicating a form of damage memory, but not significantly affecting the fatigue life. Minor damage is healed faster and a prolonged resting time heals more damage [34, 145, 154].

The optimal temperature for bitumen to self-heal has been identified as the softening point temperature. This temperature is affected by ageing, which increases the softening point and hence increases the viscosity. Temperatures above the softening point temperature result in drainage of bitumen from the dynamic shear rheometer test configuration [132].

The healing of two surfaces by monitoring the complex modulus through a dynamic shear rheometer reveals that coalescence of the surfaces does not result in the same complex

modulus as a one-piece sample, implying a weak connection. Thus, the former surface is potentially the location of cracks reappearing. The complex modulus increases asymptotically (faster in the beginning and slower at the end) and is positively affected by higher temperatures and a compressive force in the direction of the gap between the surfaces [36, 150].

The addition of filler to bitumen, known as mastic, reduces its self-healing. This is partly owed to the increase of viscosity of the mixture. The reduction is linearly proportional to the ratio of filler to bitumen. Moreover, the mineral composition of the filler has a significant influence on the self-healing. Limestone has the lowest self-healing whereas Portland cement has a higher self-healing potential [173]. Since mastic differs from pure bitumen, it has been proposed that for self-healing mastic coated aggregates should be considered. However, there are uncertainties of segregation, heterogeneity and hardening by concerning mastic instead of bitumen [166].

2.5.5.3 Self-healing at the mesoscale (mortar)

Self-healing of cracks in asphalt mortar beams has revealed that the healed beams bear less force compared to the initial beams [17]. Hence, only a part of the material properties can be recovered during the self-healing. Figure 2.15 shows the disappearance of a macro crack. The crack healed from the bottom (location of the notch) upwards, indicating the drainage of bitumen into the crack. Furthermore, an increase in temperature increased the self-healing rate and the threshold temperature for healing coincided with the Newtonian flow behaviour of bitumen [17]. This threshold temperature was in a similar range to the softening point temperature determined for self-healing in bitumen [132], showing the correlation between the viscoelastic thermal behaviour of bitumen and the self-healing of bituminous materials. An increase in bitumen content increased the self-healing during rest periods of fatigue tests. A comparison of aged mortar with field aged mortar indicated different self-healing properties and that laboratory aged mortar overestimated the self-healing [174].

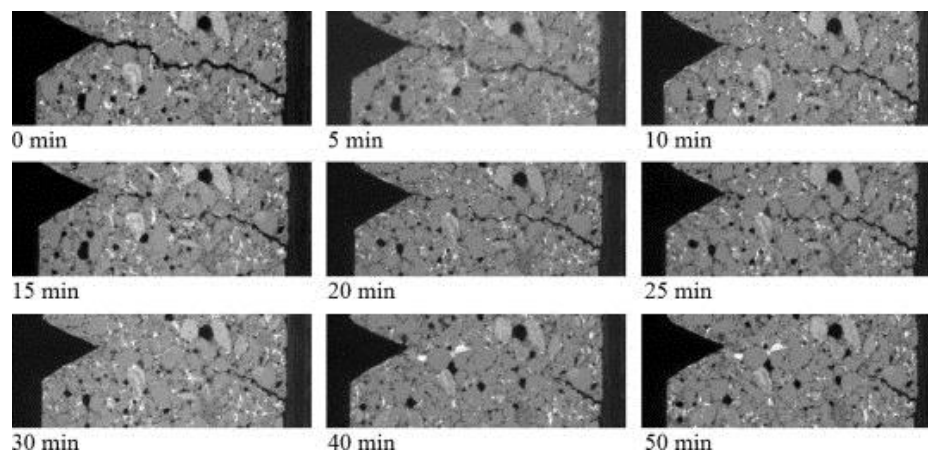


Figure 2.15: Computer tomography (CT) scans of one beam showing the disappearance of a crack with a width of approximately 200 μm [17].

2.5.5.4 Self-healing at the macroscale (asphalt)

Fracture-based and fatigue-based testing of asphalt mixtures has revealed that the self-healing starts at temperatures above 25 $^{\circ}\text{C}$ [35, 149, 156], which is higher than the observed threshold temperature of bitumen at about 10 $^{\circ}\text{C}$, indicating the influence of the

combination of bitumen and aggregates. However, this temperature is lower than the suggested threshold in asphalt mortar, around 50 °C [17], which was additionally confirmed for fracture based asphalt self-healing [32]. The optimal self-healing temperature range for asphalt self-healing has been determined to be above 30 °C and below 85 °C, to avoid drainage of bitumen from the test sample [156] or below 55 °C, to avoid the reduction of structural performance [149], which can not be healed [175]. In general, an increase in temperature was beneficial for the self-healing and resulted in higher self-healing rates [176, 177]. Other factors positively affecting the asphalt self-healing are resting or healing time [162, 177] and pressure [13, 178]. An ambiguous effect was given by bitumen modification. In the case of micro cracks, modifications, such as styrene-butadiene-styrene polymers or crumb rubber, were shown to enhance the self-healing [149, 176, 177]. In the case of macro cracks, modifications caused a slower self-healing [35], similar to the reduced self-healing in bitumen [157, 172, 179].

The self-healing of micro cracks due to fatigue damage is related to the wetting of the crack surfaces and the interdiffusion. An initial strength gain is attributed to the cohesion of the crack surfaces and has been found to be proportional to the dispersive part of the surface tension. The long-term strength recovery is slow and proportional to the polar part of the surface tension [167, 180]. The self-healing of macro cracks shows that only a part of the original strength could be recovered [35] and that only cracks of a certain crack width can be healed [149]. Self-healing is more efficient at lower damage level [162], such as micro cracks, and the self-healing rate is influenced by strain, as the distance between the crack surfaces increases [176].

Despite the laboratory evidence of the self-healing in asphalt and the limited field based research, the identified temperature threshold for asphalt self-healing and the slow self-healing rate at low temperatures might be the cause of the absence of self-healing in road structures, as rest periods have not been found to improve its lifetime [181].

2.5.5.5 Induced self-healing in asphalt

Since self-healing in asphalt is a slow process and rest periods depend on the usage of the road sections, different methods have been developed to enhance the self-healing ability and trigger it at a controlled time. Induced self-healing occasionally replaces compounds of asphalt and could be seen as an extrinsic self-healing approach. However, without a specific external stimulus, unlike extrinsic self-healing, the self-healing would be identical to the existent intrinsic self-healing shown by asphalt.

The induced self-healing methods have focused on the increase of the temperature in order to reduce the viscosity of bitumen. This has mainly been achieved by using electromagnetic radiation. Depending on the wavelength, metallic particles have been added to the mixture or have replaced a part of the aggregates, to make the composition susceptible to the radiation [27, 29, 182-185].

If the wavelength is in the near infrared spectra, no additional substances are added to the asphalt. The infrared radiation heats the surface of asphalt and the heat is transferred by conduction to lower layers. A drawback of this method is that the time depends on the conductive heat transfer in asphalt to heat certain depths in the asphalt [28, 155].

Moreover, an increase in radiation intensity could damage the surface layer due to enhancing chemical reactions [186, 187].

Microwaves have the advantage to penetrate asphalt. To increase the efficiency of microwave heating, metallic particles (steel fibres, sand or filler) have been added to the asphalt mixture. The heat is generated in the particle and transferred to the bitumen, which expands and has lower viscosity to close cracks. A high temperature generation could damage the bitumen [27, 182, 188, 189]. Therefore, it would be ideal to control the power and intensity of the microwaves.

Using a varying electromagnetic field to generate electrical currents in metal particles, which increases their temperature by the Joule effect, is known as induction heating. The penetration depth of this method depends on the wavelength, permeability and specific conductivity of the material [184]. Similar to the usage of microwaves, electrically conductive particles, mainly metal particles, are heated which transfer the heat to the surrounding bitumen, lowering its viscosity and causing thermal expansion. Bitumen flows into cracks by capillary force, gravity and enhanced flow due to expansion, illustrated in Figure 2.16. It has been shown that macro cracks are closed with this method [29, 32, 175, 190, 191], as well as the fatigue life being extended [156, 192]. The content of electrically conductive material has ranged between 1wt.% and 6wt.% for steel fibres [193], up to 14wt.% for steel wool [194] and up to about 20wt.% for conductive sand [149]. Induction heating promotes self-healing; simultaneously, the air void distribution changes, showing a higher air void content towards the top surface [149, 182]. Sample temperatures for an optimal self-healing result without damaging the sample by heating are between 60 °C and 130 °C [32, 192, 195]. The starting temperature for self-healing coincides with the Newtonian transition temperature [32, 149].

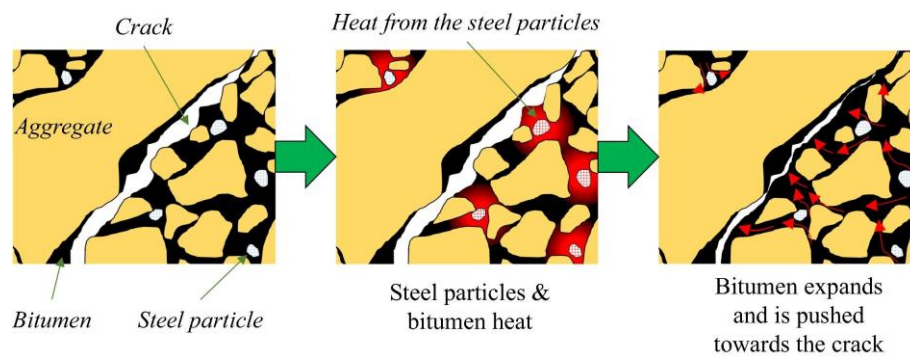


Figure 2.16: A schematic representation of the self-healing process during induction heating [28].

2.5.5.6 Extrinsic self-healing in asphalt

Unlike the healing agent for polymers, which mainly polymerises inside a crack after being released from a capsule, the healing agent is changed to a rejuvenator for asphalt. Rejuvenators are mainly oil based liquids or low viscous bitumen to reduce the percentage of the asphaltene fraction in bitumen after adding the rejuvenator to achieve a similar composition before ageing occurs [196]. Instead of polymerising inside a crack, the rejuvenator diffuses into the surrounding bitumen, lowering the viscosity and allowing thereby bitumen to drain into the crack [29, 197, 198] and simultaneously an opposed diffusion of bitumen molecules into the rejuvenator increases the viscosity, avoiding the

rejuvenator bleeding out. Figure 2.17 shows the uniform distribution of capsules within asphalt and the local released content of broken capsules.

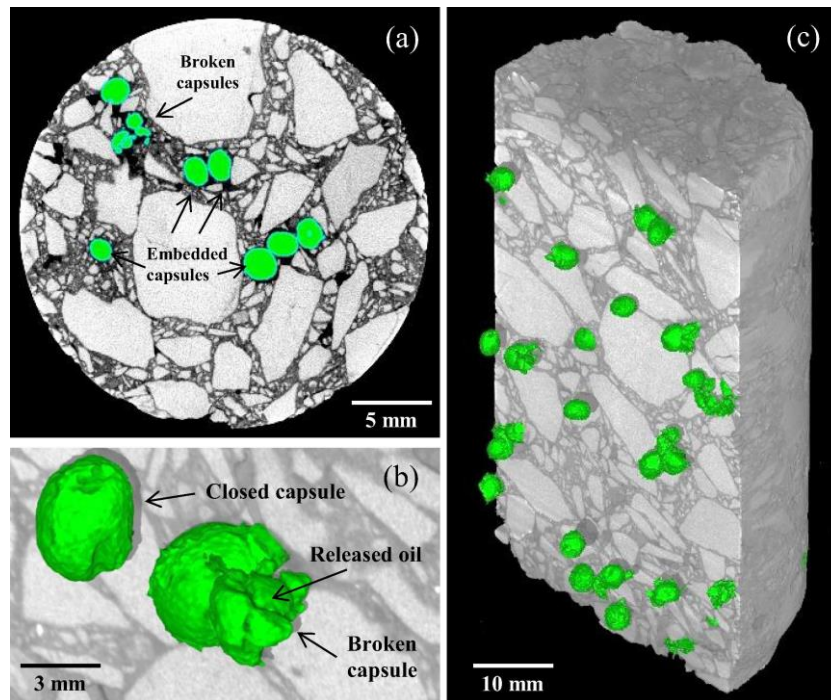


Figure 2.17: (a) Cross section of asphalt containing capsules. (b) Reconstruction of the embedded capsules from CT-scans, showing undamaged and damaged capsules with oil release. (c) Spatial distribution of capsules [199].

The capsules containing the rejuvenator have to be designed to withstand the asphalt mixing and compaction process of asphalt production so that a sufficient amount of undamaged capsules remain. This requires thermal stability and mechanical strength [200]. Two different capsule structure types are used to contain the rejuvenator. The first type is an in situ polymerisation. A polymer is formed around rejuvenator droplets. Polymers used included urea-formaldehyde [201], phenol-formaldehyde [202], methanol-melamine-formaldehyde [200, 203], calcium alginate [198] or cellulose [204]. The second type consists of a core and an outer shell to enhance the mechanical stability and prevent the rejuvenator from draining or diffusing out. The core structure can be porous aggregates or a polymer capsule (first type). Shell materials include calcium alginate, epoxy resin or cement [26, 198, 205]. Different sizes and materials for the capsules release their content at different times, which is a crucial factor in finding the optimum time to achieve maximum healing.

2.6 Summary

Bitumen is a black viscoelastic liquid, produced by petroleum refineries. Due to its adhesive and hydrophobic properties, it is used in road construction as binder to coat and adhere mineral aggregates together. Bitumen exhibits a microstructural order, which relates to its fractional distribution. Low induced damage to these microstructural formations is optically recovered as the less viscous periphase penetrates the fractured catana phase to fill the strain induced cracks. Further indications that healing relates to the flow of bitumen at the nanoscale and microscale was obtained by the observation of cracks or artificially created gaps in the material, which showed a gravitationally driven

drainage into the crack or gap. As the viscosity of bitumen depends on its fractional and chemical composition, its self-healing ability is related to the composition, favouring long-chain aliphatic molecules (mainly saturate and aromatic fractions).

The self-healing ability of bitumen transfers to bituminous mixtures. Mastic, a mixture of bitumen and filler, has a reduced self-healing potential, as filler increases the viscosity of the mixture. At the mesoscale in asphalt mortar, filling of cracks was observed to occur from the bottom of the crack to the top, an indication for gravitationally driven flow. An external factor influencing the self-healing occurrence, self-healing rate, as well as the viscosity of bitumen is temperature. Self-healing in asphalt in general occurs at temperatures above 25 °C, depending on the mixture design, and the optimal self-healing temperature ranges from 30 °C to 85 °C. This is influenced by modifiers and additives added to bitumen. Polymer modified bitumen had positive and negative effects on the recovery of characteristics depending on the characteristic investigated.

As self-healing in bituminous mixtures is assumed to mainly be a flow process, the time to heal damage is affected by damage degree and bitumen's viscosity. In order to reduce the healing time, two main methods to reduce the viscosity are deployed. The first method increases the temperature of asphalt. The temperature increase is caused by electromagnetic radiation, either infrared radiation, microwave radiation or generating a fluctuating magnetic field, which requires conductive materials within asphalt to increase its temperature through Joule heating. The second method is an extrinsic self-healing method of capsules containing a rejuvenator. The viscosity of bitumen is reduced once the capsule is damaged and releases its content, which diffuses into bitumen.

Since the identification of viscosity as a main influencing factor for the self-healing of bitumen and bituminous mixtures, less focus has been on other factors like surface tension or pressure, for example internally generated pressure due to thermal expansion. Furthermore, as asphalt used in road construction is exposed to multiple environmental factors, their influence on the self-healing ability is even less understood. Therefore, this research aims to address these open questions.

3 Materials and methods

3.1 Materials

Six different bitumen types were used as the primary material to investigate the material properties. Furthermore, three different aggregate types and one type of filler were used in connection with five bitumen types to manufacture asphalt mortar mixtures. The self-healing was determined on asphalt mortar beams.

3.1.1 Bitumen

Six different bitumen types were used throughout the research. These bitumen types are commonly used for road construction. Bitumen was obtained from Pazkar in Israel, Shell and Total in the Netherlands and one was an internally available blend at the research facility at the University of Nottingham (UoN). Penetration grades and acronyms of the bitumens used are provided in Table 3.1.

Table 3.1: Overview of bitumen supplier, grades and acronyms used.

supplier	Pazkar	Shell	Shell	Total	Total	UoN
penetration grade	45/55	50/70	70/100	40/60	70/100	70/100
acronym	P47	S46	S70	T44	T74	N83

3.1.2 Aggregates

Three different types of aggregates (sand 1, sand 2 and metal grit) and one type of filler were used. The gradation of the aggregates is provided in Table 3.2. The metal grit was added to sand 1 to allow the generation of heat by induction heating. Sand 1 (no specification from provider) had a density of 2363 kg m^{-3} . Sand 2 (Hints sand) had a density of 2650 kg m^{-3} and consisted mainly of silicates (94.62% SiO_2). The metal grit (no specification from provider) was a metal grit and had a density of 7520 kg m^{-3} . The filler used was a limestone filler (Longcliffe limestone) with a density of 2644 kg m^{-3} .

Table 3.2: Gradation of mineral aggregates used.

sieve size [μm]	percent passing [wt.%]		
	sand 1	sand 2	metal grit
5600	100.0	100.0	100.0
4000	99.8	99.8	100.0
2800	99.8	99.7	100.0
2000	90.9	99.6	81.9
1000	65.4	99.2	21.6
500	43.5	97.9	0.1
250	19.6	70.8	0.0
125	5.6	10.8	0.0
63	1.8	2.1	0.0

3.1.3 Asphalt mortar, mastic and bitumen beams

In order to study the self-healing mechanism of a complete macro fracture in asphalt mortar, beams with dimensions of 30 mm in height, 30 mm in width and 100 mm in length were manufactured. The manufacturing moulds were made out of polytetrafluorethylene (PTFE) and had a triangular notch at the midpoint of the bottom area (running parallel to the short side) to produce a predetermined breaking point for the three-point breaking test. PTFE was chosen, as it is resistant to most chemical agents, heat resistant till 200 °C and has improved high temperature mechanical properties and a low coefficient of friction, which allowed an effortless removal of the beam produced.

Mortar was produced by mixing a defined proportion of bitumen and aggregates at 180 °C. All components were preheated to 180 °C in an oven (Hot Box oven, Gallenkamp) before mixing in defined dosages together to produce the mixtures. The beams were manufactured by filling the PTFE moulds with the mixture or pure bitumen. The poured mixture was manually compacted. Mastic and bitumen beams required no compaction as the material was free-flowing. The beams were cooled to ambient temperature for the mortar mixture (20 ±2 °C) or to -17 ±1 °C in a freezer (Chester Freezer 412 Litre, CFH382AWK, Hoover) for mastic and bitumen beams. All beams were stored in a freezer at -17 ±1 °C to avoid deformation and to ensure a brittle and clean complete fracture during the mechanical testing.

The mixture compositions used are provided in Table 3.3.

Table 3.3: Mixture compositions used for manufacturing the asphalt mortar beams.

mixture	sand type	wt.% of sand	wt.% of metal grit	wt.% of added filler	bitumen type	wt.% of bitumen
mixture 1	sand 1	74	11	0	S46, S70, T44, T74 or P47	15
mixture 2	sand 1	85	0	0	S46, S70, T44, T74 or P47	15
mixture 3	sand 1	81.5	0	3.5	T74	15
mixture 4	sand 1	78.5	0	6.5	T74	15
mixture 5	sand 1	76.5	0	8.5	T74	15
mixture 6	sand 1	73.5	0	11.5	T74	15
mixture 7	sand 1	28.5	0	56.5	T74	15
mixture 8	sand 1	95	0	0	T74	5
mixture 9	sand 1	90	0	0	T74	10
mixture 10	sand 1	80	0	0	T74	20
mixture 11	sand 1	72	0	0	T74	28
mixture 12	sand 2	85	0	0	S70	15

3.2 Methods

The following methods were used to characterise bitumen, mortar beams and the self-healing process of a complete fracture.

3.2.1 Needle penetration

The needle penetration value was determined according to standard BS EN 1426 [206]. Bitumen was heated to 160 °C and subsampled into small tins with a depth of 30 mm. During the subsampling, the trapping of air bubbles inside the bitumen had to be avoided and afterwards tins were covered to prevent dust pollution on the surface. Tins cooled to ambient temperature were submerged in deionised water within glass beakers, which were placed inside a water bath heated at 25 °C. Glass beakers with bitumen tins were removed from the bath and placed under a penetrometer (Setamatic). A stainless steel needle was placed a short distance above the bitumen surface and the automated measurement was started. A total weight of 100 g was applied on the needle to penetrate the bitumen and the distance covered after 5 s was recorded. The test was performed three times, points were at least 10 mm from the brim and to previous points and a clean needle was used for each new measurement. The result is provided as the arithmetic mean in 10^{-1} mm.

3.2.2 Softening point

The ring and ball method was used to determine the softening point of bitumen according to standard BS EN 1427 [207]. Bitumen heated to 150 °C was poured into two preheated rings with an inner diameter of 15.9 mm and a height of 6.4 mm. The rings prepared with bitumen were allowed to cool at ambient temperature for at least 30 min. Any excess material was cleanly cut away and the rings were placed in the assembly for the test. The assembly was placed inside a deionised water bath, which was at a temperature of 5 °C. The assembly was left 15 min to 20 min at 5 °C and then moved to the testing apparatus (automated Ring & Ball Tester, RB36 5G, ISL). At the start of the test, a steel ball with a mass of 3.5 g was placed in the centre of each ring. The apparatus stirred the water bath by a magnetic stirrer and heated the water at a steady rate of 0.083 °C s⁻¹ (5 °C min⁻¹). The softening point was recorded as the temperature when bitumen deformed/flowed a vertical distance of 25 mm.

3.2.3 Bitumen ageing

Bitumen 16-975 S70, T74 and P47 was aged by laboratory ageing methods to represent short-term and long-term ageing.

3.2.3.1 Rolling Thin Film Oven Test (RTFOT)

According to standard BS EN 12607-1 [208], 35.0 g ±0.5 g of bitumen was sampled into glass tubes. The filled tubes were placed horizontally into a rotator, which was inside an oven. The rotator had an angular speed of 15 min⁻¹ ±0.2 min⁻¹. A constant air stream (4.0 l min⁻¹ ±0.2 l min⁻¹) was applied onto the tubes every full rotation for the ageing

duration of 75 min 1 min after reaching the temperature of $163 \text{ }^{\circ}\text{C} \pm 1 \text{ }^{\circ}\text{C}$. After the ageing treatment, bitumen was removed from the glass tubes and the same initial bitumen was merged into one sample container.

3.2.3.2 Pressure Ageing Vessel (PAV)

RTFOT aged bitumen was decanted into stainless steel pans, resulting in a film thickness of approximately 3.2 mm. The filled pans were put into a frame and the frame was put into a preheated to $110 \text{ }^{\circ}\text{C}$ pressure vessel. Temperature and pressure inside the vessel were regulated to 20.7 bar and $110 \text{ }^{\circ}\text{C}$. The ageing duration was $20 \text{ h} \pm 10 \text{ min}$ [209]. After the ageing, bitumen was transferred into sample storage containers.

3.2.4 Viscosity

The viscosity was measured from $60 \text{ }^{\circ}\text{C}$ or $70 \text{ }^{\circ}\text{C}$ to $160 \text{ }^{\circ}\text{C}$ with a spindle rheometer (Brookfield DV-II+ Pro Viscometer) and from $30 \text{ }^{\circ}\text{C}$ to $70 \text{ }^{\circ}\text{C}$ or $80 \text{ }^{\circ}\text{C}$ with a dynamic shear rheometer (Bohlin Instruments C-Vor 200) in temperature steps of $10 \text{ }^{\circ}\text{C}$.

The spindle rheometer consists of rotating spindle viscometer, spindle, sample container and temperature control device, which were all levelled. Bitumen was heated to $160 \text{ }^{\circ}\text{C}$ until liquefied to stir and 9.5 g of bitumen was transferred to the sample container. The sample amount was adjusted to an equivalent volume for mastic mixtures. Investigating the influence of water on the bitumen viscosity, 9.5 g of bitumen was spread on a silicone film. The bitumen film had a thickness of approximately 2 mm. The film was immersed in deionised water for 10 days. Afterwards, the film was removed from the water and introduced into the sample container, where it was left for 4 hours and any excess water was removed from the container before conducting the viscosity measurement. The sample container with bitumen was placed into the temperature control device and the spindle was lowered into the sample. The temperature was set to $160 \text{ }^{\circ}\text{C}$ and the spindle rotation was set to a low shear rate. For water treated bitumen, the initial temperature was set to $60 \text{ }^{\circ}\text{C}$. After a constant temperature was reached in the sample, the spindle rotation was adjusted to a torque near 50%, if possible, and a manual record was taken after the values stabilised. The record included temperature ($^{\circ}\text{C}$), viscosity (mPa·s), torque (%), shear rate (s^{-1}) and shear stress (Pa). The temperature was decreased or increased in $10 \text{ }^{\circ}\text{C}$ steps and recorded until the maximum torque was exceeded at lower temperatures.

The dynamic shear rheometer was used in parallel plate geometry with a plate diameter of 25 mm. Bitumen was heated to $160 \text{ }^{\circ}\text{C}$ and a sufficient amount of bitumen was effused onto the lower plate. The upper plate was moved downwards until the gap between the plates was $1025 \text{ }\mu\text{m}$. Excess bitumen was cut off after a short cooling period of 2 to 3 minutes and the gap was adjusted to $1000 \text{ }\mu\text{m}$. The temperature was regulated by liquid cooling with a mixture of water and ethane-1,2-diol (ethylene glycol) (80:20). The controlling software (Bohlin software: Gemini 200) was set to temperature steps of $10 \text{ }^{\circ}\text{C}$ from $30 \text{ }^{\circ}\text{C}$ to $80 \text{ }^{\circ}\text{C}$ with a constant shear stress of 0.2 Pa.

3.2.5 Viscoelasticity

The viscoelastic properties of bitumen were measured with a dynamic shear rheometer (Bohlin Instruments C-Vor 200). Sample preparation was identical to the process

described in 3.2.4 for the dynamic shear rheometer. Two different tests were carried out. The first test was an amplitude sweep to determine the linear elastic region. The second test was a frequency sweep. The frequency range was from 0.01 Hz to 20 Hz with 11 data points logarithmically scaled. Shear strain was set to 0.01% for P47 and T44, to 0.05% for T74 and S46 and 0.07% for S70, as identified from the amplitude sweep test. The temperature was increased from 30 °C to 80 °C in 10 °C increments.

3.2.6 Density and thermal expansion coefficient

Density and thermal expansion coefficient were determined by a capillary stoppered pycnometer. The test was a modification of standard BS EN 15326 [210]. The volume of the stoppered pycnometer was $25 \text{ cm}^3 \pm 2 \text{ cm}^3$. The weight of stoppered pycnometer was measured after a stable temperature was achieved. After weighing the weight to the nearest 0.1 g of the empty stoppered pycnometer m_0 and the stoppered pycnometer filled with deionised water m_w , the pycnometer was dried and filled to 3/4 with 160 °C preheated bitumen or mastic, m_b . The hot, filled pycnometer was cooled down to ambient temperature and then submerged in a deionised water bath before obtaining its weight m_s . The weight was recorded after a thermal equilibrium was achieved. Before measuring the weight, water on the outside of the stoppered pycnometer was removed by a dry, dust free cloth. Density measurement procedure was carried out at 24.8 °C, 38.6 °C, 47.8 °C and 56.8 °C and the densities were calculated by the following equation:

$$\rho = \frac{m_b - m_0}{(m_w - m_0) - (m_s - m_b)} \rho_w \quad (3.1)$$

with ρ_w as the density of deionised water at the relevant temperature.

The coefficient of thermal expansion was derived from a linear regression of the logarithmised density values plotted against temperature.

3.2.7 Bulk density and void characteristics of bituminous material

The weight m_1 of the selected beams manufactured was determined by a laboratory balance (30000D SCS, Precisa, $\pm 0.1 \text{ g}$). The beams were sealed by a foil (aluminium foil tape, 3M) in a way that the internal voids were part of the volumetric material composition and that no water would penetrate through the foil layer. The mass m_2 of the dry sealed beam was determined. The sealed beam was immersed in tempered water and its mass was recorded m_3 . The following equation was used to calculate the bulk density:

$$\rho_b = \frac{m_1}{\frac{(m_2 - m_3)}{\rho_w} - \frac{(m_2 - m_1)}{\rho_{foil}}} \quad (3.2)$$

with ρ_w as the density of the water and ρ_{foil} is the density of the foil [211], which was provided by the laboratory.

The air void content (vol.%) of the mixture was calculated by the following equation:

$$V_m = \frac{\rho_m - \rho_b}{\rho_m} 100 \quad (3.3)$$

where ρ_m is the maximum density of the mixture, calculated from the densities of the components, and ρ_b is the bulk density of the beam [212].

3.2.8 Capillary rise

Two different set-ups were used to monitor the movement of bitumen in a capillary. Figure 3.1 shows the principle of the set-ups of the two experiments performed. The available diameters of the capillaries used (CM Scientific Ltd) were 1 mm, 0.7 mm, 0.5 mm, 0.3 mm and 0.1 mm and all had a length of 100 mm.

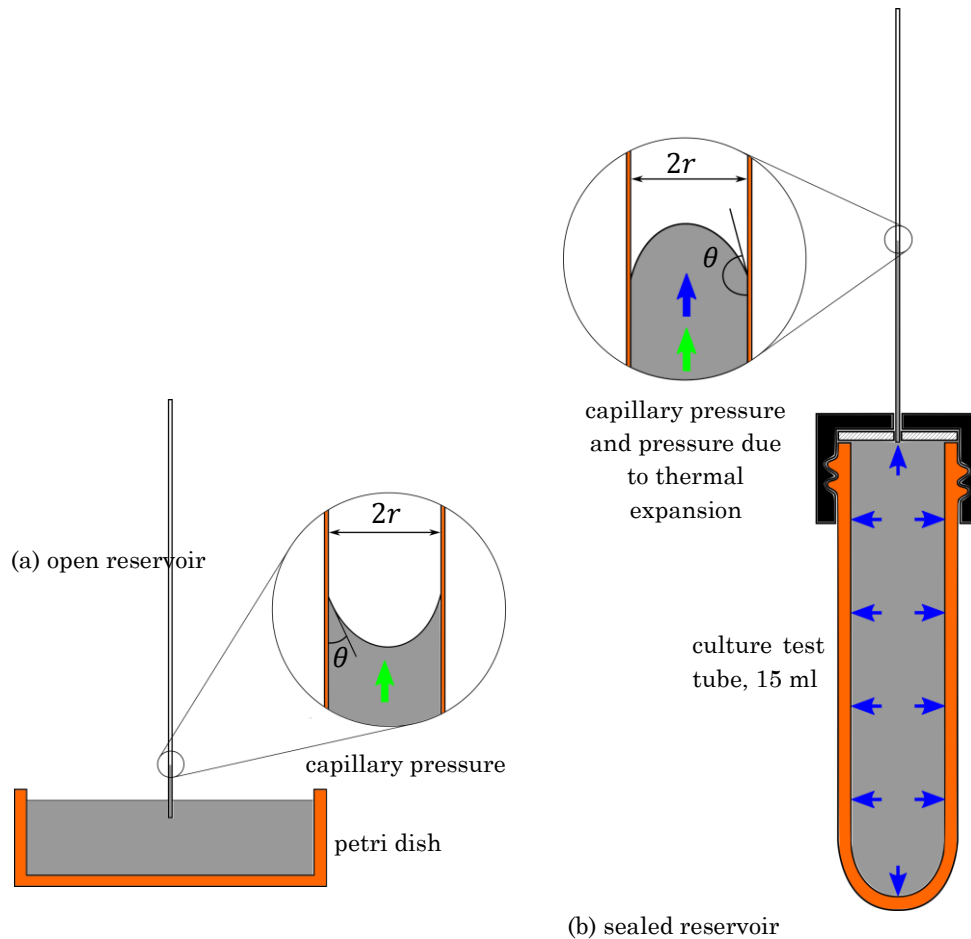


Figure 3.1: Scheme of the capillary flow test (a) without and (b) with thermal expansion pressure [213].

The first set-up, Figure 3.1(a), consisted of five different capillary diameters. These capillaries were glued perpendicular to the bottom edge on a glass tile. The glass tile had a horizontal spaced lines with a spacing of 2 mm till 50 mm and afterwards the line spacing was 5 mm. The prepared glass tile was placed vertically on a preheated petri dish containing bitumen, which was itself inside a vacuum oven (VT6060M, Heraeus). Test temperatures were 40 °C, 60 °C, 80 °C, 100 °C and 120 °C.

In the second set-up, Figure 3.1(b), a single capillary was inserted in a 15 ml culture test tube filled with bitumen through its lid. Any gap between capillary and lid was sealed with silicone. The capillary diameters used were 1 mm to 0.3 mm with 1 mm the main investigated diameter. Graph paper was placed behind the capillary. Four prepared culture test tubes were placed in a tube holder and the set-up was placed inside an oven. The oven temperatures were 40 °C, 60 °C, 80 °C and 100 °C.

The rise of bitumen inside the capillary was recorded with a full HD video camera (AW920, Ausdom) for 24 hours. Also, the final capillary height of the first set-up was recorded for diameters above 0.3 mm.

3.2.9 Surface tension

Three different methods were used to determine the surface tension of bitumen. The first method is a direct determination of the surface tension due to the Young-Laplace equation by using the rising height of bitumen inside a capillary. The other two methods, sessile droplet method and Wilhelmy-plate method, used probe liquids with known surface tension to allow the calculation of the surface tension of bitumen.

3.2.9.1 Capillary height method

The direct method uses the equilibrium height of the capillaries (see 3.2.8) to calculate the surface tension for bitumen N83, S70 and T74. The surface tension was calculated by the following equation [214]:

$$\gamma = \frac{hg\rho r}{2 \cos \theta} \quad (3.4)$$

where h is the height of the bitumen inside the capillary (m), g is gravitational acceleration (m s^{-2}), ρ is the bitumen density (kg m^{-3}), r is the inner radius of the capillary (m) and θ is the contact angle (rad).

3.2.9.2 Sessile droplet method

The second method used was the sessile droplet method. One side of a microscope glass slide (microscope slides, 76 mm x 26 mm, Thermo Scientific) was covered with a bitumen film. A flat surface was achieved by using bitumen heated to 160 °C and the covered slide has allowed to rest for 24 hours at ambient temperature. To investigate the influence of water on the surface tension, prepared microscope slides were immersed in deionised water for 10 days and any water was removed by dry air from the surface before testing. To disperse droplets of test liquid and measure the contact angle a goniometer (rame-hart instrument co.) was used. The probe liquids used were water (sigma-Aldrich, for HPLC), glycerol (Sigma-Aldrich, >98% purity), diiodomethane (Sigma-Aldrich, 99+% purity), ethane-1,2-diol (Fisher Chemical, >99% purity) and methanol (Fisher Scientific, >99.9 purity). Droplets of probe liquid in the range of 3 ml to 6 ml were placed on the bitumen film and the contact angle between droplet and film was measured by software (DROPimage Standard). The surface tension was calculated as the least square fit of the average contact angle measured. A detailed description of the calculation method can be found in [78]. The tests were performed at ambient temperature.

3.2.9.3 Wilhelmy plate method

The last method used to determine the surface tension was the Wilhelmy plate method. Bitumen was heated to 160 °C and placed on a heating plate to ensure low viscosity during the preparation process. A microscope cover glass slide (cover glasses, 24 mm x 40 mm, Menzel-Gläser, Thermo Scientific) was dipped into bitumen, so that both sides of the slide had a continuous flat surface. Slides were stored upside down for 24 hours. The dynamic contact angle was measured by a microbalance (ThermoCahn Radian Series 300 and

WinDCA32) at ambient temperature. The slides were lowered into probe liquids at a speed of $40 \mu\text{m s}^{-1}$ until a distance of 6 mm has been covered. The probe liquids were water (sigma-Aldrich, for HPLC), glycerol (Sigma-Aldrich, >98% purity), diiodomethane (Sigma-Aldrich, 99+% purity) and ethane-1,2-diol (Fisher Chemical, >99% purity). The advancing and receding contact angle was calculated using the software. An average of three measurements for advancing and receding angle was used to calculate the surface tension.

3.2.10 Fractional distribution

The fractional composition of five bitumens was analysed to gain insight into the complex chemical composition of bitumen and to correlate these to the self-healing mechanism. A general separation into asphaltene and maltene fraction was performed at the University of Nottingham, according to standard BS 2000-143 [215]. A separation into saturate, aromatic, resin and asphaltene fractions was done at the Belgian Road Research Centre (BRRC) and Repsol. Furthermore, the wax content was determined at the University of Nottingham, according to standard BS EN 12606-1 [216].

The separation into fractions at the Belgian Road Research Centre was performed according to a modified standard IP 469 [217], by thin layer chromatography – Iatroscan (TLC-FID analyser MK-6s, SES GmbH Analytical Systems). The quartz rods used were coated with a thin layer of silica. The analysis was carried out in two steps. First, the asphaltene fraction was determined by eluting bitumen in dichloromethylene and methanol (95:5) with the maltene fraction as elution. This was followed by eluting the saturate fraction, using heptane, and aromatic fraction, using a toluene and heptane solution (80:20). The resin fraction was subsequently determined as the difference of saturate, aromatic and asphaltene fraction from the whole bitumen sample used. The process was repeated seven times.

The separation performed at Repsol was by following standard ASTM D4124-9 [218].

3.2.11 Attenuated total reflection Fourier transformed infrared spectroscopy

The infrared spectra were obtained on a Bruker Tensor 27 with a diamond anvil in attenuated total reflection set-up. A single spectrum ranged from 4000 cm^{-1} to 500 cm^{-1} with a 4 cm^{-1} resolution and consisted of 128 scans with automated background correction. A drop of bitumen was placed on the anvil and the spectrum was obtained. Afterwards the anvil was cleaned with different solvents to ensure a contamination free spectrum. The post-processing (OPUS spectroscopy software, Bruker) included a cutting of the spectrum to 4000 cm^{-1} to 550 cm^{-1} , a rubber band baseline correction (64 points) and normalisation (minimum-maximum method).

3.2.12 Bitumen and mortar flow in a Hele-Shaw cell

To observe the effect of water on the flow of bitumen and mortar, the movement of the contact line in a Hele-Shaw cell (the initial condition is illustrated in Figure 3.2) was monitored under air and deionised water conditions. Pure bitumen and two different mortar mixtures (weight ratios of 50:50 and 15:85) were used for the test. Bitumen and mixtures were heated to $160 \text{ }^\circ\text{C}$ and poured into a rectangular mould of $74 \text{ mm} \times 24 \text{ mm}$

to produce a film of approximately 1.5 mm thickness. A triangular notch with a base of 10 mm and a height of 10 mm was cut out in the middle of the long side of the film, as illustrated in Figure 3.2. Afterwards, the film was placed between two microscope slides (76 mm x 26 mm, Thermo Scientific) to form a Hele-Shaw cell. The sides of the cell without the triangular notch were sealed with plasticine (Newplast) to prevent material loss during the experiment. The Hele-Shaw cell was placed vertically with the triangular notch at the top inside an incubator (TC 140 G, Lovibond) at 40 °C. The medium surrounding the cell and filling the notch was either air or deionised water, inside a bath with transparent walls. The movement of the contact line was recorded by taking a picture every 10 min for 5 hours with an HD camera (AW920, Ausdom).

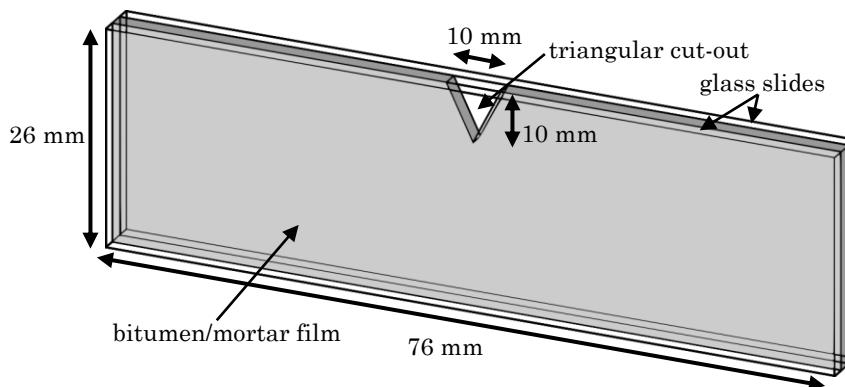


Figure 3.2: Illustration of a Hele-Shaw cell, containing a bitumen film (grey coloured) with a triangular cut-out between two glass microscope slides [219].

3.2.13 Determining gap flow and drainage composition

The material flow was investigated by placing broken beams inside silicone moulds and using the horizontal gap between the two mould pieces as opening, as shown in Figure 3.3. The opening was circumferential at a height of approximately 15 mm from the bottom of the beams and the distance between both mould pieces forming the opening was approximately 1 mm. The recovery of the crack, as well as the flow, was induced at 100 °C by a convection heating oven (Hot Box oven, Gallenkamp). The length and thickness of the flow were measured by a calliper. Afterwards, the material drained into the opening between the mould pieces was removed and weighed into glass vials. About 20 ml methyl benzene (Fisher Scientific, 99.98% purity) was added into each vial, which dissolved the bitumen. The content of the vial was transferred onto a filter paper (Fisherbrand QT210, fine retention and slow flow rate), collecting the filtrate in a 250 ml round-bottom flask. Filter paper including filter cake was placed inside an extractor (as specified in standard BS 2000-143 [215]). Methyl benzene was added until the round-bottom flask was filled with approximately 100 ml. The flask was placed on top of a heating mantle and the extractor was connected to a Davies condenser. The extraction was performed until the filter paper was clear of dark (black to brown) stains and no eluant was transparent. The filter cake was weighted and further sieved through two sieves with a mesh aperture of 1 mm and 63 µm.

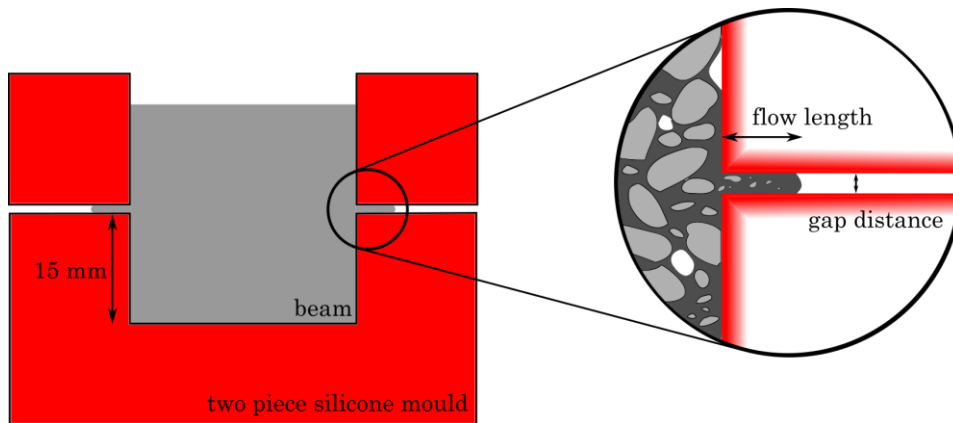


Figure 3.3: Illustration of the gap flow experiment, as the beam is placed within the two piece silicone mould. Self-healing and the flow of material was enhanced by convection heating.

3.2.14 Self-drainage of viscous liquids on a vertical surface

The film thickness of bitumen and mastic due to gravitational flow was determined in order to estimate the amount of bitumen or mastic which could freely flow bigger aggregates into the cracks. Therefore, bitumen or mastic was heated to 160 °C and glass slides (76 mm x 26 mm, Thermo Scientific) were coated with a thick film over the length of approximately 60 mm, as shown in Figure 3.4. The filler bitumen ratios in the mastic mixtures were 9:81, 50:50 and 70:30. Coated glass slides were placed hanging vertically inside an oven (VT6060M, Heraeus) at temperatures of 60 °C, 80 °C, 100 °C and 120 °C. The slides remained in the oven until no further dropping was observed. The film thickness was determined 15 mm and 45 mm from the upper film edge, as indicated in Figure 3.4.

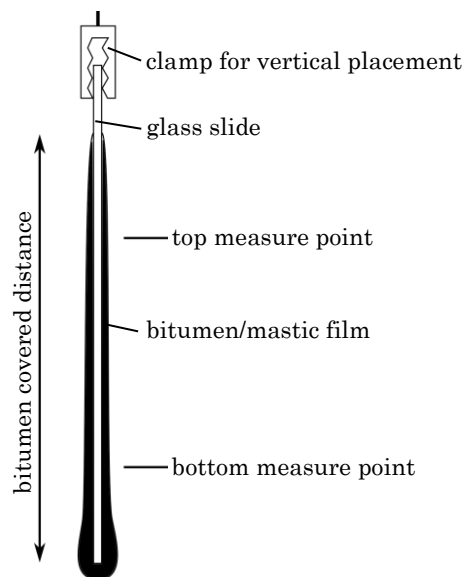


Figure 3.4: Bitumen/mastic coated microscope glass slide, which was placed vertically inside an oven, and the measurement points to determine the film thickness.

3.2.15 Specific surface area

The specific surface area of sand 1 and sand 2 was measured by dynamic vapour sorption (DVS advantage, surface measurement systems). The system was cleaned with ethanol

and purged with nitrogen (BOC) at a flow rate of 100 SCCM (standard cubic centimetres per minute). After a stable baseline of the balance was reached, the balance was zeroed and a total of about 1 g of counter weights was placed in one pan of the balance. The other pan was filled by weight with nearly the same amount of sand. After 30 min, to have a stable weight reading, the automated test was started. The test sequence consisted of a drying phase at 120 °C, at the end of which the dry weight of the sample was recorded, followed by a stepwise increase of partial water pressure. The increase per step was 10% partial pressure from 0% to 90% and the duration of each step was 60 min. The recorded data were analysed with the implemented (Dynamic Vapour Sorption – Advantage 2.1.5.1) Brunauer-Emmett-Teller theory to obtain the specific surface area.

3.2.16 Water evaporation

To correlate the self-healing and the evaporation of water in asphalt mortar beams and to confirm the duration of drying, the weight of beams saturated with deionised water was periodically recorded after removing the beams from the water tank. The evaporation was recorded at temperatures of 20 °C and 40 °C for 24 hours and at 5 °C, 12 °C and 20 °C for 72 hours. The weight loss was measured by a digital balance (Obhaus Ranger 3000), with a resolution of 0.05 g. To control the temperature, the digital balance was positioned inside an incubator (TC 140 G, Lovibound). Three repetitions per temperature were performed to obtain an average evaporation curve. In addition, the initial water saturated weight of a mortar beam and its weight after 24 hours at 60 °C were recorded. A periodic record was not possible due to the temperature limit of the balance used.

3.2.17 Mechanical testing (three-point breaking)

The self-healing ratio was determined by three-point breaking tests (servo-pneumatic universal testing machine with a fan assisted temperature cabinet, Cooper Technology). The set-up of the testing and dimensions are shown in Figure 3.5. The frozen beams were removed from the freezer and instantly broken by three-point breaking. The test was stress controlled with a rate of $10.2 \text{ N} \cdot \text{s}^{-1} \pm 0.6 \text{ N} \cdot \text{s}^{-1}$. The same test was performed after the samples were subjected to self-healing conditions. The self-healing ratio SR (-) was defined as the maximum load for breaking after self-healing, F_H (N), to the initial breaking force, F_I (N), represented by Eq. (3.5). The conditions were modified to determine the initial recovery ratio and the influence of water on the initial recovery ratio. Since water would freeze inside the freezer, in order to avoid determining the breaking force of ice, the beams were not frozen before breaking the beams a second time by three-point breaking.

$$SR = \frac{F_H}{F_I} \quad (3.5)$$

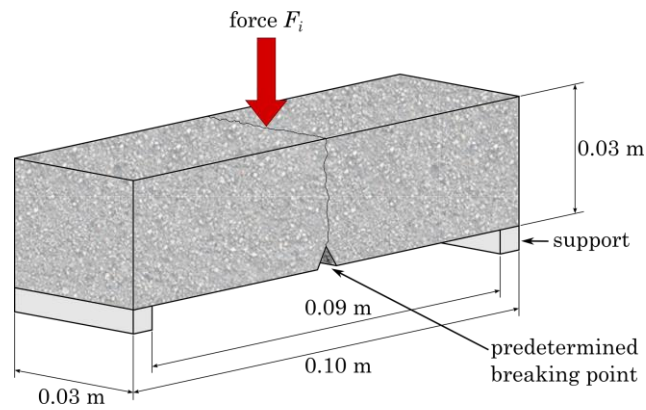


Figure 3.5: Dimensions of the asphalt mortar beam and the three-point breaking test set-up. The point of force was vertically aligned with the predetermined breaking point in the middle of the underside of the beam [25].

3.2.18 Self-healing conditions

An overview of the conditions regarding support, heating method and influence of water is provided in Table 3.4.

Table 3.4: Overview of self-healing conditions.

heating method	support		
	PTFE mould	silicone mould	without mould
convection heating/cooling	A	A	A/W
induction heating	-	A	-

A: air; W: water

The self-healing conditions refer to the surrounding conditions of the beams during the self-healing time. The first differentiation is based on the support during healing. Two different moulds were used to support the beams, as shown in Figure 3.6, and beams were healed without support from moulds. The first mould was the manufacturing mould made of PTFE. The second mould was a two piece silicone mould with dimensions approximately 1 mm smaller than the beams, which applied a circumferential pressure of $0.045 \text{ N} \cdot \text{mm}^{-2}$ to the beams. The third support condition was without moulds, as the manufactured beams with 15wt.% bitumen proved to be dimensionally uncompromised during convection heating up to $120 \text{ }^\circ\text{C}$.

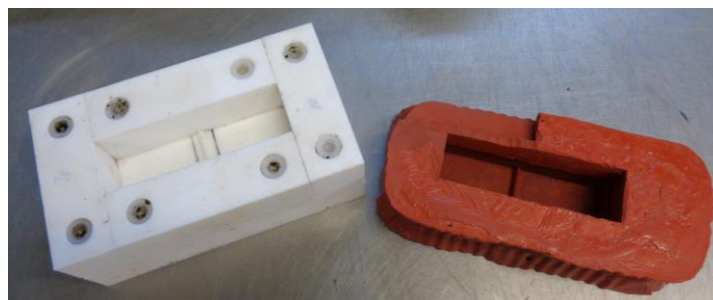


Figure 3.6: Moulds used to support the asphalt mortar beams during heat induced self-healing. PTFE mould (left) consisted of five pieces and was also used to manufacture the beams and a two piece silicone mould (right).

Two different heating methods were used to increase the temperature of the beams to enhance the self-healing. The first heating method was convection heating. For temperatures from 5 °C to 40 °C an incubator (TC 140 G, Lovibond) was used and for higher temperatures an oven (Hot Box oven, Gallenkamp) was used. The temperatures used were 5 °C, 8 °C, 12 °C, 20 °C, 40 °C, 60 °C, 80 °C, 100 °C and 120 °C. The second heating method was induction heating, which was performed on samples containing the metal grit. A 6 kW induction heating generator (EasyHeat, Ambrell Company) was used at a frequency of 348 kHz and the current intensity was set to 50 A, 80 A, 100 A, 200 A and 300 A. The beams were supported by silicone moulds and placed centrally under a three-winding flat square coil of 150 mm x 150 mm at a distance of approximately 10 mm, as shown in Figure 3.7. The surface temperature was monitored for convection and induction heating by an infrared camera (micro-epsilon, TIM 160, UFPA, 160x120 pixels).

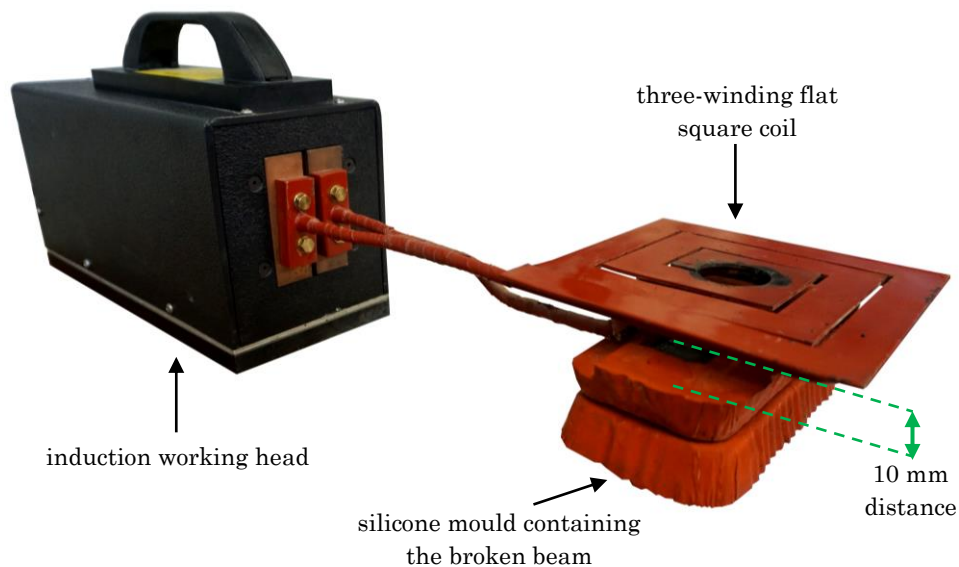


Figure 3.7: Beam supported by silicone mould underneath the induction heating set-up with induction heating heat and three-winding flat square coil [25].

The influence of water on the self-healing mechanism was studied on the mixture 12 with 15wt.% bitumen S70 and 85wt.% sand 2. Three different conditionings of beams were investigated, as illustrated in Figure 3.8. The first condition (water-water) consisted of immersing the broken beams in deionised water at 20 °C for 10 days, to saturate them, followed by assembling the beam halves wet and allowing the beams to self-heal while immersed in deionised water. The second condition (water-air) was assembling the beam halves after immersing them in deionised water at 20 °C for 10 days and allowing the beams to self-heal in air. The third condition (air-air) consisted in assembling the dry beam halves and allowing them to self-heal in air. The durations allowed for the self-healing were 5 hours, 1 day, 3 days, 7 days and 10 days. After self-healing, the beams were stored at 20 °C for 24 hours, to dry them before freezing at -17 °C. In addition, a series of beams from the first condition without a drying phase was fractured with and without freezing to identify the influence of water and ice on the crack self-healing.

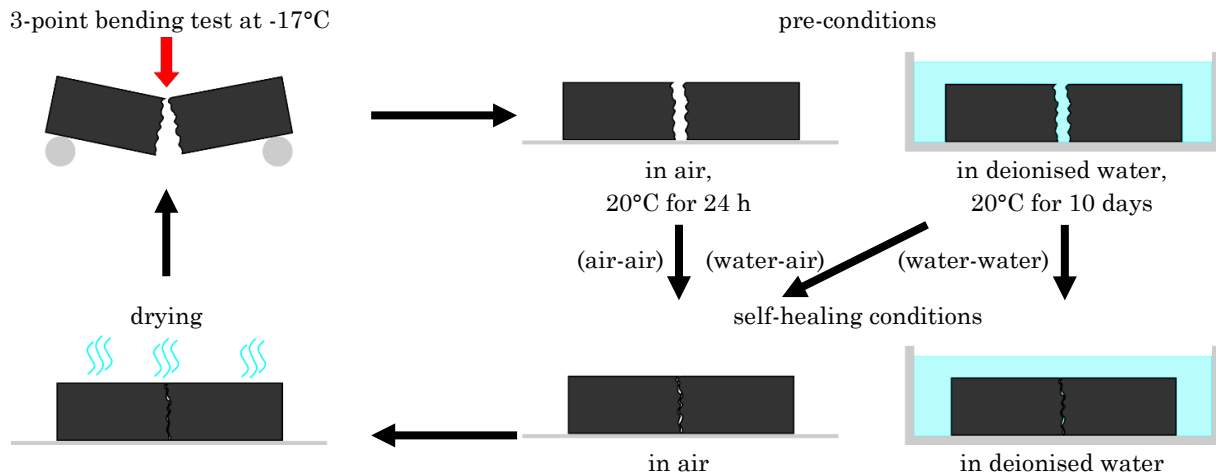


Figure 3.8: Procedure to evaluate the self-healing of asphalt mortar beams in air and in water [219].

To ascertain the effect of air pressure on the complete fracture self-healing of asphalt mortar, beams were healed under a range of air pressures. Beam halves were assembled and placed on a frame inside a temperature controlled 7 litre pressure vessel (heatable reactor with reactor controller PARR 4842, Parr Instruments company). Two temperatures were studied, 20°C and 40°C . The pressure was applied at a rate of approximately $0.008\text{ bar}\cdot\text{s}^{-1}$ ($0.5\text{ bar}\cdot\text{min}^{-1}$) from a compressed air gas cylinder (BOC) until 0 bar, 5 bar, 10 bar and 20 bar were reached. The duration of the self-healing was 1 hour after the intended gas pressure inside the vessel was reached. Afterwards, the pressure vessel was decompressed within 30 min.

All beams were stored directly after the healing process inside a freezer (Chest Freezer 412 Litre, CFH382AWK, Hoover) at $-17^{\circ}\text{C} \pm 1^{\circ}\text{C}$ to avoid further healing until testing. Testing conditions were the same as for the initial three-point breaking, unless otherwise stated.

3.2.19 Adhesion testing and healing

The fracture strength of bitumen and aggregate was tested by a pneumatic adhesion tensile testing instrument (PATTI, PATTI QUANTUM GOLD – Adhesion Tester with F-4 piston, Semicro Division, M.T.Taylor Engineering). Therefore, cylindrical aggregate plates with a diameter of 100 mm and a height of 20 mm, which were cut from a limestone boulder using a diamond edged saw and polished with sand paper, were cleaned with an organic solvent (white spirit BS245, Bartoline) and subsequently water. Aggregate plates were dried at 105°C and afterwards kept at 70°C for at least an hour. The metal pull-stubs with a diameter of 20 mm were cleaned with the same organic solvent. The bitumen was heated to 150°C and then poured onto the prepared aggregate plates. Immediately after pouring an appropriate amount of bitumen onto the plates, a metal pull-stub was pressed onto the plate to establish a good bond. The film thickness was controlled by the pull-stub geometry and was approximately 0.8 mm. Any excess bitumen was removed by using a heated spatula after cooling to ambient temperatures. For the test, a piston of 73 mm was screwed on top of the pull-stub. The air pressure was provided by a CO_2 cartridge and manually controlled for a constant rate of pressure. The maximum tensile pressure was converted to a pull off tensile strength. After testing, the samples were

placed in the original position and stored at approximately 8 °C for 24 hours, before the test was repeated to account for any self-healing during this duration.

3.2.20 Computer tomography scans (CT scans)

The visualisation of a macro crack through asphalt mortar was done by an X-ray μ CT scans using a Phoenix Nanotom 180NF (GE Sensing & Inspection Technologies GmbH). The scanner consisted of a 180 kV nanofocus X-ray tube and a 5 megapixel flat panel detector. Scans of two broken cylindrical beams (8 mm in diameter and about 19 mm in height), to meet the dimensional requirements of the equipment, were performed. The sample was stuck to a sample holder and the scan took approximately 1.5 hours. Scanning conditions were 90 kV energy and 80 μ A current for the X-ray source. The exposure time per image was 500 ms and the average of three images per 0.013 rad rotation was taken. Images were analysed with the corresponding software to operate the Nanotom (Datos|x2.0 reconstruction, GE Sensing & Inspection Technologies GmbH) and the image software (ImageJ 1.49k, Fiji, NIH).

3.2.21 Optical images

To visualise the crack through the material, a beam was cut into two halves. The cut was parallel to the long side of the beam. The halves were broken at low temperature and assembled at ambient temperature. The crack was magnified by an optical microscope (Nikon eclipse LV100ND, control Nikon LV-NCNT2) with different objective lenses (5x/0.15, 10x/0.3 and 50x/0.80). The distances between the crack surfaces were measured at several positions along the crack and pictures were taken by an implemented camera (Nikon digital sight DS-Ri1). A second Microscope (Nikon SMZ800) was used to observe the crack surface and images were obtained by the implemented camera (CMEX DC.5000, EUROMEX). Regular images were taken with a camera (α 6000, Sony; with SEL30M35 and SELP1650, E-mount lenses, Sony) for documentation.

4 Self-healing of cracks

A conceptual model of self-healing in asphalt is provided, followed by a physical model. For the physical model, the crack was pictured as a parallel plate capillary, as the self-healing is regarded as a flow process. Hence, the Navier-Stokes equation for the flow of a liquid in a capillary was used to derive an equation to calculate the self-healing ratio with respect to time. This equation was later used to fit experimentally obtained self-healing ratios to verify its validity. The pseudo healing energy parameter is described to make different heating methods comparable, which for this research were convection heating and induction heating.

4.1 Conceptual model of asphalt self-healing

After a macro crack is induced in the asphalt, either due to repeated loading as a result of micro crack propagation or thermal contraction at low temperature with or without loading [3], the material's inherent self-healing mechanism initiates once the temperature is above a certain threshold [149]. An additional condition for self-healing to happen is that the cause of the damage (mostly stress due to loading or temperature change) vanishes, as the self-healing rate is slower than the damage rate [31]. A positive temperature change contributes to the approach of the fracture surfaces. This reduces the distance between the surfaces or even can press the surfaces together if the difference in temperatures is high enough. The expansion coefficient for asphalt is similar to its contraction coefficient [74, 220], though due to relaxation at elevated temperatures cracks, especially low temperature induced cracks, are likely to remain closed after the self-healing.

Since bitumen and mineral aggregates have different thermal expansion coefficient, with bitumen having a higher coefficient [3, 74], expanding bitumen is drained into the crack as the temperature of asphalt increases. Even if the temperature remains constant, asphalt self-heals above the threshold temperature, as material flows due to gravity and capillary pressure [17] into the crack, filling it. The individual self-healing mechanism, which results in a filling of the fracture, is sensitive to temperature and an increased temperature increases the rate of filling and reduces the time for recovering from induced damage.

Depending on the fracture progression, fractures through mineral aggregates can be brought into contact, but without adhesive connection, a tension load bearing connection is not established [156]. These sections of a fracture can be adhered to each other by bituminous material flowing into the void between the aggregate halves, which can be due to capillary flow or gravity driven flow.

The temperature distribution for roads changes during a day and with the seasons [221, 222]. Colder temperatures, below the threshold temperature, prevent self-healing and support damage progression, in contrast warmer temperatures enhance the self-healing. A temperature gradient develops during warm periods from the surface into the structure [221]. A similar gradient would be present for the self-healing. Near the surface the contribution due to thermal expansion governs the self-healing and further from the surface the hydrostatic pressure in the material becomes more important. In addition, the viscosity would follow an inverse temperature profile.

Similar mechanisms occur for thermally enhanced self-healing like induction heating or microwave heating. Heated particles emit thermal energy into their surroundings, which comprise the bitumen around these particles, and material is pressed into the fracture due to expansion and the reduced viscosity [28]. For extrinsic self-healing, like capsule based healing, the main contribution in closing a fracture is the diffusion of a healing agent, which is stored inside the hollow capsule and is released into the fracture as damage occurs, to lower the viscosity of bitumen, which drains into the crack [29, 197].

4.2 Physical model of asphalt self-healing

The self-healing mechanism requires a minimum of internal energy to be initiated. The internal energy of a system can be increased either by work (pressure-volume work) or by heat transfer. Both methods of energy transfer induce each other (realistic materials) and thus in a system, such as asphalt, mortar, mastic or bitumen, a combination of work and heat transfer occur. Since bitumen and asphalt properties are temperature dependent and a positive heat transfer and/or work result in an increased temperature of the system, the minimum internal energy can be connected to a critical minimum temperature. This critical minimum or threshold temperature is pressure dependent and is either associated with the glass transition temperature of bitumen [223] or the transition temperature from a non-Newtonian fluid to a Newtonian fluid (assumed as 90% of the ideal Newtonian behaviour of a fluid) [149].

The fracture surfaces through mortar or asphalt have to be in close vicinity for the self-healing mechanism to happen. It is assumed that mainly bitumen or material with a high bitumen content drains from the surrounding mixture into the fracture. This drainage happens until an equilibrium of pressures is reached. These pressures include surface tension, gravity acting on bitumen within the fracture and in the surrounding mixture (hydrostatic pressure) and additional pressure due to thermal expansion or mechanical loading. In this research, a two-dimensional parallel plate channel (a capillary with one infinite radius orthogonal to the shortest radius between centre and capillary wall) was used to represent the fracture. The dynamic balance describing the motion of the material inside the fracture is given by the Navier-Stokes Equation [224, 225] and presented in Eq. (4.1).

$$\frac{d(\rho h \dot{h})}{dt} = \frac{\gamma \cos(\theta)}{a} - \frac{3\eta h}{a^2} \dot{h} - \Delta\rho g h \sin(\varphi) + p \quad (4.1)$$

inertia
capillary
viscous
gravity
additional
pressure

where $\Delta\rho$ is the difference in density ($\text{kg}\cdot\text{m}^{-3}$) between flowing medium and replaced medium, h is the length or height (m) flowed through by the material in the fracture, \dot{h} is the derivation of the length with time – velocity ($\text{m}\cdot\text{s}^{-1}$), t it the time (s), γ is the surface tension ($\text{N}\cdot\text{m}^{-1}$), θ is the dynamic contact angle (rad), which is velocity dependent [226], a is the half gap width (m), η is the viscosity ($\text{Pa}\cdot\text{s}$) of the flowing material, g is the gravity acceleration ($\text{m}\cdot\text{s}^{-2}$), φ is the angle of the inclination (rad) of the fracture to the vertical and p is the additional pressure (Pa) caused internally (thermal expansion or hydrostatic pressure of the surrounding material) or externally (loading).

The inertia term can be neglected since bitumen is a highly viscous material and the transition time from a visco-inertial flow to a purely viscous flow [227, 228] is approximately reached in nanoseconds for the bitumen types used. The dynamic contact angle depends on the velocity of the moving material in a capillary and can be roughly assumed to be linearly dependent [229].

$$\gamma \cos(\theta) = \gamma - \beta \frac{dh}{dt} \quad (4.2)$$

where β is the friction coefficient ($\text{kg m}^{-1} \text{s}^{-1}$) in regard to the linear assumption for the flow over a dry solid surface or on a thin film of a prewetted surface.

A liquid flows through a capillary from the opening and the sides of the capillary are solid or prewetted. In contrast, the fracture surface of asphalt or mortar is self-permeable, allowing a bitumen rich mixture, like mastic, to drain from the surroundings into the fracture. This circumstance is satisfied by the assumption of a constant length l_c (m) in the viscous loss term. Hence, Eq. (4.1) simplifies to

$$0 = \frac{\gamma - \beta \frac{dh}{dt}}{a} - \frac{3\eta l_c}{a^2} \frac{dh}{dt} - \Delta\rho g h \sin(\varphi) + p = \frac{\gamma}{a} - \left(\frac{3\eta l_c}{a^2} + \frac{\beta}{a} \right) \frac{dh}{dt} - \Delta\rho g h \sin(\varphi) + p \quad (4.3)$$

The second term on the right side in Eq. (4.3) represents all the dissipative losses during the flow process. The equation is solved with an initial condition of $h(0) = h_0$, which represents an initial contact at the start of the recovery.

$$h(t) = \frac{\gamma + ap}{a\Delta\rho g \sin(\varphi)} \left(1 - e^{-\frac{a^2\Delta\rho g \sin(\varphi)}{a\beta + 3\eta l_c} t} \right) + h_0 e^{-\frac{a^2\Delta\rho g \sin(\varphi)}{a\beta + 3\eta l_c} t} \quad (4.4)$$

Three cases are of interest with regard to the inclining angle φ . If φ equals 0 or π , the fracture/channel is horizontal and Eq. (4.4) shows no result. Therefore Eq. (4.3) has to be solved with $\varphi = 0$.

$$h(t) = \frac{a\gamma + a^2p}{a\beta + 3\eta l_c} t + h_0 \quad (4.5)$$

In the horizontal case, the length flowed through by the fluid is linearly proportional to time, as shown by Eq. (4.5). If φ equals $\frac{\pi}{2}$, $\sin(\varphi)$ equals to 1 and represents a vertical fracture with fluid moving upwards inside the fracture. An equilibrium height can be calculated if time approaches infinity.

$$h(t) = \frac{\gamma + ap}{a\Delta\rho g} \quad (4.6)$$

Eq. (4.6) is similar to Jurin's law (Eq. (3.4)) for calculating the equilibrium height of a liquid inside a capillary tube due to surface tension (capillary pressure) and hydrostatic pressure of the fluid inside the capillary. The rise of material inside a fracture has a natural limit, which is the distance to the surface, which is not included in the equations, as it is assumed that the gap has infinite expansion in two dimensions. In the last case, φ is equal to $-\frac{\pi}{2}$. This is likewise a vertical fracture, though the material is moving downwards. There is no equilibrium height and material is drained until depletion. This

draining effect might explain the decrease in the self-healing ratios after reaching a maximum [17], in addition to the consideration of thermal damage and ageing.

Developing Eq. (4.4) in a Taylor series, Eq. (4.5) will be obtained if only terms of first order are considered. A linearised approach and the cases of $\varphi = 0, \pi$ or $-\frac{\pi}{2}$ would result in a quadratic increase of the filled area inside the fracture. Only if $\varphi = \frac{\pi}{2}$ increase is limited. Therefore, this case will be further used to calculate the area in the fracture, as filling of the crack is limited by geometric factors, the available material and if impurities or air is trapped during the flow process, which causes the self-healing rate to decrease with increasing time due to displacement.

In this research, frozen prismatic beams were subjected to three-point breaking to obtain a complete fracture. The force to break a beam can be calculated by using the Euler-Bernoulli beam theory [230]. Eq. (4.7) gives the force for a symmetrically loaded and supported beam with load applying in the middle of the beam.

$$F = \frac{8\sigma_u I_y}{LH} \quad (4.7)$$

where F is the force to break the beam (N), σ_u is the ultimate stress (N m⁻²), I_y is the second moment of area (m²), L is the distance between the supports (m) and H is the height of the beam (m).

The self-healing is time dependent and hence, the force after a period of self-healing will increase.

$$F(t) = \frac{8\sigma_u(t)I_y(t)}{LH(t)} \quad (4.8)$$

where $F(t)$, $\sigma_u(t)$, $I_y(t)$ and $H(t)$ are time dependent now.

The transmittable force increases with time, as the interface gradually disappears due to crosslinking and entanglement of molecules across the interface [173]. A similar increase was proposed for asphalt [150]. However, the self-healing is limited and the ultimate stress might be lower after the self-healing duration as fractures through stones, which might be filled with bitumen/mastic, are mechanically weaker compared to the original aggregate. The second moment of area increases with increasing self-healed crack area. The vertical distance between two self-healing fronts can be used as the height to calculate the second moment of area, assuming the self-healing front is constant in width. For a complete healed crack interface, the vertical distance between the self-healing fronts becomes the height of the beam. The second moment of area is in general calculated as follows [230]:

$$I_y(t) = \int_A z^2 dA(t) \quad (4.9)$$

where z is the perpendicular distance from the axis to $dA(t)$ (m) and $dA(t)$ is the differential area of an arbitrary shape (m²).

For the initial self-healing, it was assumed that the flowing material front is rotationally symmetrical for each contact point and the number of contact points c_p (-) remains constant [17]. The area of rotationally symmetrical contact points was calculated by using $h(t)$ of Eq. (4.4) as the radius. At the beginning of the self-healing, the area will be small, thus the individual second moment of area will be negligible compared to the proportion due to the parallel axis theorem ($z \gg \frac{h}{2}$).

$$\begin{aligned}
I_{y,start}(t) &= c_p z^2 \pi (h(t))^2 \\
&= c_p z^2 \pi \left(\left(\frac{\gamma + ap}{a\Delta\rho g \sin(\varphi)} \right)^2 \left(1 - e^{-\frac{a^2 \Delta\rho g \sin(\varphi)}{a\beta + 3\eta l_c} t} \right)^2 \right. \\
&\quad + 2 \frac{\gamma + ap}{a\Delta\rho g \sin(\varphi)} h_0 \left(e^{-\frac{a^2 \Delta\rho g \sin(\varphi)}{a\beta + 3\eta l_c} t} - e^{-2\frac{a^2 \Delta\rho g \sin(\varphi)}{a\beta + 3\eta l_c} t} \right) \\
&\quad \left. + h_0^2 e^{-2\frac{a^2 \Delta\rho g \sin(\varphi)}{a\beta + 3\eta l_c} t} \right)
\end{aligned} \tag{4.10}$$

After the initial contact, the areas self-healed in the crack increase and coalesce. This process is simplified into limiting the growth of the initial points to the size as they coalesce, which is mathematically the case if $\varphi = \frac{\pi}{2}$, resulting in a limited growth function.

$$\begin{aligned}
I_y(t) &= c_p z^2 \pi \left(\left(\frac{\gamma + ap}{a\Delta\rho g} \right)^2 \left(1 - e^{-\frac{a^2 \Delta\rho g}{a\beta + 3\eta l_c} t} \right)^2 \right. \\
&\quad \left. + 2 \frac{\gamma + ap}{a\Delta\rho g} h_0 \left(e^{-\frac{a^2 \Delta\rho g}{a\beta + 3\eta l_c} t} - e^{-2\frac{a^2 \Delta\rho g}{a\beta + 3\eta l_c} t} \right) + h_0^2 e^{-2\frac{a^2 \Delta\rho g}{a\beta + 3\eta l_c} t} \right)
\end{aligned} \tag{4.11}$$

Further, the self-healing ratio is defined in a mechanical sense as fracture force after self-healing to initial fracture force, identical to Eq. (3.5).

$$S(t) = \frac{F(t)}{F_i} \tag{4.12}$$

Substituting Eq. (4.8) and Eq. (4.11) in Eq. (4.12) leads to the following equation for the recovery ratio:

$$S(t) = S_0 e^{-2\frac{a^2 \Delta\rho g}{a\beta + 3\eta l_c} t} + C \left(1 - e^{-\frac{a^2 \Delta\rho g}{a\beta + 3\eta l_c} t} \right)^2 + D \left(1 - e^{-\frac{a^2 \Delta\rho g}{a\beta + 3\eta l_c} t} \right) e^{-\frac{a^2 \Delta\rho g}{a\beta + 3\eta l_c} t} \tag{4.13}$$

with

$$S_0 = \frac{8\sigma_u c_p z^2 \pi h_0^2}{F_i L \dot{H}} c_p z^2 \pi h_0^2 = \frac{F_{adhesive}}{F_i} \tag{4.14}$$

$$C = \frac{8\sigma_u c_p z^2 \pi}{F_i L \dot{H}} \left(\frac{\gamma + ap}{a\Delta\rho g} \right)^2 \tag{4.15}$$

$$D = \frac{16\sigma_u c_p z^2 \pi \gamma + ap}{F_i L \dot{H}} \frac{1}{a \Delta \rho g} h_0 \quad (4.16)$$

where \dot{H} is the vertical height of connected area fronts, which are furthest apart (m).

Eq. (4.13) is an augmentation of the equation published by García [17]. It incorporates a term for initial recovery due to adhering of the fracture surfaces on contact. The time dependency of the initial self-healing in Eq. (4.13) arose from the decreasing contribution of the initial starting height on the final height, which is determined by the equilibrium of forces. Further, parameters C and D are not independent. The ratio of C and D is equal to the ratio of driving pressures for the material movement in the fracture (surface energy and additional pressure) to the hydrostatic pressure caused by the initial contact height.

$$\frac{C}{D} = \frac{\gamma + ap}{2a\Delta\rho gh_0} \quad (4.17)$$

Considering that the driving pressures are considerably higher than the hydrostatic pressure from the initial contact, parameter D can be neglected. This results in the following simplified equation to calculate the self-healing ratio:

$$S(t) = S_0 e^{-2c_1 t} + C(1 - e^{-c_1 t})^2 \quad (4.18)$$

with

$$c_1 = \frac{a^2 \Delta \rho g}{a\beta + 3\eta l_c} \quad (4.19)$$

as healing exponent.

Although obtained through physical considerations, the final equation was obtained by considering the known shape of the self-healing ratio over time as a limited growth function, which is shown in section 6. This is owing to the unknown and individual healing of fractures, which is generalised in the equations.

4.2.1 Modelling the energy input into the self-healing system

Since the minimum internal energy required for the self-healing of fractures is connected to a critical minimum temperature, this temperature can be measured during experiments and related to field measurements. Measuring temperature is easily accessible compared to the parameters to calculate the internal energy due to heat transfer (like thermal expansion coefficient, compressibility coefficient and heat capacity) and an inhomogeneous distribution in the system.

A simple calculation of a pseudo healing energy parameter was proposed by García, Bueno, Norambuena-Contreras, Partl [32]. This parameter represents the area below a temperature-time curve during the self-healing, as illustrated in Figure 4.1.

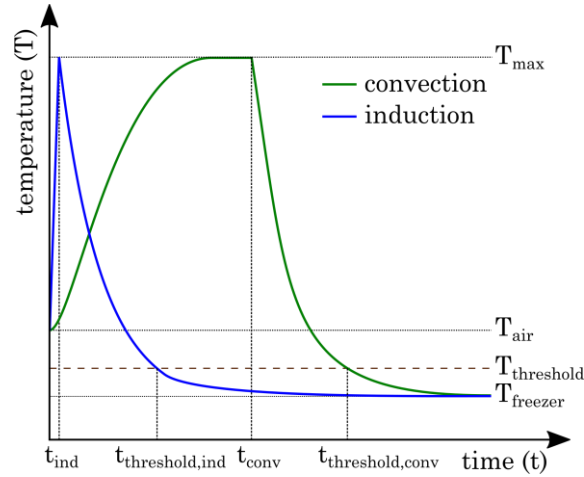


Figure 4.1: Temperature development of convection and induction heating [25].

As illustrated in Figure 4.1, the heating method affects the calculation of the pseudo healing energy parameter due to different temperature-time curve progressions. Therefore, the temperature progression has to be determined for each heating method. For convection heating, the mathematical expression for the time-temperature area is based on the convection heat transfer equation for heating and cooling [231]:

$$\begin{aligned} \tau_{conv} = & T_{max}t_{conv} - \frac{T_{max} - T_{air}}{k_h} (1 - e^{-k_h t_{conv}}) + T_{freezer}(t_{threshold,conv} - t_{conv}) \\ & - \frac{T_{max} - (T_{max} - T_{air})e^{-k_h t_{conv}} - T_{freezer}}{k_c} (e^{-k_c(t_{threshold,conv} - t_{conv})} - 1) \end{aligned} \quad (4.20)$$

where k_h and k_c are positive constants (s^{-1}), which are proportional to the heat transfer coefficient and inversely proportional to the heat capacity and density, T_{max} is the maximum temperature (K), T_{air} is the temperature (K) at the start of the recovery, which is assumed to be the air temperature for laboratory samples and the temperature when the fracture surfaces were in contact, $T_{freezer}$ is the freezer temperature (K), t is time (s) with t_{conv} marking the transition from heating to cooling and $t_{threshold,conv}$ marking the drop below the threshold temperature.

Induction heating generates heat by inducing eddy currents in electrically conductive particles which generate heat by Joule heating. The internal heat source is distributed in the material and emits the heat to the surrounding material. The temperature increase can be linearly approximated, which is in accordance with experimental results showing a linear increase of the average surface temperature with heating time [184, 192]. During heating and after heating is stopped, the internal heat sources emit heat to the surrounding bitumen and aggregates of lower temperature until a temperature equilibrium within the material is reached. The surface temperature decreases faster compared to the more homogenous convection heating, as an inhomogeneous convection cooling occurs on the surface till a homogenous temperature is reached. To consider this effect, the cooling curve was divided into two branches, applying Newton's law of cooling for each branch of the cooling curve. The pseudo healing energy parameter was calculated as follows:

$$\begin{aligned}
\tau_{ind} = & T_{air}t_{ind} + \frac{T_{max} - T_{air}}{2}t_{ind} + T_{freezer}(t_{threshold,ind} - t_{ind}) \\
& - \frac{T_{max} - T_{freezer}}{k_{c1}}\left(e^{-k_{c1}(t_{cooling}-t_{ind})} - 1\right) \\
& - \frac{T_{max} - T_{freezer}}{k_{c2}}\left(e^{-k_{c2}(t_{threshold,ind}-t_{cooling})} - 1\right)
\end{aligned} \tag{4.21}$$

where t_{ind} is the induction heating time (s), $t_{cooling}$ is the time (s) for the rapid cooling branch with the positive exponential constant k_{c1} (s^{-1}), followed by the second cooling branch with exponent k_{c2} (s^{-1}) till the threshold temperature is reached.

Eq. (4.20) and Eq. (4.21) are used in section 7 to compare the two different heating methods used, convection heating and induction heating. The temperature-time curve progression, which was the input to calculate the pseudo healing energy parameter is shown in section 7.1.

5 Material properties of bitumen, aggregates and their mixture

As the material characteristics influence the self-healing, shown in Eq. (4.13) to Eq. (4.16), the material properties of six different bitumens commonly used in road construction were investigated and a correlation analysis for five of these bitumen was performed, as self-healing was investigated for five bitumens on asphalt mortar beams. In addition, the properties of the mastics and mortars manufactured are outlined. The influence of water on the viscosity and surface tension of one bitumen can be found in section 9.1.

5.1 Physical, rheological and chemical properties of bitumen

5.1.1 Conventional tests

Two common standardised tests were performed to determine the conventional properties of the bitumen used, namely needle penetration test and softening point. The six bitumens used were grouped into two clusters according to their results, as shown in Figure 5.1. Bitumen with higher softening point temperatures showed lower needle penetration values and vice versa, which is due to the design of the tests, as they are indirectly related to the bitumen viscosity. The differences between the two clusters were significant (ANOVA, $n_{i,softening}=2$ and $n_{i,needle}=4$, $\alpha \leq 0.05$, single factor), which is also shown in a good linear correlation coefficient (Pearson's correlation coefficient) of -0.94, which is a statistically significant correlation. Whereas, the differences within each cluster were not significant.

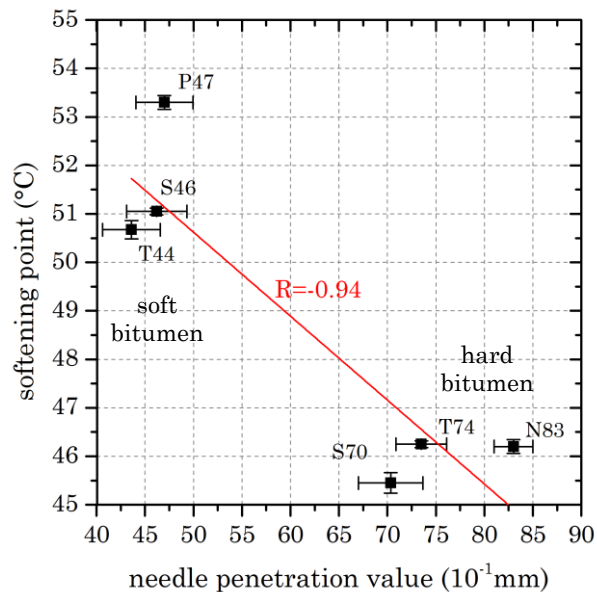


Figure 5.1: Relation between needle penetration and softening point for the six bitumens tested with a linear regression (Pearson's R value). Error bars represent the standard deviation of the needle penetration (horizontal) and the softening point (vertical).

5.1.2 Viscosity

As the self-healing of asphalt cracks is regarded to be a flow process, the viscosity of bitumen is one of the properties that determines the self-healing rate. Figure 5.2(a) shows the obtained viscosities of the bitumens used for the temperature range of 30 °C to 160 °C

for the two different methods used. Bitumen with a higher softening point had a lower viscosity and bitumen with a lower softening point has a higher viscosity, which correlates to the results shown in Figure 5.1. Furthermore, significant differences in the viscosities measured due to the method used were observed, as shown in Figure 5.2(b). Viscosities obtained by the same method showed a good linear correlation, shown in Figure 5.2(b) for viscosities obtained by spindle rheometer at 100 °C and 160 °C. Viscosities obtained by the dynamic shear rheometer were less linear correlated, which may be attributed to the sample preparation and a stronger influence of the fractional composition at a lower temperature, especially the wax content.

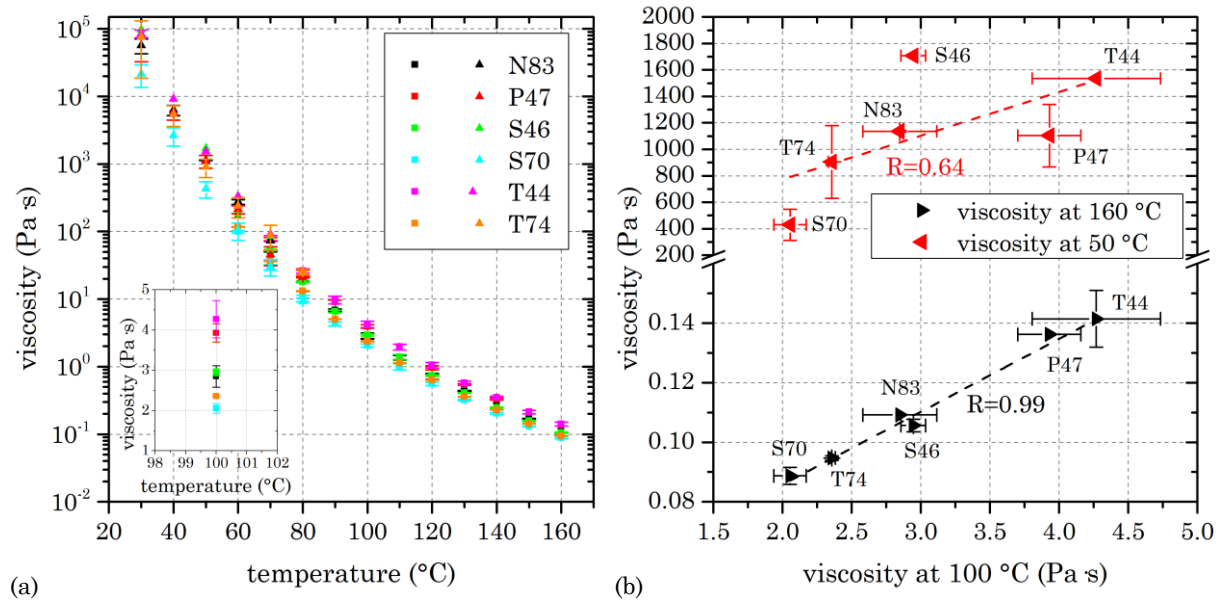


Figure 5.2: (a) The viscosity decreases with increasing temperature, shown for the 6 bitumen types used. The viscosities were measured by spindle rheometer (■) and dynamic shear rheometer (▲). The detailed window shows the viscosity at 100 °C. (b) Correlation of viscosities obtained at 160 °C (spindle rheometer) and 50 °C (dynamic shear rheometer) to the viscosity at 100 °C (spindle rheometer), showing a good correlation for the results obtained by the same method and a minor correlation between different methods. Error bars represent the standard deviation.

Furthermore, ageing increases the viscosity of bitumen. Therefore, four bitumens (P47, S70, T44 and T74) were aged by standard laboratory methods, shown in Figure 5.3. Short-term ageing, due to RTFOT, increased the viscosities by about 3 magnitudes. The initial sequence from low to high viscosity, S70, T74, P47 and T44, changed to S70, T74, T44 and P47, though the viscosities of T44 and P47 were similar for the non-aged bitumen. Long-term ageing, obtained by treating bitumen by RTFOT+PAV, slightly further increased the viscosities. The sequence of bitumens ordered by viscosity changed to T74, S70, T44 and P47, which can be seen in the detailed window in Figure 5.3. Ageing is a factor that has to be considered for the self-healing of asphalt road construction, as the significant increase after short-term ageing, simulating the production and paving process, could prolong the time to close a crack.

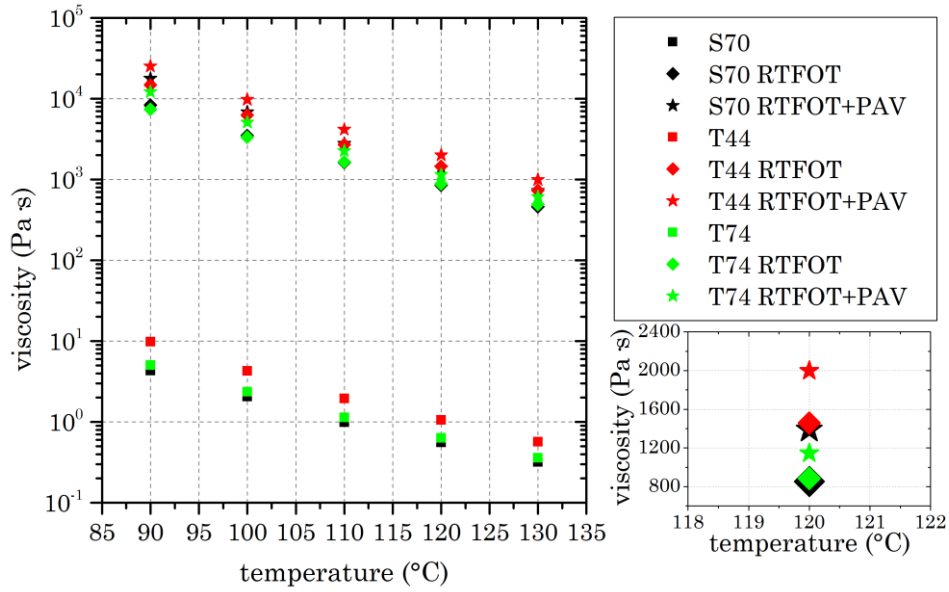


Figure 5.3: Increase in viscosity due to standard laboratory ageing for bitumen S70, T44 and T74. The detail shows the aged bitumen viscosities at 120 °C and the change in sequence.

5.1.3 Viscoelasticity

Bitumen is a viscoelastic multiphase material, whose colloidal microstructures are the origin of its unique rheological properties, varying from viscous behaviour to elastic behaviour. The flow of bitumen into a crack was related to the near-Newtonian behaviour that bitumen expresses at higher temperatures. The relationship of the complex viscosity and the frequency can be expressed by a power law function [32].

$$\eta^* = m |\omega|^{n-1} \quad (5.1)$$

where η^* is the complex viscosity (Pa · s), m and n are fitting parameters (Pa and no unit) and ω is the frequency (s⁻¹).

Since the complex viscosity is related to the complex or dynamic modulus by Cox Merz rule [232, 233], Eq. (5.1) can be written as:

$$G^* = \frac{m |\omega|^n}{\gamma} \quad (5.2)$$

where G^* is the complex modulus (Pa) and γ is the shear strain (-).

The power law exponent n or flow behaviour index was obtained for each temperature. The complex modulus was plotted against the frequency and fitted to a linear function in a log-log plot, shown in Figure 5.4 for bitumen T74. The slope of the linear function represents the flow behaviour index. An index of one corresponds to a Newtonian fluid. Whereas, $n < 1$ represents a time independent non-Newtonian fluid of the pseudoplastic type and $n > 1$ represents a dilatant fluid [234]. The transition from a pseudoplastic to a near Newtonian fluid has been stated to be at 0.9 [32].

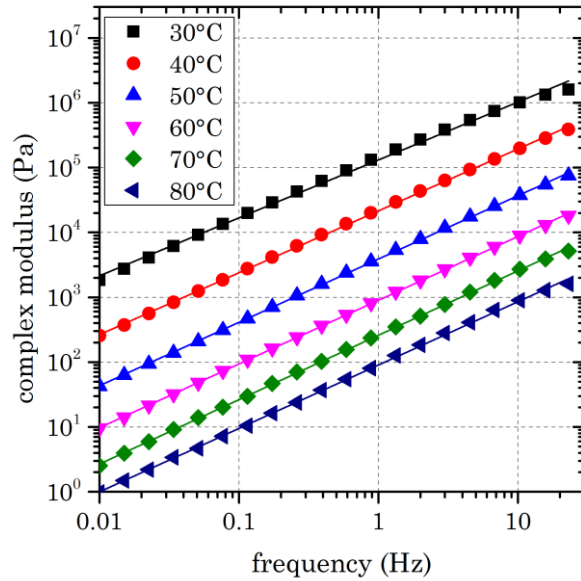


Figure 5.4: Isotherms of the complex modulus for bitumen T74 for temperatures from 30 °C to 80 °C. The plot in the log-log scale was linearly fitted with a Pearson’s correlation coefficient of 0.9987 for 30 °C to 0.9997 for 80 °C.

It was observed that the complex modulus increased with increasing frequency. The increase was not linear, as a concave trend was observable, which increased with decreasing temperature, hence, making the flow behaviour index dependent on the frequency range observed. The highest standard deviation was calculated for bitumen T44, about 0.023 at 70 °C and the lowest standard deviation was calculated for bitumen T74, about 0.0006 at 40 °C. This shows the variability of this method and possible error ranges. Furthermore, the transition point of 0.9 is arbitrarily chosen and was validated by experimental results [32, 149, 194].

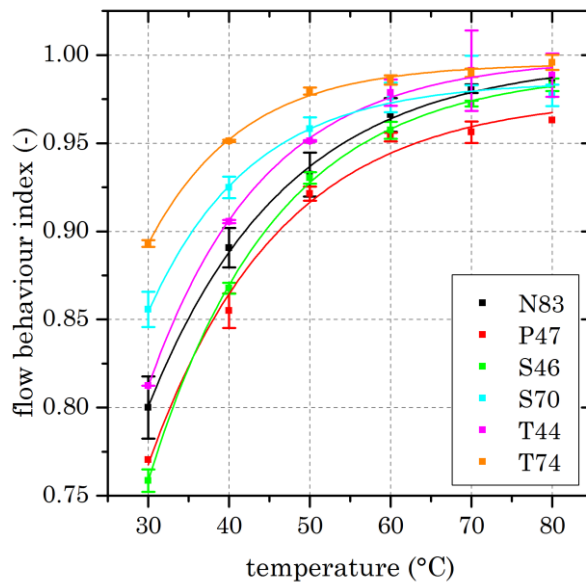


Figure 5.5: Calculated flow behaviour indexes of the six different bitumen used for temperatures from 30 °C to 80 °C. Error bars represent the standard deviation. The flow behaviour index was fitted by an asymptotic function ($fbi = a - b * c^T$).

Figure 5.5 shows the flow behaviour index for the six bitumen types used for temperatures ranging from 30 °C to 80 °C. It can be seen that the index increases with increasing temperature and asymptotically approaches a value close to one. Hence, the flow behaviour index calculated was fitted by an asymptotic function to determine the transition temperature. The transition temperatures are provided in Table 5.1. Due to the variation in standard deviations for different bitumens, the temperature accuracy ranged between 0.05 °C and 3.75 °C. Considering the possible variation in temperature, certain results may not be distinguishable, for example P47 and S46 or T44 and N83.

Table 5.1: Newtonian transition temperatures of the six bitumen studied.

bitumen	transition temperature [°C]
P47	46.2
S46	44.4
S70	35.5
T44	39.1
T74	31.0
N83	41.9

5.1.4 Density and thermal expansion

The rise of bitumen in a vertical capillary, Eq. (4.4) for $\varphi = \frac{\pi}{2}$ and Eq. (4.6), is affected by the density difference. Furthermore, the self-healing model, Eq. (4.13) and Eq. (4.18), includes the density difference, which affects the self-healing ratio parameters, Eq. (4.15) and Eq. (4.16), and the self-healing rate, Eq. (4.19). The densities determined, provided in Table 5.2, were similar for a cluster (hard or soft bitumen) and significantly (ANOVA, $n_i=5$, $\alpha \leq 0.05$, single factor) different between clusters.

Table 5.2: Mean and standard deviation of bitumen densities and volumetric thermal expansion coefficients (CTE).

property	P47	S46	S70	T44	T74	N83
density [kg m ⁻³] at 25 °C	1024.8 ±0.5	1034.0 ±0.2	1019.7 ±0.1	1025.9 ±0.3	1019.9 ±0.6	1019.9 ±1.1
vol. CTE [10 ⁻⁴ · K ⁻¹]	6.29 ±0.01	6.44 ±0.08	6.59 ±0.08	5.99 ±0.08	6.26 ±0.07	5.97 ±0.10

The volumetric thermal expansion coefficient (vol. CTE) of bitumen is provided in Table 5.2. The coefficients were similar for all bitumen types used. However, they differed significantly (ANOVA, $n_i=3$, $\alpha \leq 0.05$, single factor) from each other, which confirms that the thermal expansion coefficient is related to the petroleum source and the production process [3].

Laboratory ageing of bitumen caused an increase in the density, from untreated to RTFOT to RFTOT+PAV, as shown in Table 5.3. A significant (t-test, $n_i \leq 4$, $\alpha \leq 0.05$, two-tailed) increase in density was found for bitumen T74 and P45. For bitumen S70 and T44 the increase was less significant. Furthermore, laboratory aged bitumen showed ambivalent results in regard to thermal expansion. RTFOT ageing decreased the volumetric thermal

expansion coefficient for bitumen S70 and T74, whereas the coefficient for bitumen T44 increased and bitumen P47 remained unchanged with a higher standard deviation. This might be related to the change in the fractional distribution during ageing, though no correlation with the asphaltene fraction was found. Bitumen further aged by PAV revealed that the thermal expansion coefficient increased for the four bitumen types investigated. The coefficient for P47 and T44 increased from original to long-term aged (RTFOT+PAV) bitumen by approximately $2 \cdot 10^{-5} \text{ K}^{-1}$. The thermal expansion coefficient of bitumen S70 after long-term ageing was similar to its original value. The coefficient of bitumen T74, despite an increase after PAV treatment, was reduced compared to the coefficient for the original bitumen.

Table 5.3: Mean and standard deviation of densities and volumetric thermal expansion coefficients (CTE) for original bitumen, RTFOT and RTFOT+PAV aged bitumen.

bitumen	density [$\text{kg} \cdot \text{m}^{-3}$] at 25 °C	vol. CTE [$10^{-4} \cdot \text{K}^{-1}$]
P47	1024.8 ± 0.5	6.29 ± 0.01
P47 RTFOT	1027.0 ± 0.2	6.29 ± 0.07
P47 RTFOT+PAV	1030.0 ± 0.2	6.48 ± 0.02
S70	1019.7 ± 0.1	6.59 ± 0.08
S70 RTFOT	1022.6 ± 0.5	6.44 ± 0.08
S70 RTFOT+PAV	1026.7 ± 0.8	6.59 ± 0.10
T44	1025.9 ± 0.3	5.99 ± 0.08
T44 RTFOT	1028.6 ± 0.1	6.03 ± 0.04
T44 RTFOT+PAV	1031.9 ± 0.2	6.17 ± 0.09
T74	1019.9 ± 0.6	6.26 ± 0.07
T74 RTFOT	1022.2 ± 0.4	6.14 ± 0.04
T74 RTFOT+PAV	1025.7 ± 0.5	6.16 ± 0.10

It is hypothesised that a positive effect on the self-healing due to an increase in the thermal expansion coefficient, which was approximately 3% for this study, might be insufficient as ageing has an opposing effect on density and viscosity. The increase in density was on average 0.2% for RTFOT and 0.5% for RTFOT+PAV and the viscosity dramatically increased as shown in Figure 5.3.

5.1.5 Bitumen flow in vertical glass capillaries

5.1.5.1 Unconfined capillary flow

Washburn [225] was among the first to formulate an equation for a liquid rising in a cylindrical capillary. The equation for a circular capillary is similar to Eq. (4.1) used to represent a crack as a parallel plate and is provided as a simplified term in Eq. (5.3).

$$\frac{dh}{dt} = \frac{r^2}{8\eta h} \left(\frac{2\gamma \cos(\theta)}{r} - \Delta\rho g h \sin(\varphi) + p \right) \quad (5.3)$$

where h is the length or height (m) in the capillary of the entering liquid, r is the radius of the capillary tube (m), θ is the dynamic contact angle (rad) between liquid and capillary

tube, φ is the angle of the inclination (rad) of the capillary, which is $\frac{\pi}{2}$ for a vertical capillary and p is any additional pressure (Pa), for example the atmospheric pressure.

The complex analytical solution of Eq. (4.1) for a cylindrical capillary can be approximated by a square root function for the short-time limit and an asymptotic function for the long-time limit [235]:

$$h(t) = \begin{cases} \left(\frac{r\gamma \cos \theta}{2\eta} t \right)^{0.5}, & \text{short-time } (t \rightarrow 0) \\ \frac{2\gamma \cos \theta}{\Delta\rho g r} \left[1 - e^{-\frac{(\Delta\rho)^2 g^2 r^3}{16\eta\gamma \cos \theta} t} \right], & \text{long-time } (t \rightarrow \infty) \end{cases} \quad (5.4)$$

Short-time refers to the asymptotic function if time approaches 0 s and long-time is the asymptotic approach to the equilibrium height as time approaches infinity. The long-time function is similar to Eq. (4.4), excluding the initial contact height.

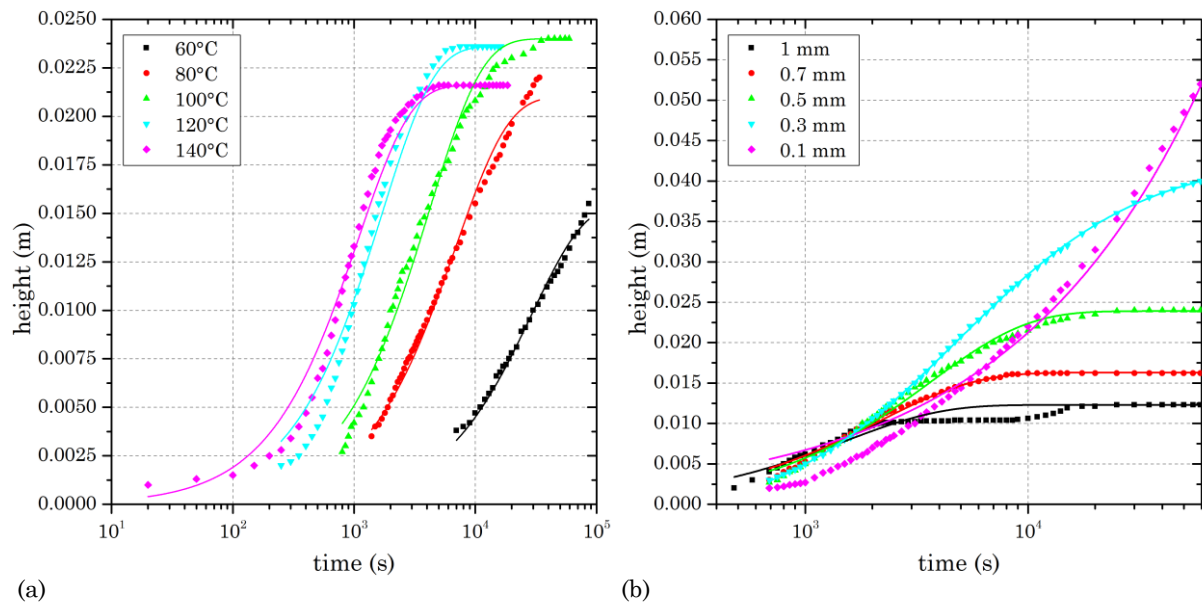


Figure 5.6: Bitumen T74 flowing in a vertical capillary due to surface tension. (a) Measured height increase inside a glass capillary of 0.5 mm diameter for a temperature range of 60 °C to 140 °C. (b) Bitumen rising in capillaries with different diameters (0.1 mm to 1 mm) at 100 °C. The data points were fitted with Eq. (5.4), the short-time limit fitting the 0.5 mm capillary at 60 °C and the 0.1 mm capillary at 100 °C, the other capillary results were fitted by long-time limit.

In Figure 5.6(a) the heights reached by bitumen T74 rising in an unconfined capillary at different temperatures against time are shown and fitted by Eq. (5.4). Figure 5.6(b) shows the rise of bitumen T74 at 100 °C for different capillary diameters. The approximation in Eq. (5.4) is accurate for the short-time and long-time limit solution, although differences between theory and measurements may derive from the assumption of a static contact angle and not accounting for pinning effects, which were observed for 1 mm and 0.7 mm capillary diameters and shown in Figure 5.6(b) for the 1 mm capillary diameter at 100 °C.

According to Washburn's equation [225] and Eq. (5.4), the flow velocity of bitumen in a capillary tube is proportional to the square of the radius. This dependency on the radius of the capillary is shown in Figure 5.6. The increasing bitumen height in a capillary tube

resulting from a reduced flow can be clearly seen for the 0.1 mm capillary, compared to the other capillary diameters used.

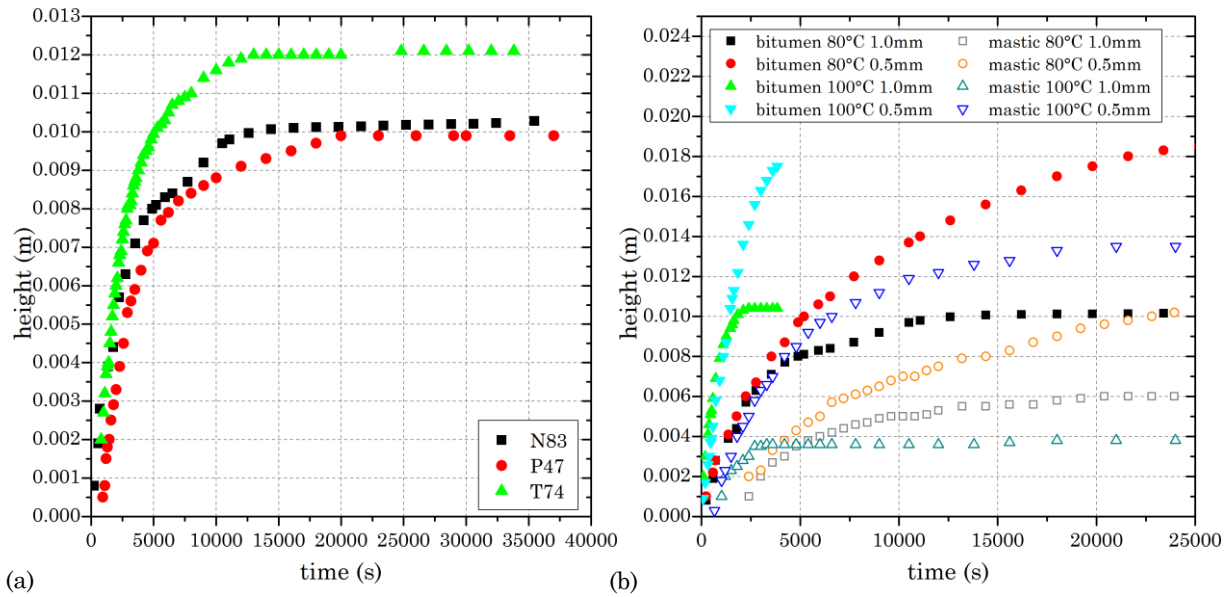


Figure 5.7: (a) Comparison of the wetting line movements for bitumen N83, P47 and T74 in unconfined conditions for a capillary diameter of 1 mm. (b) Rise of bitumen N83 and mastic (50wt.% bitumen N83 and 50wt.% filler) in a vertical capillary with diameters of 1 mm and 0.5 mm.

The bitumen was rising faster with increasing temperature, as viscosity decreased, and the capillary equilibrium height decreased, due to the decrease in surface tension with increasing temperature. This is in agreement with Eq. (5.4). The influence of viscosity on the flow inside a capillary is further shown in Figure 5.7(a) for three different bitumens. The monitored wetting line moved faster for bitumen with lower viscosity. This was further confirmed by comparing the wetting line movement of bitumen and mastic, shown in Figure 5.7(b). Adding filler reduced the viscosity of the mixture, resulting in a slower rising of the liquid in the capillary, and the increased density of the flowing material inside the capillary reduced the equilibrium height, as the hydrostatic pressure in the capillary increased in Eq. (3.4). During the duration of the liquid rising in the capillary, sedimentation occurred, a higher amount of filler was found at the bottom of the petri dish. Regarding self-healing, as it is assumed that the drainage of bitumen into a crack is similar to the flow of bitumen through a capillary tube, it can be expected that reducing the viscosity of bitumen results in an increase in the self-healing rate. The viscosity is in the exponent of Eq. (5.4) and Eq. (4.13), thus only influencing the rate and not the potential maximum self-healing ratio. For this reason, the viscosity may be considered as the main factor affecting the asphalt self-healing rate.

5.1.5.2 Confined capillary flow

In the confined capillary experiment, a temperature increase resulted in the development of an internal pressure inside the culture test tube, due to thermal expansion. This internal pressure contributed to the flow of bitumen in the capillary. Hence, pressure caused an accelerated movement of the meniscus as shown in Figure 5.8 compared to the unconfined capillary flow of bitumen. The pressure further changed the contact angle observed. The concave meniscus from the unconfined capillary flow changed to a convex meniscus, due to the pressured flow through the capillary. Figure 5.8(a) shows the

increase of flow rate with increasing temperature. Two effects occurred simultaneously, the viscosity decreased with increasing temperature and the pressure increased due to the difference of actual and initial temperature, enhancing the flow of bitumen inside the capillary. Furthermore, the pressure developed caused the equilibrium height to exceed the capillary length of 100 mm. In addition, Figure 5.8(b) shows the influence of the capillary diameter on the flow rate of bitumen. Findings were similar to the results of the unconfined flow experiment and in accordance with Eq. (4.1). The flow through a capillary tube is reduced as the diameter decreases.

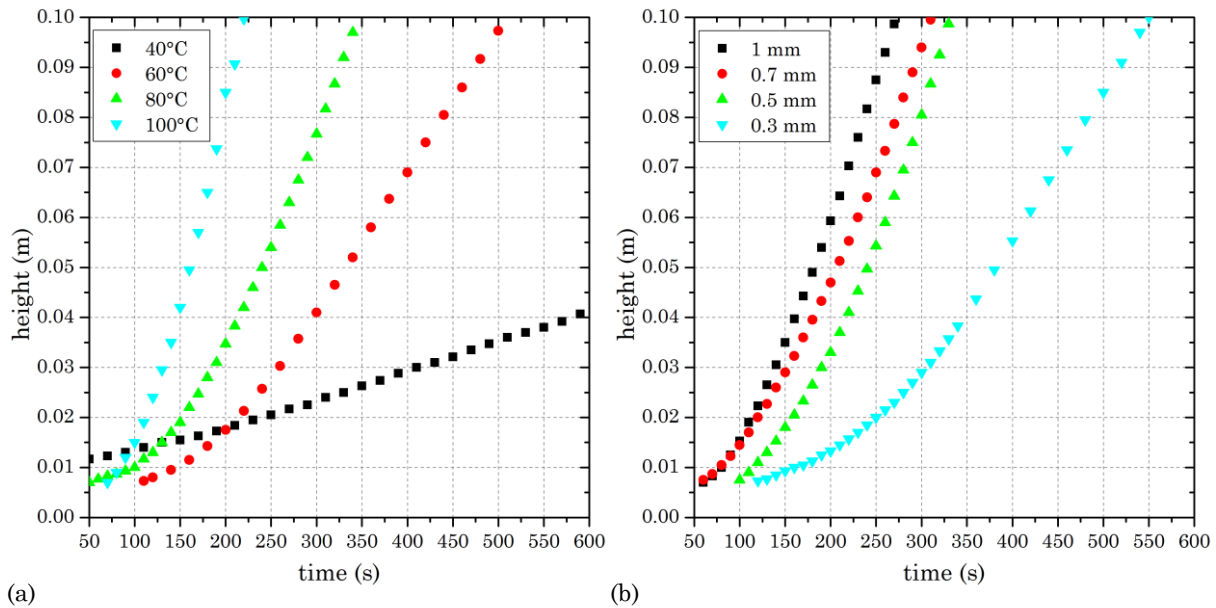


Figure 5.8: Bitumen S70 flowing through a vertical capillary, enhanced by internal pressure due to thermal expansion. (a) Wetting line movement for a 1 mm capillary diameter at different temperatures. (b) The influence of the diameter, 0.3 mm to 1 mm, on the bitumen flow at 80 °C.

Figure 5.9 shows the movement of wetting lines for bitumen S46, S70, T44 and T74. Bitumen T74 showed the fastest movement, despite bitumen S70 having lower viscosity and a higher volumetric thermal expansion coefficient. Furthermore, the velocities of the moving wetting lines were calculated as the slope in the near linear section (between 0.02 m and 0.08 m). The velocity increased with increasing temperature, though no significant correlation between velocity and bitumen viscosity was found. In addition, the velocity was not correlated to the volumetric thermal expansion coefficient. The reason for this could be an increase in viscosity during the preparation, as bitumen S70 showed a higher viscosity increase due to ageing than bitumen T74.

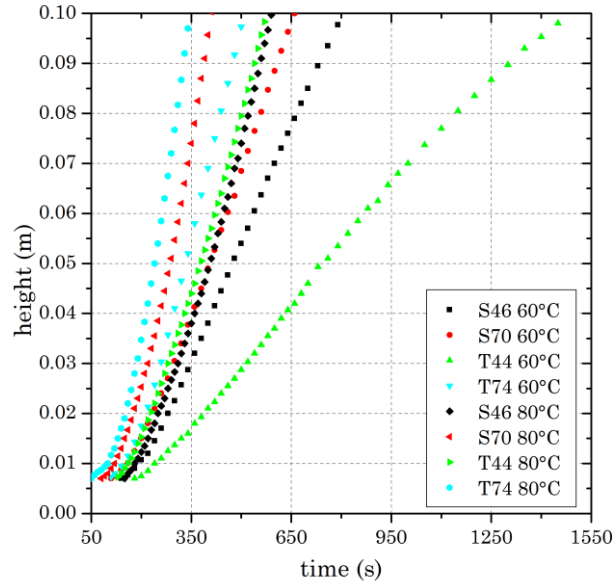


Figure 5.9: Wetting line movements for bitumen S46, S70, T44 and T74 for the confined capillary experiment with a capillary diameter of 1 mm at 60 °C and 80 °C.

5.1.6 Surface tension

Three different methods were used to obtain the surface tension of bitumen. The first two methods, namely sessile drop method and Wilhelmy plate method, used probe liquids with known surface tension to indirectly determine the surface tension of bitumen at 20 °C through the measurement of contact angles. The surface tensions calculated from the contact angle for the six bitumen tested are provided in Table 5.4.

Table 5.4: Calculated surface tensions from the contact angle obtained by sessile drop method and Wilhelmy plate method. Values are the obtained by using the mean of the contact angle, for the Wilhelmy plate method the advancing contact angle was used, and the range provided is the difference between the maximum and minimum surface tension calculated from the extreme contact angles.

surface tension [mJ m^{-2}]	P47	S46	S70	T44	T74	N83
sessile drop method	25.5	24.5	24.7	23.2	24.5	24.3
	± 2.5	± 1.3	± 0.6	± 2.3	± 2.1	± 0.8
Wilhelmy plate method	17.7	20.9	22.8	20.9	25.4	-
	± 1.6	± 1.1	± 1.0	± 1.3	± 1.7	-

No significant linear correlation between the methods was found, which partly can be related to the difference in method and software used to measure the contact angle for each probe liquid. Furthermore, probe liquids left indentations on the surface of the softer bitumen and diiodomethane slowly dissolves bitumen [78], explaining the higher variations for the sessile drop method.

In addition, the surface tension was calculated for three bitumens (N83, P47 and T74) from the equilibrium height of the bitumen in the capillaries using Jurin's law (see Eq. (3.4) or Eq. (4.6) for $p = 0$). Therefore, the contact angle between bitumen and the glass capillary was measured. Figure 5.10(a) shows the contact angle measured for three different bitumens at different temperatures after the bitumen reached the equilibrium

height in the capillary. In general, the contact angle decreased with increasing temperature, indicated by the linear regression. Although having a negative correlation with temperature, bitumen N83 showed an increase in the average contact angle in the temperature range from 60 °C to 90 °C. Since no significant differences for the contact angles of bitumen N83 was determined, this trend in increasing contact angle with temperature is regarded as a possible artefact. The contact angles of bitumen P47 and T74 showed a significant (ANOVA, $n_i=4$, $\alpha \leq 0.05$, single factor) decrease with increasing oven temperature. The variation in contact angle was on average 5° (0.087^{rad}), which was attributed to two main contributors. One contribution to the variation is the resolution of the camera used to record the contact angle (approximately 8° per pixel) and the other contributor is a possible change in fractional distribution or content of functional groups, affecting the contact angle. Furthermore, Figure 5.10(a) and its implied trend is in accordance with the observed contact angle decline with temperature for long chain *n*-alkenes [139] and the increased wettability of bitumen as temperature increases [2, 77].

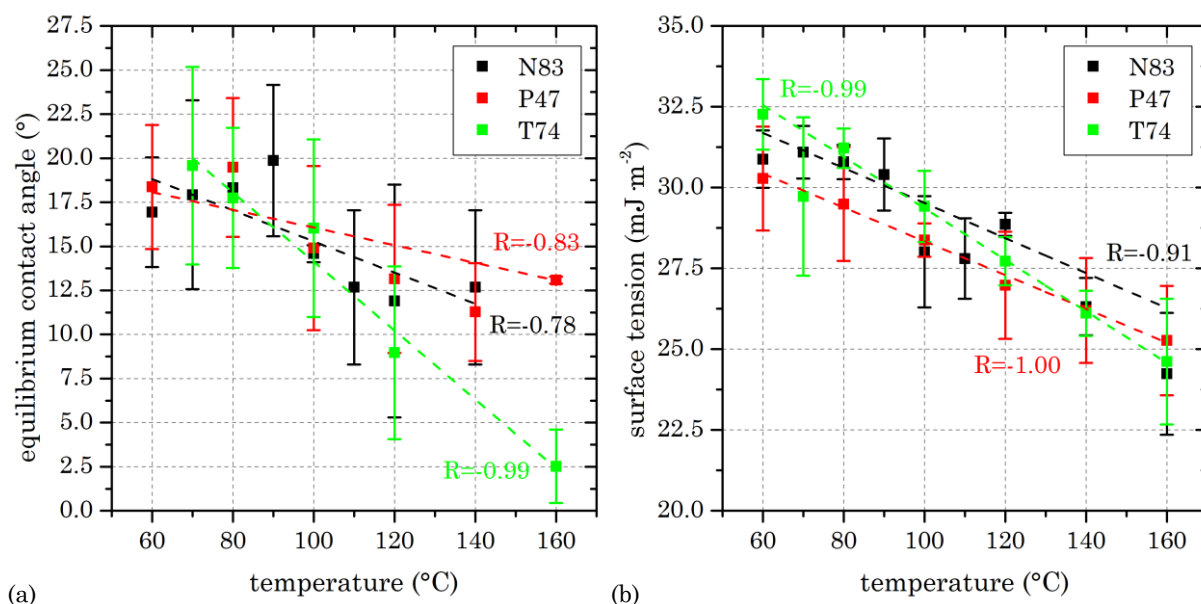


Figure 5.10: (a) Contact angle of bitumen N83, P47 and T74 at different temperatures. The variation in angle was partly related to the resolution of the camera and partly to a change in bitumen fractions during the experiment. (b) Surface tensions calculated from the corresponding equilibrium heights in the capillaries. Error bars represent the standard deviation.

It is well known that the surface tension of bitumen is affected by temperature, decreasing as temperature increases [80]. The surface tensions calculated are shown in Figure 5.10(b) and the surface tension decreased linearly with increasing temperature. This decrease was significant (ANOVA, $n_i=4$, $\alpha \leq 0.05$, single factor) for the three bitumen types investigated. The variation in the surface tension calculated mainly originate from the height of different capillary diameters. The influence of the contact angle accuracy resulted in a variation of approximately ± 0.68 mJ·m⁻² (about 2.3%), which is less than the observed variation of approximately ± 1.22 mJ·m⁻². This was further implied by the calculated capillary constant (product of radius and equilibrium height), which was identical to surface tension in Figure 5.10(b).

Comparing the surface tension obtained by the capillary method with the surface tensions obtained by the two indirect methods used, the surface tension calculated from the equilibrium capillary heights was significantly higher than the surface tensions obtained by sessile drop method or Wilhelmy plate method. The capillary method is considered to precisely determine the surface tension of a liquid. However, the difference in meniscus and wetting line during the height measurement, the vertical positioning of the capillaries during the experiment, the extrapolation of the bitumen density and possible ageing effects due to the high temperatures would affect the calculated surface tension. Moreover, to obtain the equilibrium capillary height, bitumen has to be heated to a certain temperature to have a more liquid behaviour. Observation of capillaries at temperatures from 20 °C to 30 °C showed no movement of bitumen through the capillaries, as the viscosity was too high to obtain any movement within an acceptable time frame. It is unknown if the surface tension increases until a certain temperature and thereafter decreases, which would justify the higher surface tension values for the capillary method and the values obtained at ambient temperature due to indirect methods.

The behaviour of surface tension and contact angle could have deep implications on the capacity of bitumen to fill cracks occurring in asphalt mixtures, as the wetting affinity is a function of contact angle and surface energy [2]. However, wettability is mostly determined by the surface texture [236], which refers to the microscopic features of the material that may affect the contact angle between bitumen and the walls of the crack or respectively the walls of the glass capillary. According to Eq. (4.13) and Eq. (4.18), an increasing temperature would have an adverse effect regarding surface tension and contact angle on the asphalt self-healing, leading to a lower self-healing ratio. Therefore, a reduced surface energy and contact angle allow a better wetting of crack surfaces through mineral aggregates, as contact angle of self-wetting would potentially be zero.

5.1.7 Dynamic contact angle inside a capillary

The dynamic contact angle as bitumen advanced upwards in a vertical capillary was calculated by rearranging Eq. (5.3) and the recorded movements in the unconfined capillaries. For the calculations a constant viscosity, measured by viscometer, was assumed during the capillary rise, the density difference was estimated by a linear extrapolation of the densities measured, surface tension and equilibrium contact angle were obtained from calculations and measurements after the equilibrium height was reached and are discussed in detail in section 5.1.6.

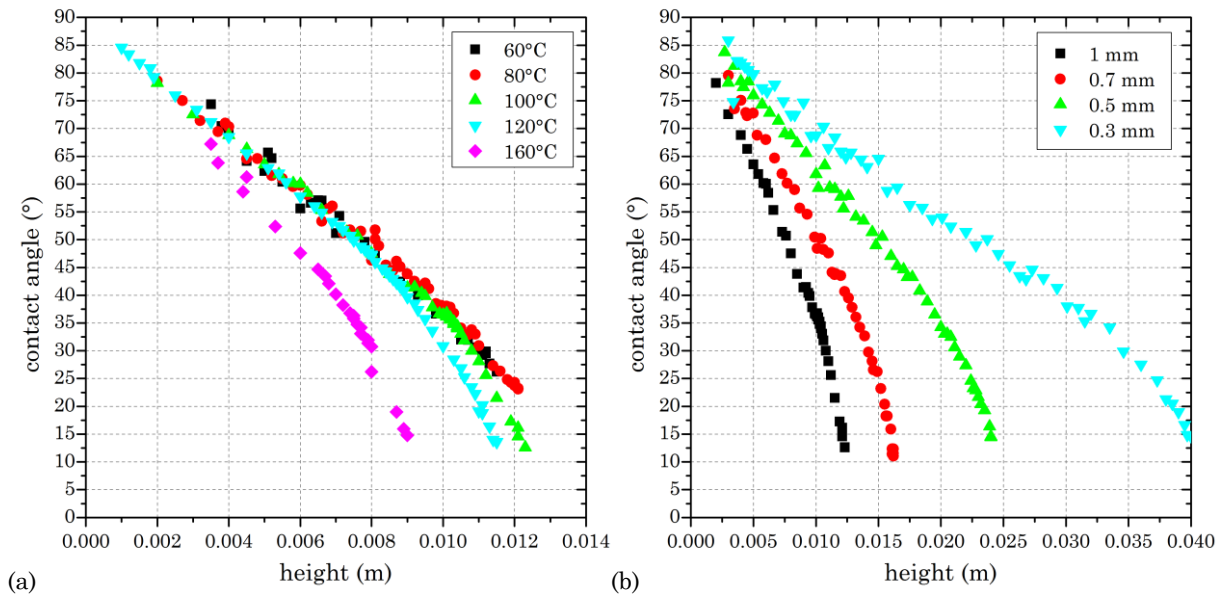


Figure 5.11: Development of contact angles calculated from the moving wetting line as bitumen T74 rose in vertical capillaries. (a) Dynamic contact angles at different capillary heights for capillaries with a diameter of 1 mm at different temperatures and (b) for different capillary diameters at 100 °C.

As bitumen started to flow into the capillary its contact angle is 90° (or $\frac{\pi}{2}$) at the capillary inlet. Subsequently, the contact angle decreases until the equilibrium contact angle is reached at the equilibrium capillary height. The change in contact angle due to the height of capillary rise is shown in Figure 5.11. The decrease in contact angle as a convex meniscus develops was nearly linear at the beginning, correlated to the nearly linear increase of heights at the start of the capillary experiment. Little influence of the viscosity was observed, as indicated by Figure 5.11(a). Different temperatures affected the equilibrium capillary height and equilibrium contact angle, though the dynamic contact angle developed similarly over the capillary height. At 160 °C the dynamic contact angle was more reduced for a certain capillary height compared to the other temperatures. This could be due to the significant reduced equilibrium capillary height. Different capillary diameters showed the same development of the contact angle, shown in Figure 5.11(b). To compare different capillary diameters, the height was normalised, which is shown in Figure 5.12(a). The contact angles became similar, which showed that the contact angle was mainly determined by the velocity of the rising bitumen and changes linearly until 70% of the equilibrium height is reached. A linear dependency of the dynamic contact angle was stated by Hamraoui, Thuresson, Nylander, Yaminsky [229] and is used in Eq. (4.2). Comparing the dynamic contact angle for bitumen N83, P47 and T74 showed no difference, as shown in Figure 5.12(b). The proportionality in regard to capillary height and that the same flow velocity introduces the same contact angle suggests that self-healing would be proportional to the crack length and can be normalised to the material flow into and through the crack.

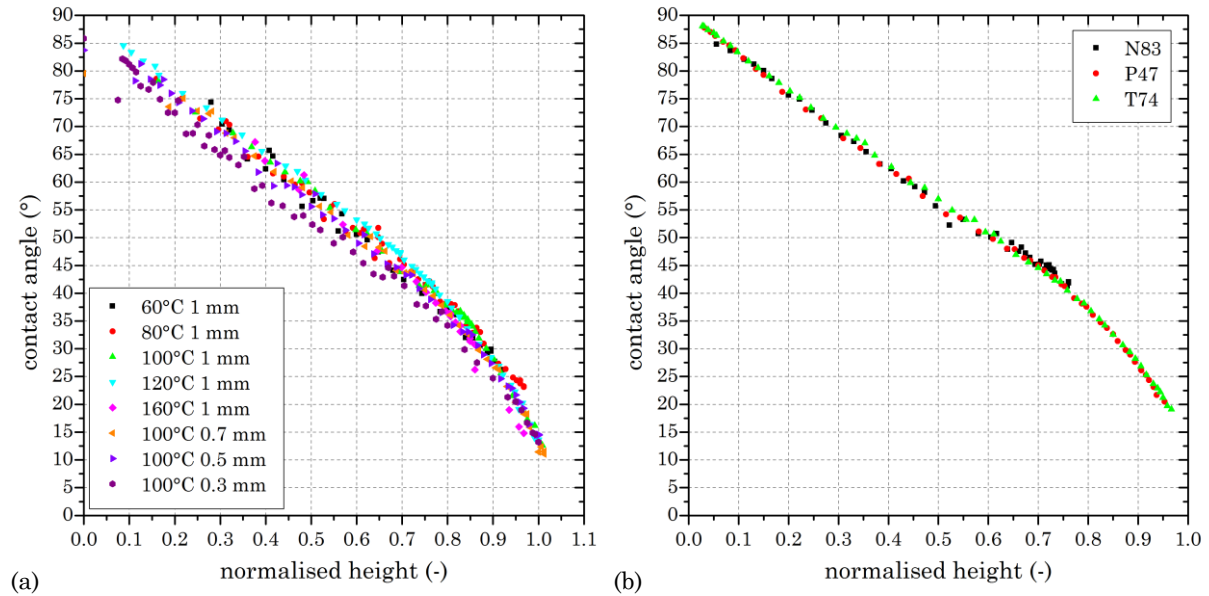


Figure 5.12: (a) Contact angles at normalised heights allow a better comparison for different temperatures and capillary diameters and (b) the comparison of different bitumen types, namely N83, P47 and T74.

5.1.8 Fractions of bitumen

The fractional distribution of bitumen has a significant influence on its physical properties. Hence, the fractional distribution for five bitumens was evaluated.

Table 5.5: Average and standard deviation (if provided) of bitumen fractions obtained from three different institutions.

fraction	P47	S46	S70	T44	T74
Solubility (UoN)					
asphaltene fraction [wt.%]	15.6±0.6	14.6±0.1	12.2±1.0	12.5±1.0	10.0±0.1
wax fraction [wt.%]	0.5	1.7	3.6	2.2	0.9
thin layer chromatography (BRRC)					
asphaltene fraction [wt.%]	15.8±0.4	15.8±0.6	13.7±0.3	15.5±0.6	11.0±0.4
saturate fraction [wt.%]	4.9±0.2	4.7±0.2	5.3±0.2	4.9±0.2	4.1±0.2
aromatic fraction [wt.%]	41.8±1.4	43.2±1.5	43.3±1.8	43.3±1.8	51.1±2.1
resin fraction [wt.%]	35.6±1.3	35.9±1.3	37.7±2.0	36.1±1.5	33.1±1.6
column chromatography (Repsol)					
asphaltene fraction [wt.%]	16.6	16.7	13.7	12.7	8.9
saturate fraction [wt.%]	19.1	20.7	22.1	16.9	18.6
aromatic fraction [wt.%]	42.3	40.3	42.1	46.3	48.3
resin fraction [wt.%]	22.0	22.4	22.1	24.1	24.2

Table 5.5 provides the percentage of each bitumen fraction. As the bitumens were commonly used in road construction and had similar viscosities (Figure 5.2(a)), the fractional composition varied only slightly between bitumens. Though different methods led to different results in the fractional distribution. In Figure 5.13 the asphaltene fractions are compared with the asphaltene fraction obtained by solubility at the

University of Nottingham (UoN) as reference. A significant linear correlation coefficient was found for the thin layer chromatography performed at BRRC ($R=0.88$) and the column chromatography performed at Repsol ($R=0.96$). The better correlation between the methods used at UoN and Repsol was attributed to the similar method to determine the asphaltene content, through a solvent extraction technique. The extraction time has a major influence on the determined asphaltene content [48, 52], explaining the difference. Further correlation between the methods used at BRRC and Repsol for the other three fractions showed no significant correlation. This was attributed to the minor differences in the fractions, especially in the percentages of the aromatic fraction for four bitumen types, determined at BRRC through thin layer chromatography, which were indistinguishable from each other. The percentage of the resin fraction was also very similar for all bitumens.

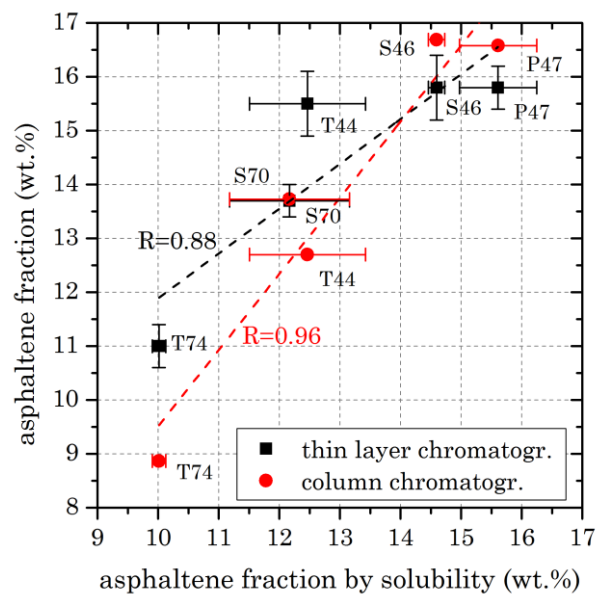


Figure 5.13: Comparison of asphaltene fraction obtained by different methods, with the asphaltene fraction obtained by solubility at UoN as reference. Error bars represent the standard deviation.

5.1.9 Infrared analysis and methyl to methylene ratio

Figure 5.14 shows the infrared spectra of bitumen. Spectra were obtained by attenuated total reflection Fourier transformed infrared spectroscopy.

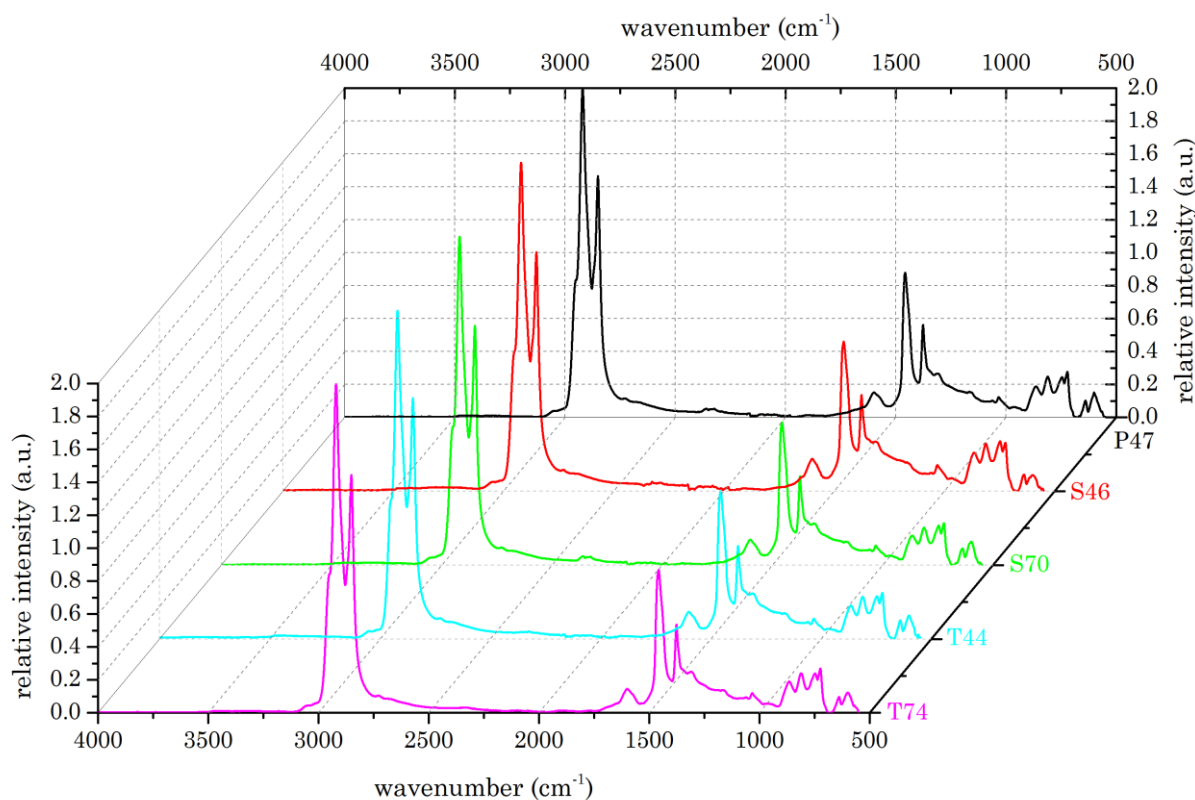


Figure 5.14: Fourier transformed infrared spectra of five different bitumens in the wavenumber range from 4000 cm^{-1} to 550 cm^{-1} .

Two bands dominate the spectrum of bitumen, the aliphatic hydrocarbon group with its asymmetric CH/methylene stretch vibration (CH_2) at 2920 cm^{-1} and its symmetric CH stretching vibration at 2850 cm^{-1} . The two shoulders at 2953 cm^{-1} and 2868 cm^{-1} refer to the asymmetric and symmetric CH_3 /methyl stretching vibration band. This aliphatic group is also present in the fingerprint region (about 1500 cm^{-1} to 500 cm^{-1} , see Figure 5.15) at 1456 cm^{-1} (asymmetric CH_3 deformation/bending vibration) and at 1375 cm^{-1} (symmetric CH_3 deformation/bending vibration). Aromatic structure is indicated by the peaks at 866 cm^{-1} , 812 cm^{-1} , 746 cm^{-1} (out of plane deformation vibration) and 1600 cm^{-1} (C double bond/alkene stretching vibration). Long-chain methylenic alkanes, chains containing more than three methylene molecules, have a peak at 723 cm^{-1} . An increase in the methylene group shifts the band closer to 720 cm^{-1} . Oxygen containing functionalities occur as sulphur oxide with an SO absorption band at 1032 cm^{-1} or as carbonyl group with weak bands at 1310 cm^{-1} (OH deformation vibration and CO stretch vibration) and 1160 cm^{-1} (CO stretch vibration). A dominant oxygen containing group used to identify ageing is the band at 1671 cm^{-1} , which is ascribed to ketones and carboxylic acids.

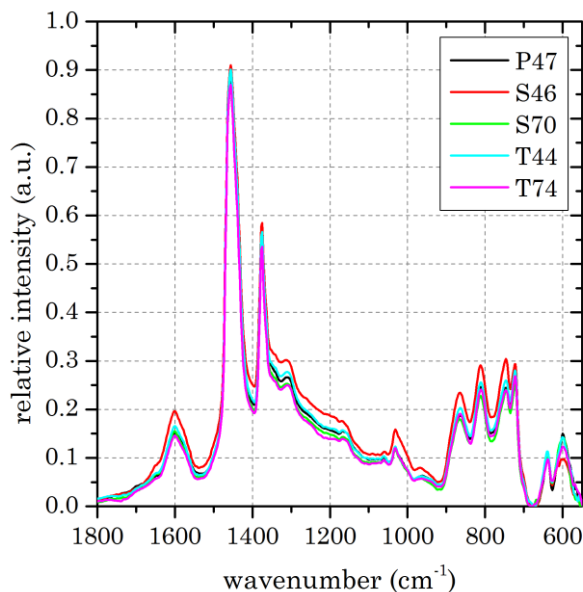


Figure 5.15: Fourier transformed infrared spectra of five bitumens in the fingerprint region from 1800 cm^{-1} to 550 cm^{-1} .

The methyl methylene hydrogen to carbon ratio (MMHC) was introduced to relate the self-healing to the chemical composition of bitumen. The MMHC ratio was calculated from the absorption intensities (the area underneath the peak) of the methyl peak at 1375 cm^{-1} and the methylene peak at 2920 cm^{-1} [237], see Eq. (5.5).

$$MMHC = \frac{\frac{W_{CH_3}}{5} + \frac{W_{CH_2}}{7}}{\frac{W_{CH_3}}{15} + \frac{W_{CH_2}}{14}} \quad (5.5)$$

where W_{CH_3} is the intensity (peak area) of $-\text{CH}_3$ symmetrical deformation vibration from 1370 cm^{-1} to 1390 cm^{-1} , W_{CH_2} is the intensity of $-\text{CH}_2-$ asymmetrical stretching vibration from 2915 cm^{-1} to 2940 cm^{-1} and 5, 7, 14 and 15 are constants of atomic weights.

The MMHC ratio is proportional to the ratio of the peak intensities and is an indicator for chain length and branching of molecules. A critical remark on the usage of the MMHC ratio is that it only accounts for aliphatic compounds and not for other compounds such as aromatic (possible stacking) or functional groups containing oxygen, nitrogen or sulphur, which influence the rheological and physical properties of bitumen and thus, the self-healing. The MMHC ratios calculated for the five bitumens used are provided in Table 5.6. The MMHC ratios for bitumen P47, T44 and T74 were identical and the ratios for bitumen S46 and S70 were close to the other ratios. This indicates that the self-healing for the five bitumens would be similar.

Table 5.6: MMHC ratios and ratios of ketone band for the five bitumens investigated by infrared spectroscopy.

bitumen	P47	S46	S70	T44	T74
MMHC ratio [-]	2.203	2.214	2.197	2.203	2.203
ketone ratio RTFOT [-]	1.49	n/a	1.53	1.33	1.44
ketone ratio PAV [-]	1.74	n/a	2.48	1.80	2.24

Ageing of bitumen is the result of internal polymerisation reactions and oxidation. Oxidation can be monitored by infrared spectroscopy as the ketone/carboxylic acid absorption band at around 1700 cm^{-1} increases, as well as sulphur oxide absorption band at around 1045 cm^{-1} . Figure 5.16 shows the infrared spectra for laboratory aged bitumens. The ketone band and sulphur oxide band increase in intensity as bitumen was aged by RTFOT and further by RTFOT+PAV. The aliphatic bands remained nearly unchanged, as saturated hydrocarbons are inert, confirmed by the literature due to a constant saturate fraction. As a consequence, the MMHC ratio is less affected by ageing and only changed on average by 0.11% for RTFOT aged bitumen and 0.15% for RTFOT+PAV aged bitumen. Absorption bands related to aromatic compounds showed a slight increase, which could be due to polymerisation reactions or change of cycloalkanes to aromatics (dehydrogenation).

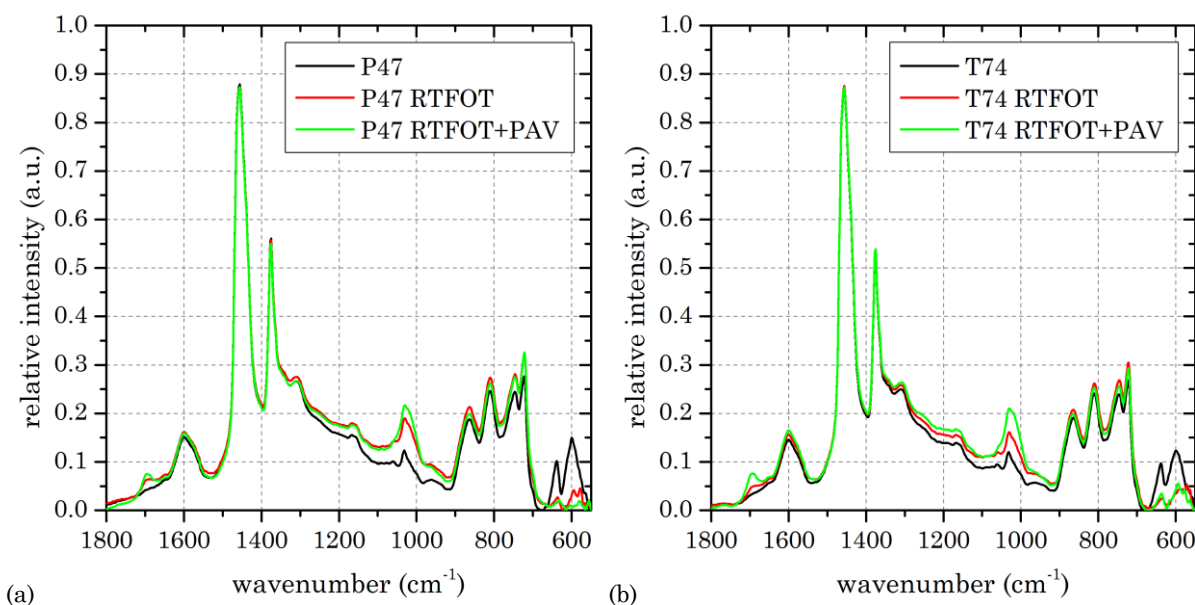


Figure 5.16: Fourier transformed infrared spectra of bitumen (a) P47 and (b) T74 in the fingerprint region for different ageing stages.

Samples obtained from the surface and the bulk of bitumen inside the petri dish of the unconfined capillary experiment were taken and analysed by infrared spectroscopy. Figure 5.17 reveals that bitumen showed signs of oxidation/ageing after 4 hours and 6 hours at $160\text{ }^{\circ}\text{C}$. After 4 hours, the oxidation for surface and bulk was similar and below laboratory RTFOT ageing. An additional two hours inside the oven increased the oxygen containing bands and the bitumen surface was oxidised to a state similar to RTFOT+PAV aged bitumen. The bulk showed a less aged state. This might affect the viscosity of bitumen flowing through the capillary, as oxidation increases the viscosity and would also cause a change in the surface tension. Moreover, changes in surface tension are minor and show no trend of either increasing or decreasing [79, 82].

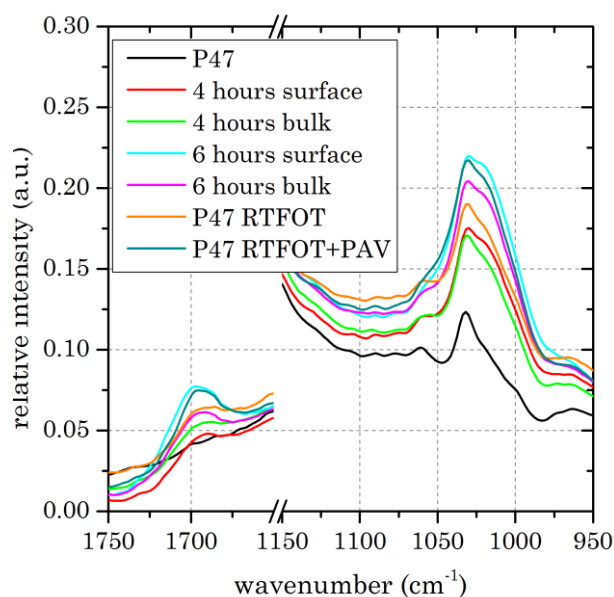


Figure 5.17: Fourier transformed infrared spectra for the ketone band (1690 cm^{-1} to 1697 cm^{-1}) and carbonyl band (1029 cm^{-1} to 1032 cm^{-1}) of bitumen P47 after 4 hours and 6 hours at $160\text{ }^{\circ}\text{C}$ as bitumen was rising inside a capillary and laboratory aged bitumen.

5.2 Correlation of bitumen properties

A Pearson's correlation analysis was performed for the bitumen characteristics determined to identify linear correlations between bitumen properties. Table 5.7 shows the correlation matrix and identifies significant correlations and trends. The fractions of bitumen provided by the Belgian Road Research Centre (BRRC) through thin layer chromatography were used for the correlations. Both fractional distributions obtained by thin layer chromatography and column chromatography were correlated to the viscosities measured and either distribution showed some known trends for different bitumen fractions, although no significant correlations were found. Moreover, the thin layer chromatography at BRRC provided a standard deviation of the fractions which was used to identify if correlations were based on significant differences within the properties.

The fractional distribution of the bitumens investigated was similar, for certain fractions in the repeatability range. Therefore, certain correlations were not significant due to the lack of a significant difference within the characteristics.

Table 5.7: Correlation table of bitumen characteristics.

material properties	needle penetration	softening point	viscosity at 100 °C	viscosity at 50 °C	transition temperature	density	vol. CTE	surface tension (SDM ¹)	surface tension (WPM ²)	asphaltene fraction	saturate fraction	aromatic fraction	resin fraction	wax fraction	MMHC
needle penetration	-														
softening point	-0.94	-													
viscosity 100 °C	-0.80	0.91	-												
viscosity 50 °C	0.09	-0.31	0.64	-											
transition temperature	-0.51	0.91	0.57	-0.32	-										
density	-0.78	0.88	0.62	-0.66	0.73	-									
vol. CTE	0.46	-0.36	-0.65	-0.11	-0.01	-0.04	-								
surface tension (SDM ¹)	0.36	-0.19	-0.44	-0.26	0.31	-0.26	0.61	-							
surface tension (WPM ²)	0.79	-0.86	-0.71	0.03	-0.94	-0.50	0.26	-0.17	-						
asphaltene fraction	-0.87	0.76	0.70	-0.05	0.91	0.85	-0.16	-0.16	-0.88	-					
saturate fraction	-0.24	0.10	0.31	0.62	0.37	-0.75	0.28	0.26	-0.20	0.59	-				
aromatic fraction	0.67	-0.61	-0.57	-0.22	-0.81	-0.12	-0.02	-0.15	0.77	-0.91	-0.78	-			
resin fraction	-0.41	0.20	0.33	0.52	0.34	-0.65	0.41	0.21	-0.13	0.66	0.96	-0.82	-		
wax fraction	0.11	-0.45	-0.03	0.60	-0.29	-0.77	0.39	0.10	0.39	0.04	0.69	-0.29	0.78	-	
MMHC	-0.54	0.51	0.65	-0.89	0.51	0.99	-0.01	-0.24	-0.33	0.39	-0.37	-0.08	-0.24	-0.38	-

Significant correlations at the 0.05 level (two-tailed) are coloured in green and at a 0.10 level (two-tailed) are coloured in yellow.

A significant difference in data/cluster to verify a trend is shown in bold.

¹ SDM: sessile drop method

² WPM: Wilhelmy plate method

Since the conventional tests of needle penetration and softening point are indirectly testing the viscosity of the material, the results of both techniques showed a significant correlation with viscosities measured by spindle rheometer and not with viscosities measured by dynamic shear rheometer. This resulted from the minor correlation between these two techniques, see section 3.2.4. The relation to density, especially for the softening point, could be owned to the inverse proportionality of density and heat capacity [238], which might have affected the temperature increase of bitumen during the experiment. The relation to the asphaltene content for the needle penetration was due to the known positive non-linear correlation between asphaltene content and viscosity [239, 240]. Since the correlation between asphaltene content and viscosity is not linear, the correlation was not significant for a linear correlation and showed more of an exponential increase.

Furthermore, significant correlations were found between the methyl methylene hydrogen to carbon ratio and both density and viscosity measured by dynamic shear rheometer. Since the methyl methylene hydrogen to carbon ratio indicates the amount of chain

branching [39], it is directly related to the viscosity. The positive linear correlation to density might be a coincidence.

The two main methods to characterise surface tension were not linearly correlated to each other, which was discussed in section 5.1.6. The surface tension measured by the sessile droplet method showed no correlation to any other measured bitumen characteristic. The surface tension measured by the Wilhelmy plate method was significantly linearly correlated to the transition temperature, softening point and asphaltene fraction. Identified trends of surface tension with regard to fraction content [82] were partly confirmed by a negative correlation of surface tensions to asphaltene content and no significant correlation to saturate, aromatics and wax content.

No significant linear correlation was found for the thermal expansion coefficient. A slight dependence on the asphaltene content exists for thermal expansion [82], though the thermal expansion is, in general, insensitive to the bitumen type [241].

5.3 Aggregate properties

The gradation of the aggregates is provided in Table 3.2. Table 5.8 provides two additional properties measured of the aggregates used, namely density (determined by pycnometer) and specific surface area (determined by dynamic vapour sorption). The determined densities were similar to the specification provided by the supplier of the material.

As the specific surface area of aggregates increases in proportion to the decreasing grain radius [69], the filler had the highest specific surface area. Furthermore, sand 2 contained a higher proportion of filler and fine aggregates compared to sand 1. Thus, resulting in a higher specific surface area for sand 2 compared to sand 1.

Table 5.8: Aggregate properties.

property	sand 1	sand 2	metal grit	filler
density at 25 °C [kg m ⁻³]	2363.0	2621.2 ±6.0.	7520.2	2609.1 ±48.8
specific surface area [m ² ·kg ⁻¹]	1851.1	3003.4	n/a	4582.5

The density of the aggregates, especially the filler density, may affect the self-healing, as the mixture of bitumen and finer aggregates might be responsible for the proposed flow process to close a crack occurring within asphalt. Therefore, an increase in density of the flowable mixture would move under gravity, though it reduces rising heights for vertical capillaries. The surface area would determine the proportion of flowable material, which is not adhering to bigger aggregates.

5.4 Mastic properties

5.4.1 Viscosity

An increasing amount of filler added to a mortar mixture increases the viscosity of the mixture [2, 84, 242]. This was also observed as limestone filler was mixed with bitumen T74 at different weight ratios. Figure 5.18(a) shows the viscosity measured for bitumen

T74 and five mastic mixtures with different filler content. An abrupt rise in viscosity was observed from the bitumen viscosity to the viscosity of the mastic containing 12wt.% filler. A nearly linear increase of viscosity with filler content was observed afterwards until 50wt.% filler content, which is shown in Figure 5.18(b). The viscosity to 70wt.% filler content increased nearly exponentially. The natural amount of filler of the sand used would increase the viscosity of the mastic. However, as different bitumen types are investigated, the influence would be identical for each bitumen and therefore the viscosity change is negligible for the correlation of different bitumen types.

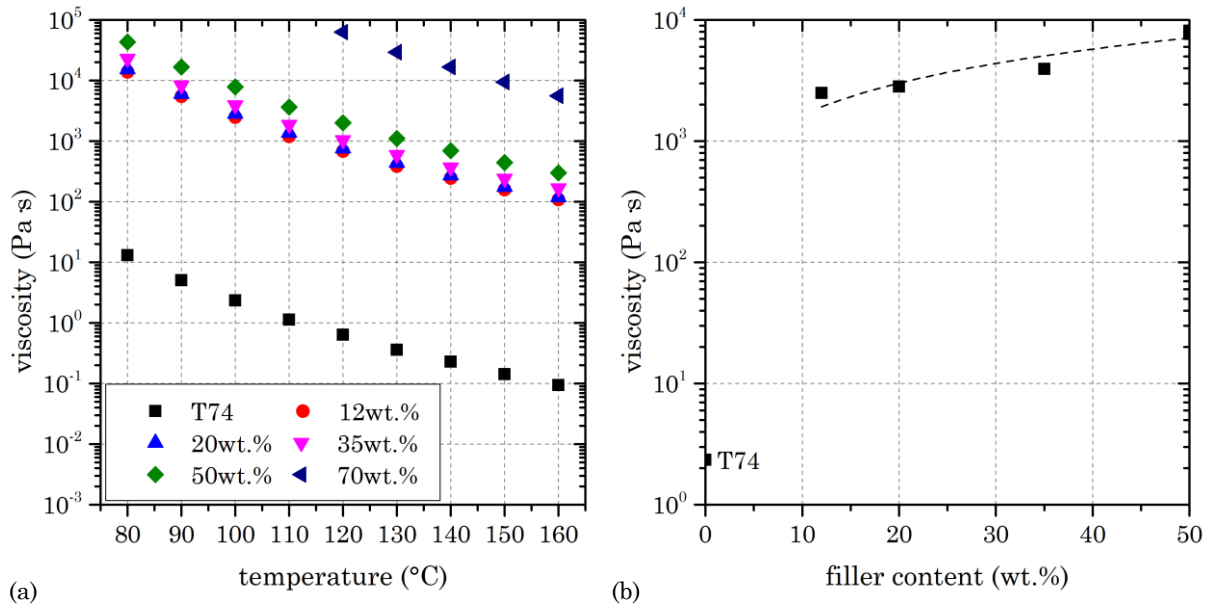


Figure 5.18: (a) Measured viscosity for bitumen T74 and resulting manufactured mastic with different limestone filler content. (b) Viscosity at 100 °C plotted against filler content. A linear function ($R=0.94$) was used to fit the viscosity measurements except 0wt.% filler.

5.4.2 Density and thermal expansion

The density of mastic increased significantly (ANOVA, $n_i=2$, $\alpha \leq 0.05$, single factor) and nearly linearly as the concentration of limestone filler increased, shown in Figure 5.19(a). Deviation from the linearity was attributed to a possible entrapment of air voids for a high filler content (70wt.%) during the measurement. The increase in density may affect the self-healing, as according to Eq. (4.13), an increase in density difference would reduce the self-healing ratio, as observed for capillaries shown in Figure 5.7(b). Although, self-healing rate increases as density increases, in contrast to the rise inside a capillary. Opposed to the increased self-healing rate is the reduction in the self-healing rate due to the increase in viscosity, which was estimated to be a nearly linear increase with increasing filler content.

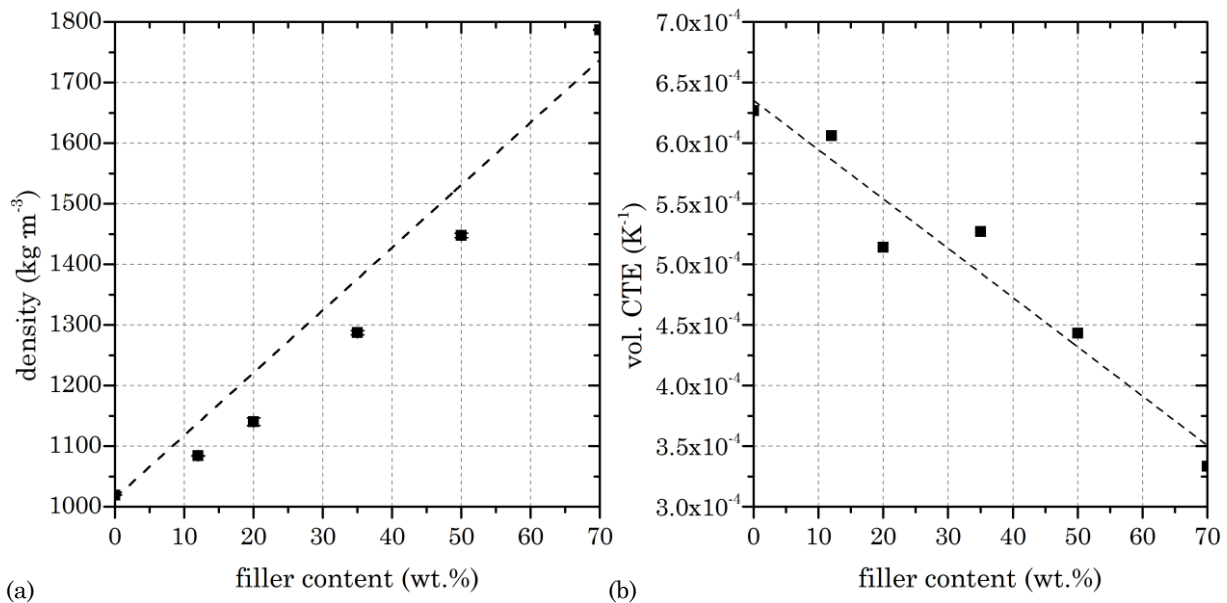


Figure 5.19: (a) Change in density with increasing filler content, fitted by a linear function ($R=0.98$). (b) Volumetric thermal expansion coefficient (vol. CTE) obtained for different limestone filler content mixed with bitumen T74 and linear regression function ($R=-0.97$).

Figure 5.19(b) shows the negative correlation between the volumetric thermal expansion coefficient and filler content. This is due to the volumetric increase of a material with a lower thermal expansion coefficient, resulting in an overall reduced thermal expansion coefficient. This suggests that a higher filler content would reduce the maximum reachable self-healing ratio and probably diminish the self-healing rate.

5.5 Asphalt mortar beam properties

The properties of the asphalt mortar beams produced depended on the mixture design, which is provided in Table 3.3. As Figure 5.20 shows, the initial breaking force of the beams was related to the weight and the mixture design. A significant trend ($\alpha \leq 0.05$, except for mixture 2 for bitumen T74) was identified; as the weight of the beam increased, the initial breaking force increased. The higher beam weight for mixture 1, as shown in Figure 5.20(a) for bitumen T74, was due to the addition of metal grit to the mixture, which had no significant influence on the breaking force. The beams of mixture 1 produced with bitumen T74 and mixture 12 produced with bitumen S70 had average weights of $186.6 \text{ g} \pm 8.9 \text{ g}$ and $150.8 \text{ g} \pm 2.6 \text{ g}$. The associated average initial breaking forces were $808.5 \text{ N} \pm 51.3 \text{ N}$ and $47937 \text{ N} \pm 36.3 \text{ N}$. A part of the scattering in weight and breaking force was attributed to the variation in mixture compaction and in dimensions. The variation in width was $\pm 0.2 \text{ mm}$ and the variation in height was $\pm 0.3 \text{ mm}$, resulting in a variation of $\pm 52 \text{ N}$ for breaking force, which is in the range of the measured force variation. The bitumen type had no significant influence on the breaking force, as shown in Figure 5.20(b), as the breaking force is mainly determined by the compaction of the asphalt and the air void distribution [116, 243]. The air void content of the beams for the different mixtures is provided in Xx.

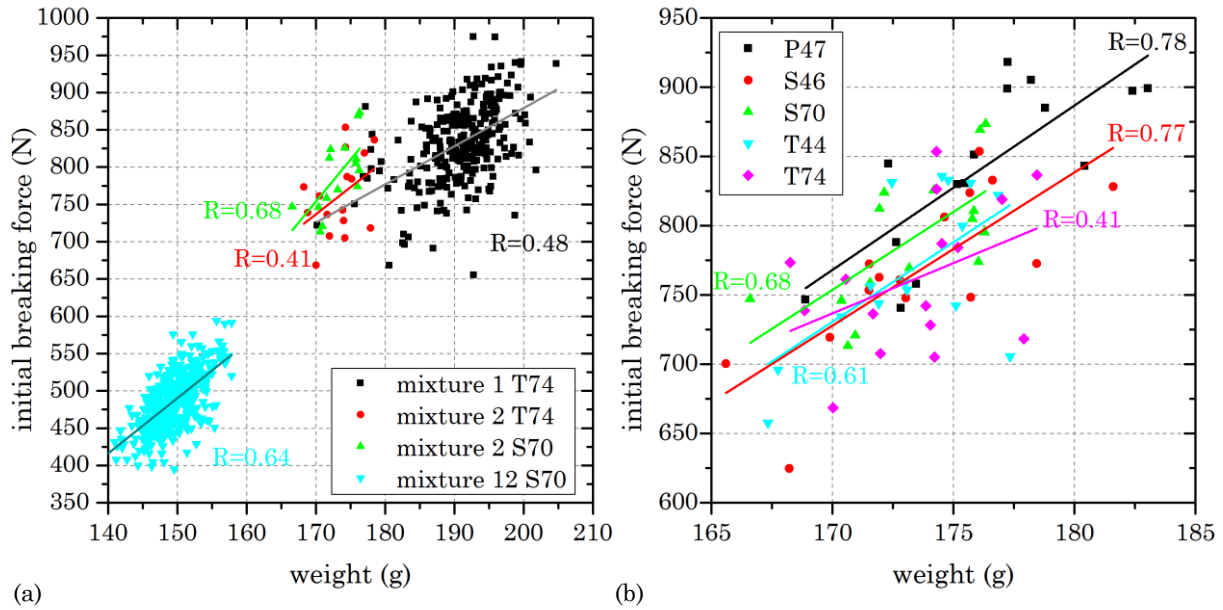


Figure 5.20: Correlation of beam weight to the initial force to break the beams during three-point breaking (a) for the three different mixture designs used and (b) for mixture 2 and different bitumen types, including Pearson's correlation coefficient for linear regression.

Table 5.9: Beam air void content for the different asphalt mortar mixtures.

mixture	bitumen content [wt.%]	total filler content [wt.%]	air void content [vol.%]
mixture 1	15	1.8	21.4 ±1.2
mixture 2	15	1.8	17.4 ±1.8
mixture 3	15	5.0	9.4 ±1.3
mixture 4	15	8.0	9.5 ±1.0
mixture 5	15	10.0	16.6 ±3.8
mixture 6	15	13.0	10.2 ±2.3
mixture 7	15	58.0	14.4 ±1.7
mixture 8	5	1.8	28.2 ±1.4
mixture 9	10	1.8	20.7 ±1.1
mixture 10	20	1.8	5.2 ±3.1
mixture 11	28	1.8	8.8 ±1.7
mixture 12	15	2.1	22.3 ±1.3

The amount of bitumen has a significant (ANOVA, $n_i=6$, $\alpha \leq 0.05$, single factor) influence on the breaking force, as shown in Figure 5.21(a). As the air void content decreased with increasing bitumen content, the initial breaking force increased until a bitumen content of 15wt.% was reached. A decline in initial breaking force for the bitumen content of 28wt.% was observed, which is related to the reduction of aggregate interlocking, resulting in a cohesive fracture. Mastic beams revealed that with increasing bitumen content the

breaking force decreases. For 30wt.% bitumen the breaking force was 605 N, which decreased to 317 N \pm 39 N for content from 50wt.% to 80 wt.%. Beams made from bitumen T74 had an initial strength of 150 N \pm 54 N and an air void content of 0.3 wt.%. The high variation in initial breaking strength of bitumen was due to the non-uniform volume reduction of pure bitumen during freezing, resulting in a concave meniscus line between the mould edges.

An increase in initial breaking force for 1.5wt.% (mixture 2) to 5wt.% filler (mixture 3), shown in Figure 5.21(b), was attributed to the reduction of air voids and the increase in breaking resistance due to the higher filler amount as mastic suspending the aggregates. Further increase of the filler content up to 13wt.% (mixture 4 to mixture 6) had no significant effect on the initial breaking force. An increasing amount of filler would potentially lower the initial breaking force, as indicated by a lower force for the beam containing 58wt.% filler (mixture 7). Furthermore, a slight particle segregation occurred in beams containing 58wt.% filler, as the lower part of the beam contained a higher amount of bigger aggregate particles compared to the upper part. This was slightly observable at the initial fracture surface and distinct segregation was observable after the self-healing.

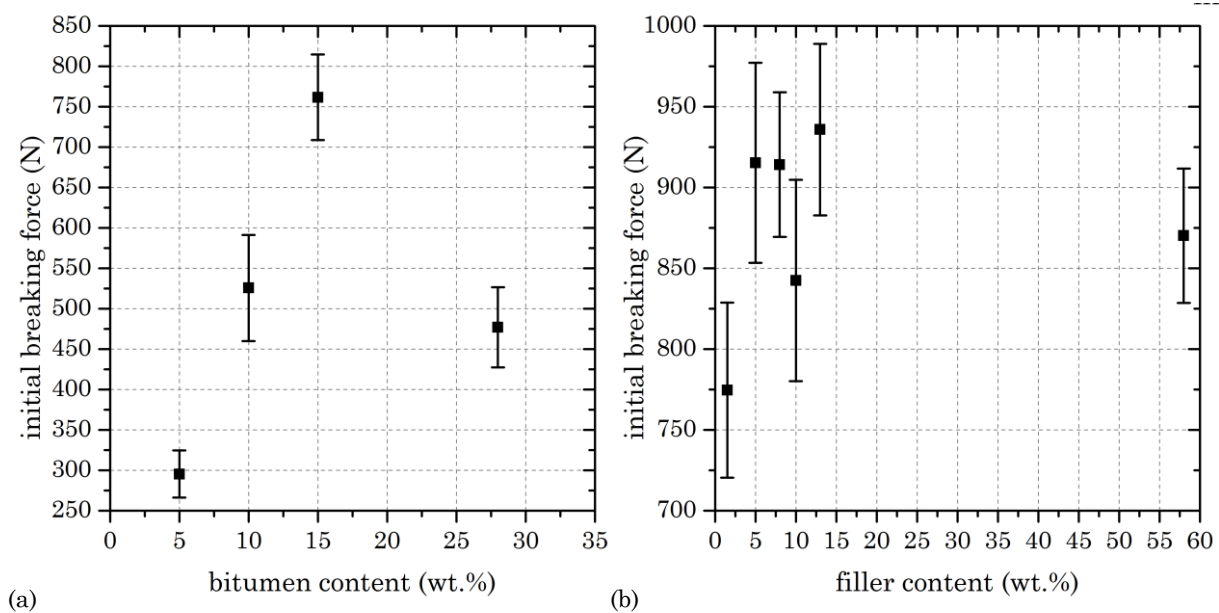


Figure 5.21: The change of initial breaking force with (a) bitumen content (mixtures 2 and mixture 8 to mixture 11) and (b) filler content (mixture 2 to mixture 7). Error bars represent the standard deviation.

5.6 Summary

Bitumen can be classified by certain characteristics, such as needle penetration or softening point. However, for the narrow range of bitumen types investigated, only general trends were confirmed. Moreover, the characterisation method had a significant influence on the results. A linear correlation for viscosities measured by spindle rheometer and dynamic shear rheometer was found. No or weak correlations were found for surface tension methods and methods to obtain the fractional distribution of bitumen.

The capillary flow, as a visualisation method related to the self-healing in asphalt, showed the dependency of the flow rate on the viscosity, which could be influenced by ageing due

to higher temperatures and pressure, as thermal expansion in the confined capillary flow experiment. The capillary height depended on the surface tension of bitumen, which decreases with increasing temperature, and the applied pressure due to expansion. Furthermore, the dynamic contact angle was nearly identical for the three bitumens investigated, indicating that the effect of contact angle due to different bitumen types is negligible.

Ageing affected viscosity, increasing the viscosity and partly changing the order of bitumen types, though it had only a minor effect on the volumetric thermal expansion coefficient of bitumen and no effect on the bitumen density.

Adding filler to bitumen, to produce mastic, had a significant influence on viscosity and thermal expansion. The viscosity linearly increased with increasing filler content and the thermal expansion linearly decreased with increasing filler content.

6 Self-healing of macro cracks due to induced heating

The self-healing of a macro crack in an asphalt mortar beam produced with bitumen T74, mixture 1 and mixture 2, has been investigated. For this, the surface temperature of the beams after heat treatment by convection heating or induction heating was measured in order to determine the existence of an equilibrium temperature. The self-healing was assessed by the ratio of forces to break the beam initially and after healing.

6.1 Thermal behaviour of asphalt mortar beams

The increase of the surface temperature of asphalt mortar beams was measured in order to determine the time to reach a constant surface temperature and its correlation to the self-healing. The change of temperature in a sample is determined by the heating method and by the material's heat capacity, conductivity and emissivity.

6.1.1 Convection heating for different oven temperatures

The average surface temperature increased with increasing duration inside the convection oven until a thermal equilibrium with the oven temperature was reached. Figure 6.1 shows the surface temperature measured by an infrared camera for beams with and without horizontal pressure. The measured surface temperatures in Figure 6.1 after reaching a thermal equilibrium are lower than the set oven temperatures due to a fast temperature drop after removing the samples from the oven and a linear temperature deviation for the infrared camera used (approximately 0.06 °C less per degree Celsius measured). Starting from ambient temperature (22 °C ±1.0 °C), the surface temperature of the mortar beams increased according to the convection heat transfer equation, which was used to fit the temperature points measured.

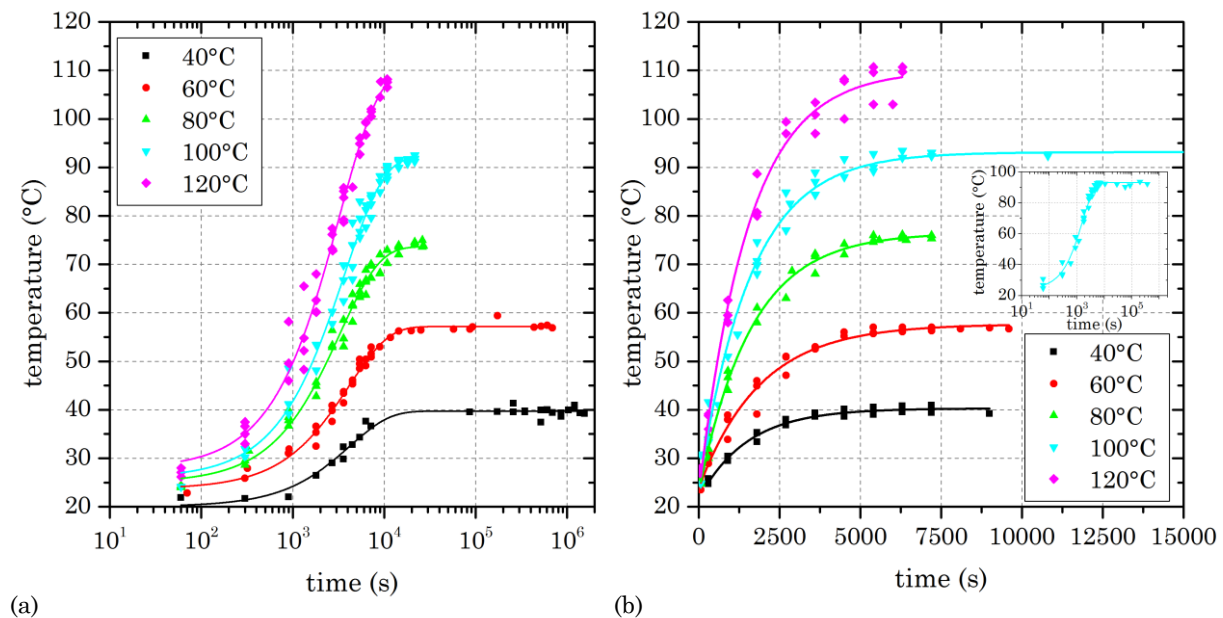


Figure 6.1: The average surface temperature measured by an infrared camera for oven temperatures of 40 °C to 120 °C for beam (a) without pressure and (b) with pressure. The detailed window in (b) shows the extended heat treatment period for 100 °C. Measurements were fitted by the convection heat transfer function ($T(t) = T_{max} - (T_{max} - T_{air})e^{-kt}$).

Table 6.1 provides the fitting parameters. The equilibrium surface temperature did not differ, as it is independent of the material. The heating exponent was on average 2.3 times higher for beams with pressure. This difference was attributed to the different thermal conductivities and heat capacities of the mould materials, which are in general higher for powder filled silicone rubber [244, 245], which was used to apply the circumferential pressure. This difference was regarded to influence the self-healing of the asphalt mortar beams in a minor way, as the lower heating rate is assumed to shift the self-healing to slightly longer healing durations.

Table 6.1: Surface temperature fitting parameters for beam without and with circumferential pressure.

oven temperature	equilibrium surface temperature [°C]	heating exponent without pressure [s ⁻¹]	heating exponent with pressure [s ⁻¹]
40 °C	40.0	$2.4 \cdot 10^{-4}$	$6.7 \cdot 10^{-4}$
60 °C	57.5	$2.4 \cdot 10^{-4}$	$5.3 \cdot 10^{-4}$
80 °C	75.1	$3.0 \cdot 10^{-4}$	$6.1 \cdot 10^{-4}$
100 °C	92.7	$2.7 \cdot 10^{-4}$	$6.2 \cdot 10^{-4}$
120 °C	110.2	$3.1 \cdot 10^{-4}$	$6.5 \cdot 10^{-4}$

6.1.2 Induction heating with different current intensities

Asphalt mortar beams were heated by induction heating with different current intensities. The surface temperatures measured for the different current intensities are shown in Figure 6.2. The average surface temperatures were fitted by a linear function, which had Pearson's correlation coefficients between 0.96 and 0.99. The fitting parameters of the linear function used are provided in Table 6.2. Figure 6.2 and Table 6.2 show that an increase in current intensity of the induction generator increased the average surface temperature measured. For 50 A and 80 A the surface temperatures were similar, which could be due to the distribution of metal particle within the beams and a slightly different distance from the induction coil. Both circumstances affect the temperature development of the beams [184]. The nearly identical surface temperature for 200 A and 300 A were due to the self-regulation of the induction generator, which regulated the current intensity to approximately 110 A.

Table 6.2: Fitting parameters for induction heating with different current intensities.

current intensity [A]	interception [°C]	slope [°C s ⁻¹]
50	29.4	0.22
80	24.1	0.20
100	26.5	0.88
200	26.1	1.25
300	28.3	1.26

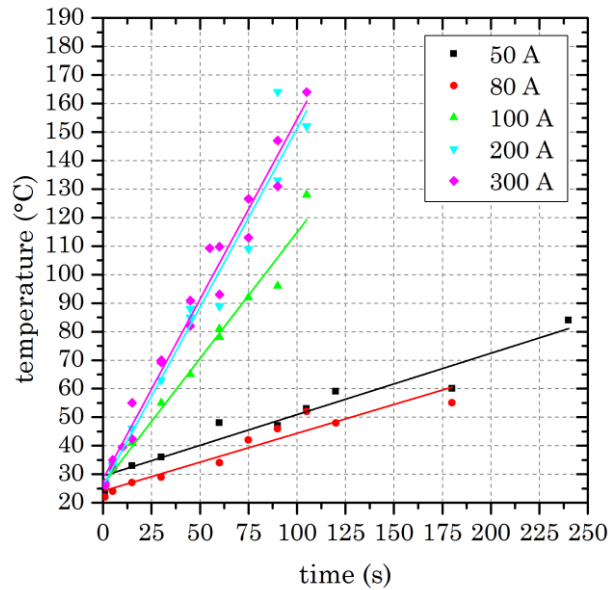


Figure 6.2: The average surface temperature measured for different induction current intensities. Measurements were fitted by a linear function ($T(t) = a + b t$).

6.1.3 Self-healing at different oven temperatures with and without circumferential pressure

The self-healing of asphalt mortar beams produced with bitumen T74 was studied for five different oven temperatures. In addition, the effect of applying a circumferential pressure was studied. The initial self-healing ratio (at 0 s to 10 s) ranged from 0.01 to 0.02, due to the adhesion of bitumen at the initial contact points when the beam halves were assembled.

For beams without circumferential pressure, the only pressure occurring during the heating duration was due to the expansion difference between mould and mortar beam. A rapid increase of the self-healing ratio to a maximum of 0.11 was observed for the first 60 seconds of heat treatment in the convection oven independent of the oven temperature. This rapid increase may be due to stress relaxation and the coalescence of contact points, which increases the contact area, rather than thermal expansion, as the temperature difference is small, as seen in Figure 6.1. This increase was insufficiently reflected in the equations to fit the self-healing ratios calculated. Thus, similar origins of the fitting curves despite the different self-healing ratios at 60 s, are shown in Figure 6.3(a). Finally, the self-healing ratio increased, following a logistic or sigmoid function, until a steady state was reached, at which the self-healing ratio did not show any further improvement. The self-healing ratio did not reach 1. This was attributed to the potential loss of material during the initial fracturing and that the cracks were partly through mineral aggregates, which original strength can not be recovered. Fractured aggregates either remain separated or bitumen/mastic drains into the gap, resulting in a lower stress transmission compared to the original aggregate. Furthermore, the steady self-healing ratio state was temperature dependent (ANOVA, $n_{i=5} \leq 18$, $\alpha \leq 0.05$, single factor) and, as the temperature increased, the steady self-healing ratio state increased, as shown in Figure 6.3(b). The average self-healing ratios asymptotically approached a value of 0.71, which could be a limit of the self-healing and only remixing the material would result in a fracture strength similar to the initial fracture strength. Figure 6.3(b) shows that the variation in self-

healing ratios decreases with increasing oven temperature, which could be due to the pressure caused by thermal expansion and the reduction in viscosity at higher temperatures.

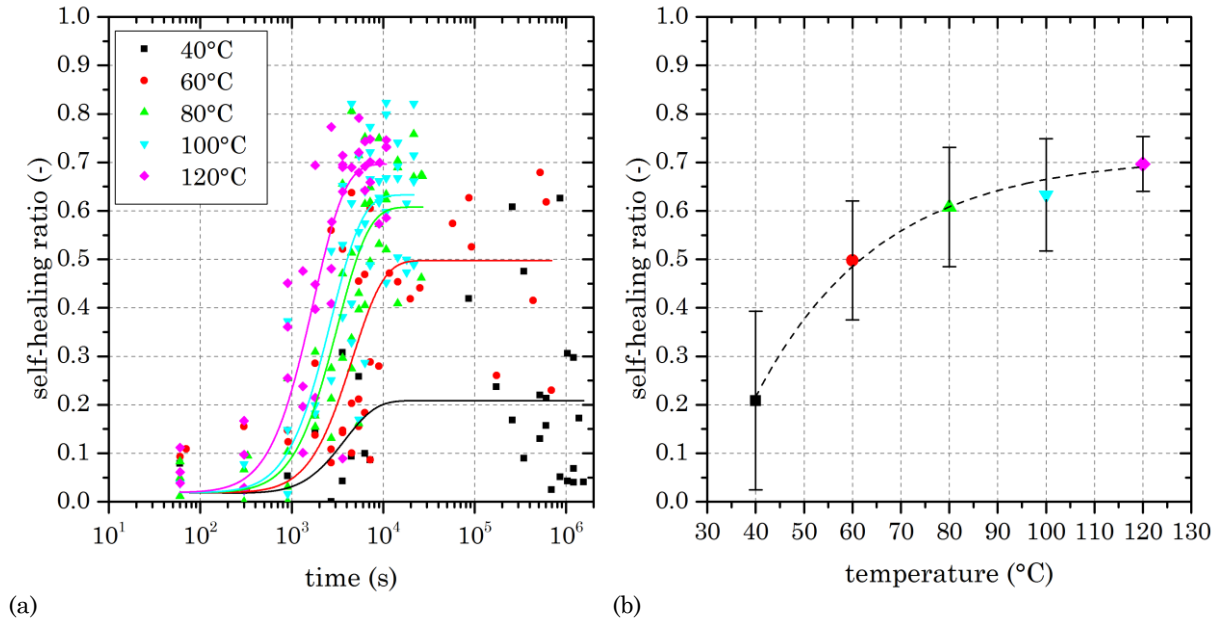


Figure 6.3: (a) Self-healing ratios for beams without circumferential pressure during the heating at oven temperatures of 40 °C, 60 °C, 80 °C, 100 °C and 120 °C. The data were fitted by Eq. (4.18). (b) The average self-healing ratios of the steady self-healing ratio state (symbols according to (a)), fitted by an asymptotic function ($S = a - b c^T$). The error bars represent the standard deviation.

To ensure that physical coherent fitting parameters are obtained from fitting Eq. (4.13) and Eq. (4.18) to the self-healing ratios, the fitting parameters were constrained. All parameters (S_0 , C , D and c_1) were limited to positive values. S_0 was allowed to take values in the range of the initial self-healing ratio range (0.01 to 0.02). Since C and D reflect the self-healing ratio limit, the sum of the parameters was limited to a maximum value of 1. An estimation for the ratio of C/D was based on the bitumen properties provided in section 5.1 and the assumptions of an initial contact area of 72.6 mm² (estimated from the adhesion breaking force and the ultimate tensile strength of bitumen of approximately 0.93 N mm⁻²). Since no deformation of the fracture surface was visible by eye, the dimension of the individual initial contact areas had to be below 70 μm. Assuming a rotationally symmetric contact area the initial height was estimated to be 50 μm, resulting in approximately 9239 contact points across the fracture surface. The average crack width of approximately 101 μm was determined by optical microscopy (see Figure 6.4). An acting hydrostatic pressure of the surrounding bitumen was assumed to be half of the beam height of 12.5 mm. The ratio of C/D was calculated to be on average 444.3. This value indicated the minor contribution of parameter D towards the self-healing equation.

Figure 6.4 shows cracks through an aggregate and along the interface between aggregate and mortar or mastic. The imperfectly fitting crack sides are due to loss of material during the breaking of the beams at low temperature and an imprecise aligning during the assembling of the halves, which led to contact points rather than contact areas and local deformation during the assembling and voids after self-healing. The gap measured was similar to other reported crack distances in asphalt mortar beams of 200 μm [17].

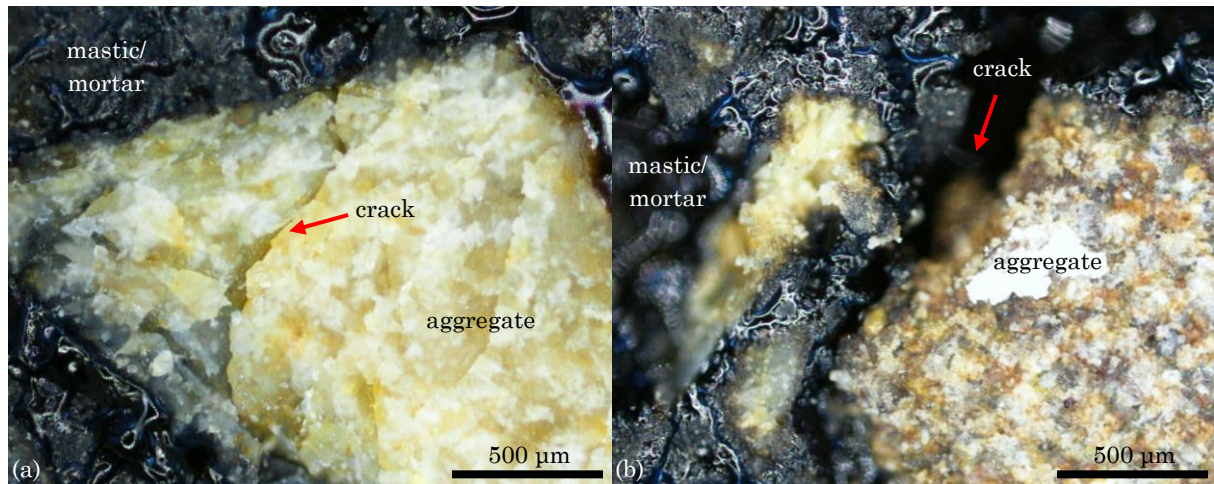


Figure 6.4: Microscope images of an asphalt mortar beam cross section with a macro crack (a) through an aggregate and (b) along the interface between aggregate and mastic/mortar with loss of material in the upper section. The crack width through the aggregate in (a) was approximately 44 μm and the crack width along the interface in (b) was approximately 126 μm .

The self-healing ratios in Figure 6.3(a) were fitted by Eq. (4.18) under physically coherent constraining conditions and the fitting parameters obtained are provided in Table 6.3. The proposed model sufficiently reflects the self-healing ratio development with advancing time. Table 6.3 further includes the fitting parameter for Eq. (4.13). The adjusted R^2 calculated were similar for both equations used to fit the data. Therefore, the simpler equation, Eq. (4.18), is sufficient to model the self-healing of asphalt mortar beams, as no decrease in the self-healing ratios calculated was observed. The C/D ratio obtained for Eq. (4.13) was higher than the estimation. However, the contribution of parameter D decreases with advancing time, as the limit of the term including parameter D is 0 as time approaches infinity.

Table 6.3: Fitting parameters and adjusted R^2 for Eq. (4.13) and Eq. (4.18) for the different oven temperatures without pressure.

fitting parameters	oven temperature				
	40 °C	60 °C	80 °C	100 °C	120 °C
S_0	0.02	0.02	0.02	0.02	0.02
Eq. (4.13) C	0.22	0.47	0.63	0.64	0.69
	D	0.33	0.53	0.04	0.27
Eq. (4.18) c_1	$1.40 \cdot 10^{-4}$	$1.93 \cdot 10^{-4}$	$4.21 \cdot 10^{-4}$	$4.55 \cdot 10^{-4}$	$7.08 \cdot 10^{-4}$
adj. R^2	0.02	0.33	0.72	0.61	0.72
Eq. (4.18) S_0	0.02	0.02	0.02	0.02	0.02
	C	0.22	0.45	0.63	0.63
Eq. (4.18) c_1	$3.71 \cdot 10^{-4}$	$3.69 \cdot 10^{-4}$	$4.32 \cdot 10^{-4}$	$5.45 \cdot 10^{-4}$	$8.44 \cdot 10^{-4}$
adj. R^2	0.03	0.30	0.72	0.61	0.72

The fracture surface after the second time of breaking the beams revealed that temperature and crack/beam geometry had a significant influence on the closing of the gap. Not healed and healed crack surfaces were distinguishable by a colour change, as identified by Kim, Little, Burghardt [38]. The delineation of the healing process occurring

in asphalt mortar beams above 40 °C is shown in Figure 6.5. At temperatures above 40°C the healing front in general started at the top of the crack and advanced downwards as the duration inside the oven increased. The movement of the healing front was not always uniform, depending on the material loss during the initial crack generation by three-point breaking. Higher temperature caused the healing front to move faster, which was consistent with higher obtained self-healing ratios. The advancing of the healing front from the top of the beam was associated with the developing temperature gradient. The temperature gradient for temperatures above 40 °C reduced the viscosity on the surface faster and the thermal expansion added to the closure by reducing the crack width. Hence, the healing followed the temperature increase from the top surface of the beam downwards. In the range of self-healing ratios from about 0.10 to 0.60, the movement of a healing front was observable. Below a self-healing ratio of 0.10, no visible change of the crack surface after the second time of breaking the beams was observed. The crack was completely closed from a visual perspective after the self-healing ratio was above 0.60. Further increase in the self-healing ratios was attributed to the closure of minor surface areas, which were not yet healed, and the increase of strength to transfer stress by diffusion of molecules across the interfaces of bulk and former crack. Self-healing at temperatures equal to or below 40 °C revealed that self-healing started mainly from locations, where the crack surfaces were closer in contact (top of the beams, within the beam or at the bottom of the beam). Therefore, the movement of the healing front was observed to be spreading across the crack surface. At ambient temperature, the hydrostatic pressure from the surrounding material was more important than the developing gradient, as the expansion of the material contributed in the reduction of the crack width, but was not enough to cause the same healing front movement as observed for beams healed at temperatures above 40 °C. This observation of the healing front moving from top to bottom of the beam was attributed to the higher temperatures used and the usage of moulds during the heating phase, causing a vertical temperature profile.

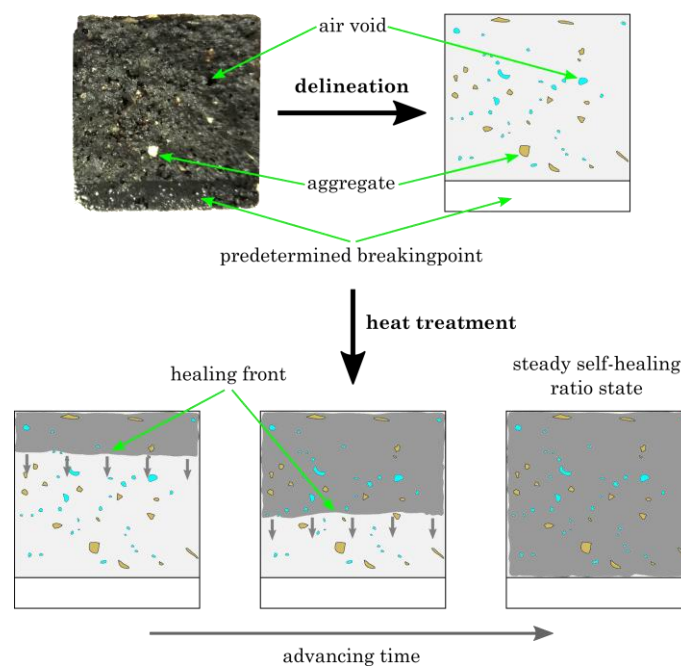


Figure 6.5: The view onto the crack surface of a broken beam and the scheme of the moving healing front with advancing time in the oven for beams at temperatures above 40 °C.

The additional circumferential pressure of 0.045 N mm^{-2} caused a rapid increase in the self-healing ratio in the range of 0.21 to 0.63 after the first 60 s of heat treatment, shown in Figure 6.6(a). This increase is two to three times higher than the self-healing ratios obtained for beams without pressure after 60 s. Healing broken beams with applied circumferential pressure at room temperature revealed that the self-healing ratio slightly increased with advancing healing duration and on average a self-healing ratio of 0.38 ± 0.10 was measured. Hence, compressive pressure enhances the self-healing of asphalt mortar beams. This was further confirmed by examining the crack surface after the second breaking, as the healing front covered the crack surface area completely with the exception of pores generated due to material loss. As identified for the PFTE moulds, a self-healing ratio above 0.60 correlates with an observable nearly complete healed fracture surface. After the rapid increase or leap in self-healing ratio, self-healing ratios further increased until a steady self-healing ratio state was reached after approximately 1200 s (20 min). The initial self-healing ratio jump was assumed to be mainly due to the pressure. The slower increase is enhanced by the pressure and mainly governed by the viscosity of the material. The steady self-healing state was temperature dependent (ANOVA, $n_{i=5} \leq 14$, $\alpha \leq 0.05$, single factor), as shown in Figure 6.6(b). The asymptotic fitting function was identical to a linear function with a Pearson's correlation coefficient of 0.98. Furthermore, Figure 6.6(b) shows that the additional pressure added due to the moulds caused higher average self-healing ratios for the steady self-healing ratio state and the standard deviation was reduced and more uniform for the set oven temperatures.

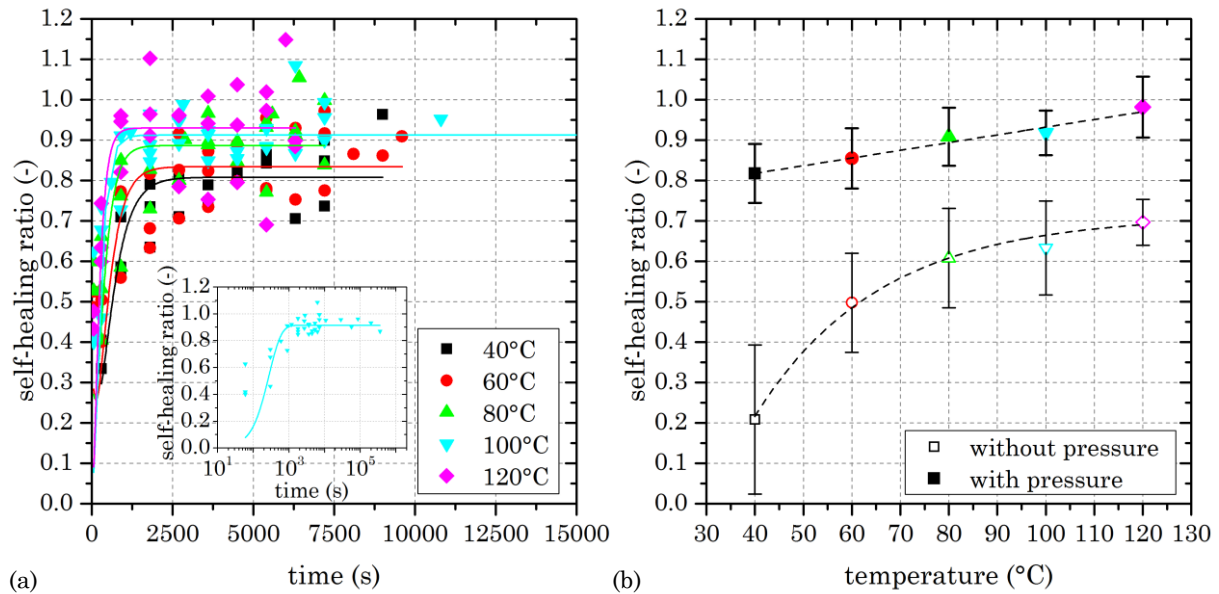


Figure 6.6: (a) Self-healing ratios for beams with circumferential pressure during the heating at oven temperatures of 40 °C, 60 °C, 80 °C, 100 °C and 120 °C. The detailed window shows an extended heat treatment period for 100 °C. The data were fitted by Eq. (4.18). (b) The average self-healing ratios of the steady self-healing ratio state (symbols according to (a)) for beams with pressure, fitted by a linear function ($R=0.98$) and for beams without pressure. The error bars represent the standard deviation.

Furthermore, comparing crack surfaces before and after healing revealed that new air voids were created due to material loss and that cracks through aggregates heal depending on the configuration of the crack and the healing temperature. Figure 6.7 shows the crack surface of two asphalt mortar beams before and after healing at 100 °C supported by silicone moulds. Smaller and bigger air voids were introduced into the material, as

material was lost during the brittle fracturing of the mortar beams. This is partly responsible for the variation in the self-healing ratio obtained for a similar duration of heat treatment. Moreover, smaller air voids were moving upwards, as the viscosity of the mortar reduces during heating, which was previously found by Menozzi, Garcia, Partl, Tebaldi, Schuetz [149]. The partial strength recovery of broken aggregates depended on the aggregate size, the temperature and the beam support. The crack through aggregates was filled with mortar/mastic only for beams with applied circumferential pressure and at higher temperature, as shown in Figure 6.7(b) and (d). Beams without pressure rarely showed filling of cracks through aggregates. Cracks occurring at the interface between mortar/mastic and aggregates predominantly reoccurred during the breaking after the self-healing. This indicates a remaining weak point for crack occurrences and the stone surface was clearer to identify.

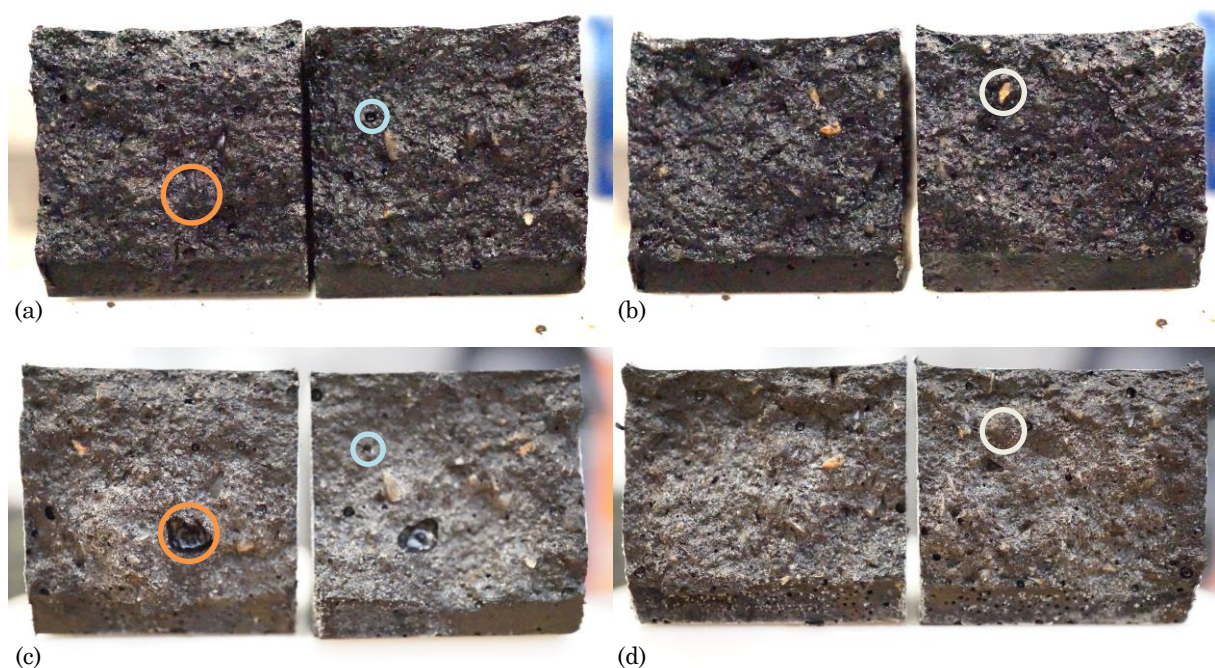


Figure 6.7: Crack surfaces of broken asphalt mortar beams. (a) and (b) show the surface after the initial three-point breaking and (c) and (d) show the surface after being heated at 100 °C supported by silicone moulds for (a) and (c) 7200 s (2 hours) and for (b) and (d) 10800 s (3 hours). The orange circle highlights the generation of new air voids due to material loss during the breaking, the pale blue circle shows the upward movement of an air void due to the decreased viscosity and the white circle shows the disappearance of a crack through a mineral aggregate, as it was likely filled with mastic to adhere both surfaces together. Moreover, not all cracks through aggregates were healed and cracks along the interface between aggregate and mastic were found, and often more visible after healing, as indicated in (a) and (c).

6.1.4 Self-healing due to induction heating with different current intensities

Induction heating of asphalt mortar beams revealed a similar development of self-healing ratios as convection heating. Figure 6.8(a) shows the initial increase in self-healing ratio to be between 0.31 and 0.56 for 1 s of heating. This followed a nearly linear increase till a steady self-healing ratio state was reached. The steady state depended on the current used and was reached after 100 s for 50 A and approximately 45 to 60 s for 100 A, 200 A and 300 A. A higher current intensity resulted in a faster self-healing ratio increase and a higher self-healing ratio after reaching a steady state. The average self-healing ratios for the steady self-healing ratio state are shown in Figure 6.8(b) and confirm results from the

measured surface temperature. 50 A and 80 A were similar in temperature and also similar in their self-healing ratios, reflecting the correlation between temperature and self-healing ratio. A significant difference (ANOVA, $n_{i=5} \leq 4$, $\alpha \leq 0.05$, single factor and t-test, $n \leq 4$, $\alpha \leq 0.05$, two-tailed) was measured for current intensities below 80 A and current intensities above 100 A. No significant difference was found between 100 A, 200 A and 300 A, already indicated due to the similar surface temperatures and the self-regulation of current intensity by the induction generator.

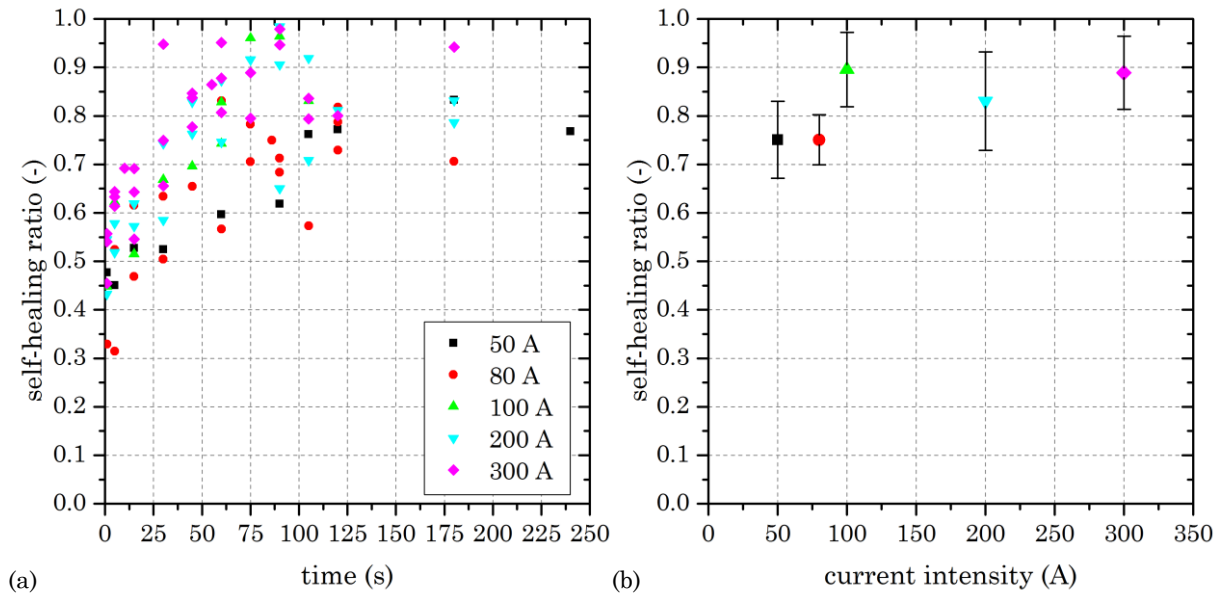


Figure 6.8: (a) Self-healing ratios calculated for current intensities of 50 A, 80 A, 100 A, 200 A and 300 A. (b) The average self-healing ratios of the steady self-healing ratio state (symbols according to (a)), showing the indistinguishable self-healing for 100 A, 200 A and 300 A due to the self-regulation of the induction generator. The error bars represent the standard deviation.

6.2 Summary

The thermal equilibrium surface temperature depended on the oven temperature. The heating rate depended on the mould material in minor way, as the materials were similar. The difference in the self-healing rate and ratio was mainly attributed to the applied horizontal pressure at a constant oven temperature. The self-healing ratios increased sigmoidally from the initial self-healing ratio, as indicated by the developed physical model. The initial self-healing ratio was related to the cohesion and adhesion of bitumen or mastic surfaces to each other and to aggregate surfaces. A steady self-healing ratio state was reached, which depended on the temperature and the circumferential pressure. The self-healing induced by convection heating did not reach a self-healing ratio of 1, 100% healed, due to the loss of material during the breaking of the beams and the non-healed fracture area through aggregates. Evaluation of the fracture surface after healing revealed that the cracks, of approximately 101 μm , closed starting at the top of the beam for temperatures above 40 $^{\circ}\text{C}$, following the temperature gradient developed. This was assumed to be due to the reduction of viscosity and the thermal expansion of the material. At 40 $^{\circ}\text{C}$ the healing front started arbitrarily from contact points. The application of circumferential pressure pressed the crack surfaces together, promoting an instantaneous gain in self-healing ratio to about 0.38.

Induction heating caused a linear temperature increase of the surface temperature with high temperature spots distributed in the material. The self-healing ratios followed a sigmoidal progression, similar to the progression for convection heating, although faster. As the current intensity increased, the self-healing ratios increased in accordance with the measured surface temperature, and the steady self-healing ratio state increased as well, showing the influence of heat transfer and thermal expansion on the self-healing ratio. It was observed that the increase in the current intensity had a limit, which was due to the self-regulation of the equipment at about 100 A, which determined the maximum achievable self-healing ratio.

7 Influence of the bitumen type on the self-healing of macro cracks

The influence of five different bitumen types on the self-healing of a macro crack in an asphalt mortar beam, manufactured from mixture 1, was investigated. The self-healing was induced by either convection heating or induction heating and a horizontal/circumferential pressure was applied during the heating phase, to reduce variability. The transformation of time to the pseudo energy healing parameter allowed a comparison between the heating methods.

7.1 Thermal behaviour of asphalt mortar beams with different bitumen types

The increase and decrease of the surface temperature of asphalt mortar beams manufactured with five different bitumen types was measured in order to calculate the pseudo healing energy parameter. Since only the heating methods were changed, this allowed a comparison mainly based on temperature.

7.1.1 Convection heating

Identical to the different oven temperatures in section 6.1.1, the surface temperature of asphalt mortar beams was measured for the five different bitumen types used, as the beams were heat treated in a convection oven to 100 °C. From ambient temperatures (21 °C ±1 °C) the average surface temperature increased until a temperature of 91.6 °C ±1.0 °C was reached, as shown in Figure 7.1. The highest surface temperatures measured were around 96.8 °C ±0.7 °C and the lowest were around 86.1 °C ±1.3 °C. The difference between surface temperature and oven temperature, as discussed in section 6.1.1, arose from a temperature drop until the surface was measured and the linear temperature deviation of the infrared camera. A temperature drop of 5 °C in the first 10 seconds after removing the samples from the oven was in accordance with Newton's law of cooling and the obtained cooling curves.

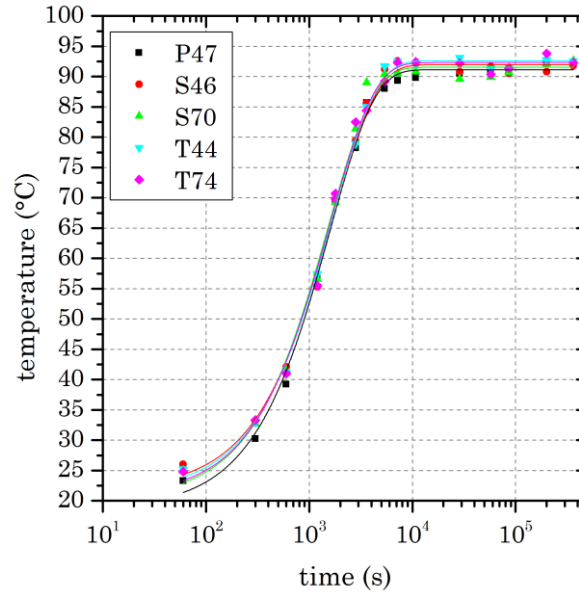


Figure 7.1: The average surface temperature measured by an infrared camera for a set oven temperature of 100 °C for asphalt mortar beams supported by silicone moulds and manufactured from five different bitumen types. Measurements were fitted by the convection heat transfer function

$$(T(t) = T_{max} - (T_{max} - T_{air})e^{-k_h t}).$$

As shown in Figure 7.1, the type of bitumen does not significantly influence the surface temperature measured. This is attributed to the dominant contribution of the mineral aggregates to the heat capacity of the mixture and the minor variation in heat capacity for different bitumen [3, 246]. The equilibrium surface temperatures, which were reached after approximately 5400 s (1.5 h) are indifferentiable (ANOVA, $n_i=5$, $\alpha < 0.05$, single factor). The temperature development for each bitumen type was accurately fitted by the equation for convection heat transfer. The fitting parameters are provided in Table 7.1.

Table 7.1: Surface temperature fitting parameters for the five different bitumen studied.

bitumen type	equilibrium surface temperature, measured [°C]	equilibrium surface temperature, fitted [°C]	heating exponent [s ⁻¹]
P47	91.5 ± 0.8	91.1	6.3 · 10 ⁻⁴
S46	91.1 ± 0.6	92.0	6.0 · 10 ⁻⁴
S70	91.0 ± 1.4	91.5	6.5 · 10 ⁻⁴
T44	92.2 ± 0.8	92.6	6.0 · 10 ⁻⁴
T74	92.0 ± 1.3	92.3	6.2 · 10 ⁻⁴

Since the type of bitumen does not significantly influence the temperature development of the sample, the self-healing will be primarily based on temperature dependent properties, such as viscosity, stiffness and thermal expansion, and not due to different temperature distributions for heat induced self-healing by convection heating.

7.1.2 Induction heating

The average surface temperatures for the five different bitumen investigated, shown in Figure 7.2, were fitted by a linear function. The Pearson's correlation coefficient for the

linear fittings were 0.74 for P47, 0.97 for S46, 0.98 for S70, 0.98 for T44 and 1.00 for T74. The fitting parameters are provided in Table 7.2. The temperature did not reach an equilibrium temperature, as the heat was locally generated by the metal particles due to Joule heating. The metal particles at the surface and in the central area underneath the induction coil reached temperatures exceeding the measurable range of the infrared camera (275 °C). The heat generated in the metal particles was released into the surrounding bitumen and mineral aggregates by thermal conduction. The lowest temperatures measured were in the range of 40 °C to 50 °C.

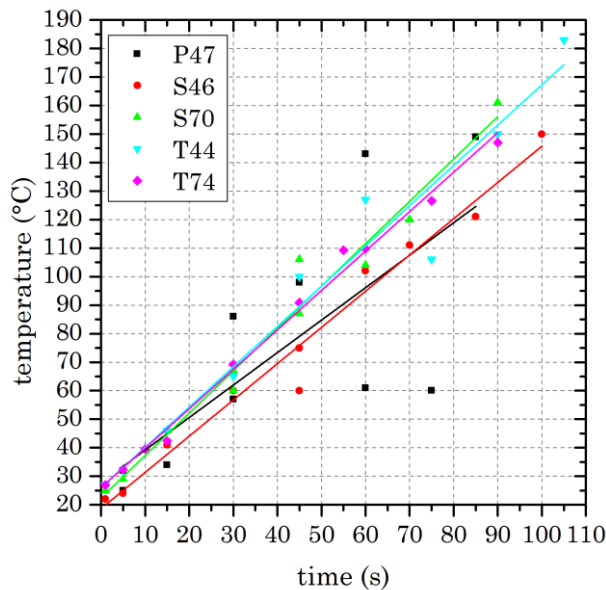


Figure 7.2: The average surface temperature measured for induction heated asphalt mortar beams manufactured with five different bitumen types. Measurements were fitted by a linear function ($T(t) = a + b t$).

Table 7.2: Fitting parameters for induction heating for different bitumen types.

bitumen type	intercept [°C]	slope [°C·s ⁻¹]
P47	27.8	1.13
S46	18.6	1.27
S70	22.4	1.49
T44	26.1	1.41
T74	26.0	1.38

As the metal particles were distributed throughout the beam, induction heating generated locally distributed heat sources of high temperature, which resulted in a much faster increase of the average surface temperature compared to convection heating. The average surface temperature increased approximately 60 times faster for induction heating. As the induction heating capacity reduces with the distance to the coil, the centre of the top surface reached higher temperatures than the surfaces at the ends of the beams. In addition, trails of smoke appeared after about 45 s during heating. The maximum temperature measured after 45 s was above 215 °C. Heating of thin bitumen films until smoke occurred confirmed that thermal degradation started at approximately 230 °C ±5 °C for the bitumen used. Furthermore, a change in the surface texture of the

beam was observed, as shown in Figure 7.3(a). The change started in the middle of the beam surface and expanded outwards with increasing heating duration. A coronal stripe, which was rich in bitumen, surrounded a rougher surface area in the centre. The outward directed coronal stripe is possibly caused by bitumen expansion due to temperature increase and the formation of gas due to thermal degradation of bitumen, leaving a “burned” surface behind. The surface was analysed by Fourier transformed infrared spectroscopy, shown in Figure 7.3(b) for bitumen T74. Induction heating resulted in an increase of the ketone and carboxyl band, indicating oxidation during the induction heating. The increase in these two bands was higher than the increase due to laboratory ageing, showing the pyrolysis occurring. Moreover, the fracture surface of the heat treated beams revealed that, for the longest duration, a porous pattern was formed ranging from the surface to a depth of approximately 10 mm. Furthermore, metal particles (one to four per beam) were extracted from the beam surface by the magnetic field after 60 s, due to the reduction in viscosity, and adhered to the coil.

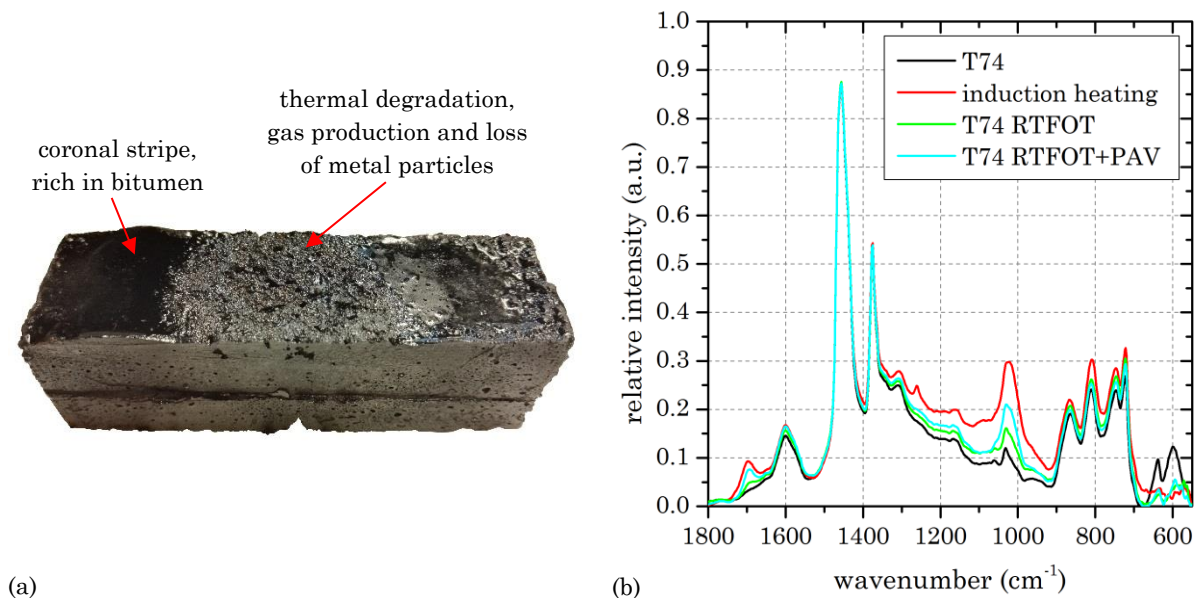


Figure 7.3: (a) Beam produced with bitumen S46 and heat treated by induction heating for 90 s. Arising fumes and the visible change of the surface texture marked the beginning of the thermal degradation of bitumen. (b) Fourier transformed infrared spectra of bitumen T74, bitumen T74 sampled from the pyrolysed area and laboratory aged bitumen T74.

7.1.3 Convection cooling

After the heat treatment of the mould supported beams, the beams within the moulds were stored inside a freezer, to prevent further self-healing and to ensure identical conditions for the second breaking of the beams. To quantify the pseudo healing energy parameter for the cooling duration, the temperature progression of one bitumen (T74) for both heating methods was measured, which is shown in Figure 7.4. Only one bitumen was used, as the temperature progression during heating was similar for all the bitumens used.

The exponential parameters for cooling were obtained by fitting the surface temperatures measured with Newton’s law of cooling [247], shown in Figure 7.4 (a). The cooling parameter for convection heated beams (k_c) was $3.6 \cdot 10^{-4} \text{ s}^{-1} \pm 0.4 \cdot 10^{-4} \text{ s}^{-1}$. In the case of induction heated beams, the temperatures measured were fitted by two individual cooling

functions. This was required, as the temperature decreased faster at the beginning of cooling, due to the hot metal particles, which released their energy as heat to the surroundings, increasing the temperature of aggregates and bitumen. Once a homogeneous temperature on the surface was reached, the temperature decrease was similar to the decrease observed for convection heated beams. The transition temperature from the faster cooling branch to the slower cooling branch depended on the heating duration. A linear increase from 25 °C to 45 °C was assumed during the first 35 s and afterwards, the transition temperature was assumed to be constant at 45 °C. These assumptions were based on the range of lower surface temperatures measured. The cooling parameter of the fast branch for induction heated beams (k_{c1}) was $37.0 \cdot 10^{-4} \text{ s}^{-1} \pm 12.0 \cdot 10^{-4} \text{ s}^{-1}$ and the cooling parameter for the slower branch (k_{c2}) was $3.6 \cdot 10^{-4} \text{ s}^{-1} \pm 0.2 \cdot 10^{-4} \text{ s}^{-1}$, which is in the same range as the cooling parameter for convection heated beams.

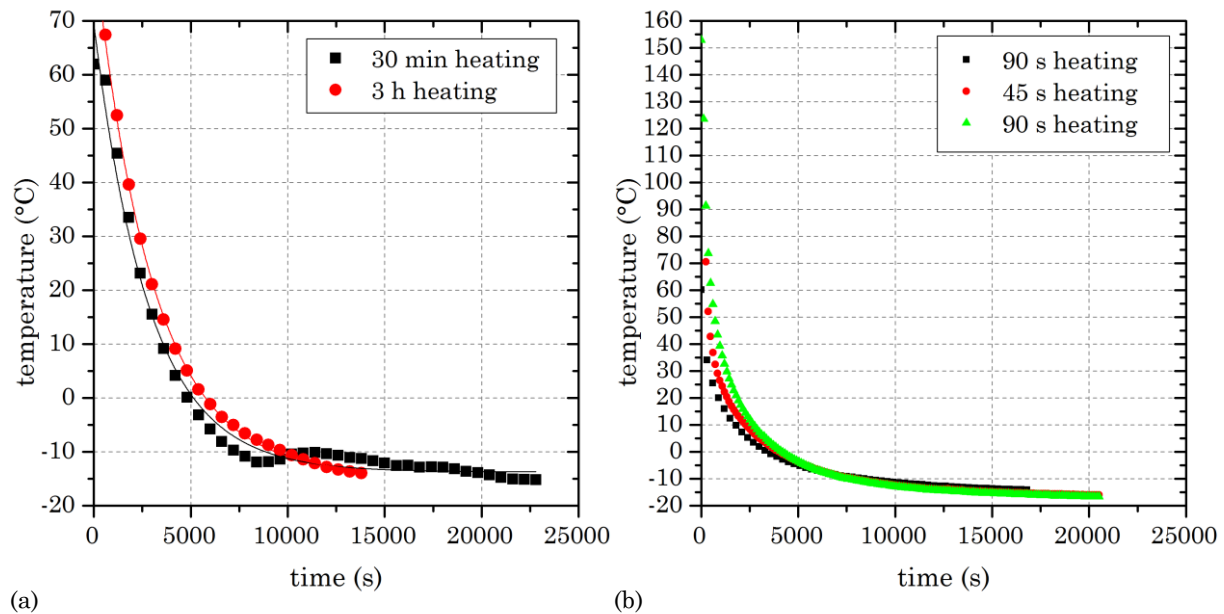


Figure 7.4: Temperature progression during cooling in the freezer for (a) convection heated beams and (b) induction heated beams. The temperature decrease for convection heated beams was fitted with Newton’s law of cooling $(T(t) = T_{freezer} + (T_{max} - T_{freezer})e^{-k_c t})$.

7.1.4 Calculation of the pseudo healing energy parameter

In order to compare the different heating methods, a pseudo healing energy parameter was introduced [32]. This parameter was calculated from the surface temperatures measured and in addition, required the determination of the threshold temperature for self-healing. For this, the beams were healed at 21 °C and 7 °C. Beams healed at 21 °C revealed a slight linear increase from 0.37 at 60 s to 0.50 at 6300 s (105 minutes). Healing at 7 °C for 12 to 110 days showed a constant self-healing ratio of 0.06 ± 0.02 , which is slightly higher than the initial self-healing ratios measured and assigned to the healing occurring before the beams reached 7 °C. Assembling beams at 7 °C revealed no measurable force during the second breaking of the beams. For the calculations of the energy parameter, the threshold temperature was estimated to be 10 °C for all bitumens used.

The pseudo healing energy parameter was calculated for each bitumen using the surface temperature measured and the assumption outlined above. A comparison between the pseudo healing energy calculated for heating and cooling revealed that heating mainly contributed to the parameter, at between 89% and 100% for convection heating and 66% to 89% for induction heating. Figure 7.5 shows the transformation of the temperature progression to the pseudo healing energy parameter. The time aspect in Eq. (4.20) and Eq. (4.21) allows the parameter to increase after a temperature equilibrium is reached, significant for convection heating. Furthermore, the transformation to the pseudo healing energy parameter showed that convection heating results in a bigger pseudo energy healing parameter compared to induction heating, due to the longer heating durations.

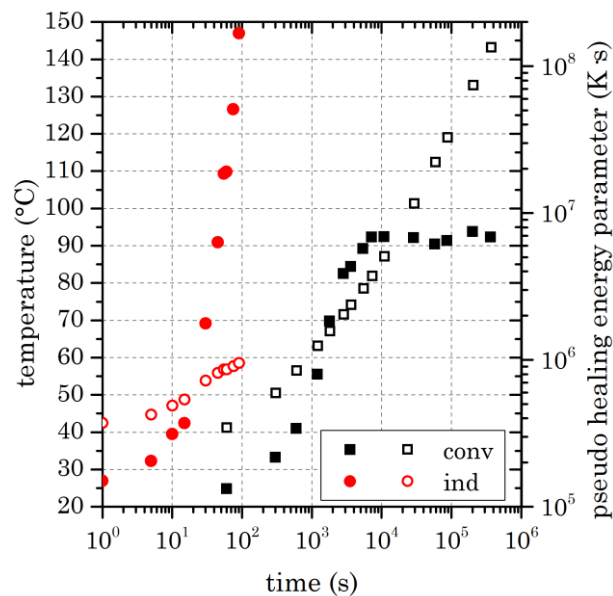


Figure 7.5: Average surface temperatures of beams produced with T74 measured at different healing durations for convection (■) and induction (●) heating. Transformation to the pseudo healing energy parameter for convection (□) and induction (○) heating.

7.2 Induced self-healing of macro cracks for different bitumen types

A horizontal/circumferential pressure was applied to the asphalt mortar beams manufactured with different bitumen types during the heating phase. The self-healing ratios obtained for convection heating showed a similar progression with advancing time for the five bitumen types, as shown in Figure 7.6. Furthermore, Figure 7.6 shows the jump in self-healing ratio from assembling to the first 60 s of heat treatment as observed for different temperatures. The steady self-healing ratio state was reached by all five bitumens after approximately 1200 s (20 min) of heating inside the convection oven.

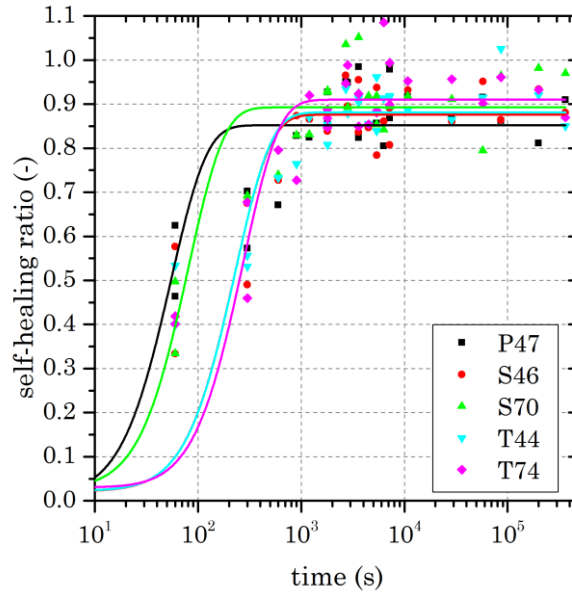


Figure 7.6: Self-healing ratios for asphalt mortar beams for convection heating at 100 °C. The bitumen used to manufacture the beams were P47, S46, S70, T44 and T74. The self-healing ratios were fitted by Eq. (4.18).

Eq. (4.18) was not able to reproduce the initial gain in self-healing ratio. The initial self-healing ratio, the average self-healing ratio of the steady self-healing ratio state and the fitting parameters for the functions shown in Figure 7.6 are provided in Table 7.3. Allowing the initial self-healing ratio constraint to be up to 0.40, the equation fitted the data more accurately and the values obtained for the parameter C were close to the average self-healing ratio for the steady self-healing ratio state.

Table 7.3: Healing properties of asphalt mortar beams for convection and induction heating and fitting parameters of Eq. (4.18) for convection heating.

parameters	Bitumen type				
	P47	S46	S70	T44	T74
S_0 measured (initial self-healing ratio)	0.016 ± 0.005	0.017 ± 0.006	0.027 ± 0.003	0.016 ± 0.008	0.027 ± 0.005
SSHRS convection	0.88 ± 0.04	0.88 ± 0.06	0.91 ± 0.06	0.92 ± 0.06	0.92 ± 0.04
SSHRS induction	0.82 ± 0.04	0.85 ± 0.08	0.85 ± 0.04	0.86 ± 0.04	0.90 ± 0.07
fitting parameters					
S_0	0.011	0.023	0.030	0.024	0.032
C	0.85	0.88	0.89	0.88	0.91
c_1	0.027	0.006	0.018	0.006	0.005

SSHRS: average self-healing ratio of the steady self-healing ratio state

Asphalt mortar beams heated by induction heating showed a similar self-healing ratio development with advancing time as convection heated beams, although the development was significantly faster as shown in Figure 7.7(a) for bitumen T44 and T74. The steady self-healing ratio state was reached after approximately 30 s; only bitumen S46 showed a different behaviour in Figure 7.7(b). The slower development of self-healing ratios for bitumen S46 resulted from the lower surface temperature measured during induction heating, shown in Figure 7.2. Hence, bitumen S46 reached the steady self-healing ratio

state later. The range between 60 s and 100 s was used to calculate the average self-healing ratio of 0.85 ± 0.08 , compared to 0.78 ± 0.11 if the steady state started at 30 s. The average self-healing ratios reached by induction heating for the five bitumens are provided in Table 7.3. It was found that similar self-healing ratios were achieved for the same surface temperature, with the beginning of the steady self-healing ratio state at approximately 57°C .

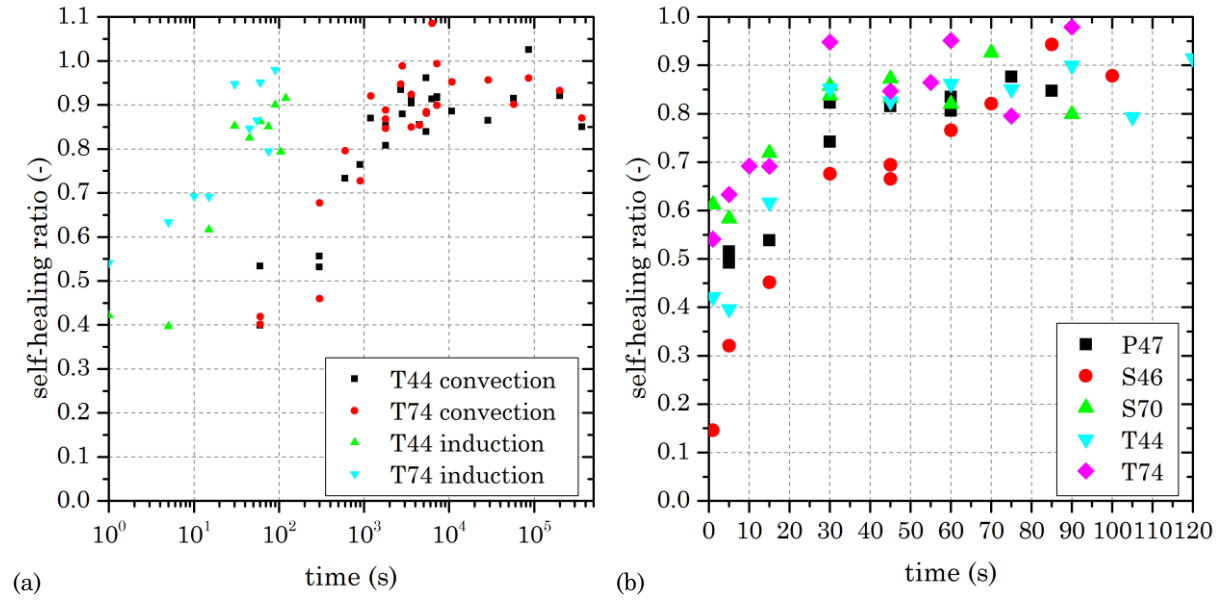


Figure 7.7: (a) Comparison of self-healing ratios for convection and induction heating of asphalt mortar beams containing bitumen T44 respectively T74. (b) Self-healing ratios for induction heated asphalt mortar beams produced with different bitumen types.

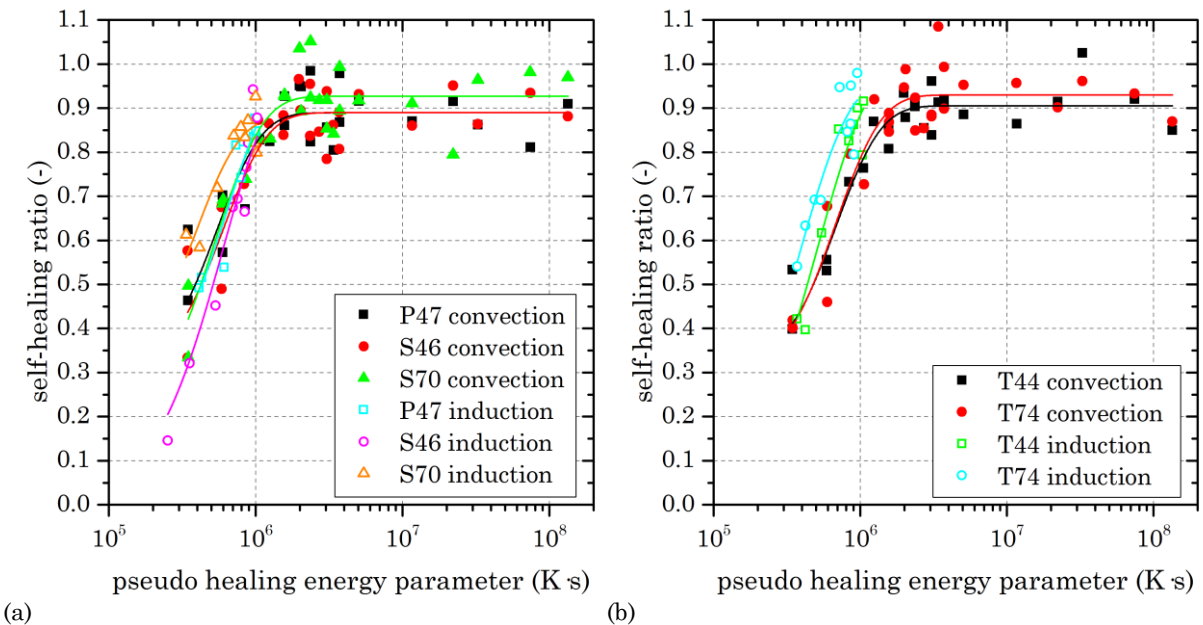


Figure 7.8: Comparison of convection and induction heated beams by using the pseudo healing energy parameter for beams manufactured with (a) bitumen P47, S46 and S70 and (b) bitumen T44 and T74. The self-healing ratios were fitted by Eq. (4.18).

Converting time into the pseudo healing energy parameter, the self-healing of induction and convection heated asphalt mortar beams became nearly identical, as shown in Figure 7.8. For beams manufactured with bitumen S70, shown in Figure 7.8 (a), the self-

healing ratios calculated were higher for induction heating for the same pseudo healing energy parameter. Bitumen S46 showed lower self-healing ratios, which was due to the lower surface temperature during heating. Figure 7.8 (b) shows the comparison of beams manufactured with bitumen T44 and T74. The self-healing ratios for induction heating were found at slightly lower pseudo healing energy parameters compared to convection heating. This is confirmed through the fitting of the self-healing ratios calculated by Eq. (4.18). The fitting parameters are provided in Table 7.4. The healing exponent c_1 indicates that the self-healing rate is faster for induction heating (for three bitumen types).

Table 7.4: Fitting parameters of Eq. (4.18) for convection and induction heated beams of Figure 7.8.

parameters	bitumen type				
	P47	S46	S70	T44	T74
convection heating					
S_0	0.00	0.00	0.00	0.00	0.00
C	0.89	0.89	0.93	0.90	0.93
c_1	$3.11 \cdot 10^{-6}$	$2.89 \cdot 10^{-6}$	$2.82 \cdot 10^{-6}$	$2.68 \cdot 10^{-6}$	$2.57 \cdot 10^{-6}$
induction heating					
S_0	0.49	0.00	0.60	0.00	0.00
C	1.00	1.00	0.88	1.00	0.97
c_1	$2.57 \cdot 10^{-6}$	$2.40 \cdot 10^{-6}$	$4.46 \cdot 10^{-6}$	$2.82 \cdot 10^{-6}$	$3.78 \cdot 10^{-6}$

Figure 7.9 shows the beginning of the steady self-healing ratio state, which reveals that in general induction heated beams reached the steady state at lower pseudo healing energy parameters than convection heated beams. The increase of self-healing ratios with pseudo healing energy parameter is nearly linear, which reflects the linear surface temperature increase during the heat treatment and the short steady state before significant thermal damage is introduced.

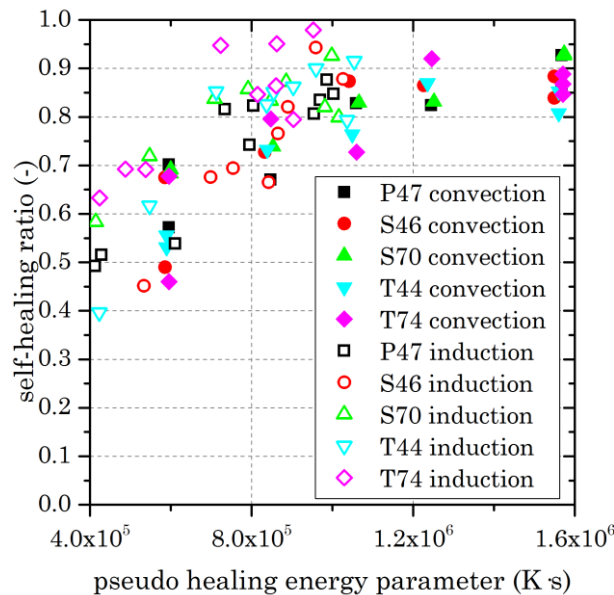


Figure 7.9: Self-healing ratio comparison of convection and induction heated beams manufactured with different bitumen types for a detailed section at the beginning of the steady self-healing ratio state.

Furthermore, the five bitumens were tested by adhesion testing (PATTI test, pull-stub diameter: 20 mm) and allowed to heal at approximately 8 °C for 24 hours before retesting. An example of the initial fracture and the fracture after healing are shown in Figure 7.10(a) and (b). The fracture was a combination of adhesive and cohesive failure for all bitumen types and due to the low temperature, material was occasionally lost during the fracturing, shown in Figure 7.10(a). The strength recovery after resting at lower temperatures for 24 hours is shown in Figure 7.10(c). Softer bitumen showed higher self-healing ratios compared to harder bitumen, which is mainly due to the lower viscosity. Due to the design of the test, a high variability in results was observed, which was attributed to the assembling of the fracture surfaces, as a misplacement could have led to a decreased self-healing, and the loss of material during the initial fracturing, as a brittle fracture was generated. Self-healing was due to flow under pressure for the adhesive test set-up. The pressure was generated by the metal stub, which had a weight of approximately 40.07 g \pm 0.05 g and applied an average pressure of 0.00125 N mm^{-2} onto the bitumen. Significant differences (t-test, $n_i=3$, $\alpha \leq 0.05$, two-tailed) were observed for bitumen P47, S46 and S70, though showing a general trend of increasing self-healing ratio with decreasing viscosity. For bitumen T44 and T74 no significant differences were deducible due to an increased variability in the results. In general bitumen with lower viscosity healed better, indicated by a higher self-healing ratio, though the fracture surface might play an essential role for the self-healing, as indicated by the self-healing ratio of bitumen P47, which had a high viscosity though it was situated between S46 and S70.

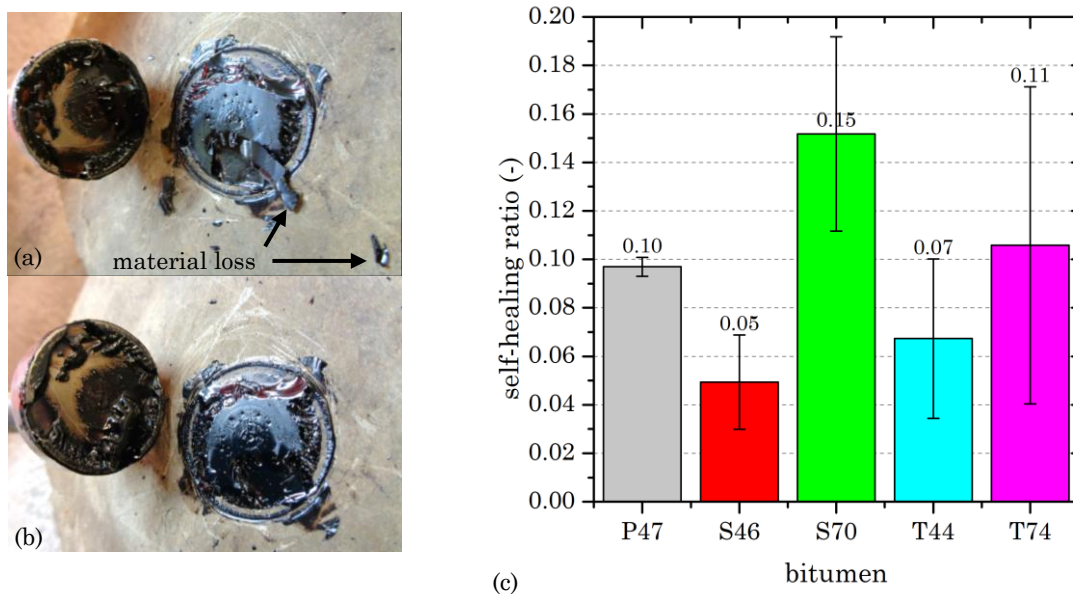


Figure 7.10: Adhesive testing of bitumen: (a) initial fracture and (b) fracture after healing for 24 h at 8 °C. (c) Average self-healing ratios obtained through adhesive testing before and after healing. Labels are the average values obtained and the error bars represent the standard deviation.

7.3 Correlation of chemical, rheological and physical parameters to self-healing parameters

Table 7.5 is an extension of Table 5.7 and continues the Pearson's correlation analysis for self-healing parameters identified and the fitting parameters introduced in Eq. (4.18).

Table 7.5: Self-healing correlation matrix.

	equilibrium surface temperature	heating exponent	induction heating slope	initial self-healing ratio	steady self-healing ratios for convection	steady self-healing ratios for induction	self-healing ratios adhesion test	convection fitting parameters	S_0	C	c_1	induction fitting parameters	S_0	C	c_1
bitumen properties															
needle penetration	-0.03	0.69	0.48	0.99	0.68	0.42	0.51	0.24	0.94	-0.54		0.10	-0.69	0.90	
softening point	-0.05	-0.53	-0.63	-0.97	-0.81	-0.60	0.06	0.18	-0.97	0.90		0.22	0.75	-0.94	
viscosity 100 °C	0.63	-0.58	-0.14	-0.92	-0.46	-0.32	-0.60	-0.06	-0.85	0.67		-0.02	0.61	-0.86	
viscosity 50 °C	0.65	0.49	0.52	0.44	0.36	0.06	0.79	0.55	0.46	-0.13		0.53	-0.58	0.57	
transition temperature	-0.50	-0.32	-0.86	-0.92	-0.92	-0.85	-0.01	-0.03	-0.94	0.85		0.15	0.53	-0.81	
density	-0.54	0.74	-0.63	-0.81	-0.65	-0.34	-0.94	-0.83	-0.95	0.25		-0.86	0.88	-0.94	
vol. CTE	-0.96	0.64	-0.44	0.50	-0.31	-0.18	0.52	0.67	0.30	0.07		0.30	-0.64	0.43	
surface tension (SDM ¹)	-0.59	0.61	-0.66	-0.13	-0.70	-0.61	0.59	0.46	0.21	0.61		0.54	-0.34	0.28	
surface tension (WPM ²)	0.13	0.17	0.70	0.86	0.83	0.88	-0.37	0.19	0.80	-0.78		-0.01	-0.53	0.68	
asphaltene fraction	-0.27	-0.39	-0.64	-0.84	-0.76	-0.73	-0.30	0.12	-0.80	0.80		0.28	0.31	-0.62	
saturate fraction	-0.14	0.37	-0.26	-0.20	-0.44	-0.50	0.67	0.76	-0.11	0.50		0.70	-0.46	0.13	
aromatic fraction	0.32	0.03	0.61	0.55	0.72	0.87	-0.27	-0.35	0.62	-0.75		-0.45	-0.13	0.43	
resin fraction	-0.35	0.28	-0.26	0.04	-0.38	-0.33	0.09	0.62	-0.27	0.40		0.44	-0.32	-0.07	
wax fraction	-0.08	0.32	0.27	0.33	0.32	0.29	0.51	0.63	0.44	-0.20		0.32	-0.76	0.57	
MMHC	-0.56	-0.74	-0.53	-0.63	-0.45	-0.01	-0.92	-0.59	-0.67	0.15		-0.63	0.68	-0.76	
thermal behaviour															
equilibrium surface temperature	-							-0.46	0.30	-0.56		-0.20	0.22	0.18	
heating exponent	-0.46	-						0.86	0.61	0.21		0.86	-0.82	0.76	
induction heating slope	0.67	0.01	-					-0.19	0.70	-0.89		-0.31	-0.27	0.56	
self-healing properties															
initial self-healing ratio	-0.14	0.64	0.52	-				0.42	0.98	-0.64		0.20	-0.77	0.94	
convection steady self-healing ratios	0.64	-0.02	1.00	0.72	-			-0.28	0.84	-0.92		-0.49	-0.41	0.73	
induction steady self-healing ratios	0.40	-0.26	0.82	0.47	0.81	-		-0.33	0.58	-0.94		-0.62	-0.14	0.38	
self-healing ratios adhesion test	0.15	0.96	0.01	0.33	0.03	-0.50	-	0.90	0.34	0.46		0.87	-0.49	0.55	

Significant correlations at the 0.05 level (two-tailed) are coloured in green and at a 0.10 level (two-tailed) are coloured in yellow.

¹ SDM: sessile drop method

² WPM: Wilhelmy plate method

Since the equilibrium temperatures are dependent on the thermal equilibrium, which is independent of material properties [248], any linear correlations found were coincidental, such as the negative linear correlation with the volumetric thermal expansion coefficient. Heating parameters for convection heating are correlated to the heat capacity and thermal conductivity of the material and for induction heating are correlated to the magnetic permeability of the material [184, 231]. However, the heating exponent and the induction

heating slope showed no significant linear correlation to any material parameter, except that the slope had a minor correlation with the transition temperature. A slight trend between density and heating exponent was identified.

The initial self-healing ratios showed a significant linear correlation with the needle penetration, softening point, viscosities measured by spindle rheometer and the transition temperature, as well as with surface tension (WPM) and the asphaltene fraction. This indicated that local surface deformations on contact points during the initial assembling of the fractured halves are mainly responsible for the initial cohesion/adhesion, resulting from the surface interaction. The steady self-healing ratio state for convection heating had a significant linear correlation with the transition temperature, and minor correlations with the softening point and surface tension (WPM). Whereas the steady self-healing ratio state for induction heating was linearly correlated to the surface tension (WPM) and had a minor significant correlation to the transition temperature and the aromatic fractions. As identified in Eq. (4.15), the maximum self-healing ratio is a function of maximum tensile stress, beam geometry, surface tension and density difference. A linear regression of the square root of surface tension divided by density to the steady self-healing ratio state revealed that for convection heating only a weak trend was identified ($R=0.72$) and for induction heating a significant correlation was found ($R=0.92$). The dependence of the steady self-healing ratio state for convection heating on viscosity indicates that for the maximum self-healing ratio flow and deformation processes might be of importance. This could be indirectly linked to the crack from, as different crack distances would result in different self-healing rates and ratios [157, 171]. The self-healing ratios obtained from the adhesion test were shown to be correlated to densities and the ethyl methylene hydrogen to carbon ratios. Derived from the design of the healing test, the self-healing should be correlated to the bitumen viscosities, which may be due to the variations in results for the adhesion test self-healing.

Linear correlations found are partly coincidental, for example, the relation between the heating exponent and self-healing ratios of the adhesion test or the induction heating slope and the convection steady self-healing ratios, as these experiments are not related to each other.

The fitting parameters of Eq. (4.18), shown in Table 7.4, were correlated to the material properties and the self-healing characteristics. The initial self-healing ratio for convection heating S_0 showed a significant linear correlation with the self-healing ratios obtained by the adhesion test, though not with the initial self-healing ratios, which were used as limits for the curve fitting. The maximum self-healing ratio C was significantly linearly correlated to the conventional test results, the transition temperature, the density and the initial self-healing ratio. A minor correlation was to the steady self-healing ratio state, which was used as a parameter limit. The self-healing rate c_1 showed significant relations with the steady self-healing ratio stage, implying a rate dependency of the maximum self-healing ratio. For induction heating, the initial self-healing ratio S_0 showed no correlation to the initial self-healing ratios measured, which is contrary to expectations as the initial self-healing ratios were used initial fitting variable. The maximum self-healing ratio C was linearly correlated to density and the heating exponent, though not to the steady self-healing ratio state for induction heating. The self-healing rate c_1 was linearly correlated

to the density and the conventional tests and further showed a minor correlation to viscosities obtained by spindle rheometer and the transition temperature. Eq. (4.19) confirms the relation of the self-healing rate to density and viscosity. A more significant correlation for these parameters for both heating methods was expected. Hence, similar material parameters, similar self-healing ratios and the variation of self-healing ratios caused similar parameters for different bitumen types.

7.4 Summary

The thermal behaviour of beams manufactured with five different bitumen types was nearly identical for convection heating. The surface temperature measured after induction heating showed that the distribution and distance from the coil might have affected beams manufactured with bitumen S46, having a lower surface temperature and lower self-healing ratios. Thermal degradation started at approximately 230 °C. This was confirmed visually by a change in the surface structure and the fracture surface, as well as by infrared spectroscopy. The spectrum showed an increase in ketone and carboxyl band, indicating oxidation. Since induction heating produced local heat sources, the surrounding material, mainly aggregates, has a lower temperature, which was in the range of 40 °C to 50 °C. Furthermore, this non-uniform heat distribution led to the splitting of the cooling curve into two separate sections to reproduce the fast cooling of the beams until a uniform temperature was reached.

The initial self-healing ratios were correlated to the viscosity, indicating the contribution of creating contact points due to deformation. The steady self-healing ratio state was related to the surface tension measured by the Wilhelmy plate method, which suggested that the maximum reachable self-healing ratio depends on the surface tension, as well as thermal expansion. The fitting parameters showed some correlation. However, the relation to physical parameters used in the equation was found to be minor. The self-healing rate parameter c_1 was correlated for induction heating to density and viscosity, but not for convection heating. The maximum self-healing ratio parameter C was not correlated to the surface tension, but showed a correlation with density for convection heating. This could be due to the significant influence of thermal expansion and pressure on the self-healing.

Comparing the two heating methods used, convection and induction heating, showed that induction heating required less time compared to convection heating. Comparing the energy input through the pseudo healing energy parameter showed that both methods achieved similar self-healing ratios for the same pseudo healing energy parameter, with induction heating using slightly less. The parameter is an easy way to compare methods, but did not reproduce the heat distribution within the sample and therefore a better parameter would be the internal energy.

8 Self-healing of macro cracks in different mortar mixtures

The influence of filler and bitumen content on the self-healing of mortar beams was investigated. The filler content varied in mixture 2 to mixture 7 with a constant bitumen amount of 15wt.% and the content of bitumen varied in mixture 2 and mixture 8 to mixture 11. A detailed composition of the mixture is provided in Table 3.3. The bitumen content is related to the amount of flowable bitumen, which could drain into the crack. The filler content influences viscosity and thermal expansion, and is assumed to reduce the self-healing. The flowable material was determined by a gap flow experiment, followed by separation of the components. Measuring the remaining thickness of bitumen films on vertical glass slides gave an estimation of the freely flowable bitumen content in asphalt mortar mixture.

8.1 Thermal behaviour of asphalt mortar beams with varying bitumen or filler content

Since the equilibrium temperature does not depend on any physical material properties [249], the surface temperature reached by convection oven heating to 100 °C was nearly identical for all variations of bitumen T74 and filler content. The variation in the amount of bitumen may affect the temperature increase, as bitumen has a lower heat conductivity than mineral aggregates [3]. The addition of limestone filler to increase the total filler content should not affect the temperature increase of the beams, as the thermal conductivity should only change insignificantly.

A slight trend in the heating exponent was present as the bitumen content was changed. The heating exponent increased with decreasing bitumen content, due to the higher heat conductivity of mineral aggregates, shown in Figure 8.1(a). However, the trend was within the surface temperature variations, shown for repeated measurement of 15wt% bitumen T74 (mixture 2).

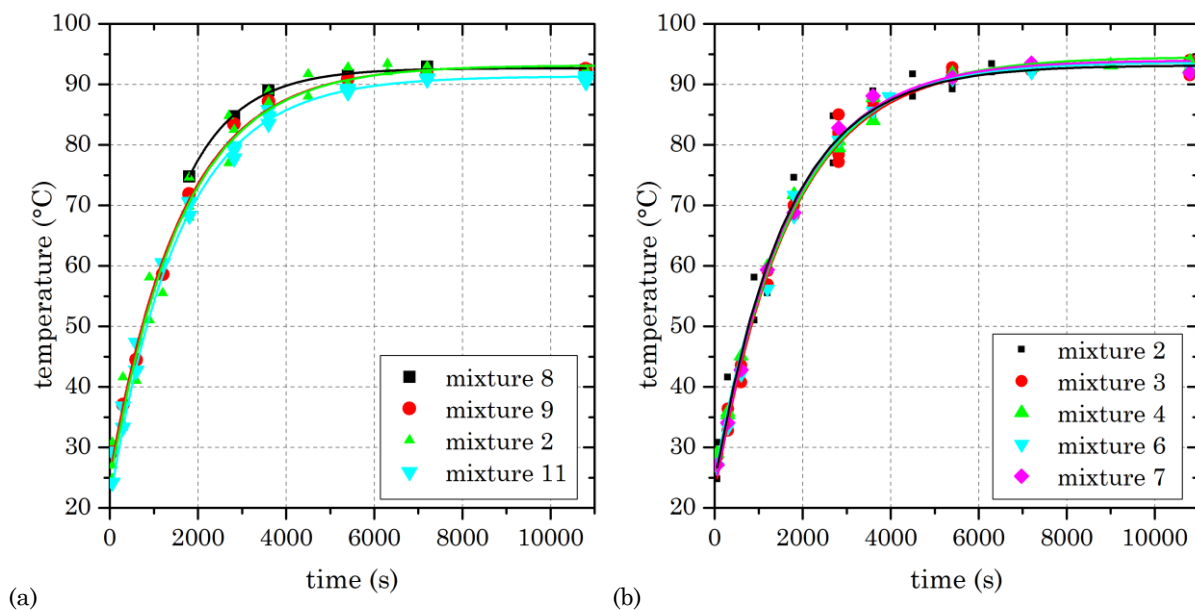


Figure 8.1: The average surface temperature of mortar beams measured by an infrared camera after convection heating at 100 °C for (a) different bitumen content and unchanged filler content of 1.5wt.% and (b) different filler content for beams with 15wt.% bitumen T74. Measurements were fitted by the convection heat transfer function ($T(t) = T_{max} - (T_{max} - T_{air})e^{-k_h t}$).

In contrast to the bitumen content, the heating exponent showed no correlation to the filler content, illustrated by the nearly identical fitting functions in Figure 8.1(b). The equilibrium surface temperatures were unaffected by variations in bitumen or filler content.

8.2 Self-healing of asphalt mortar beams with varying bitumen or filler content

The bitumen content has a clear influence on the self-healing of asphalt. An increase in bitumen content increases the self-healing. Furthermore, the type of filler affects the self-healing and an increase in filler content results in decreasing self-healing [173].

Although a slight trend of a slower surface temperature increase with increasing bitumen content was indicated, the self-healing rate showed an opposite trend, as shown in Figure 8.2(a), indicating that an increased bitumen content results in an easier flow at lower temperatures. Moreover, the steady self-healing ratio state increases with increasing bitumen content, as shown in Figure 8.2(b), although, this trend was not significant (ANOVA, $n_{i=4} \leq 4$, $\alpha \leq 0.05$, single factor). In addition, a higher occurrence of self-healing ratios above 1 was observed as the bitumen content increased. This was due to the higher deformability of the asphalt mortar beams as the amount of bitumen in the beams increased, which caused a change from the original shape of the beams to the form of the silicone mould, which was 1 mm smaller. Thus, the height of the beams slightly increased, resulting in the higher observed self-healing ratios.

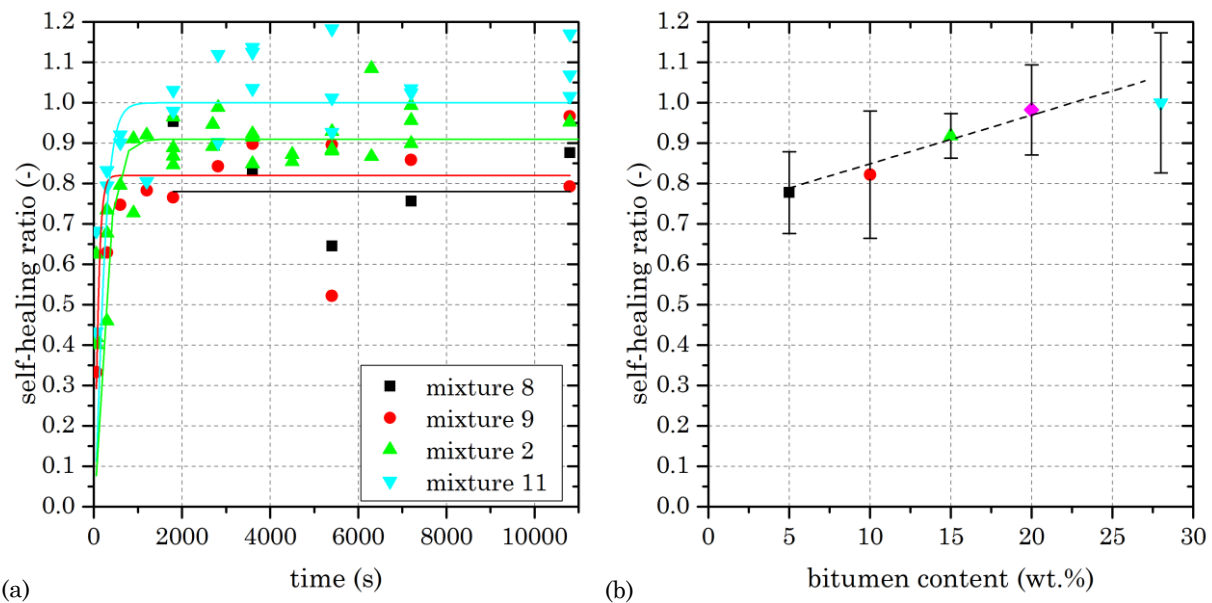


Figure 8.2: (a) Self-healing ratios calculated for different bitumen content of asphalt mortar beams and (b) the average self-healing ratios of the steady self-healing ratio state (symbols according to (a)), fitted by a linear function ($R=0.97$). The error bars represent the standard deviation.

A low amount of filler added to the mixture (1.5wt.% to 13wt.%, mixture 2 to mixture 6) had no significant effect on the self-healing performance of the asphalt mortar beams. Figure 8.3(a) shows that only a filler content of 58wt.% (mixture 7) decreases the self-healing rate, by approximately 81% compared to the other variations in filler content. Despite a decrease in mastic viscosity with increasing filler content, a filler to bitumen ratio below 1 caused no significant change in the self-healing. Furthermore, the average

self-healing ratios for the steady self-healing ratio stage were indistinguishable (ANOVA, $n_{i=5} \leq 4$ and $n_{10wt.\%} = 2$, $\alpha \leq 0.05$, single factor), as shown in Figure 8.3(b). On the one hand, this confirms that the viscosity has no effect on the steady self-healing ratio state and on the other hand, the filler amount does not affect the steady self-healing ratio state either.

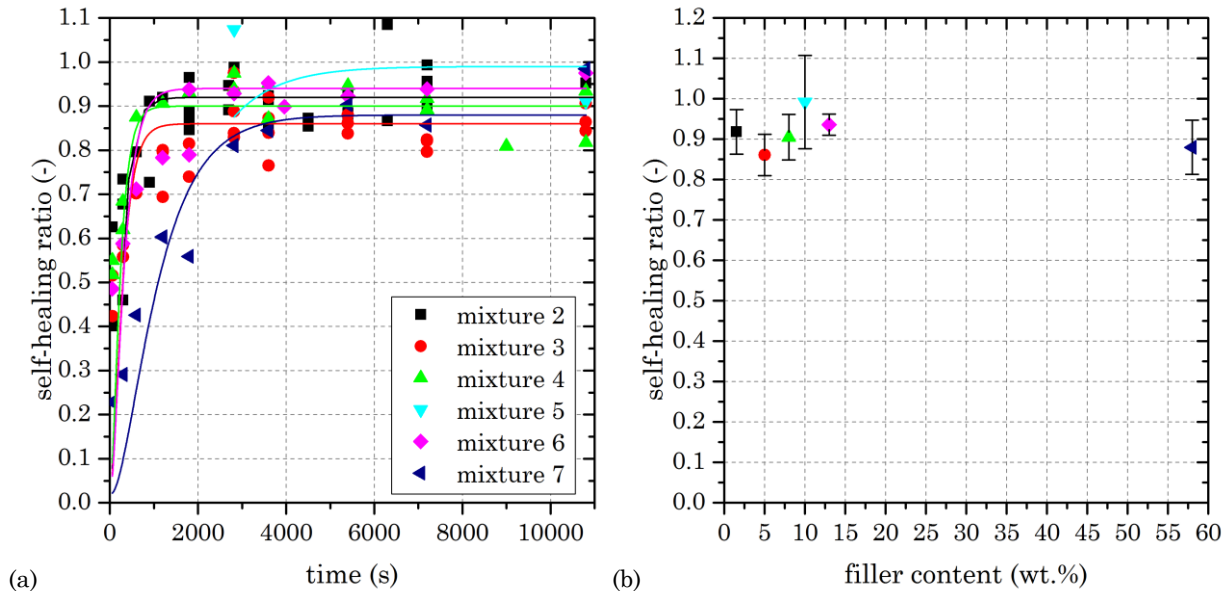


Figure 8.3: (a) Self-healing ratios for different filler contents of asphalt mortar beams and (b) the average self-healing ratios of the steady self-healing ratio state (symbols according to (a)). The error bars represent the standard deviation.

8.3 Flow of mastic and mortar

To determine the material flowing into the crack, a gap of approximately 1 mm between the two halves of the silicone moulds was used to collect material flowing into the gap, as shown in Figure 3.3. The average distance covered by the material was recorded. Furthermore, the collected material was separated into aggregates and bitumen. The aggregates obtained were sieved into three size ranges (below 64 μm , 64 μm to 1 mm and above 1 mm).

The distance covered by the material flowing into the gap depended on the bitumen and filler content of the beams. An amount below 15wt.% bitumen showed no sign of flowing into the gap. A slight deformation of the beams due to the circumferential pressure was noticeable and decreased with decreasing bitumen content. A part of the mixture was found to flow into the gap for beams manufactured with 28wt.% bitumen (mixture 11). The distance covered by the material (flow distance) increased nearly linear with time, as shown in Figure 8.4. This is in accordance with Eq. (4.5), which mathematically describes a horizontal capillary flow.

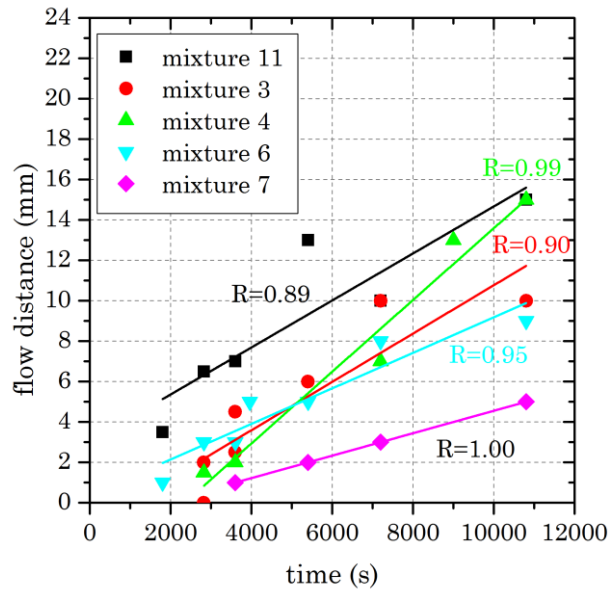


Figure 8.4: Distance covered by material flowing into the gap between the silicone moulds for beams with 28wt.% bitumen (mixture 11) and beams with 15wt.% bitumen and varying filler content from 5wt.% (mixture 3) to 58wt.% (mixture 7).

Figure 8.4 further shows the flow distance for beams with varying filler content, which was linearly increasing with healing duration. An increase to 5wt.% (mixture 3) of filler from the original 1,5wt.% caused drainage of material into the gap. The variation of filler content in the range of 5wt.% to 13wt.% was less distinguishable, which was similar to the steady self-healing ratio states and the self-healing rate for these filler contents. The reduced flow velocity and distance for a 58wt.% filler content (mixture 7) was also seen in the slow initial rise of self-healing ratios and the increased viscosity with a higher filler content of a mastic mixture. Since self-healing occurred in beams with lower bitumen or filler content, only an adequate flow of material into/towards the crack is able to partially close it. If the content of flowable material is increased, due to higher bitumen content or by adding filler, cracks can be closed more easily, depending on the viscosity of the flowable material.

Moreover, the material flowing into the gap, the simulated crack, was separated into bitumen and aggregates, which were further split into three particle size groups. Table 8.1 reveals that the material collected from the gap and analysed was a mixture of bitumen and aggregates. Figure 8.5 shows that with increasing filler content of the mixture, the filler content of the material in the gap increased and the bitumen content decreased. This opposing trend is assumed to be caused by the increased friction force of the flowing material due to the decrease of the density difference between the fluid and bigger particles, allowing it to carry more and bigger aggregate particles into the gap [250, 251]. The decrease of fine particles found in the gap for beams with a filler content of 58wt.% is due to the high amount of filler in the beams, shifting the weight ratio of other aggregate particle size groups.

Table 8.1: Weight ratios of material flowing into the gap between the silicone moulds.

mixture	11 (28wt.% bitumen)	3 (5wt.% filler)	6 (13wt.% filler)	7 (58wt.% filler)
bitumen content [wt.%]	38.2 ±13.3	48.6 ±3.8	41.4 ±3.3	18.5 ±1.5
filler content (<64 µm) [wt.%]	25.4 ±0.9	14.6 ±2.4	19.9 ±4.9	41.0 ±3.8
fine particle content (64 µm to 1 mm) [wt.%]	27.4 ±10.0	29.5 ±3.9	38.7 ±11.0	16.3 ±0.1
particle content >1 mm [wt.%]	0.7 ±0.6	0.1 ±0.1	0.0	1.2 ±0.1

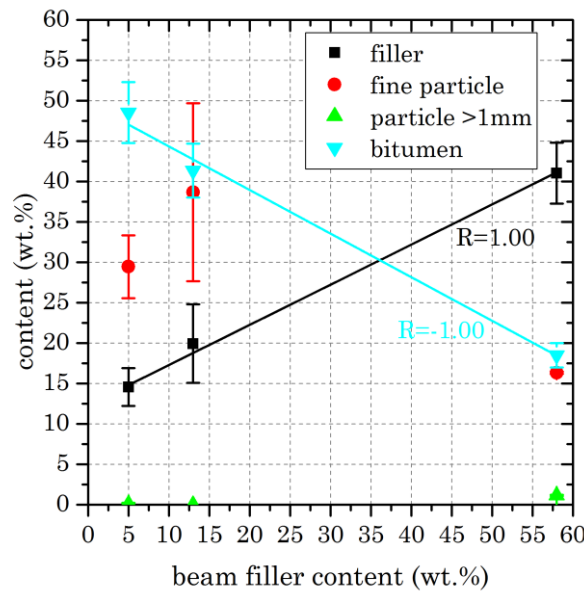


Figure 8.5: Relation between the filler content of the beam, the aggregate size groups and bitumen content extracted from the material flowed into the gap of the silicone moulds. The error bars represent the standard deviation.

A self-drainage experiment was used to quantify the bonded and freely available material (bitumen, mastic or mortar), which remains or has the potential to flow, respectively. The self-drainage of a liquid and the remaining thin thickness are position, time and viscosity dependent [252-254], as shown in Eq. (8.1) [254] and illustrated in Figure 8.6.

$$z = \left(\frac{\eta x}{\Delta \rho g t} \right)^{0.5} \quad (8.1)$$

where z is the film thickness (m), η is the viscosity (Pa·s), x is the vertical downward distance from the beginning of the film (m), $\Delta \rho$ is the density difference between film and the surrounding medium, which is the density if the medium is air (kg m^{-3}), g is the gravitational acceleration (m s^{-2}) and t is the time (s). The exponent of 0.5 is occasionally replaced by a characteristic parameter. As an example, a characteristic parameter of 0.642 to 0.645 has been identified for mineral oil [255].

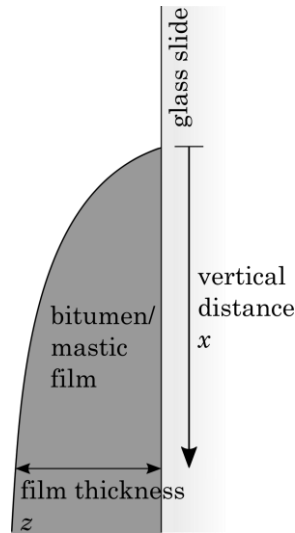


Figure 8.6: Profile of the film on a vertical glass slide and geometric variables of Eq. (8.1).

The remaining bitumen film thicknesses on vertical glass slides at temperatures of 60 °C, 80 °C, 100 °C and 120 °C are shown in Figure 8.7(a). The film thickness reduces with increasing temperature. In Figure 8.7(b) the film thickness is plotted against the square root of the viscosity, showing the significant trend for the measurements at the position of 45 mm (bottom), which is in accordance with Eq. (8.1). The thickness measured at the position of 15 mm (top) was not significantly different, which could be the thickness of the adsorption bitumen on the glass slide. The average thickness of the bitumen film at the top position was 30 μm ±4 μm. The adsorption of bitumen would not be available for any flow movement, as it would be bound to the aggregates of the asphalt.

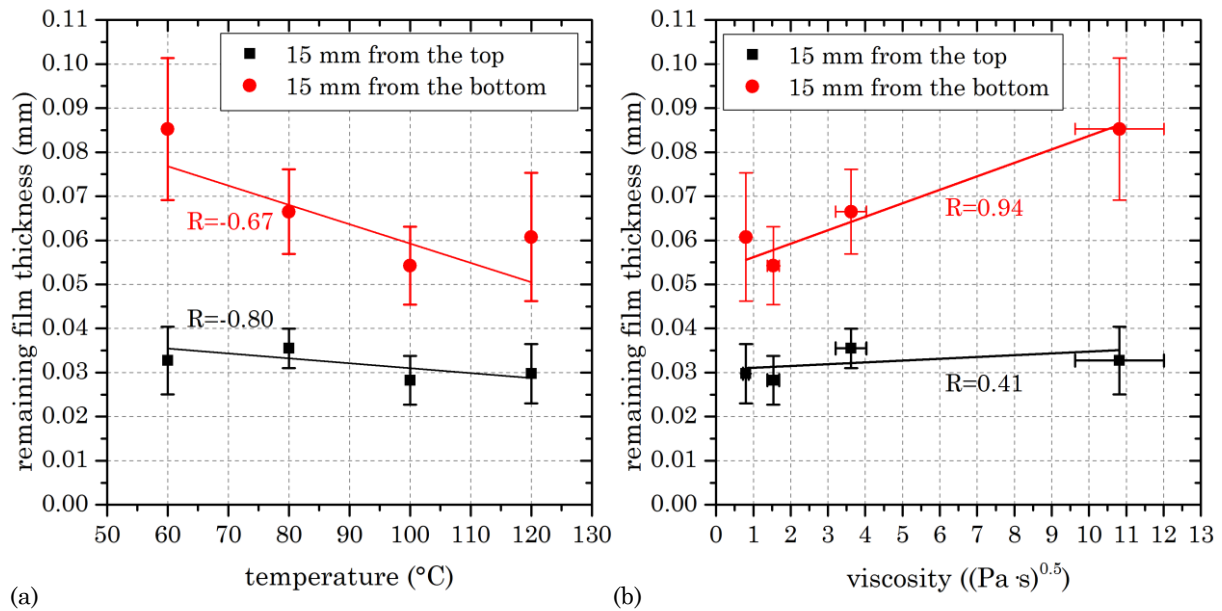


Figure 8.7: (a) Film thickness of bitumen T74 on vertical glass slides measured at two different locations on the slides. Top refers to the position at 15 mm from the start of the film and bottom is the position at 45 mm. The measurements were taken after bitumen drained from the slides in the oven at temperatures of 60 °C, 80 °C, 100 °C and 120 °C. (b) Plotting the film thickness measured against the corresponding bitumen viscosities for the oven temperatures. The error bars represent the standard deviation.

The self-drainage test was further performed with three different mastics (12wt.%, 35wt.% and 50wt.% bitumen). Figure 8.8(a) shows that the film thickness at the position of 15 mm

from the beginning of the film on the glass slide decreased for 35wt.% and 50wt.% from 60 °C to 100 °C. The thickness for 60 °C is in the range of the filler size (<64 μm), except for the 12wt.% mastic mixture. Higher temperatures allowed nearly complete drainage of filler particles, resulting in a film thickness similar to bitumen without filler, shown in Figure 8.7(a). The thickness at 45 mm from the start of the film is shown in Figure 8.8 (b) and had a similar trend as the 15 mm position. At 60 °C a thicker film remained, which covered the glass slide. This bitumen film decreased to a thinner film at temperatures ranging from 80 °C to 120 °C with no further decrease in thickness. Adding filler increased the density difference for gravitational flow, which resulted in a better drainage according to Eq. (8.1) until a film thickness similar to a pure bitumen film remained.

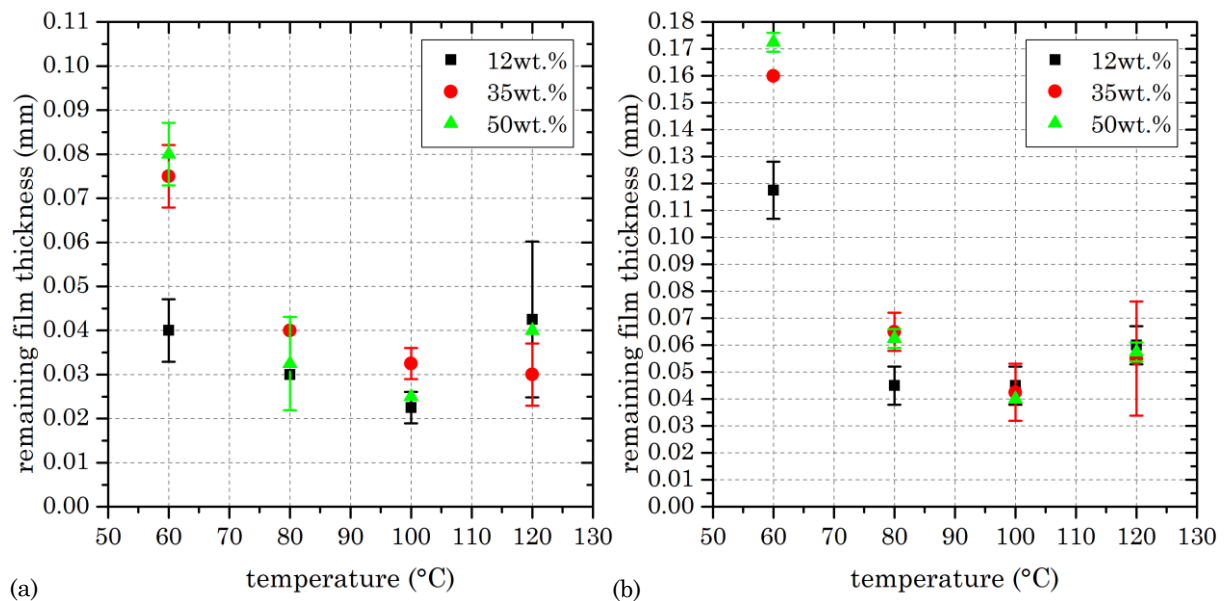


Figure 8.8: Mastic film thickness on glass slides measured (a) 15 mm from the top and (b) 45 mm from the start of the film at temperatures of 60 °C, 80 °C, 100 °C and 120 °C. The error bars represent the standard deviation.

The average remaining mastic film thickness was $43 \mu\text{m} \pm 14 \mu\text{m}$ for temperatures ranging from 80 °C to 120 °C, which is $13 \mu\text{m}$ more compared to the average bitumen film thickness of $30 \mu\text{m} \pm 4 \mu\text{m}$. The mastic film thickness did not decrease with viscosity, as shown in Figure 8.9, which indicates an adsorption film on the surface and the limit of the draining potential. Using the surface area of the aggregates of sand 1, see Table 5.8, and the thickness of the adsorption layer of bitumen/mastic, the minimum amount of bitumen for a free flow to occur was calculated to be approximately 5.4wt.% for the mixture used. Considering mastic with a total filler amount of 5wt.% to 30wt.%, the amount of bitumen for mastic to flow nearly linearly reduces from 5.5wt.% to 2.3wt.%. This shows the strong linkage between bitumen and filler to achieve a flowable material system. Below this threshold of bitumen or mastic content, the material would be unlikely to drain into the crack. This estimation was based on free gravitational driven flow and did not consider capillary effects and a general deformation of the crack surfaces due to compressive pressure or thermal expansion, which affects the drainage of material into cracks.

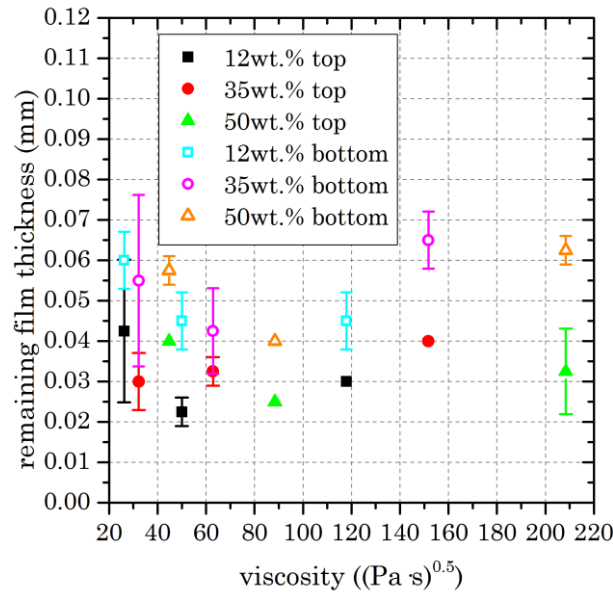


Figure 8.9: Film thickness of mastic mixtures at positions of 15 mm and 45 mm from the upper beginning of the film covering a glass slide at 100 °C plotted against its according viscosity at 100 °C. The error bars represent the standard deviation.

8.4 Summary

The amount of filler did not influence the surface temperature progression and similar self-healing ratios were achieved. The self-healing rate slightly increased with increasing filler content. The surface temperature developed slower for increasing bitumen content, due to the increased thermal conductivity in the beams. The self-healing rate was less affected by the bitumen content. However, the steady self-healing ratio state increased as the bitumen content increased, which was attributed to the change in fracture progression. A higher bitumen content resulted mainly in cohesive cracks, which were more likely to heal. A high bitumen content further deformed during the heating phase, increasing the height of the beam due to the applied circumferential pressure.

The gap flow experiment revealed that an amount of 5wt.% to 15wt.% bitumen did not result in a flow of material into the gap, only at 28wt.% was a flow observed. The addition of filler resulted in material draining into the gap and with increasing filler content the flow rate was reduced. Similar self-healing and flow rates were observed for beams with filler contents of 5wt.% to 13wt.%. The material draining into the gap was proportional in composition to the beam mixture, although with a higher bitumen content.

Gravitational drainage of bitumen and mastic from glass slides resulted in an adhesive film thickness of 30 µm for bitumen and 43 µm for mastic. Using the surface area of aggregates, the amount of bitumen or mastic in a mortar mixture which could freely drain was calculated to be above approximately 5.4wt.% for bitumen. For mastic, the amount of bitumen decreases linearly with increasing filler content.

9 Influence of water on the self-healing mechanism

It is important to understand the concept of self-healing in connection with environmental conditions in order to design roads with an improved intrinsic self-healing asphalt or extrinsic self-healing asphalt with healing systems, which can operate during these conditions. To this purpose, the effect of water on the strength recovery of macro cracks was investigated together with the change of viscosity and surface tension of bitumen in the presence of water.

Water shows an influence on the self-healing of polymers. This is either due to the interaction with the available reversible bonds or due to the change of the polymer properties. This can occur, as water can be absorbed into the molecular structure of the polymer, causing swelling, especially in hydrophilic polymers [256]. However, water can be used to activate the self-healing ability of certain polymers either by adjusting the pH level of water or due to the activation of hydrogen bonds [256, 257]. So far the research on the interaction between bitumen and mineral aggregates in the presence of water has revealed a general negative influence of water on the binder bond strength, due to the affinity of water to aggregates. This affinity depends on the mineral content of the aggregate surface (carbonate and silica) [118, 172, 258]. In addition, bitumen absorbs a small amount of water, which is in general negligible [3], though it affects the properties of bitumen and is responsible for moisture damage [111, 259]. In this connection, it has been theorised that water may influence the polar component of bitumen, which is associated with the long-term self-healing [20]. A minor positive effect on the binder bond strength recovery at an intermediate healing duration has been reported, though before and afterwards a negative effect was observed, with a rapid decrease in the long-term [172].

It is likely that water influences every stage of the self-healing process. For example, during the stage of surface rearrangement water influences the topological changes on the surface of bitumen [122, 260], due to the effect of water on the surface energy and its affinity to certain bitumen components [261]. Furthermore, water can prevent a rapid approach of crack surfaces due to the build-up of excess pore water pressure [262]. The gravitational drainage is diminished due to buoyancy, as the density of water is similar to bitumen. Any water in the crack has to be displaced by asphalt. On the molecular level, absorbed water can diffuse to the former crack interface and accumulate to a water lens [119], opening up the crack again. Moreover, the moisture damage caused by water can cloud the effect of crack self-healing as the material as a whole is weakened [259, 263].

9.1 The effect of water on selected bitumen properties

9.1.1 The effect on bitumen's viscosity

According to Katti, Chaudhri [264], the viscosity of a mixture depends on the molar fractions x_i (-), the viscosity of the individual liquids η_i (Pa·s) and the partial molar volume of the liquids V_i (m³·mol⁻¹). The interrelation is given by the following equation:

$$\ln(\eta_{mixture}V_{mixture}) = x_1 \ln(\eta_1V_1) + x_2 \ln(\eta_2V_2) \quad (9.1)$$

The viscosity of bitumen used was 10.89 Pa·s at 80 °C and the molar volume of bitumen was estimated at 1070 m³·mol⁻¹ [41]. The viscosity of water at 80 °C is 35.37·10⁻⁵ Pa·s with a molar volume of 18.54 m³·mol⁻¹. Therefore, according to Eq. (9.1), at 80 °C the viscosity of the mixture of bitumen and water, assuming a water absorption of 0.1% for bitumen and a linear change in molar volume with water uptake, is 10.74 Pa·s. The theoretical value is about 1.3% lower than the viscosity of bitumen at this temperature. To confirm this result, the viscosity of bitumen was measured with and without deionised water treatment. Figure 9.1 shows the experimental results. No significant differences (t-test, n_b=4, n_{b+w}=3, α≤0.05, two-tailed) between the viscosity of bitumen and bitumen treated with deionised water was found for temperatures ranging from 70 °C to 110 °C. Only at 60 °C was a significant difference observed. The slightly higher viscosity for bitumen treated with deionised water may derive from the neglect of the interaction of molecules [265], ageing effects or microstructural alterations [260] during the storage of the bitumen films in deionised water.

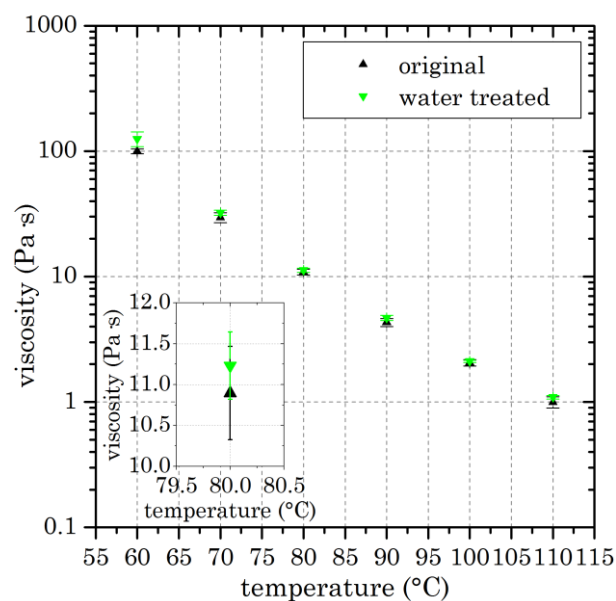


Figure 9.1: Viscosity of bitumen S70, untreated (original) and immersed in deionised water for 10 days (water treated), for the temperature range of 60 °C to 110 °C. The detail window shows the viscosity at 80 °C to illustrate the close similarities between original and water treated bitumen. Error bars represent the standard deviation of the viscosity.

As the viscosity did not significantly change, the self-healing should not be affected according to Eq. (4.13) respectively Eq. (4.18).

9.1.2 The effect on bitumen's surface tension

The surface tension of bitumen is dominated by the dispersive or Lifshitz-van der Waals component [78], resulting from the interactions of non-polar molecules or non-polar parts of molecules [41]. The other surface tension component is the polar or Lewis acid-base component, which is not present in certain materials and derives mainly from polar functionalities in bitumen [139]. The total surface tension of the bitumen used was

calculated from contact angle measurements to be 24.68 mJ m^{-2} , with a dispersive component of 24.59 mJ m^{-2} and a polar component of 0.08 mJ m^{-2} . Due to the treatment with deionised water for 10 days, an increase in the polar component to 21.51 mJ m^{-2} was observed (see Figure 9.2). The dispersive component remained nearly unchanged and thus, the total surface tension increased to 43.01 mJ m^{-2} . Three possible mechanisms may be responsible for this change in surface tension due to water exposure. The first mechanism is the diffusion of water into bitumen, which results in the surface tension of a mixture. However, the amount of water absorbed by bitumen is negligible [3] and the interaction of water molecules and bitumen molecules has not yet been quantified. The second mechanism is the generation of a double layer [266]. Due to the polar nature of water, the molecules of bitumen rearrange at the interface of the liquids to diminish the potential difference. Hence, a higher concentration of polar functional groups accumulates at the bitumen surface, increasing the polar component of the surface tension. The third mechanism is the change in surface morphology due to water exposure [122, 260], which is closely related to the first and second mechanism, as water influences the molecular interactions between bitumen molecules. Furthermore, a microscopic change in the surface morphology could affect the macroscopic quantity surface tension [139]. It is highly likely that a combination of the three mechanisms described is responsible for the change in surface tension observed. The total surface tension of the water treated bitumen after one day of drying was 34.43 mJ m^{-2} , with a dispersive component of 34.42 mJ m^{-2} and a polar component of 0.01 mJ m^{-2} . This result would imply a reverse mechanism during the drying process, which increases the dispersive component at the surface, as shown in Figure 9.2.

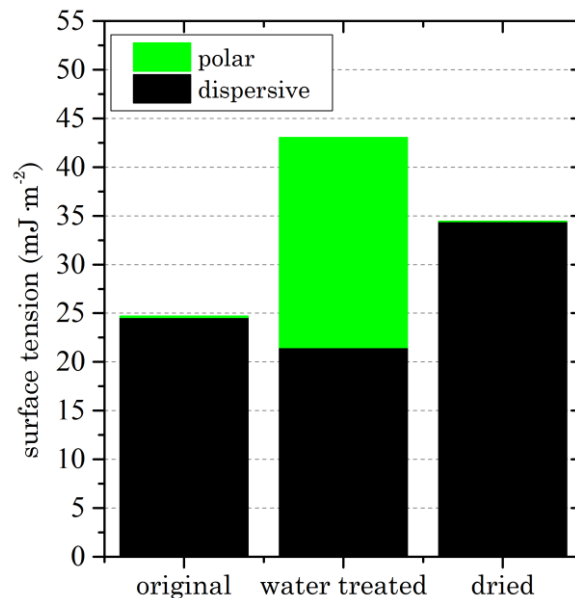


Figure 9.2: Comparison of the surface tension from bitumen S70 (original), bitumen immersed in water for 10 days (water treated) and water treated bitumen after drying for 1 day (dried).

Fourier transformed infrared spectroscopy confirmed the presence of water in the surface layer of bitumen, which was immersed for 10 days in deionised water. The spectra obtained of water treated bitumen after 0 min drying, 45 min drying and 1 day drying are shown in Figure 9.3, including the original bitumen, which was untreated, and deionised water. The water spectrum has two distinct bands. The broad band centred at

approximately 3300 cm^{-1} is related to the OH stretch vibration of water and the band at 1635 cm^{-1} is related to the OH bending vibration [267]. Figure 9.3(a) shows the OH stretching band. A definite change in the bitumen spectrum was observed, as the absorption intensity of the band increased from the original to the water treated spectrum. This confirms the presence of water in the surface layer of bitumen. During drying, the band intensity decreased due to the diffusion and evaporation of water from the surface. The spectrum approaches the original bitumen spectrum. Figure 9.3(b) shows the OH bending band of water, which is shifted to higher wavenumbers (1645 cm^{-1}) due to the interactions with bitumen molecules [268]. This band was present as well for the original bitumen, which is due to humidity. Furthermore, the band at 1600 cm^{-1} is associated with the CC ring stretching vibration of aromatics and conjugated alkenes [269], which was unaffected by water. The band at 1700 cm^{-1} is related to the CO stretching vibration of carboxyl groups and is an indicator for ageing [8]. The increase in the intensity of the carboxyl band could be due to ageing during the water immersion, which would explain the slight increase in viscosity observed. However, the band decreases after 1 day of drying, supporting the hypothesis of accumulation of polar functional groups at the bitumen-water interface and the decrease of the polar component of the surface tension during drying. Hence, the development of a polar layer at the interface is likely, as water soluble bitumen compounds have been identified in previous research [1, 43] and a minor change on the fluorescence spectra of bitumen due to water immersion has been reported [43].

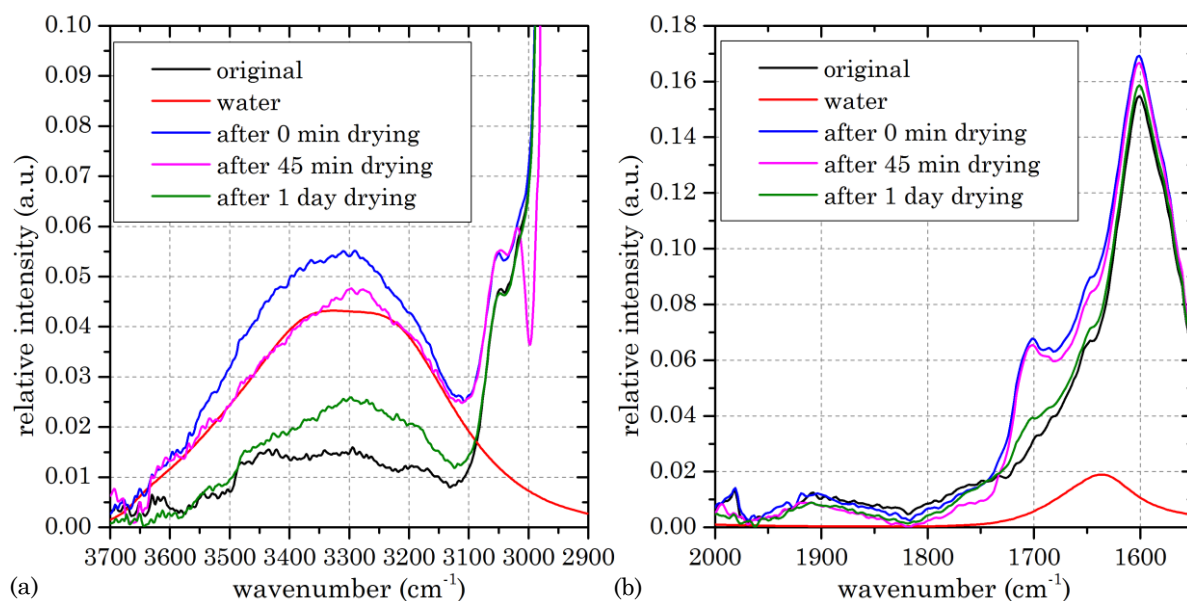


Figure 9.3: Infrared spectra of bitumen S70 (original), deionised water (water) and bitumen immersed in deionised water for 10 days after three different drying periods (0 min, 45 min and 1 day). (a) Region of the OH stretching band at approximately 3300 cm^{-1} , including the CH stretching vibration of cyclic alkenes with internal double bond at 3050 cm^{-1} and the CH stretching vibration of vinylene groups at 3018 cm^{-1} . (b) Region of the OH bending band at 1645 cm^{-1} , including the aromatic ring stretching vibration at 1600 cm^{-1} and the carboxyl group stretching vibration at 1700 cm^{-1} .

The change in surface tension of bitumen would affect the self-healing, as the short-term self-healing rate has been found to be proportional to the dispersive component and the long-term self-healing has been found to be proportional to the polar component [180]. Therefore, the short-term self-healing might be unaffected by water, as the dispersive

component changes less in comparison to the polar component, which increases due to water exposure and decreases due to drying. The long-term self-healing would benefit from the water exposure, though moisture damage might attenuate positive effects on the self-healing.

9.2 The effect of water on the gravitational flow

To investigate the flow behaviour of bitumen and mortar under different surrounding conditions (air or deionised water), the change of a triangular shaped cut-out in a Hele-Shaw cell was monitored.

In the case of air and bitumen, the cut-out changed due to the gravity driven flow of bitumen from the side to adjust for the different liquid levels. This would result in a horizontal level in the cell after infinite time. Hence, the depth of the cut-out reduces, shown in Figure 9.4, and the tip angle changes accordingly, shown in Figure 9.5. In the case of water and bitumen, no movement of the tip was recorded as shown in Figure 9.4, due to the similar densities of water and bitumen, which results in a negligible density difference for the gravitationally driven flow. A change in the shape was observed and is due to the minimisation of free surface energy at the interface of water and bitumen, resulting in a more U-form shape of the cut-out. The change in the angle of the cut-out tip for both fluids filling the cut-out, shown in Figure 9.5, showed that the bitumen level is approaching a horizontal level for air, as the tip angle increased continuously over the period of 5 hours observation. Longer observation of the bitumen flow in air revealed that a complete horizontal level was not achieved, which was attributed to the surface tension between bitumen and glass, the high viscosity of bitumen and the decreasing height difference which drives the flow process. In the case of water, the tip angle increased until approximately 91° was reached after approximately 2 hours and then remained constant, as a result of the surface area minimisation.

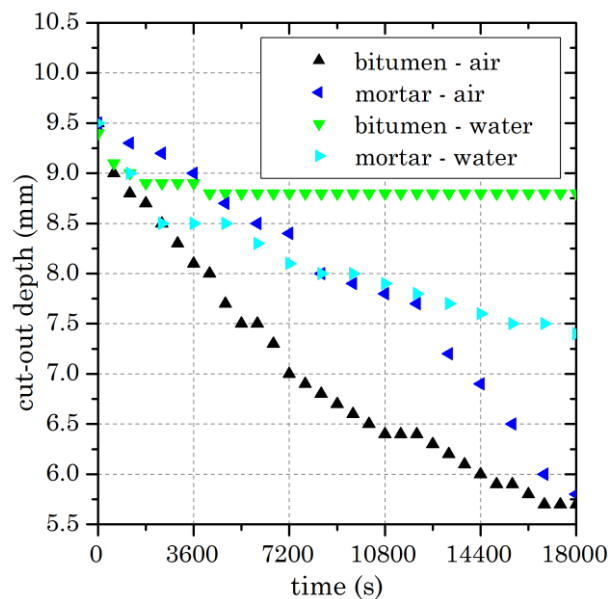


Figure 9.4: The filling of the triangular cut-out in the Hele-Shaw cell resulted in a decrease of the cut-out depth, shown on examples of bitumen and mortar (50wt.% bitumen) with similar starting depth for medium air and water filling the cut-out and the surrounding.

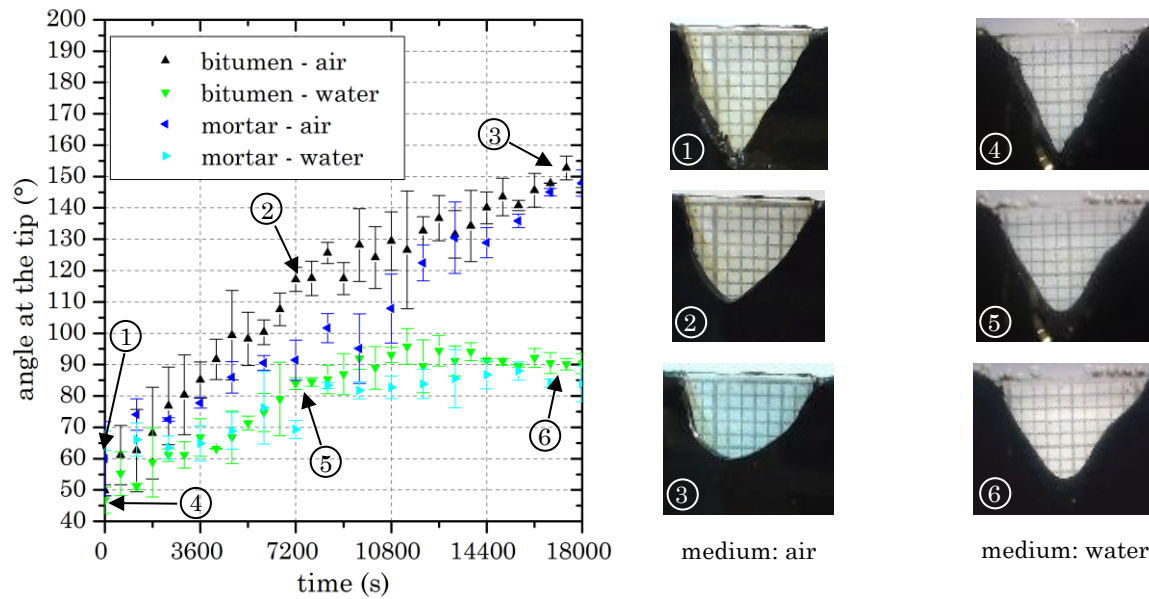


Figure 9.5: The change of angle at the tip of the cut-out for the Hele-Shaw cell experiment with bitumen and mortar (50wt.% bitumen) with time. Filling medium was either air or water. The error bars represent the standard deviation of the angles measured. The change of the triangular cut-out for bitumen is shown for three different durations.

As a consequence of water filling the triangular cut-out, bitumen does not flow into it, as the driving density difference for gravitational flow is negligible. This would imply for the self-healing of a macro crack filled with water that the self-healing rate is either reduced or zero, which is in agreement with Eq. (4.13) and Eq. (4.18), as the density difference is a driving force for capillary and gravitational flow. Furthermore, water may change the crack surface morphology, as the free surface energy is minimised.

Moreover, the effect of deionised water on the gravitational flow was investigated for two mastic mixtures. The first mixture had 50wt.% bitumen and the second mixture had 15wt.% bitumen. Adding 50wt.% of sand 2 to bitumen S70, had two implications. The first implication was an increased viscosity [84, 242] resulting in a reduced flow. The second implication was the increased density difference between mortar mixture and water. Thus, a flow was observed for the case of water and mortar which decreased the depth of the cut-out, as shown in Figure 9.4. Despite a flow occurring, the change in tip angle was similar to the change observed for bitumen for water and air, shown in Figure 9.5. The approximation towards a 91° tip angle suggests that a complete horizontal levelling for the mortar mixture under water would not happen and that the free surface energy minimisation simultaneously affects the flow, which may result in a partly filled macro crack for self-healing. A further increase in the amount of sand 2 to the ratio of the main beam mixture (15wt.% bitumen) resulted in no visually observable movement of the mortar mixture. Several factors are responsible for this development: a drastic increase of viscosity, friction between aggregates or between aggregates and the glass slides and probably the development of a grain skeleton, stopping the flow at the macroscale.

Increasing the density difference between bitumen and the filling medium of a macro crack, for example adding a low proportion of aggregates or filler, would enhance the flow of bitumen into the crack, though this has to be balanced against the increasing viscosity. For a low proportion of aggregate content added to bitumen, self-healing under water may

be possible. However, an increase in the aggregate content could stop the flow at a macro level.

9.3 Water evaporation from asphalt mortar beams

The evaporation of water was monitored to determine the drying duration and the remaining water inside of water conditioned beams after healing in air. In addition to the gravimetric analysis, computed tomography scans of a smaller cylindrical beam were analysed on the evaporation of water within pores and a macro crack.

The manufactured mortar beams had an air void fraction of 0.22 ± 0.01 . A part of the air voids was filled with water during the immersion in deionised water for 10 days. The amount of absorbed water into the beam and thus, filling its void structure was $5.24 \text{ g} \pm 0.49 \text{ g}$ per beam, resulting in approximately 25% to 32% of water filled voids. During the observation of 24 hours, the water content in the beams decreased nearly exponentially, as shown in Figure 9.6 for the investigated temperature range of 5 °C to 40 °C. Due to the removal of excess water at the surface, only stage two drying (due to diffusion and capillary transport) was recorded for the beams. The decrease in weight due to evaporation increased with increasing temperature. After 24 hours, almost all water was evaporated for beams dried at 40 °C. Water evaporation at 20 °C, 12 °C and 5 °C resulted in moisture remaining in the beams. The water content for 20 °C, 12 °C and 5 °C further decreased over the time of 48 hours.

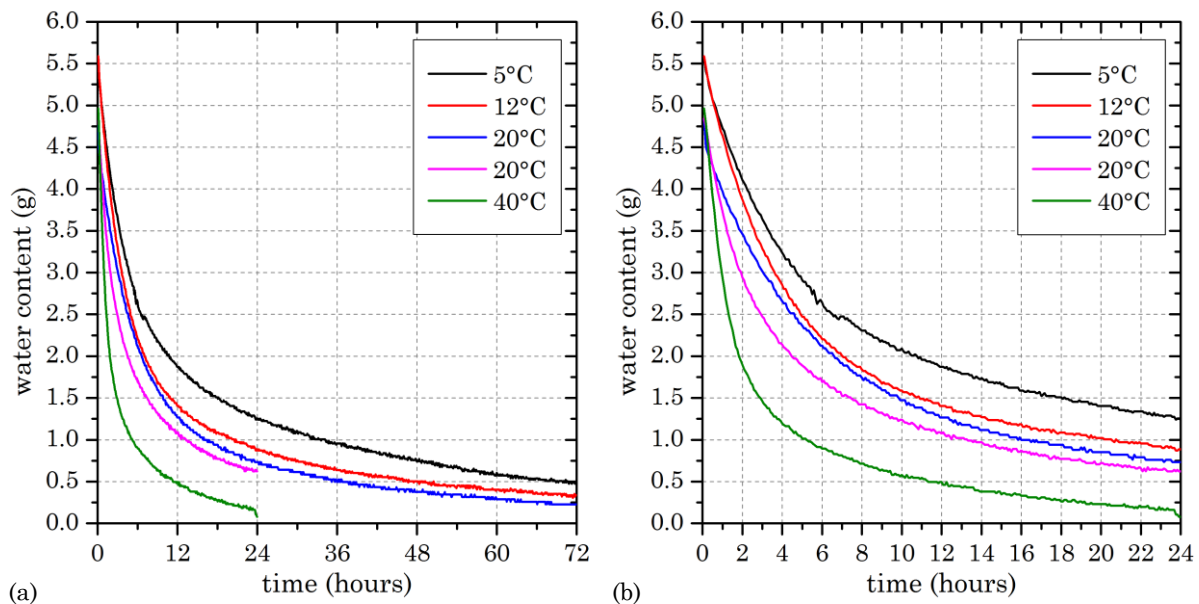


Figure 9.6: The decrease of average water content in asphalt mortar beams due to evaporation at 5 °C, 12 °C, 20 °C and 40 °C, (a) shown for 3 days and (b) detailed shown for the first 24 hours.

The CT-scan revealed that due to breaking at low temperature, material was lost in the crack interface, occasionally resulting in bigger air voids along the crack. Furthermore, most air voids of the CT samples were filled with deionised water at the beginning of the drying/self-healing phase. This may be due to the reduced size of the sample, allowing a full saturation after 10 days immersing in deionised water. After 3 hours of drying most water (less than 5wt.%) was evaporated from the CT sample. The faster evaporation was assumed to be due to the shorter diffusion length to the surface. Bigger air voids including

the crack, dried faster, which is in agreement with water disappearing first in bigger pores, more gradually in smaller pores in porous media [270, 271]. The remaining water was likely to be trapped in smaller pores and to be in equilibrium with the atmospheric humidity. A visual confirmation was obtained after breaking the healed, dried and frozen beams, as no traces of ice were found on the crack surface. Figure 9.7 shows that water nearly uniformly evaporated from the sample. The cylindrical mortar samples for the CT scan, which were healed without water saturation, showed no sign of healing. The crack remained visible after 24 hours and no change in air void content was observed. This may be due to a size effect, as the cylindrical beam was smaller compared to the beams, which were mechanically tested.

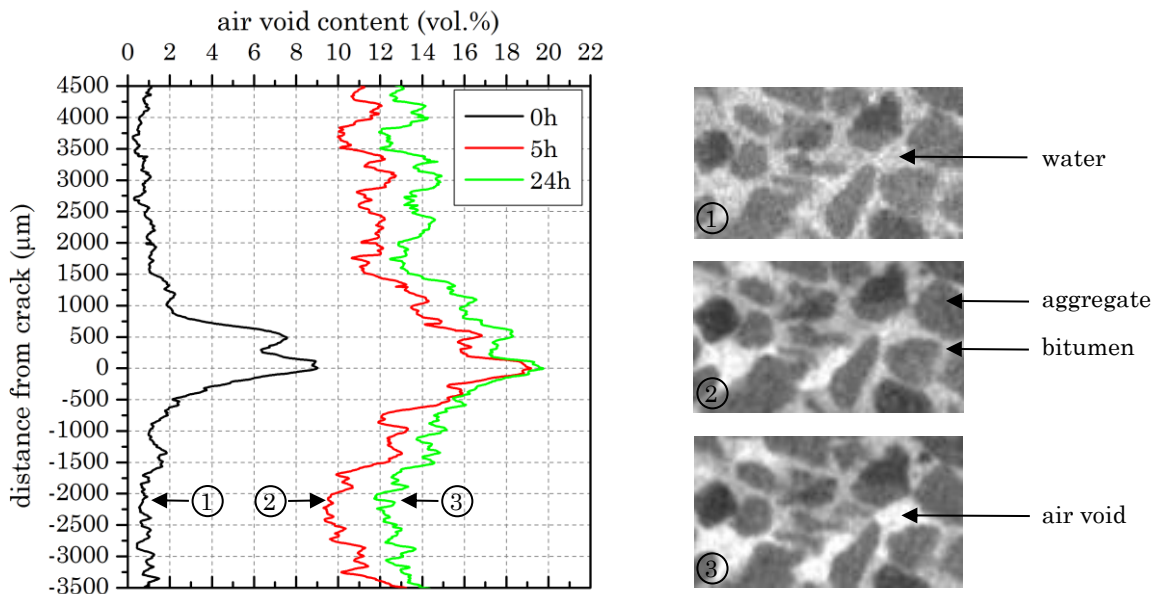


Figure 9.7: Calculated air void content for each slide generated from the CT scans of a deionised water saturated cylindrical beam. The maximum air void content, at the centre of the crack, was defined as the point of origin. The images, related to drying durations of 0 hours, 5 hours and 24 hours, show the appearance of air voids as water evaporates from the sample.

9.4 Self-healing of asphalt mortar beams

Assembling the beam halves at 20 °C resulted in an adhesive strength gain of 20.8 N \pm 6.3 N. As beams were assembled after immersing in deionised water for 10 min, the adhesive strength gain dropped significantly. The measured strength was 8.8 N \pm 6.8 N. This may be due to the reduction of initial contact area by the excess water pore pressure, which builds up during the assembling and prevents the approach of the crack surfaces. Moreover, residual adhesive strength after wetting indicates that the crack surface was incompletely wetted by deionised water, due to the hydrophobic nature of bitumen.

In addition to the three conditions with drying phase, the self-healing was also measured for beams which had been assembled in deionised water and allowed to self-heal immersed in deionised water, without a 24 h drying phase at 20 °C before testing under three-point breaking. The self-healing conditions were 20 °C and 40 °C for 1 day, 3 days 7 days and 10 days. The forces obtained were for all self-healing conditions 0 N. This drop from an initial adhesive strength gain to no load bearing connection was attributed to the changed surface

tension and free surface energy minimisation. Due to the higher polar component, water would diffuse along the previous fracture and accumulate there, and consequently separating the initial contact points. Moreover, as seen in Figure 9.4, water reduces the gravitational flow and the interface between water and bitumen changes due to free surface energy minimisation, as indicated in Figure 9.5, which could lead to separation of contact points and further separation of crack surfaces. From this it is evident that water within a macro crack prevents self-healing.

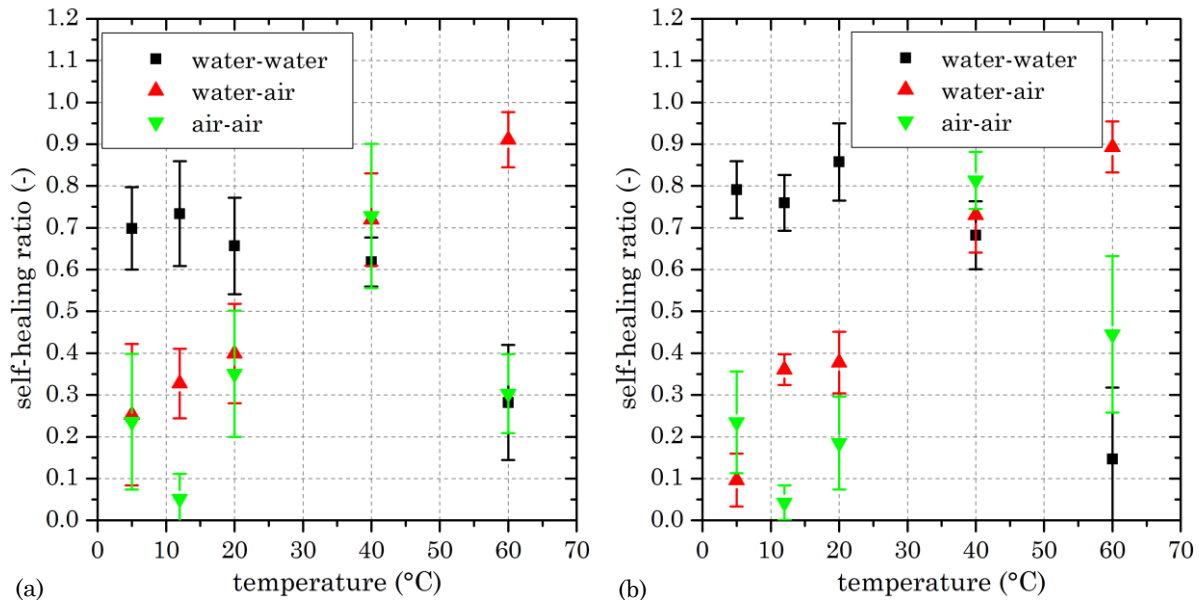


Figure 9.8: Self-healing ratios calculated for the three conditions (water-water, water-air and air-air) for the temperature 5 °C, 12 °C, 20 °C, 40 °C and 60 °C after (a) 3 days and (b) 10 days. The error bars represent the standard deviation of the self-healing ratios calculated.

In the case of water-water (conditioned in deionised water and allowed to self-heal in deionised water, see Figure 3.8), no significant differences in the self-healing ratios for temperatures of 5 °C, 12 °C, 20 °C and 40 °C for any self-healing duration in deionised water were found, as shown for two durations in Figure 9.8. The average self-healing ratios for these temperatures and durations were between 0.50 and 0.95. Significantly lower self-healing ratios were found for 60 °C. The decrease in self-healing ratios with increasing immersion time for beams immersed in deionised water at 60 °C was due to the phenomenon of stripping. Stripping is the diffusion of water to the interface between aggregate and bitumen and separates both phases by forming a water layer between them. This phenomenon occurs faster at higher temperatures [111, 121]. Furthermore, the average self-healing ratio decreased with increasing time immersed in deionised water, although the trend was not significant. As was explained in the previous paragraph, water prevents the self-healing of asphalt mortar beams; for this reason, these results are attributed to the self-healing occurring during the drying phase, as water evaporates from the beams.

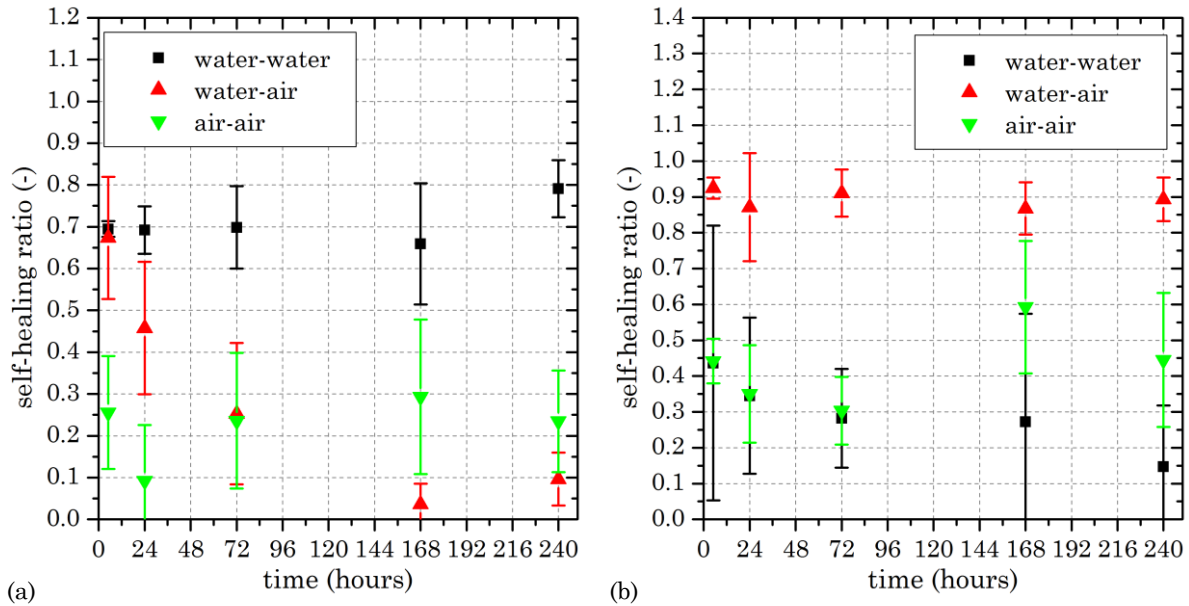


Figure 9.9: Self-healing ratios calculated for the three conditions (water-water, water-air and air-air) at different healing durations for (a) 5 °C and (b) 60 °C. The error bars represent the standard deviation of the self-healing ratios calculated.

Asphalt mortar beams healed under the condition of air-air (conditioned in air and allowed to self-heal in air) did not show a clear trend or order with temperature and the self-healing ratios seemed to be constant with time for each temperature, as evident in Figure 9.9. The lower self-healing ratios for 5 °C to 20 °C, as shown in Figure 9.8, may be due to the temperature threshold for self-healing [156]. The difference between 40 °C and 60 °C, which was significant, was attributed to the decreased structural stability at 60 °C, which resulted in slight deformation of the beams during the removal from the oven. Hence, the crack could have been partly reopened.

In the case of water-air (conditioned in deionise water and allowed to self-heal in air, see Figure 3.8), the self-healing ratio increased with increasing temperature, as shown in Figure 9.8. After 5 hours of self-healing in air, beams at 60 °C showed the highest self-healing ratio, which was on average 0.89. The difference in self-healing ratios between 40 °C and 60 °C was significant for all self-healing durations. In Figure 9.9(a) a decrease in the self-healing ratio is shown. In general it was observed that the self-healing ratio started between 0.65 and 0.75 and decreased gradually with time for the beams healed at 20 °C, 12 °C and 5 °C. The self-healing ratio stabilised after approximately 3 days for 20 °C and 12 °C and after 7 days for 5 °C. The decrease in self-healing ratios for each temperature and the differences between temperatures were significant.

Moreover, Figure 9.10 shows the relation between the decreasing self-healing ratios for the case of water-air and the amount of water in the mortar beams for the same period of healing, obtained from Figure 9.6. A higher water content at the end of the healing duration resulted in a higher self-healing ratio. It was hypothesised that the internal water pressure might be responsible for this by increasing the additional pressure onto the crack, which is part of Eq. (4.13) and Eq. (4.18). A low water content at the beginning of the drying step mainly resulted in an approach to similar self-healing ratios as observed for beams self-healed under air-air condition, shown in Figure 9.9(a).

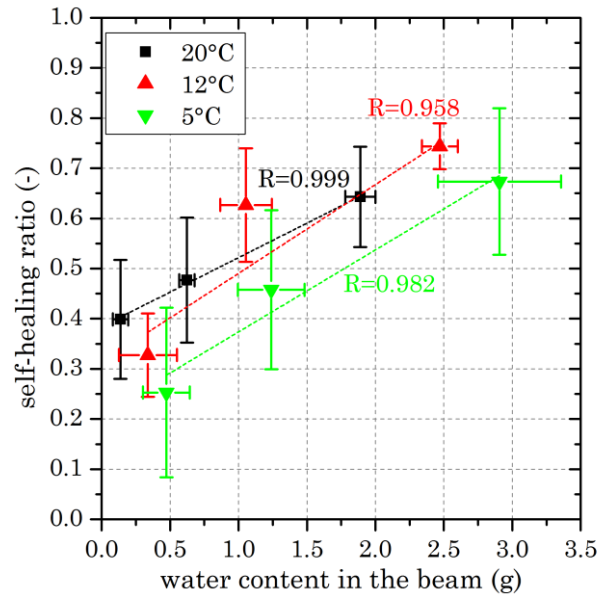


Figure 9.10: Correlation between the remaining amount of water within the beams and the self-healing ratio for water-air for temperatures of 5 °C, 12 °C and 20 °C. The error bars represent the standard deviation of the self-healing ratios calculated respectively the water content measured.

Mechanically testing the beams used to obtain the water evaporation curves in Figure 9.6, revealed that the self-healing ratios for beams immersed in deionised water and dried increased with increasing temperature. The self-healing ratios obtained, which are shown in Figure 9.11, are in the range of the self-healing ratios for the water-air case. Beams healed without deionised water showed only initial self-healing ratio for 5 °C and 12 °C after 3 days, confirming a possible temperature threshold for self-healing between 12 °C and 20 °C. This was followed by increasing self-healing ratios with increasing temperature. At 60 °C a significantly higher self-healing ratio was calculated compared to the air-air case. This may be attributed to the different underlayment used (rigid underlayment) to remove the beams from the oven. Comparing both methods in Figure 9.11 revealed that the additional water pressure existing during drying enhances the self-healing of asphalt mortar beams for temperatures below 60 °C, initiates self-healing below the temperature threshold and reduces the variability of results. The reduction of variability due to pressure was already identified in section 6.1.3.

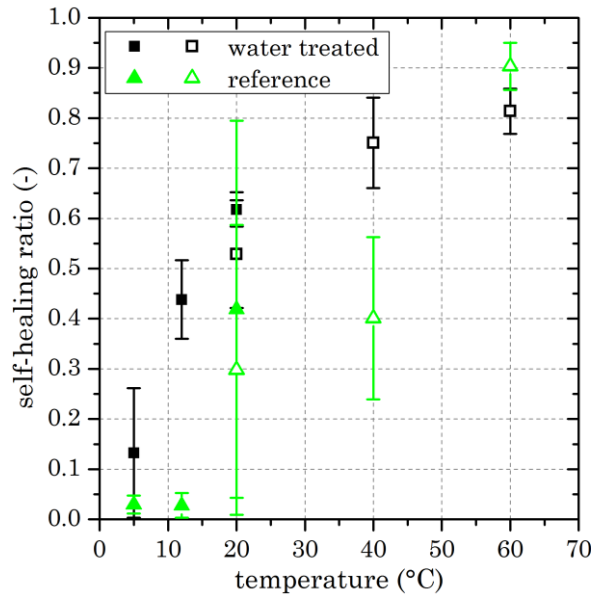


Figure 9.11: Due to the immersion in deionised water, dried beams (water treated) showed a better self-healing behaviour compared to innately dried beams (reference). The duration of drying/healing was 1 day (■ and ▲) and 3 days (□ and △). The error bars represent the standard deviation of the self-healing ratios calculated.

In order to validate that the increase of hydrostatic pressure by water retained in the pores of the asphalt mortar beam is the main cause for the improved self-healing, the effect of uniform pressure on the self-healing was investigated. Therefore a uniform air pressure was applied during the self-healing duration of one hour. Figure 9.12 shows that the additional pressure had no significant influence on the self-healing ratios. As the pressure was applied as gas pressure, the pressure resulting on the crack surface was zero, thus, having no contribution to the self-healing.

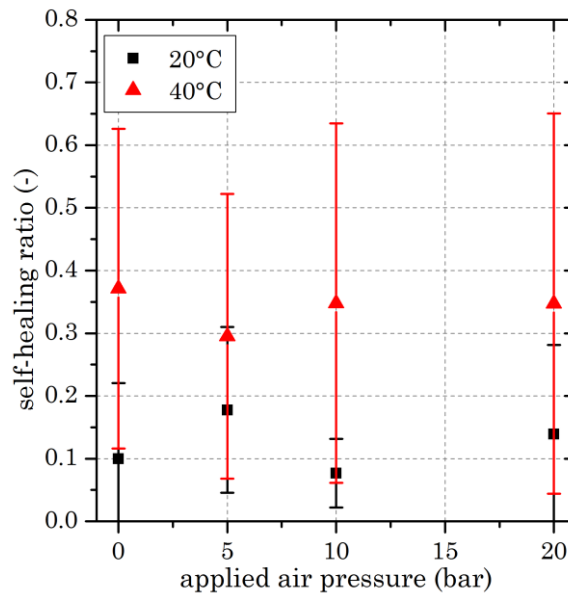


Figure 9.12: Self-healing ratios of beams heated at 20 °C and 40 °C for one hour with additional air pressure applied, ranging from 0 to 20 bar. The error bars represent the standard deviation of the self-healing ratios calculated.

9.5 Summary

Water had no influence on the viscosity of bitumen, although it increased the polar component of the surface tension, which was reversible due to drying.

The flow of bitumen inside a Hele-Shaw cell was driven by gravity. As water filled the triangular cut-out, the vertical movement of bitumen was prohibited, due to the similar densities between water and bitumen and only a shape change of the cut-out occurred, due to the minimisation of surface energy. No flow for the mortar mixture was observed at the macro scale, mainly due to the wedge of aggregates between the two glass slides.

Water affected the self-healing of asphalt mortar beams. In the presence of water, the initial self-healing ratio was reduced, which was attributed to the excess pore water pressure, reducing the amount of initial contact area. Furthermore, beams did not heal in deionised water, only during the drying step did self-healing occur. This was due to the remaining pore water, applying pressure on the material in the direction of the crack. Hence, this closed the crack, for beams healed at a temperature below 20 °C, allowing a higher water content to be present at the beginning of the drying phase at 20 °C, which lowered the viscosity enough to allow closing of the crack.

10 Summary and conclusion

Understanding the recovery phenomenon in bituminous materials is important for a precise prediction of its contribution to the lifetime of the material. Self-healing alone is not the solution to an infinite damage-recovery cycle because of the huge uncertainties during the process. Uncertainties influencing the self-healing of asphalt include the damage level and the point in time when self-healing occurs, the contribution of self-healing during the damage periods, type of crack (adhesive or cohesive), ageing stage and environmental conditions, such as temperature, humidity and degree of foreign substances filling the crack. To overcome specific uncertainties, material additives were designed to manually or autonomously trigger or enhance the self-healing.

10.1 Summary

The material properties of six bitumen types, two different sands, one limestone filler and metal grit were investigated to later correlate these properties with self-healing properties of asphalt mortar beams.

Based on the conventional testing methods, the six bitumen types investigated were grouped into two clusters, namely hard and soft bitumen. The grouping was partly reflected in the results of viscosity, density measurements and the transition temperature. The fractional distributions for the bitumen were similar, resulting in similar rheological, physical and chemical properties. Furthermore, the fractional distribution is sensitive to the analytical methods used to determine the fractional content. However, a significant linear correlation between the two methods used in this study was found. A considerable indication of the contribution of ageing on the self-healing was reflected in a change of order (ordered by viscosity) due to ageing, which was partly present in the results for self-healing.

Considering the self-healing in asphalt as a capillary like flow process, surface tension and the contact angle influence the viscous flow. The surface tension of bitumen is temperature dependent and sensitive to the method used. The sessile droplet method resulted in higher values for the surface tension compared to the Wilhelmy plate method and neither methods were related to the surface tension calculated from the equilibrium height of bitumen in a capillary. The flow of bitumen inside a glass capillary further revealed that the dynamic contact angle is similar for the three bitumens investigated, N83, P47 and T74, for a normalised capillary height, showing the dependency of the contact angle on a normalised velocity. Moreover, since the dynamic contact angles were nearly identical, the self-healing, assumed to be similar to the capillary flow, would be similar and only dependent on the viscosity of bitumen and the surface tension. Adding filler to bitumen resulted in a reduced capillary velocity due to increased viscosity and a reduced equilibrium capillary height due to the increase in density. Fourier transformed infrared spectroscopy showed that during the unconfined capillary experiment, ageing occurred. The relative intensity of the ketone and carbonyl band increased with increasing duration and temperature, respectively. The band was more intense for the surface compared to the bulk. This affected the flow of bitumen, as the viscosity would change during the experiment, but had less effect on the surface tension, as a linear relationship with temperature was confirmed. A confined capillary experiment revealed the considerable

contribution of pressure to the flow of bitumen inside a capillary. Expanding bitumen in the confined volume due temperature increase resulted in a fast rise of bitumen inside the capillary. The dynamic contact angle increased to values greater than 90° and the equilibrium capillary height was above the capillary length of 10 cm.

The methyl methylene hydrogen to carbon ratio was calculated from the infrared spectra and was similar for the bitumens investigated. This is in line with the similar fractional distributions. In addition, the ratio was less affected by ageing. Hence, it is not found to be a suitable parameter to predict the self-healing of bitumen.

The correlation of all bitumen properties determined revealed significant linear correlations between the methyl methylene hydrogen to carbon ratio and the viscosity measured by the dynamic shear rheometer and the density of bitumen. Furthermore, the surface tension measured by the Wilhelmy plate method correlated with the asphaltene content of the bitumen. Other properties were not linearly correlated or due to the variation of the property, no significant trend was identified and these properties can be seen to be constant for the bitumens used.

Since self-healing in asphalt involves the interaction of bitumen and aggregates, hence the properties of the different mortar mixtures used were analysed. Adding filler to bitumen resulted in a higher viscosity of the mixture compared to bitumen and resulted in a near-linear increase in the density and the thermal expansion of the mastic with filler content. The initial force to break the asphalt mortar beams depended on the mixture design, but was less affected by the density of the aggregates. This arose from adding metal grit to the mixture to be able to heat the beams via induction heating, resulting in a shift to a higher weight for the beams but similar breaking forces were measured. Bitumen content had a significant effect on the breaking force, as the bitumen content increased the breaking increased until an optimum, after which increasing amounts of bitumen decreased the initial breaking force. This is due to the decrease of air voids with increasing bitumen content until the interlocking of the aggregates is reduced by bitumen. The amount of filler had no significant influence on the breaking force and only a slight trend of a decreasing breaking force with increasing filler was noticed.

During convection heating, the application of a horizontal/circumferential pressure did not affect the equilibrium temperature, but a faster increase in surface temperature was observed for beams with pressure. This was attributed to the difference in thermal conductivity and heat capacities of the mould materials. The bitumen type and the amount of filler had no influence on the surface temperature measured. A difference was observed due to bitumen content, whereby increasing bitumen content decreased surface temperature. Since the equilibrium temperature is not material dependent, a similar temperature was reached by each beam regardless of mixture design and supporting mould. Induction heating caused a linear increase in surface temperature and the increase was defined by the current intensity. A limit in heating velocity was observed above 110 A, as the self-regulation of the induction heater limited the current intensity. The high power output increased the temperature of the metal particles, resulting in a fast increase of the average surface temperature. After 45 s occurrence of smoke indicated thermal degradation, which was visibly confirmed by a change in the surface. This burnt rough surface appeared in the middle of the upper side of the beam surrounded by a bitumen

rich corona and reached approximately 10 mm deep. A dramatic ageing/thermal degradation was confirmed by infrared spectroscopy, as the intensity of bands used to indicate ageing increased, which exceeded band intensities of laboratory aged bitumen.

The minimum temperature for self-healing for asphalt mortar beams was narrowed to be between 8 °C and 20 °C. This temperature range is below the Newtonian transition temperature and above the glass transition temperature, which were previously suggested as starting temperatures for self-healing. Since a mixture of bitumen and aggregates was identified as likely to fill cracks, the temperature threshold for self-healing was determined in reference to the mixture design.

In general, the self-healing ratio increased until a steady state was reached, referred to as the steady self-healing ratio state. The initial self-healing ratios due to the adhesive nature of bitumen were between 0.01 and 0.03 and were correlated to the viscosity and surface tension of the bitumen, as the initial contact points adhere to each other and are generated by the slight pressure during the assembling. This resulted in a deformation of the fracture surface at the contact points, increasing the contact area. The circumferential pressure applied to the beams by the silicone moulds caused a rapid increase in self-healing ratios to a range between 0.21 and 0.63. Afterwards, the self-healing ratios increased and slowly approached the steady self-healing ratio state.

The steady self-healing ratio state was reached after 1200 s for convection heating and after 30 s for induction heating, showing the timesaving benefit of induction heating. For polytetrafluorethylene (PTFE) moulds, increasing temperature increased the steady self-healing ratio state asymptotically and decreased the variation in self-healing ratios. For beams with a circumferential pressure, a linear relationship was found and the variation was constant over the temperature range. Due to the circumferential pressure, the self-healing ratios were higher and approached the steady self-healing ratio state faster than moulds without additional pressure. For induction heating, the steady self-healing ratio stage was less dependent on the current intensity and was within the range of variation.

Representing the self-healing ratios as a function of a pseudo healing energy parameter, self-healing for convection and induction heating became more similar. This indicates that a similar total pseudo healing energy is required to achieve a certain self-healing ratio, independent of the heating method. The pseudo energy parameter can be criticised for only considering surface temperature and not the temperature distribution within the sample. The internal energy might be a better energy parameter and this requires the determination of the heat transfer into and from the sample and the work, which can be split into pressure-volume work and isochoric work.

Correlation of the self-healing properties to bitumen properties revealed that the steady self-healing ratio state is linearly correlated to the softening point, transition temperature and the surface tension measured by the Wilhelmy plate method. Because certain bitumen properties were similar or because no significant correlations were found between the very similar self-healing properties of different bitumen types. Moreover, the similarities and the contribution of pressure to the self-healing validates the proposed self-healing model.

To determine the flowable material in a mixture, a gap of approximately 1 mm between the two pieces silicone mould was generated and the material accumulated in the gap was

collected and analysed. A bitumen content below 15wt.% resulted in no material inside the gap. Increasing the filler content caused material to drain into the gap. The filler content affected the flow speed in the gap, reducing the flow as the amount of filler increased. The material collected had a similar composition to the mixture, though it was enriched with bitumen. Due to the gap height mainly filler and finer aggregates were found to be draining into the gap. The amount and size of aggregates that are able to flow in the mixture depend on the ratio of friction force and density difference between bigger aggregates and the flowable mixture, mostly mastic.

Another considerable factor for the self-healing of different mortar asphalt beam mixtures is the fracture surface, as an optimum bitumen content was found for the initial breaking force around 15wt.% bitumen. The decrease in breaking force for lower bitumen content was attributed to the increase in air voids and the decrease in breaking force for higher bitumen content was attributed to the lower probability of fracturing aggregates. For an increased filler content, a slight decrease in breaking force was observed, which was not significant. Reducing the amount of crack area through aggregates, increased the self-healing ratio, as more crack area was recovered and similar strength could be restored.

The threshold for freely moving bitumen was estimated to be approximately 5.4wt.% bitumen for the mixture used. The amount of bitumen is further influenced by the filler content, which negatively correlates to the bitumen content for a flowable mixture.

The effect of water on the self-healing of macro cracks in asphalt mortar beams was investigated for three different conditions: conditioning in deionised water and healing in deionised water (water-water), conditioning in deionised water and healing in air (water-air) and conditioning and healing in air (air-air).

The initial self-healing ratio, resulting from the adhesiveness of bitumen during assembling of the broken beam halves was significantly reduced from 20.8 N in dry conditions to 8.8 N for wetted beams. This reduction was attributed to the excess pore water pressure during the assembling, which reduced the formation of initial contact points.

In the case when the asphalt mortar beams were conditioned in deionised water and self-healed in water (water-water condition) without a drying phase, the mortar beams showed no self-healing independent of the temperature and self-healing duration. This was mainly caused by the similar densities of water and bitumen, which stopped the bitumen from flowing into the crack. In addition, the increased polar contribution to the surface tension attracts water, separating initial contact points. Furthermore, the presence of water in the crack causes a change in crack geometry to minimise surface energy. The uniformly applied air pressure to the mortar beams supports this, as the additional uniform pressure had no influence on the self-healing. The high self-healing ratios obtained were attributed to the drying phase. Moreover, at above 60°C stripping occurred, which decreased the average self-healing ratio with water exposure time.

In the case of the water-air condition, the self-healing ratios increased with increasing temperature. The highest self-healing ratio was observed during the first hours, which was attributed to the increased remaining water content in the pores of the beams and thus, an increased hydrostatic water pressure onto the crack. This positive pressure was

gradually reduced with time as the water evaporated from the beams. This was only observable for temperatures below 20°C, as at higher temperatures the self-healing was coupled with the water evaporation.

Water affects the surface tension of bitumen, increasing the polar content nearly doubled the surface tension of bitumen investigated. Allowing an immersed bitumen surface to dry for 1 day showed that the surface tension decreased, likely by reducing its polar component. This was confirmed by ATR FT-IR spectra, as bands of polar functional groups increased after water immersion and decreased during drying. The effect of water on the viscosity of bitumen was minor to negligible.

Figure 10.1 shows the scheme of the self-healing process. After a crack is initiated, the surface of the crack smoothens as the surface energy is minimised, resulting in a texture and colour change of a crack surface. Bringing both crack surfaces together as the beam halves are assembled creates the first initial contact point. These contact points are the cause of the initial adhesion of the beam halves, measured as initial self-healing rate. Starting from these contact points, bitumen or mastic drains into the crack due to surface tension and gravity. In addition, as temperature increases, bitumen and aggregates expand. As the volumetric thermal expansion coefficient of bitumen is higher than that for mineral aggregates, the expanding bitumen or mastic may promote the formation of additional contact points and the increase of contact area of existing contact points by flowing into the crack. Reduced viscosity at higher temperatures increases the self-healing rate and in combination with thermal expansion, this might cause healing following the temperature gradient. Additional compressive pressure, due to an external force or due to pore water, supports the approach of the crack surfaces and the increase in contact area. After the thermal equilibrium is reached, pressure due to thermal expansion might be reduced due to relaxation and creep. A prolonged time at the steady state temperature may reduce the breaking strength of the beam, as bitumen or mastic is drained to the bottom of the beam through gravitational flow and further could be drained from the beam. As a result of the flow of bitumen or mastic into the crack and air voids, new air voids can be generated during the cooling, due to contraction of the material and the preference of bitumen to remain in smaller pores, including cracks.

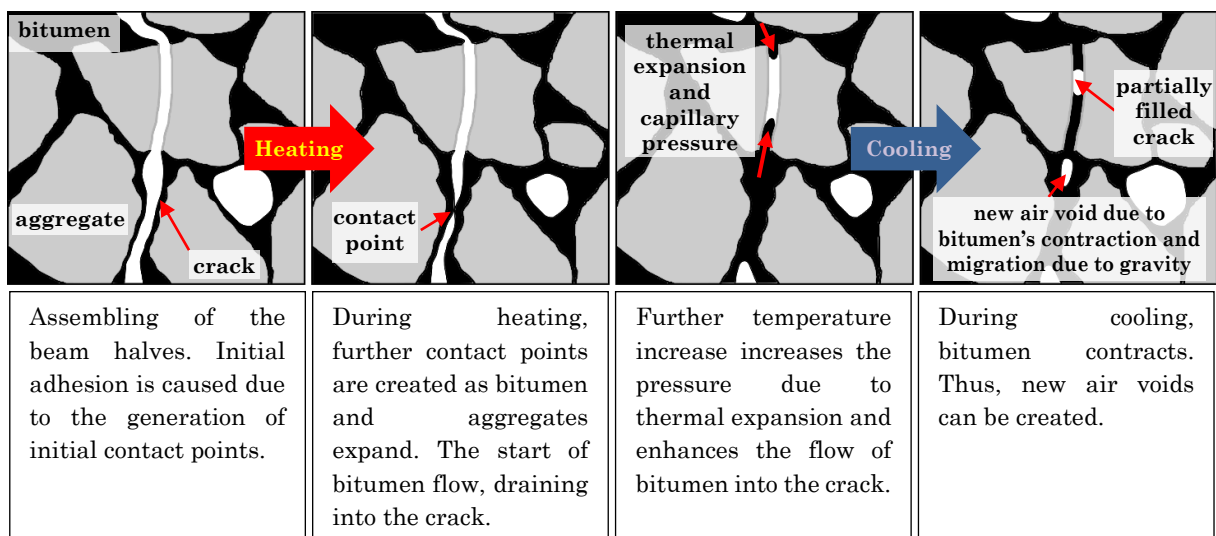


Figure 10.1: conceptual model illustrating the self-healing process [213].

10.2 Conclusion

The self-healing in asphalt mortar beams is a flow process. By identifying bitumen and mixture characteristics and correlating these characteristics to self-healing properties, it was concluded that the self-healing in asphalt mortar beams manufactured with conventional bitumen types is nearly unaffected by the bitumen type. A dependency of the self-healing ratio on the surface tension measured by the Wilhelmy plate method indicated its influence. However, the surface tension was measured at ambient temperature in contrast to the higher temperatures during the self-healing and this relationship did not occur for other methods. The indistinguishable steady self-healing ratio states and similar self-healing ratios reflected the similar bitumen properties. Since self-healing was accelerated due to temperature increase, the similar self-healing might have originated from the similar thermal expansion coefficient.

The influence of pressure on self-healing was shown by applying a horizontal pressure during healing and different oven temperatures. By applying a horizontal pressure, the steady self-healing ratio state increased compared to beams without additional pressure. Furthermore, the steady self-healing ratios increased with increasing surface temperature of both, convection and induction, heating methods. Since the derived self-healing equation suggests that viscosity would only affect the self-healing rate and not the self-healing ratio, pressure due to thermal expansion caused the increase in self-healing ratio and reduced variability.

The mixture design of the asphalt mortar had a significant influence on the self-healing. To begin with, the fracture path determined the breaking force and the self-healing ratio. Fracturing less aggregates due to a higher bitumen or filler content, reduced the breaking force. Although, the self-healing was increased as a higher area of similar bearing capacity was recoverable (“healable”). The mixture design further determined the material flowing or closing the crack, which was found to be of similar composition to the mixture itself with a higher amount of bitumen and finer particles.

As weather exposed road construction material, self-healing was prevented in the presence of water. The initial self-healing ratio was reduced or non-existent and water inside the crack hindered the flow of bituminous material into the crack during the self-healing duration of 10 days. Drying the beams revealed that the hydrostatic pore water contributed as perpendicular pressure onto the crack surface, allowing the self-healing of the crack. The water content of the beam before drying correlated with the self-healing ratios obtained, as a higher water content resulted in a higher self-healing ratio. Furthermore, self-healing occurred in asphalt mortar beams below 20°C, which did not occur for beams without water-filled pores, showing the contribution of pressure onto the self-healing process.

10.3 Recommended further investigations on self-healing

Based on the findings and the limitations of this study, the following recommendations are proposed:

- Since only commonly used bitumen types were used, a broader range of bitumen properties could identify trends more clearly and would allow determination of the influence of the trend and its weight.
- Certain bitumen properties, like surface tension, density or spectrum, are determined at ambient temperatures. This study enhanced the self-healing by increasing temperature due to heating, which might alter results. Hence, it would be desirable to measure and monitor properties at the self-healing temperature which further would allow to evaluate the occurrence and influence of ageing.
- As self-healing is a flow process, the bituminous material draining into the crack was indirectly determined. A direct observation of the flow process through an imaging method like CT-scans is possible. Although, current limits are resolution, sample size and temperature. Probing the fracture surface on its composition at the nanoscale to microscale would reveal changes before and after healing, which could identify flowing material.
- Testing self-healing under environmental conditions would clarify if water has a negative influence, preventing self-healing, or a positive influence, due to pressure during a drying phase, on self-healing.

Bibliography

- [1] Asphalt Institute, European Bitumen Association. The Bitumen Industry - a Global Perspective: Production, Chemistry, Use, Specification and Occupational Exposure. Asphalt Institute; 2015.
- [2] Traxler RN. Asphalt: Its composition, properties, and uses. Reinhold Pub. Corp.; 1961.
- [3] Read J, Whiteoak D. The shell bitumen handbook. Thomas Telford; 2003.
- [4] Papagiannakis AT, Masad EA. Pavement design and materials. John Wiley & Sons; 2017.
- [5] Huang YH. Pavement analysis and design. Prentice Hall; 1993.
- [6] Tschegg E, Jamek M, Lugmayr R. Fatigue crack growth in asphalt and asphalt-interfaces. *Engineering Fracture Mechanics* 2011;78(6):1044-1054.
- [7] Mobasher B, Mamlouk MS, Lin H-M. Evaluation of crack propagation properties of asphalt mixtures. *Journal of Transportation Engineering* 1997;123(5):405-413.
- [8] Petersen JC. A review of the fundamentals of asphalt oxidation: chemical, physicochemical, physical property, and durability relationships. *Transportation Research Circular* 2009(E-C140):68.
- [9] Nishizawa T, Shimeno S, Sekiguchi M. Fatigue analysis of asphalt pavements with thick asphalt mixture layer. *Eighth International Conference on Asphalt Pavements*. Seattle, Washington; 1997.
- [10] Francken L. Fatigue performance of a bituminous road mix under realistic test conditions. *Transportation Research Record* 1979(712).
- [11] Zeng G, Yang X, Yin A, Bai F. Simulation of damage evolution and crack propagation in three-point bending pre-cracked asphalt mixture beam. *Construction and Building Materials* 2014;55:323-332.
- [12] Wool RP. Self-healing materials: a review. *Soft Matter* 2008;4(3):400-418.
- [13] Bazin P, Saunier J. Deformability, fatigue and healing properties of asphalt mixes. *Intl Conf Struct Design Asphalt Pvmts*. 1967.
- [14] Van Dijk W, Moreaud H, Quedeville A, Uge P. The fatigue of bitumen and bituminous mixes. *Presented at the Third International Conference on the Structural Design of Asphalt Pavements, Grosvenor House, Park Lane, London, England, Sept. 11-15*. 1. 1972.
- [15] Sun D, Sun G, Zhu X, Ye F, Xu J. Intrinsic temperature sensitive self-healing character of asphalt binders based on molecular dynamics simulations. *Fuel* 2018;211:609-620.
- [16] Lv Q, Huang W, Xiao F. Laboratory evaluation of self-healing properties of various modified asphalt. *Construction and Building Materials* 2017;136:192-201.
- [17] García Á. Self-healing of open cracks in asphalt mastic. *Fuel* 2012;93:264-272.
- [18] Tan Y, Shan L, Richard Kim Y, Underwood BS. Healing characteristics of asphalt binder. *Construction and Building Materials* 2012;27(1):570-577.
- [19] Qiu J, van de Ven M, Molenaar A. Crack-healing investigation in bituminous materials. *Journal of Materials in Civil Engineering* 2012;25(7):864-870.
- [20] Bhasin A, Little DN, Bommavaram R, Vasconcelos K. A framework to quantify the effect of healing in bituminous materials using material properties. *Road Materials and Pavement Design* 2008;9:219-242.
- [21] Kim B, Roque R. Evaluation of healing property of asphalt mixtures. *Transportation Research Record: Journal of the Transportation Research Board* 2006(1970):84-91.
- [22] Si Z, Little D, Lytton R. Characterization of microdamage and healing of asphalt concrete mixtures. *Journal of Materials in Civil Engineering* 2002;14(6):461-470.
- [23] Williams D, Little D, Lytton R, Kim Y, Kim Y. Microdamage healing in asphalt and asphalt concrete, volume II: Laboratory and field testing to assess and evaluate microdamage and microdamage healing. No. FHWA-RD-98-142; 2001.
- [24] Phillips M. Multi-step models for fatigue and healing, and binder properties involved in healing. *Eurobitume workshop on performance related properties for bituminous binders, Luxembourg*. 1998.
- [25] Grossegger D, Gomez-Meijide B, Vansteenkiste S, Garcia A. Influence of rheological and physical bitumen properties on heat-induced self-healing of asphalt mastic beams. *Construction and Building Materials* 2018;182:298-308.
- [26] García Á, Schlangen E, van de Ven M, Sierra-Beltrán G. Preparation of capsules containing rejuvenators for their use in asphalt concrete. *Journal of Hazardous Materials* 2010;184(1-3):603-611.

- [27] Gallego J, del Val MA, Contreras V, Páez A. Heating asphalt mixtures with microwaves to promote self-healing. *Construction and Building Materials* 2013;42:1-4.
- [28] Gómez-Mejide B, Ajam H, Lastra-González P, Garcia A. Effect of air voids content on asphalt self-healing via induction and infrared heating. *Construction and Building Materials* 2016;126:957-966.
- [29] Garcia A, Schlangen E, Van de Ven M. Two ways of closing cracks on asphalt concrete pavements: microcapsules and induction heating. *Key Engineering Materials*. 417-418. Trans Tech Publications; 2010:573-576.
- [30] Kim YH, Wool RP. A theory of healing at a polymer-polymer interface. *Macromolecules* 1983;16(7):1115-1120.
- [31] Little D, Kim Y, Benson F. Investigation of the Mechanism of Healing in Asphalt: Report to the National Science Foundation. Texas A&M University, College Station 1987.
- [32] García A, Bueno M, Norambuena-Contreras J, Partl MN. Induction healing of dense asphalt concrete. *Construction and Building Materials* 2013;49:1-7.
- [33] Kim YR, Little DN, Lytton R, D'Angelo J, Davis R, Rowe G, et al. Use of dynamic mechanical analysis (DMA) to evaluate the fatigue and healing potential of asphalt binders in sand asphalt mixtures. *Asphalt Paving Technology: Association of Asphalt Paving Technologists-Proceedings of the Technical Sessions*. 71. Association of Asphalt Paving Technologist; 2002:176-206.
- [34] Santagata E, Baglieri O, Tsantilis L, Chiappinelli G. Fatigue and healing properties of nano-reinforced bituminous binders. *International Journal of Fatigue* 2015;80:30-39.
- [35] Moreno-Navarro F, Sol-Sánchez M, Rubio-Gámez MC. Exploring the recovery of fatigue damage in bituminous mixtures: the role of healing. *Road Materials and Pavement Design* 2015;16(sup1):75-89.
- [36] Qiu J, Van de Ven M, Wu S, Yu J, Molenaar A. Investigating self healing behaviour of pure bitumen using dynamic shear rheometer. *Fuel* 2011;90(8):2710-2720.
- [37] Ghosh SK. Self-healing materials: fundamentals, design strategies, and applications. Wiley Online Library; 2009.
- [38] Kim YR, Little DN, Burghardt R. SEM analysis on fracture and healing of sand-asphalt mixtures. *Journal of Materials in Civil Engineering* 1991;3(2):140-153.
- [39] Kim YR, Little DN, Benson FC. Chemical and mechanical evaluation on healing mechanism of asphalt concrete (with discussion). *Journal of the Association of Asphalt Paving Technologists* 1990;59.
- [40] Simanzhenkov V, Idem R. Crude oil chemistry. CRC Press; 2003.
- [41] Lesueur D. The colloidal structure of bitumen: Consequences on the rheology and on the mechanisms of bitumen modification. *Advances in Colloid and Interface Science* 2009;145(1):42-82.
- [42] Grossegger D. Investigation of bitumen ageing through bitumen separation and luminescence spectroscopy. Vienna Young Science Symposium 2015 (Poster presentation); 2015.
- [43] Großegger D. Investigation of Aged, Non-aged Bitumen and their Bitumen Fractions. (Master dissertation). Vienna University of Technology; 2015.
- [44] Alvarez E, Marroquín G, Trejo F, Centeno G, Ancheyta J, Díaz JA. Pyrolysis kinetics of atmospheric residue and its SARA fractions. *Fuel* 2011;90(12):3602-3607.
- [45] Šebor G, Blažek J, Nemer MF. Optimization of the preparative separation of petroleum maltenes by liquid adsorption chromatography. *Journal of Chromatography A* 1999;847(1-2):323-330.
- [46] Redelius P, Soenen H. Relation between bitumen chemistry and performance. *Fuel* 2015;140:34-43.
- [47] Mullins OC, Sheu EY, Hammami A, Marshall AG. Asphaltenes, heavy oils, and petroleomics. Springer Science & Business Media; 2007.
- [48] Alboudwarej H, Beck J, Svrcek W, Yarranton H, Akbarzadeh K. Sensitivity of asphaltene properties to separation techniques. *Energy & Fuels* 2002;16(2):462-469.
- [49] Andersen SI, Stenby EI. Thermodynamics of asphaltene precipitation and dissolution investigation of temperature and solvent effects. *Fuel Science and Technology International* 1996;14(1-2):261-287.

- [50] Ganeeva YM, Yusupova TyN, Romanov GVe. Asphaltene nano-aggregates: structure, phase transitions and effect on petroleum systems. *Russian Chemical Reviews* 2011;80(10):993-1008.
- [51] Hofko B, Eberhardsteiner L, Füssl J, Grothe H, Handle F, Hospodka M, et al. Impact of maltene and asphaltene fraction on mechanical behavior and microstructure of bitumen. *Materials and Structures* 2016;49(3):829-841.
- [52] Redelius P. Asphaltenes in bitumen, what they are and what they are not. *Road Materials and Pavement Design* 2009;10(sup1):25-43.
- [53] Pauli A, Grimes R, Beemer A, Turner T, Branthaver J. Morphology of asphalts, asphalt fractions and model wax-doped asphalts studied by atomic force microscopy. *International Journal of Pavement Engineering* 2011;12(4):291-309.
- [54] Das PK, Kringos N, Wallqvist V, Birgisson B. Micromechanical investigation of phase separation in bitumen by combining atomic force microscopy with differential scanning calorimetry results. *Road Materials and Pavement Design* 2013;14(sup1):25-37.
- [55] Handle F, Füssl J, Neudl S, Grossegger D, Eberhardsteiner L, Hofko B, et al. The bitumen microstructure: a fluorescent approach. *Materials and Structures* 2016;49(1-2):167-180.
- [56] Schmets A, Kringos N, Pauli T, Redelius P, Scarpas T. On the existence of wax-induced phase separation in bitumen. *International Journal of Pavement Engineering* 2010;11(6):555-563.
- [57] Yu X, Burnham NA, Tao M. Surface microstructure of bitumen characterized by atomic force microscopy. *Advances in Colloid and Interface Science* 2015;218:17-33.
- [58] Pahlavan F, Mousavi M, Hung A, Fini EH. Investigating molecular interactions and surface morphology of wax-doped asphaltenes. *Physical Chemistry Chemical Physics* 2016;18(13):8840-8854.
- [59] Mikhailenko P, Kadhim H, Baaj H. Observation of bitumen microstructure oxidation and blending with ESEM. *Road Materials and Pavement Design* 2017;18(sup2):216-225.
- [60] Grossegger D. Microstructural aging of bitumen. *6th Eurasphalt & Eurobitume Congress*. Prague, Czech Republic; 2016:7.
- [61] Nellensteyn F. The constitution of asphalt. *Journal of the Institute of Petroleum Technologists* 1924;10:311-325.
- [62] Kringos N, Schmets A, Scarpas A, Pauli T. Towards an understanding of the self-healing capacity of asphaltic mixtures. *Heron* 2011;56(1/2):45-74.
- [63] Lu X, Langton M, Olofsson P, Redelius P. Wax morphology in bitumen. *Journal of Materials Science* 2005;40(8):1893-1900.
- [64] Gaskin J. On bitumen microstructure and the effects of crack healing. (Doctoral dissertation). University of Nottingham; 2013.
- [65] Bearsley S, Forbes A, Haverkamp RG. Direct observation of the asphaltene structure in paving-grade bitumen using confocal laser-scanning microscopy. *Journal of Microscopy* 2004;215(2):149-155.
- [66] Masson J, Polomark G, Collins P. Time-dependent microstructure of bitumen and its fractions by modulated differential scanning calorimetry. *Energy & fuels* 2002;16(2):470-476.
- [67] Nahar S, Schmets A, Scarpas A, Schitter G. Temperature and thermal history dependence of the microstructure in bituminous materials. *European Polymer Journal* 2013;49(8):1964-1974.
- [68] Lyne ÅL, Wallqvist V, Rutland MW, Claesson P, Birgisson B. Surface wrinkling: the phenomenon causing bees in bitumen. *Journal of Materials Science* 2013;48(20):6970-6976.
- [69] Panda R, Das SS, Sahoo P. An empirical method for estimating surface area of aggregates in hot mix asphalt. *Journal of Traffic and Transportation Engineering (English Edition)* 2016;3(2):127-136.
- [70] Fischer H, Dillingh E. On the investigation of the bulk microstructure of bitumen—Introducing two new techniques. *Fuel* 2014;118:365-368.
- [71] Bigg P. Density of water in SI units over the range 0-40 C. *British Journal of Applied Physics* 1967;18(4):521.
- [72] Mastrofini D, Scarsella M. The application of rheology to the evaluation of bitumen ageing. *Fuel* 2000;79(9):1005-1015.
- [73] Lu X, Isacson U. Effect of ageing on bitumen chemistry and rheology. *Construction and Building Materials* 2002;16(1):15-22.

- [74] Mamlouk MS, Witczak MW, Kaloush KE, Hasan N. Determination of thermal properties of asphalt mixtures. *Journal of Testing and Evaluation* 2005;33(2):1-9.
- [75] Wada Y, Hirose H. Glass transition phenomena and rheological properties of petroleum asphalt. *Journal of the Physical Society of Japan* 1960;15(10):1885-1894.
- [76] Rossi CO, Caputo P, Baldino N, Lupi FR, Miriello D, Angelico R. Effects of adhesion promoters on the contact angle of bitumen-aggregate interface. *International Journal of Adhesion and Adhesives* 2016;70:297-303.
- [77] Guerrero-Barba II F, Cabrerizo-Vílchez MA, Rodríguez-Valverde MA. Bitumen spreading on calcareous aggregates at high temperature. *Journal of Materials Science* 2014;49(22):7723-7729.
- [78] Hefer AW, Bhasin A, Little DN. Bitumen surface energy characterization using a contact angle approach. *Journal of Materials in Civil Engineering* 2006;18(6):759-767.
- [79] Wei J-M, Zhang Y-Z. Influence of aging on surface free energy of asphalt binder. *International Journal of Pavement Research and Technology* 2010;3(6):343-351.
- [80] Drelich J, Bukka K, Miller JD, Hanson FV. Surface tension of toluene-extracted bitumens from Utah oil sands as determined by Wilhelmy plate and contact angle techniques. *Energy & Fuels* 1994;8(3):700-704.
- [81] Vargha-Butler E, Potoczny Z, Zubovits T, Budziak C, Neumann A. Surface tension of bitumen from contact angle measurements on films of bitumen. *Energy & Fuels* 1988;2(5):653-656.
- [82] Wei J, Dong F, Li Y, Zhang Y. Relationship analysis between surface free energy and chemical composition of asphalt binder. *Construction and Building Materials* 2014;71:116-123.
- [83] Traxler R, Schweyer H, Romberg J. Rheological properties of asphalt. *Industrial & Engineering Chemistry* 1944;36(9):823-829.
- [84] Romberg J, Traxler R. Rheology of asphalt. *Journal of Colloid Science* 1947;2(1):33-47.
- [85] Bazyleva AB, Hasan MA, Fulem M, Becerra M, Shaw JM. Bitumen and heavy oil rheological properties: Reconciliation with viscosity measurements. *Journal of Chemical & Engineering Data* 2009;55(3):1389-1397.
- [86] Argüelles-Vivas FJ, Babadagli T, Little L, Romaniuk N, Ozum B. High temperature density, viscosity, and interfacial tension measurements of bitumen-pentane-biodiesel and process water mixtures. *Journal of Chemical & Engineering Data* 2012;57(10):2878-2889.
- [87] Ukwuoma O, Ademodi B. The effects of temperature and shear rate on the apparent viscosity of Nigerian oil sand bitumen. *Fuel Processing Technology* 1999;60(2):95-101.
- [88] Mouillet V, De La Roche C, Chailleux E, Coussot P. Thixotropic behavior of paving-grade bitumens under dynamic shear. *Journal of Materials in Civil Engineering* 2011;24(1):23-31.
- [89] Masson J, Collins P, Polomark G. Steric hardening and the ordering of asphaltenes in bitumen. *Energy & Fuels* 2005;19(1):120-122.
- [90] Traxler R. A review of the rheology of bituminous materials. *Journal of Colloid Science* 1947;2(1):49-68.
- [91] Isacson U, Zeng H. Low-temperature cracking of polymer-modified asphalt. *Materials and Structures* 1998;31(1):58-63.
- [92] Stangl K, Jäger A, Lackner R. Microstructure-based identification of bitumen performance. *Road Materials and Pavement Design* 2006;7(sup1):111-142.
- [93] Boczkaj G, Przyjazny A, Kamiński M. Characteristics of volatile organic compounds emission profiles from hot road bitumens. *Chemosphere* 2014;107:23-30.
- [94] Grossegger D, Grothe H, Hofko B, Hospodka M. Fluorescence spectroscopic investigation of bitumen aged by field exposure respectively modified rolling thin film oven test. *Road Materials and Pavement Design* 2017:1-9.
- [95] Polacco G, Filippi S, Merusi F, Stastna G. A review of the fundamentals of polymer-modified asphalts: Asphalt/polymer interactions and principles of compatibility. *Advances in Colloid and Interface Science* 2015;224:72-112.
- [96] Lu X, Isacson U. Compatibility and storage stability of styrene-butadiene-styrene copolymer modified bitumens. *Materials and Structures* 1997;30(10):618-626.
- [97] Champion L, Gerard J-F, Planche J-P, Martin D, Anderson D. Low temperature fracture properties of polymer-modified asphalts relationships with the morphology. *Journal of Materials Science* 2001;36(2):451-460.

- [98] Masson J, Collins P, Robertson G, Woods J, Margeson J. Thermodynamics, phase diagrams, and stability of bitumen–polymer blends. *Energy & Fuels* 2003;17(3):714-724.
- [99] Pérez-Lepe A, Martínez-Boza F, Attané P, Gallegos C. Destabilization mechanism of polyethylene-modified bitumen. *Journal of Applied Polymer Science* 2006;100(1):260-267.
- [100] Fawcett A, McNally T, McNally G, Andrews F, Clarke J. Blends of bitumen with polyethylenes. *Polymer* 1999;40(23):6337-6349.
- [101] Fawcett A, McNally T. Blends of bitumen with various polyolefins. *Polymer* 2000;41(14):5315-5326.
- [102] Fawcett AH, McNally T, McNally G. An attempt at engineering the bulk properties of blends of a bitumen with polymers. *Advances in Polymer Technology: Journal of the Polymer Processing Institute* 2002;21(4):275-286.
- [103] Luo W-q, Chen J-c. Preparation and properties of bitumen modified by EVA graft copolymer. *Construction and Building Materials* 2011;25(4):1830-1835.
- [104] Capitão S, Picado-Santos L, Martinho F. Pavement engineering materials: Review on the use of warm-mix asphalt. *Construction and Building Materials* 2012;36:1016-1024.
- [105] Herrin M, Goetz WH, Campen W. Effect of aggregate shape on stability of bituminous mixes (with discussion). *Highway Research Board Proceedings*. 33. 1954:293-308.
- [106] Wedding PA, Gaynor RD. The effect of using crushed gravel as the coarse and fine aggregate in dense graded bituminous mixtures (with discussion). *Association of Asphalt Paving Technologists Proceedings*. 30. 1961:469-492.
- [107] Csanyi LH. Functions of fillers in bituminous mixes. *Highway Research Board Bulletin* 1962(329).
- [108] Lee D-y. The effect of filler on asphalt cement mastics. (Doctoral dissertation). Iowa State University; 1964:119.
- [109] Roberts FL, Kandhal PS, Brown ER, Lee D-Y, Kennedy TW. Hot mix asphalt materials, mixture design and construction. National Asphalt Pavement Association Research and Education Foundation 1991:506.
- [110] Rubio MC, Martínez G, Baena L, Moreno F. Warm mix asphalt: an overview. *Journal of Cleaner Production* 2012;24:76-84.
- [111] Caro S, Masad E, Bhasin A, Little DN. Moisture susceptibility of asphalt mixtures, Part 1: mechanisms. *International Journal of Pavement Engineering* 2008;9(2):81-98.
- [112] Mohammad LN, Wu Z, Zhang C, Khattak MJ, Abadie C. Variability of air voids and mechanistic properties of plant-produced asphalt mixtures. *Transportation research record* 2004;1891(1):85-97.
- [113] Kumar P, Gupta A. Case studies on failure of bituminous pavements. *First International Conference on Pavement Preservation California Department of Transportation Federal Highway Administration Foundation for Pavement Preservation*. 2010:505-518.
- [114] Miró R, Martínez AH, Moreno-Navarro F, del Carmen Rubio-Gámez M. Effect of ageing and temperature on the fatigue behaviour of bitumens. *Materials & Design* 2015;86:129-137.
- [115] El Hussein HM, El Halim AA, Kennepohl GJ. Assessment of the influence of compaction method on asphalt concrete resistance to moisture damage. *Construction and Building Materials* 1993;7(3):149-156.
- [116] Harvey J, Tsai B-W. Effects of asphalt content and air void content on mix fatigue and stiffness. *Transportation Research Record: Journal of the Transportation Research Board* 1996(1543):38-45.
- [117] Yin A, Yang X, Yang S, Jiang W. Multiscale fracture simulation of three-point bending asphalt mixture beam considering material heterogeneity. *Engineering Fracture Mechanics* 2011;78(12):2414-2428.
- [118] Lytton R. Adhesive fracture in asphalt concrete mixtures. Book edited by Youtcheff J. 2004.
- [119] Masad E, Arambula E, Ketcham R, Abbas A, Martin AE. Nondestructive measurements of moisture transport in asphalt mixtures. *Asphalt Paving Technology-Proceedings* 2007;76:919.
- [120] Vasconcelos KL, Bhasin A, Little DN. History dependence of water diffusion in asphalt binders. *International Journal of Pavement Engineering* 2011;12(5):497-506.
- [121] Vasconcelos KL, Bhasin A, Little DN, Lytton RL. Experimental measurement of water diffusion through fine aggregate mixtures. *Journal of Materials in Civil Engineering* 2010;23(4):445-452.

- [122] Hung AM, Goodwin A, Fini EH. Effects of water exposure on bitumen surface microstructure. *Construction and Building Materials* 2017;135:682-688.
- [123] Blaiszik B, Kramer S, Olugebefola S, Moore JS, Sottos NR, White SR. Self-healing polymers and composites. *Annual Review of Materials Research* 2010;40:179-211.
- [124] Prager S, Tirrell M. The healing process at polymer–polymer interfaces. *The Journal of Chemical Physics* 1981;75(10):5194-5198.
- [125] Jud K, Kausch H. Load transfer through chain molecules after interpenetration at interfaces. *Polymer Bulletin* 1979;1(10):697-707.
- [126] Diesendruck CE, Sottos NR, Moore JS, White SR. Biomimetic self-healing. *Angewandte Chemie International Edition* 2015;54(36):10428-10447.
- [127] Döhler D, Michael P, Neumann S, Binder WH. Selbstheilende Polymere: Biomimetische Materialien. *Chemie in unserer Zeit*. 50. 2015:90-101.
- [128] Döhler D, Michael P, Binder W. Principles of Self-Healing Polymers. In: *Self-Healing Polymers: From Principles to Applications*, Binder WH. Wiley-VCH Verlag GmbH & Co. KGaA; 2013, p. 5-60.
- [129] Li G, Meng H. 1.1 Review of existing self-healing systems. *Recent Advances in Smart Self-Healing Polymers and Composites* 2015:1.
- [130] Shojaei A. Modeling of self-healing smart composite materials. In: *Recent Advances in Smart Self-Healing Polymers and Composites*, Li G, Meng H. Woodhead Publishing/Elsevier; 2015, p. 21-52.
- [131] Wu DY, Meure S, Solomon D. Self-healing polymeric materials: a review of recent developments. *Progress in Polymer Science* 2008;33(5):479-522.
- [132] Tang J, Liu Q, Wu S, Ye Q, Sun Y, Schlangen E. Investigation of the optimal self-healing temperatures and healing time of asphalt binders. *Construction and Building Materials* 2016;113:1029-1033.
- [133] Yang Y, Urban MW. Self-healing polymeric materials. *Chemical Society Reviews* 2013;42(17):7446-7467.
- [134] Toohey KS, Sottos NR, Lewis JA, Moore JS, White SR. Self-healing materials with microvascular networks. *Nature Materials* 2007;6(8):581-585.
- [135] Zhu DY, Rong MZ, Zhang MQ. Self-healing polymeric materials based on microencapsulated healing agents: From design to preparation. *Progress in Polymer Science* 2015;49:175-220.
- [136] Jonkers HM. Self healing concrete: a biological approach. In: *Self healing materials*: Springer; 2007, p. 195-204.
- [137] Jonkers HM. Bacteria-based self-healing concrete. *Heron* 2011;56((1/2)):12.
- [138] Butt H-J, Kappl M. *Surface and interfacial forces*. John Wiley & Sons; 2018.
- [139] Neumann AW, Spelt JK. *Applied Surface Thermodynamics*. Marcel Dekker Incorporated; 2010.
- [140] Jud K, Kausch H, Williams J. Fracture mechanics studies of crack healing and welding of polymers. *Journal of Materials Science* 1981;16(1):204-210.
- [141] Bommavaram RR, Bhasin A, Little DN. Determining intrinsic healing properties of asphalt binders: role of dynamic shear rheometer. *Transportation Research Record* 2009;2126(1):47-54.
- [142] Karlsson R, Isacsson U, Ekblad J. Rheological characterisation of bitumen diffusion. *Journal of Materials Science* 2007;42(1):101-108.
- [143] Moghadam AD, Schultz BF, Ferguson J, Omrani E, Rohatgi PK, Gupta N. Functional metal matrix composites: self-lubricating, self-healing, and nanocomposites-an outlook. *The Journal of the Minerals, Metals and Materials Society (JOM)* 2014;66(6):872-881.
- [144] Nakao W, Takahashi K, Ando K. Self-healing of surface cracks in structural ceramics. *Self-healing Materials* 2009;6:183-217.
- [145] Little DN, Bhasin A, Darabi MK. Damage healing in asphalt pavements: Theory, mechanisms, measurement, and modeling. In: *Advances in Asphalt Materials*, Benedetto HD. Oxford: Woodhead Publishing; 2015, p. 205-242.
- [146] Das PK, Birgisson B, Jelagin D, Kringos N. Atomic force microscopy to characterize the healing potential of asphaltic materials. In: *Atomic Force Microscopy: Imaging, Measuring and Manipulating Surfaces at the Atomic Scale*, Bellitto V. INTECH; 2012, p. 209-230.
- [147] Lee H-J, Kim YR. Viscoelastic continuum damage model of asphalt concrete with healing. *Journal of Engineering Mechanics* 1998;124(11):1224-1232.

- [148] Palvadi S, Bhasin A, Little DN. Method to quantify healing in asphalt composites by continuum damage approach. *Transportation Research Record* 2012;2296(1):86-96.
- [149] Menozzi A, Garcia A, Partl MN, Tebaldi G, Schuetz P. Induction healing of fatigue damage in asphalt test samples. *Construction and Building Materials* 2015;74:162-168.
- [150] Qiu J. Self Healing of Asphalt Mixtures: Towards a Better Understanding of the Mechanism. (Doctoral dissertation). TU Delft, Delft University of Technology; 2012.
- [151] Zeiada WA, Souliman MI, Kaloush KE, Mamlouk M. Endurance limit for HMA based on healing concept using uniaxial tension-compression fatigue test. *Journal of materials in civil engineering* 2013;26(8):04014036.
- [152] Carpenter SH, Shen S. Dissipated energy approach to study hot-mix asphalt healing in fatigue. *Transportation Research Record* 2006;1970(1):178-185.
- [153] Shen S, Carpenter S. Development of an asphalt fatigue model based on energy principles (with discussion and closure). *Journal of the Association of Asphalt Paving Technologists* 2007;76.
- [154] Santagata E, Baglieri O, Dalmazzo D, Tsantilis L. Rheological and chemical investigation on the damage and healing properties of bituminous binders. *Journal of the Association of Asphalt Paving Technologists* 2009;78.
- [155] Salih S, Gómez-Meijide B, Aboufoul M, Garcia A. Effect of porosity on infrared healing of fatigue damage in asphalt. *Construction and Building Materials* 2018;167:716-725.
- [156] Liu Q, Schlangen E, van de Ven M. Induction healing of porous asphalt concrete beams on an elastic foundation. *Journal of Materials in Civil Engineering* 2012;25(7):880-885.
- [157] Qiu J, Van de Ven M, Wu S, Yu J, Molenaar A. Evaluating self healing capability of bituminous mastics. *Experimental Mechanics* 2012;52(8):1163-1171.
- [158] Bhasin A, Bommavaram R, Greenfield ML, Little DN. Use of molecular dynamics to investigate self-healing mechanisms in asphalt binders. *Journal of Materials in Civil Engineering* 2010;23(4):485-492.
- [159] Shen S, Lu X, Liu L, Zhang C. Investigation of the influence of crack width on healing properties of asphalt binders at multi-scale levels. *Construction and Building Materials* 2016;126:197-205.
- [160] Sun D, Lin T, Zhu X, Tian Y, Liu F. Indices for self-healing performance assessments based on molecular dynamics simulation of asphalt binders. *Computational Materials Science* 2016;114:86-93.
- [161] Canestrari F, Virgili A, Graziani A, Stimilli A. Modeling and assessment of self-healing and thixotropy properties for modified binders. *International Journal of Fatigue* 2015;70:351-360.
- [162] Darabi MK, Al-Rub RKA, Little DN. A continuum damage mechanics framework for modeling micro-damage healing. *International Journal of Solids and Structures* 2012;49(3):492-513.
- [163] Shan L, Tan Y, Underwood S, Kim YR. Application of thixotropy to analyze fatigue and healing characteristics of asphalt binder. *Transportation Research Record* 2010;2179(1):85-92.
- [164] Di Benedetto H, Nguyen QT, Sauzéat C. Nonlinearity, heating, fatigue and thixotropy during cyclic loading of asphalt mixtures. *Road Materials and Pavement Design* 2011;12(1):129-158.
- [165] Traxler R, Coombs C. The colloidal nature of asphalt as shown by its flow properties. *The Journal of Physical Chemistry* 1936;40(9):1133-1147.
- [166] Mazzoni G, Stimilli A, Canestrari F. Self-healing capability and thixotropy of bituminous mastics. *International Journal of Fatigue* 2016;92:8-17.
- [167] Santagata E, Baglieri O, Tsantilis L, Dalmazzo D. Evaluation of self healing properties of bituminous binders taking into account steric hardening effects. *Construction and Building Materials* 2013;41:60-67.
- [168] Nahar S, Schmets A, Scarpas A, Schitter G. Microstructural changes in bitumen at the onset of crack formation. *European Polymer Journal* 2014;56:17-25.
- [169] Nahar S, Schmets A, Scarpas A, Schitter G. Temperature induced healing in strained bituminous materials observed by atomic force microscopy. *ICSHM 2013: Proceedings of the 4th International Conference on Self-Healing Materials, Ghent, Belgium, 16-20 June 2013*. Magnel Laboratory for Concrete Research; 2013.

- [170] Nahar S. Phase-separation characteristics of bitumen and their relation to damage-healing. (Doctoral dissertation). Delft University of Technology; 2016.
- [171] Lu X. Investigation of the Fracture Healing and Mechanism of Asphalt Binders. (Doctoral dissertation). Washington State University; 2013.
- [172] Lv Q, Huang W, Zhu X, Xiao F. On the investigation of self-healing behavior of bitumen and its influencing factors. *Materials & Design* 2017;117:7-17.
- [173] Sun D, Lin T, Zhu X, Cao L. Calculation and evaluation of activation energy as a self-healing indication of asphalt mastic. *Construction and Building Materials* 2015;95:431-436.
- [174] Van de Ven M. The Influence of Ageing on the Fatigue and Healing Properties of Bituminous Mortars. *Procedia-Social and Behavioral Sciences* 2012;53:256-265.
- [175] Liu Q, García Á, Schlangen E, van de Ven M. Induction healing of asphalt mastic and porous asphalt concrete. *Construction and Building Materials* 2011;25(9):3746-3752.
- [176] Shen S, Chiu H-M, Huang H. Characterization of Fatigue and Healing in Asphalt Binders. *Journal of Materials in Civil Engineering* 2010;22(9):846-852.
- [177] Chen Y, Simms R, Koh C, Lopp G, Roque R. Development of a test method for evaluation and quantification of healing in asphalt mixture. *Road Materials and Pavement Design* 2013;14(4):901-920.
- [178] Moreno-Navarro F, Ayar P, Sol-Sánchez M, Rubio-Gámez MC. Exploring the recovery of fatigue damage in bituminous mixtures at macro-crack level: the influence of temperature, time, and external loads. *Road Materials and Pavement Design* 2017;18(sup2):293-303.
- [179] Sun D, Sun G, Zhu X, Pang Q, Yu F, Lin T. Identification of wetting and molecular diffusion stages during self-healing process of asphalt binder via fluorescence microscope. *Construction and Building Materials* 2017;132:230-239.
- [180] Little DN, Bhasin A. Exploring Mechanism of Healing in Asphalt Mixtures and Quantifying its Impact. In: *Self healing materials*: Springer; 2007, p. 205-218.
- [181] Pell P. Fatigue characteristics of bitumen and bituminous mixes. *International Conference on the Structural Design of Asphalt Pavements University of Michigan, Ann Arbor*. 203. 1962.
- [182] Norambuena-Contreras J, Garcia A. Self-healing of asphalt mixture by microwave and induction heating. *Materials & Design* 2016;106:404-414.
- [183] Wan J, Xiao Y, Song W, Chen C, Pan P, Zhang D. Self-Healing Property of Ultra-Thin Wearing Courses by Induction Heating. *Materials* 2018;11(8):1392.
- [184] García Á, Schlangen E, van de Ven M, Liu Q. A simple model to define induction heating in asphalt mastic. *Construction and Building Materials* 2012;31:38-46.
- [185] Liu Q, Schlangen E, García Á, van de Ven M. Induction heating of electrically conductive porous asphalt concrete. *Construction and Building Materials* 2010;24(7):1207-1213.
- [186] Das PK, Kringos N, Birgisson B. Microscale investigation of thin film surface ageing of bitumen. *Journal of Microscopy* 2014;254(2):95-107.
- [187] Gray MR, Le T, Wu XA. Role of pressure in coking of thin films of bitumen. *The Canadian Journal of Chemical Engineering* 2007;85(5):773-780.
- [188] Phan TM, Park D-W, Le THM. Crack healing performance of hot mix asphalt containing steel slag by microwaves heating. *Construction and Building Materials* 2018;180:503-511.
- [189] Sun YH, Liu QT, Wu SP, Shang F. Microwave heating of steel slag asphalt mixture. *Key Engineering Materials*. 599. Trans Tech Publ; 2014:193-197.
- [190] García A, Norambuena-Contreras J, Partl MN. Experimental evaluation of dense asphalt concrete properties for induction heating purposes. *Construction and Building Materials* 2013;46:48-54.
- [191] Liu Q, Wu S, Schlangen E. Induction heating of asphalt mastic for crack control. *Construction and Building Materials* 2013;41:345-351.
- [192] Liu Q, Schlangen E, van de Ven M, van Bochove G, van Montfort J. Evaluation of the induction healing effect of porous asphalt concrete through four point bending fatigue test. *Construction and Building Materials* 2012;29:403-409.
- [193] García Á, Schlangen E, van de Ven M, van Vliet D. Induction heating of mastic containing conductive fibers and fillers. *Materials and Structures* 2011;44(2):499-508.
- [194] García A, Norambuena-Contreras J, Bueno M, Partl MN. Influence of steel wool fibers on the mechanical, thermal, and healing properties of dense asphalt concrete. *Journal of Testing and Evaluation* 2014;42(5):1107-1118.

- [195] Dai Q, Wang Z, Hasan MRM. Investigation of induction healing effects on electrically conductive asphalt mastic and asphalt concrete beams through fracture-healing tests. *Construction and Building Materials* 2013;49:729-737.
- [196] Shen J, Amirkhanian S, Tang B. Effects of rejuvenator on performance-based properties of rejuvenated asphalt binder and mixtures. *Construction and Building Materials* 2007;21(5):958-964.
- [197] Zhang H, Bai Y, Cheng F. Rheological and self-healing properties of asphalt binder containing microcapsules. *Construction and Building Materials* 2018;187:138-148.
- [198] Micaelo R, Al-Mansoori T, Garcia A. Study of the mechanical properties and self-healing ability of asphalt mixture containing calcium-alginate capsules. *Construction and Building Materials* 2016;123:734-744.
- [199] Norambuena-Contreras J, Yalcin E, Garcia A, Al-Mansoori T, Yilmaz M, Hudson-Griffiths R. Effect of mixing and ageing on the mechanical and self-healing properties of asphalt mixtures containing polymeric capsules. *Construction and Building Materials* 2018;175:254-266.
- [200] Su J-F, Schlangen E, Qiu J. Design and construction of microcapsules containing rejuvenator for asphalt. *Powder technology* 2013;235:563-571.
- [201] Li R, Zhou T, Pei J. Design, preparation and properties of microcapsules containing rejuvenator for asphalt. *Construction and Building Materials* 2015;99:143-149.
- [202] Lv L, Yang Z, Chen G, Zhu G, Han N, Schlangen E, et al. Synthesis and characterization of a new polymeric microcapsule and feasibility investigation in self-healing cementitious materials. *Construction and Building Materials* 2016;105:487-495.
- [203] Su J-F, Qiu J, Schlangen E, Wang Y-Y. Experimental investigation of self-healing behavior of bitumen/microcapsule composites by a modified beam on elastic foundation method. *Materials and Structures* 2015;48(12):4067-4076.
- [204] Barrasa RC, López VB, Montoliu CM-P, Ibáñez VC, Pedrajas J, Santarén J. Addressing durability of asphalt concrete by self-healing mechanism. *Procedia-Social and Behavioral Sciences* 2014;162:188-197.
- [205] García Á, Schlangen E, Van de Ven M. Properties of capsules containing rejuvenators for their use in asphalt concrete. *Fuel* 2011;90(2):583-591.
- [206] EuropeanStandard. EN 1426. *Bitumen and bituminous binders. Determination of needle penetration*. EN 1426. BSI; 2015.
- [207] EuropeanStandard. EN 1427. *Bitumen and bituminous binders. Determination of the softening point. Ring Ball method*. EN 1427. BSI; 2015.
- [208] EuropeanStandard. EN 12607-1. *Bitumen and bituminous binders. Determination of the resistance to hardening under influence of heat and air. RTFOT method*. EN 12607-1. BSI; 2014.
- [209] EuropeanStandard. EN 14769. *Bitumen and bituminous binders. Accelerated long-term ageing conditioning by a Pressurized Ageing Vessel (PAV)*. EN 14769. BSI; 2012.
- [210] EuropeanStandard. EN 15326. *Bitumen and bituminous binders. Measurement of density and specific gravity. Capillary-stoppered pycnometer method*. EN 15326. BSI; 2009.
- [211] EuropeanStandard. EN 12697-6. *Bituminous mixtures. Test methods for hot mix asphalt. Determination of bulk density of bituminous specimens*. EN 12697-6. BSI; 2012.
- [212] EuropeanStandard. EN 12697-8. *Bituminous mixtures. Test methods for hot mix asphalt. Determination of void characteristics of bituminous specimens*. EN 12697-8. BSI; 2003.
- [213] Grossegger D, Garcia A. Influence of the thermal expansion of bitumen on asphalt self-healing. *Applied Thermal Engineering* 2019;156:23-33.
- [214] Liu S, Li S, Liu J. Jurin's law revisited: Exact meniscus shape and column height. *The European Physical Journal E* 2018;41(3):46-53.
- [215] BritishStandard. BS 2000-143. *Methods of test for petroleum and its products. Determination of asphaltenes (heptane insolubles) in crude petroleum and petroleum products*. BS 200-143. BSI; 2004.
- [216] EuropeanStandard. EN 12606-1. *Bitumen and bituminous binders. Determination of the paraffin wax content. Method by distillation*. EN 12606-1. BSI; 2015.
- [217] EnergyInstitute. IP 469. *Determination of saturated, aromatic and polar compounds in petroleum products by thin layer chromatography and flame ionization detection*. IP469-2934869. energy institute; 2001.

- [218] ASTMInternational. ASTM D4124-09. *Standard Test Method for Separation of Asphalt into Four Fractions*. ASTM D4124-09. ASTM International, West Conshohocken, PA: ASTM International; 2009.
- [219] Grossegger D, Garcia A. The effect of water and pressure on the self-healing of macro cracks in asphalt mortar beams. *Construction and Building Materials* under review.
- [220] Islam MR, Tarefder RA. Determining thermal properties of asphalt concrete using field data and laboratory testing. *Construction and Building Materials* 2014;67:297-306.
- [221] Asaeda T, Ca VT, Wake A. Heat storage of pavement and its effect on the lower atmosphere. *Atmospheric Environment* 1996;30(3):413-427.
- [222] Al-Abdul Wahhab H, Balghunaim F. Asphalt pavement temperature related to arid Saudi environment. *Journal of Materials in Civil Engineering* 1994;6(1):1-14.
- [223] Narayan S, Krishnan J, Deshpande A, Rajagopal K. Nonlinear viscoelastic response of asphalt binders: An experimental study of the relaxation of torque and normal force in torsion. *Mechanics Research Communications* 2012;43:66-74.
- [224] Barraza HJ, Kunapuli S, Edgar A. Advancing contact angles of Newtonian fluids during “high” velocity, transient, capillary-driven flow in a parallel plate geometry. *The Journal of Physical Chemistry B* 2002;106(19):4979-4987.
- [225] Washburn EW. The dynamics of capillary flow. *Physical Review* 1921;17(3):273-283.
- [226] Dussan E. On the spreading of liquids on solid surfaces: static and dynamic contact lines. *Annual Review of Fluid Mechanics* 1979;11(1):371-400.
- [227] Hamraoui A, Nylander T. Analytical approach for the Lucas–Washburn equation. *Journal of Colloid and Interface Science* 2002;250(2):415-421.
- [228] Fries N, Dreyer M. The transition from inertial to viscous flow in capillary rise. *Journal of Colloid and Interface Science* 2008;327(1):125-128.
- [229] Hamraoui A, Thuresson K, Nylander T, Yaminsky V. Can a dynamic contact angle be understood in terms of a friction coefficient? *Journal of Colloid and Interface Science* 2000;226(2):199-204.
- [230] Mang HA, Hofstetter G. *Festigkeitslehre*. Springer; 2000.
- [231] Davies J. *Conduction and induction heating*. The Institution of Engineering and Technology (IET); 1990.
- [232] Doraiswamy D, Mujumdar A, Tsao I, Beris A, Danforth S, Metzner A. The Cox–Merz rule extended: a rheological model for concentrated suspensions and other materials with a yield stress. *Journal of Rheology* 1991;35(4):647-685.
- [233] Cox W, Merz E. Correlation of dynamic and steady flow viscosities. *Journal of Polymer Science* 1958;28(118):619-622.
- [234] Mehrotra AK, Patience GS. Unified entry length for newtonian and power-law fluids in laminar pipe flow. *The Canadian Journal of Chemical Engineering* 1990;68(4):529-533.
- [235] Zhmud B, Tiberg F, Hallstensson K. Dynamics of capillary rise. *Journal of Colloid and Interface Science* 2000;228(2):263-269.
- [236] Tarrer A, Wagh V. The effect of the physical and chemical characteristics of the aggregate on bonding. Strategic Highway Research Program, National Research Council Washington, DC, USA 1991.
- [237] Haley GA. Unit sheet weights of asphalt fractions determined by structural analysis. *Analytical Chemistry* 1972;44(3):580-585.
- [238] Oktay H, Yumrutaş R, Akpolat A. Mechanical and thermophysical properties of lightweight aggregate concretes. *Construction and Building Materials* 2015;96:217-225.
- [239] Luo P, Gu Y. Effects of asphaltene content on the heavy oil viscosity at different temperatures. *Fuel* 2007;86(7-8):1069-1078.
- [240] Altgelt K, Harle O. The effect of asphaltenes on asphalt viscosity. *Industrial & Engineering Chemistry Product Research and Development* 1975;14(4):240-246.
- [241] Saal R. Physical properties of asphaltic bitumen. 2. Surface phenomena, thermal and electrical properties, etc. Amsterdam: Elsevier Science Publishing Co., Inc; 1950:77-108.
- [242] Einstein A. Eine neue Bestimmung der Moleküldimensionen. *Annalen der Physik* 1906;324(2):289-306.
- [243] Li X-J, Marasteanu M. Using semi circular bending test to evaluate low temperature fracture resistance for asphalt concrete. *Experimental Mechanics* 2010;50(7):867-876.
- [244] Price DM, Jarratt M. Thermal conductivity of PTFE and PTFE composites. *Thermochimica Acta* 2002;392:231-236.

- [245] Cherney EA. Silicone rubber dielectrics modified by inorganic fillers for outdoor high voltage insulation applications. *Electrical Insulation and Dielectric Phenomena, 2005. CEIDP'05. 2005 Annual Report Conference on*. Institute of Electrical and Electronics Engineers (IEEE); 2005:1-9.
- [246] Masson J, Polomark G. Bitumen microstructure by modulated differential scanning calorimetry. *Thermochimica Acta* 2001;374(2):105-114.
- [247] Vollmer M. Newton's law of cooling revisited. *European Journal of Physics* 2009;30(5):1063-1084.
- [248] Stephan K, Mayinger F. *Thermodynamik: Band 2: Mehrstoffsysteme und chemische Reaktionen. Grundlagen und technische Anwendungen*. Springer-Verlag; 2013.
- [249] Callen HB. *Thermodynamics and an Introduction to Thermostatistics*. Wiley; 1998.
- [250] Dietrich WE. Settling velocity of natural particles. *Water Resources Research* 1982;18(6):1615-1626.
- [251] Cheng N-S. Simplified settling velocity formula for sediment particle. *Journal of Hydraulic Engineering* 1997;123(2):149-152.
- [252] Peralta JM, Meza BE, Zorrilla SE. Analytical solutions for the free-draining flow of a Carreau-Yasuda fluid on a vertical plate. *Chemical Engineering Science* 2017;168:391-402.
- [253] Ali A, Underwood A, Lee Y-R, Wilson DI. Self-drainage of viscous liquids in vertical and inclined pipes. *Food and Bioprocesses* 2016;99:38-50.
- [254] Jeffreys H. The draining of a vertical plate. *Mathematical Proceedings of the Cambridge Philosophical Society*. 26. Cambridge University Press; 1930:204-205.
- [255] Morey FC. Thickness of a liquid film adhering to surface slowly withdrawn from the liquid. *Journal of Research of the National Bureau of Standards* 1940;25:385-393.
- [256] Xia NN, Xiong XM, Rong MZ, Zhang MQ, Kong F. Self-healing of polymer in acidic water toward strength restoration through the synergistic effect of hydrophilic and hydrophobic interactions. *ACS Applied Materials & Interfaces* 2017;9(42):37300-37309.
- [257] Ahn BK, Lee DW, Israelachvili JN, Waite JH. Surface-initiated self-healing of polymers in aqueous media. *Nature Materials* 2014;13(9):867.
- [258] Petersen J, Plancher H, Ensley E, Venable R, Miyake G. Chemistry of asphalt-aggregate interaction: relationship with pavement moisture-damage prediction test. *Transportation Research Record* 1982(843):95-104.
- [259] Ahmad M, Mannan UA, Islam MR, Tarefder RA. Chemical and mechanical changes in asphalt binder due to moisture conditioning. *Road Materials and Pavement Design* 2018;19(5):1216-1229.
- [260] dos Santos S, Partl MN, Poulikakos LD. Newly observed effects of water on the microstructures of bitumen surface. *Construction and Building Materials* 2014;71:618-627.
- [261] Hefer AW, Little DN, Lytton RL. A synthesis of theories and mechanisms of bitumen-aggregate adhesion including recent advances in quantifying the effects of water. *Journal of the Association of Asphalt Paving Technologists* 2005;74:139-196.
- [262] Terzaghi K. *Theoretical Soil Mechanics*. New York: JohnWiley & Sons; 1943.
- [263] Kim Y-R, Little D, Lytton R. Effect of moisture damage on material properties and fatigue resistance of asphalt mixtures. *Transportation Research Record: Journal of the Transportation Research Board* 2004(1891):48-54.
- [264] Katti P, Chaudhri M. Viscosities of Binary Mixtures of Benzyl Acetate with Dioxane, Aniline, and m-Cresol. *Journal of Chemical & Engineering Data* 1964;9(3):442-443.
- [265] Fort R, Moore W. Viscosities of binary liquid mixtures. *Transactions of the Faraday Society* 1966;62:1112-1119.
- [266] Samec Z. Electrical double layer at the interface between two immiscible electrolyte solutions. *Chemical Reviews* 1988;88(4):617-632.
- [267] Coker D, Reimers J, Watts R. The infrared absorption spectrum of water. *Australian Journal of Physics* 1982;35(5):623-638.
- [268] Bayly J, Kartha V, Stevens W. The absorption spectra of liquid phase H₂O, HDO and D₂O from 0.7 μ m to 10 μ m. *Infrared Physics* 1963;3(4):211-222.
- [269] Campbell PG, Wright JR. Infrared spectra of asphalts: some aspects of the changes caused by photooxidation. *Journal of Research of the National Bureau of Standards* 1964;68C(2):115-123.

- [270] Jerjen I, Poulikakos LD, Plamondon M, Schuetz P, Luethi T, Flisch A. Drying of Porous Asphalt Concrete Investigated by X-Ray Computed Tomography. *Physics Procedia* 2015;69:451-456.
- [271] Poulikakos L, Gilani MS, Derome D, Jerjen I, Vontobel P. Time resolved analysis of water drainage in porous asphalt concrete using neutron radiography. *Applied Radiation and Isotopes* 2013;77:5-13.